

Development of Innovative Techniques for the Manufacture of Bioresorbable Composites Intended as Fracture Fixation Devices

By

Fernando Barrera Betanzos

(BSc, MSc)

Thesis submitted to the University of Nottingham for the degree of

Doctor of Philosophy

September 2017

If I have seen further, it is by standing on the shoulders of two giants; my parents,

Prócoro Barrera Nabor
&
Lucrecia Betanzos Fuentes

Abstract

In this project innovative manufacturing processes have been developed and characterised for the efficient and effective fabrication of PGF-PLA composites which have adequate properties for the fixation of fractured bones in flat and curved geometries.

Fully bioresorbable composite plates where produced by compression moulding of unidirectional phosphate glass fibre mats and PLA films alternatively stacked inside the mould cavity. The implementation of cyclic pressure during the compression moulding consolidation stage resulted in the production the strongest PGF-PLA composites hitherto reported. The strength of the composites consolidated via cyclic pressure was at least 30% higher with respect to the control samples fabricated using the conventional static pressure profile, reaching values of 480 MPa for plates reinforced with 0.45 fibre volume fraction. The increases in composite strength were attributed to the influence of pressure cycling on the fibre network permeability, melt viscosity and capillary pressure, leading to improved fibre impregnation with respect to statically applied pressure, obviating the need for elevated processing temperatures to reduce the melt viscosity. Pressure cycling seemed to promote the formation of transcrystalline layer around the fibres which could have also contributed to the superior properties of composites consolidated under cyclic pressure.

PGF-PLA composite rods with cylindrical cross sections were manufactured via uniaxial compression and plane strain forging of preconsolidated composite blanks obtained from compression moulded composite plates. Forging under uniaxial conditions reduced both the flexural strength and the elastic modulus of all the composite rods in comparison to the compression moulded composite plates by as much as 85% and 47%, respectively, for the $0.35v_f$ samples consolidated under cyclic pressure, as a result of the fracture of the fibres consequent to the extensional flow.

Fibre fracture was prevented through confinement of the deformation to the ***x-y*** plane during plane strain forging. The mechanical properties of the compression moulded composite plates were preserved in the forged composite rods with 0.15 and 0.25 fibre volume fractions, but the high segregation of fibres in the $0.35v_f$ and $0.45v_f$ compression moulded composite

plates fabricated with thick glass fibre mats led to the reduction of both the flexural strength and modulus of the forged composite rods with respect to the compression moulded composite plates by as much as 74% and 29%, respectively, for the $0.45v_f$ consolidated under cyclic pressure, as a result of the nucleation of intra-ply cracks during plane strain forging. The deleterious effect of intra-ply cracks in the plane strain forged composite rods was significantly reduced by stacking a larger number of thinner phosphate glass fibre mats prior to compression moulding of the $0.35v_f$ and $0.45v_f$ composite plates.

The properties of the forged composite rods decreased in aqueous media. The initial loss of strength and modulus was attributed to the water-mediated lubrication of the fibre-matrix interface. Further decreases in mechanical properties were related to the fibre diameter reduction as a result of quick glass dissolution, which impaired the frictional stress transfer. Complete loss of the reinforcing effect of glass fibres was observed after 15 days of immersion in aqueous media.

Cylindrical PGF-PLA composite rods were also produced via a new and leaner manufacturing method consisting in compression moulding of thermoplastic hybrid preforms. Hybrid preforms were produced by depositing a sheath of PLA on phosphate glass fibre bundles continuously fed into a cross head extrusion die. Due to the characteristics of the technique, composites could be reinforced with both as-drawn and annealed phosphate glass fibres which were embrittled as a result of anisotropy relaxation and the formation of a surface tensile layer following heat treatment.

On account of the effect of annealing on the phosphate glass fibres mechanical properties, the flexural strength of as-drawn fibre reinforced compression moulded composite rods was higher with respect to annealed fibre reinforced ones, the former reaching maximum strength values of 371 MPa for the 0.45vf samples in comparison to 278 MPa for the latter.

The flexural moduli of the composites rods manufactured through consolidation of PLA-sheathed fibre bundles were the highest hitherto reported for bioresorbable composites reaching values in excess of 30 GPa for the samples with $0.45v_f$. The higher modulus values of this type of rods with respect to conventional laminated composites were associated with their

unique reinforcement distribution achievable by compression moulding of PLA-sheathed fibre bundles.

Annealed fibre reinforced composites showed a better retention of mechanical properties in wet conditions with respect to as-drawn fibre reinforced ones, as a result of the slow degradation of annealed fibres, managing to present values even exceeding the human cortical bone range during the 30 day *in vitro* degradation study.

Acknowledgements

My deepest gratitude goes to my supervisors Dr Ifty Ahmed and Prof David Grant for their continuous support. Your resourcefulness kept me from chasing shadows and pointed me in the right direction.

I would like to acknowledge the staff in the ITRC workshop, namely Mr Paul Johns, Ben Jennison and Harry Crocker for their assistance in setting up the extrusion line and other numerous technical issues. Without their patience and proactive attitude this project would have never been possible.

Thanks to my friends in the Advanced Materials Group, Dr Uresha Patel, Ana Encerrado Flores, Dr Chenkai Zhu, Yunqi Wang, Chao Tan and Towhid Islam for making the endless hours in the laboratory and office a pleasant experience. I would gladly go through each one of them just for the joy of being with you. A special recognition to my colleague Ana Braz De Souza for her support in the thermal characterisation of numerous samples produced in the latest stage of this project.

My full appreciation to the University of Bradford and their staff, Prof Phil Coates, Dr Adrian Kelly, Dr Dimitrios Vgenopoulos, Dr Karthik Nair and Mr Glen Thompson for their technical support during my multiple visits to their facilities.

I extend my gratitude to the National Council of Science and Technology of Mexico (CONACyT) and the EPSRC Centre for Innovative Manufacturing in Medical Devices for jointly funding this PhD programme.

I am particularly thankful to my sister Ana Laura Barrera Betanzos and my friends Fernando Ramírez Mota, Luis Ángel Hernández Arenas, Noé Seijo González, Rodrigo Gómez Martínez, Luis Carlos Oviedo García, Mariana Aguilar Vivia, Omar Iracheta Cabrera, Érika Barbosa Rangel, Guillermo Moreno Medina, Alma Martínez González, Danai Galaziou, Amber Rawlings, Christel Karim, and specially Tomás González who assisted me in the pursuit of happiness. You will always be with me regardless of where I am.

The greatest distinction and my admiration go to my parents whose countless efforts and perseverance have inspired me through the harshest and most painful moments. I am honoured to be your son.

List of Publications

1. Barrera Betanzos, F., M. Gimeno-Fabra, J. Segal, D. Grant, and I. Ahmed, *Cyclic pressure on compression-moulded bioresorbable phosphate glass fibre reinforced composites.* Materials & Design, 2016. **100**: p. 141-150.
2. F. Barrera Betanzos, M. Gimeno-Fabra, D. Grant, and I. Ahmed, Poster title: Manufacture of Bioresorbable Fibre Reinforced Composites for Fracture Fixation Devices, UK Society for Biomaterials, 31st August-3rd September 2014, Liverpool, UK.
3. F. Barrera Betanzos, M. Gimeno-Fabra, D. Grant, and I. Ahmed, Poster title: Manufacturing Phosphate-Glass Fibre Reinforced Composite Rods as Bioresorbable Intramedullary Nails, MeDe Innovation Annual Conference 2015: Advancing Orthopaedic Medical Manufacturing, Nottingham, UK.
4. F. Barrera Betanzos, M. Gimeno-Fabra, D. Grant, and I. Ahmed, Poster title: Combinational Manufacturing of Composites: Towards bioresorbable fracture fixation, MeDe Innovation Annual Conference 2016: The Future of Manufacturing of Medical Devices, 28th January, Newcastle, UK.
5. F. Barrera Betanzos, M. Gimeno-Fabra, D. Grant, and I. Ahmed, Poster title: Innovative techniques for the Manufacture of Fully Bioresorbable Composites, 10th World Biomaterials Congress, May 17th-22nd 2016, Montreal Canada.

Table of Contents

Abstract i
Acknowledgements iv
List of Publications v
Table of Contents vi
List of Figures x
List of Tables xviii
Abbreviations and Nomenclature xx
I) Introduction 1
II) Aims and Objectives 4
1 Literature Review 6
1.1 Bone: The Material 6
1.2 Bone Metabolism 9
1.3 Bone Fracture 9
1.3.2 Primary or Direct Bone Healing 10
1.3.3 Secondary or Indirect Fracture Healing 11
1.4 Fracture Management 12
1.4.1 Intramedullary Rods 12
1.5 Biomaterials in Orthopaedics 14
1.5.1 Metallic Biomaterials 14
1.5.2 Polymeric Biomaterials 16
1.5.3 Ceramic Biomaterials 24
1.5.4 Polymer-matrix Reinforced Composite Biomaterials 35
2 Materials and Methods 48
2.1 Glass Synthesis 48
2.2 Melt-drawn Fibre Production and Fibre Heat Treatment 48
2.3 X-ray Diffraction 49
2.4 Glass Density Measurements 49
2.5 Single Fibre Tensile Test 50
2.6 Glass Thermal Analysis 50
2.7 Glass Viscosity Measurements 50
2.8 *In Vitro* Phosphate Glass Dissolution Studies 50
2.8.1 Phosphate Bulk Glass Dissolution Study 50
2.8.2 Phosphate Glass Fibre Dissolution Studies 51
2.9 Energy Dispersive X-ray (EDX) Analysis 53
2.10 Scanning Electron Microscopy (SEM) 53
2.11 Fibre Reinforced Composite Plate Manufacturing via Laminate Stacking 54

2.12 Fibre Reinforced Composite Rod Manufacturing via Forging 56

2.13 Fibre Reinforced Composite Rod Manufacturing via Consolidation of PLA-sheathed Phosphate Glass Fibre Bundles.....58

2.13.1 Production of Bare PLA-sheaths via Tubing-type Crosshead Extrusion 58

2.13.2 Production of PLA-sheathed Fibre bundles via Tubing-type Crosshead Extrusion 60

2.13.3 Manufacture of Fibre Reinforced Composite Rods via Compression Moulding of PLA-sheathed Fibre Bundles 61

2.14 PLA Rotational Viscosity Measurements 62

2.15 Void Content Determination.....62

2.16 Fibre reinforced Composite Rod *In Vitro* Degradation Study.....64

2.17 Flexural Testing 65

2.18 Differential Scanning Calorimetry (DSC).....65

2.19 Advanced Polymer Chromatography (APC).....66

3 Results..... 67

3.1 Characterisation and *In Vitro* Degradation Studies of Bioresorbable Bulk Glass and Fibres of the $45P_2O_5{\cdot}16CaO{\cdot}13Na_2O{\cdot}24MgO{\cdot}2Fe_2O_3$ mol% Composition 67

3.1.1 Glass Viscosity 67

3.1.2 Melt-drawn Fibre Production.....67

3.1.3 X-ray Glass Powder Diffraction.....69

3.1.4 Glass Compositional EDX Analysis 70

3.1.5 Glass Thermal Analysis 70

3.1.6 Single Fibre Tensile Test 71

3.1.7 Phosphate Bulk Glass *In Vitro* Degradation 72

3.1.8 Phosphate Glass Fibre *In Vitro* Degradation.....72

3.2 Manufacture of Fully Bioresorbable Fibre Reinforced PGF-PLA Composite Plates via Cyclic Pressure-assisted Compression Moulding 79

3.2.1 PLA Rotational Viscosity.....79

3.2.2 Compression Moulded PGF-PLA Composite Plates Flexural Properties 82

3.2.3 PGF-PLA Compression Moulded Composite Plates Thermal Analysis 84

3.2.4 PGF-PLA Compression Moulded Composite Plates Void Content Analysis 86

3.2.5 Compression Moulded PF-PLA Composite Plates SEM Cross Sectional Analysis 87

3.2.6 Compression Moulded PGF-PLA Composite Plates GPC Analysis 88

3.2.7 Effect of Processing Variables on Cyclic Pressure-assisted PGF-PLA Composite Plate Compression Moulding.....89

3.3 Effect of Forging on Mechanical Properties and *In Vitro* Degradation of Fully Bioresorbable Fibre Reinforced PGF-PLA Composite Rods 92

3.3.1 Forged Composite Rods SEM Cross Sectional Imaging 92

3.3.2 Effect of Forging on PGF-PLA Composite Rods Flexural Properties 94

3.3.3 Effect of Forging on PGF-PLA Composite Rods Structure 97

3.3.4 Effect of Glass Fibre Mat Thickness on the Properties of PGF-PLA Composite Rods Fabricated via Forging 98

3.3.5 In Vitro Degradation of PGF-PLA Composite Rod Fabricated via Forging 99

3.3.6 Thermal Analysis of PGF-PLA Composite Rods Fabricated via Forging 106

3.3.7 GPC Analysis of PGF-PLA Composite Rods Fabricated via Forging 108

3.4 Manufacture of Fully Bioresorbable Composite Rods via Compression Moulding of Polymer Sheathed Fibre Bundles 109

3.4.1 Production of Bare PLA-sheath via Crosshead Extrusion 109

3.4.2 SEM Cross Sectional Imaging of PGF-PLA Composite Rods Fabricated via PLA-sheathed Fibre Bundle Compression Moulding 112

3.4.3 Void Content Analysis of PGF-PLA Composite Rods Fabricated via PLA-sheathed Fibre Bundle Compression Moulding 113

3.4.4 Flexural Properties of PGF-PLA Composite Rods Fabricated via PLA-sheathed Fibre Bundle Compression Moulding 114

3.4.5 *In Vitro* Degradation of PGF-PLA Composite Rod Fabricated via PLA-sheathed Fibre Bundle Compression Moulding 115

3.4.6 Thermal Analysis of PGF-PLA Composite Rods Fabricated via Compression Moulding of PLA-sheathed Fibre Bundles 124

3.4.7 GPC Analysis of PGF-PLA Composite Rods Fabricated via Compression Moulding of PLA-sheathed Fibre Bundles 128

4 Discussion 129

4.1 Characterisation and *In Vitro* Degradation Studies of Bioresorbable Bulk Glass and Fibres of the $45P_2O_5{\cdot}16CaO{\cdot}13Na_2O{\cdot}24MgO{\cdot}2Fe_2O_3$ mol% composition 129

4.1.1 Melt-Drawn production and Characterisation of P45Fe2 Phosphate Glass Fibres 129

4.1.2 Dissolution Studies of P45Fe2 Bulk Glass and Glass Fibres ..133

4.2 Manufacture of Fully Bioresorbable Fibre Reinforced PGF-PLA Composite Plates via Cyclic Pressure-assisted Compression Moulding ...138

4.2.1 Rheological Characterisation of 3251D Poly(lactic acid) 138

4.2.2 Effect of Processing Variables in Cyclic Pressure-assisted Compression Moulding of Fibre Reinforced Composite Plates 139

4.2.3 Characterisation of Compression Moulded Composite Plates 141

4.3 Effect of Forging on Mechanical Properties and *In Vitro* Degradation of Fully Bioresorbable Fibre Reinforced PGF-PLA Composite Rods 148

4.3.1 Effect of Uniaxial Compression Forging on Fibre Reinforced Composite Rods 148

4.3.2 Effect of Plane Strain Forging on Fibre Reinforced Composite Rods 150

4.3.3 Effect of Glass Fibre Mat Thickness in Plane Strain Forged Fibre Reinforced Composite Rods 151

4.3.4 In Vitro Degradation Study of Bioresorbable Fibre Reinforced Composite Rods Manufactured via Plane Strain Forging of Preconsolidated Composite Blanks 153

4.4 Manufacture of Fully Bioresorbable Composite Rods via Compression Moulding of Polymer Sheathed Fibre Bundles 165

4.4.1 Production of bare PLA-sheath via Tubing-type Crosshead Extrusion 165

4.4.2 Characterisation of Bioresorbable Fibre Reinforced Composite Rods Manufactured via Compression Moulding of PLA-sheathed Fibre Bundles 166

4.4.3 In Vitro Degradation Study of Bioresorbable Fibre Reinforced Composite Rods Manufactured via Compression Moulding of PLA-sheathed Fibre Bundles 172

4.5 Mechanical Performance of PLA-reinforced Composites in Wet Conditions 181

5 Conclusions and Future Work 185

5.1 Conclusions 185

5.1.1 Characterisation and *In Vitro* Degradation Studies of Bioresorbable $45P_2O_5{\cdot}16CaO{\cdot}13Na_2O{\cdot}24MgO{\cdot}2Fe_2O_3$ mol% Bulk Glass and Glass fibres 185

5.1.2 Manufacture of Fully Bioresorbable Fibre Reinforced PGF-PLA Composite Plates via Cyclic Pressure-assisted Compression Moulding 186

5.1.3 Effect of Forging on Mechanical Properties and In Vitro Degradation of Fully Bioresorbable Fibre Reinforced PGF-PLA Composite Rods 188

5.1.4 Manufacture of Fully Bioresorbable Composite Rods via Compression Moulding of Polymer Sheathed Fibre Bundles 190

5.2 Future work 194

References 199

List of Figures

Figure 1.1: Hierarchical structure of bone. 6

Figure 1.2: SEM image of a mineralised collagen fibre. The black regions represent the nanosized non-stoichiometric hydroxyapatite crystals..... 7

Figure 1.3: Photograph of a proximal tibia section showing an outer thin layer of cortical (compact) bone and the inner trabecular (cancellous) bone network comprising trabecular plates and rods. Network voids are filled with bone marrow in living specimens. 7

Figure 1.4: Schematic of the femoral bone structure. 8

Figure 1.5: Photomicrography of osseous tissue (300x H&E stain) showing the three types of cells involved in bone remodelling, namely: i) giant multinucleated osteoclasts, ii) bone forming osteoblasts and iii) extracellular matrix-trapped osteocytes..... 9

Figure 1.6: Schematic representation of primary fracture healing through "cutting cone" remodelling units, after fixation with a dynamic compression plate that deviates the force pathway, shielding the fracture site from stresses. 11

Figure 1.7: Schematic representation of the indirect fracture healing process, displaying the main stages towards stabilisation through callus formation viz.: a) haematoma formation and coagulation, b) acute inflammation and c) repair via callus development. 12

Figure 1.8: Intramedullary nail femoral bone fracture fixation and interlocking screws in the femoral neck. 13

Figure 1.9: a) Radiographs of a mid-shaft femoral fracture treated with distally and proximally locked intramedullary nails, showing bone union progressing by secondary fracture healing with callus formation (from left to right). The third image in a) shows an external mineralised 'hard' callus, and a central cartilaginous 'soft' callus; b) radiograph of radial fracture reduction via compression plating, showing primary bone healing without the formation of a visible external callus. 14

Figure 1.10: Common metallic implants used in the orthopaedics field; a) stainless steel dynamic compression plates, b) Vitalium (Co-Cr) alloy total knee replacement and c) titanium total hip replacement 15

Figure 1.11: Polymeric debris discharging sinus formed as a result of foreign-body reaction to a PGA screw. The sinus emerged 11 weeks after implantation 17

Figure 1.12: L- and D- enantiomers of (2-hydroxy propionic acid) or lactic acid 18

Figure 1.13: Polymerisation route of PLA from L- and D-lactic acid monomeric units.....19
Figure 1.14: Schematic representation of a spherulite 20

Figure 1.15: Hydrolytic cleavage of poly(lactic acid) chains.....20

Figure 1.16: Schematic representation of the crystallite disposition in a semicrystalline PLA sample. The amplification of the region enclosed by dashed lines illustrates the high concentration of carboxyl and hydroxyl groups (closed and open circles, respectively) in the amorphous regions after their rejection from crystalline domains.....21

Figure 1.17: Schematic representation of the polymer chain arrangement in amorphous PLA products. Open circles represent carboxyl end-groups, while closed ones depict hydroxyl moieties.....22

Figure 1.18: Simplified diagram of *in vivo* PLA degradation sequence 23

Figure 1.19: Intramolecular transesterification reaction pathways leading to the formation of oligomeric rings (left) and the production of acetaldehyde plus carbon monoxide (right).....24

Figure 1.20: Structural units found in phosphate based glasses.....27

Figure 1.21: Ionic crosslinks between adjacent polymer-like phosphate chains 28

Figure 1.22: Ion-exchange reaction in which protons associate with NBO and crosslinking cations are released into solution 30

Figure 1.23: Hydrolytic cleavage of P-O-P bonds.....30

Figure 1.24: Effect of cooling rate on the volume of a glass forming melt.....33

Figure 1.25: Cross section SEM images of $50P_2O5{\cdot}40CaO{\cdot}10NaO_2$ mol% phosphate glass fibres after a) 6 h and 72 h of SBF conditioning.....34

Figure 1.26: Commercially available thermoplastic hybrid preforms.....38

Figure 1.27: Distribution of bioactive glass spheres in a PLA matrix with 40 wt% of filler. No adhesion was observed between the polymer and BG spheres.....41

Figure 1.28: Distribution of TCP particles in a PLA matrix with 20 wt% of filler. No adhesion is observed between the polymer and TCP particles.....41

Figure 1.29: SEM micrograph of a compression moulded PLA composite plate reinforced with 10 mm phosphate glass chopped fibres.....42

Figure 2.1: Device set-up for the extraction of conditioning media during glass fibre dissolution studies. 52

Figure 2.2: (right) Exploded view of the purpose-built compression moulding tool and (left) transverse cross section of the compression moulding tool assembly during the consolidation stage. 54

Figure 2.3: Schematic representation of the nominal temperature and pressure processing schemes for the PLA-PGF composites: a) static pressure and b) cyclic pressure case. 55

Figure 2.4: Manufacturing cycle for composite forged rods. Composite plates were consolidated through either static or cyclic pressure compression moulding. The 4.5 mm × 110 mm × 110 mm plates (thickness × width × length) were then sectioned along the fibre direction into 4.5 mm × 3 mm × 110 mm rectangular blanks (SEM cross sectional view is shown in the inset) and forged at 90°C under 5 bar pressure into cylindrical rods (SEM cross sectional view is shown in the inset) using two die configurations, namely: i) the blank was constrained in the fibre direction to produce a 4 mm rod under plane strain conditions and ii) the blank was free to deform in the fibre direction to produce a 4 mm rod under uniaxial compression. 57

Figure 2.5: Exploded view of the crosshead tubing-type configuration used for PLA-sheathing of phosphate glass fibre bundles. 58

Figure 2.6: Manufacturing cycle of phosphate glass fibre-reinforced bioresorbable composite rods produced via compression moulding of PLA-sheathed glass fibre bundles. 61

Figure 3.1: (a) Melt-quenched P45Fe2 bulk glass and (b) melt-drawn glass fibres. 67

Figure 3.2: (a) Influence of the temperature on the viscosity of P45Fe2 glass. (b) Differences in the furnace set temperature and the temperature measured in a region close to the bushing nozzle. 68

Figure 3.3: Influence of drawing speed on the diameter (±SD) of fibres drawn at 1000°C with a glass load of approximately 300 g. 68

Figure 3.4: Powder X-ray diffraction patterns of P45Fe2 bulk glass and glass fibres in the as-drawn and annealed condition. 69

Figure 3.5: DSC thermograms of P45Fe2 bulk glass and glass fibres in the as-drawn and annealed condition. The inset shows a magnification of the region highlighted by the dashed blue line. 71

Figure 3.6: (a) % Mass loss profile (±SD) for P45Fe2 bulk glass conditioned in PBS at 37°C and (b) pH variation of the media collected from the bulk glass degradation vials. 72

Figure 3.7: SEM images of (left) annealed and (right) as-drawn fibres of the P45Fe2 composition, respectively, at (a) & (b) day 0, (c) & (d) day 1, (e) & (f) day 3, (g) & (h), day 15 and (i) & (j) day 30 of immersion in PBS at 37°C. 74

Figure 3.8: SEM images of (left) annealed and (right) as-drawn fibres of the P45Fe2 composition, respectively, at (a) & (b) day 0, (c) & (d) day 1, (e) & (f) day 3, (g) & (h), day 15 and (i) & (j) day 30 of immersion in deionised water at 37°C. 75

Figure 3.9: (a) % Mass loss, m_{LF}, (±SD) and (b) fibre diameter (±SD) variation for annealed (purple markers and purple lines) and as-drawn fibres (red markers and red lines) conditioned in deionised water 'DI' and PBS at 37°C,

respectively. The inset of (a) shows the variation (±SD) of the conditioning media collected from as-drawn and annealed fibres. The % mass loss and the fibre diameter variation profiles for PBS conditioning were denoted by solid markers and solid lines, whereas the % mass loss and fibre diameter variation for deionised water conditioning were denoted by open markers and dashed lines. 76

Figure 3.10: Estimated % mass loss, m_E, as calculated from diameter reduction of as-drawn (red markers) and annealed (purple markers). The estimated % mass loss profiles for PBS conditioning were denoted by solid markers and solid lines, whereas the corresponding values for deionised water conditioning were denoted by open markers and dashed lines. The open purple circles and open red squares represent the estimated % mass loss for annealed and as-drawn fibres, respectively. 79

Figure 3.11: Dynamic linear viscoelastic measurements conducted on 3251D PLA. (a) Influence of oscillation frequency, ω, on the storage modulus, G', loss modulus, G'', and complex viscosity, η*, of PLA at the reference temperature of 180°C. (b), (c) & (d) Evolution of the complex viscosity, storage and loss modulus of 3251D PLA with oscillation frequency at different test temperatures, respectively. 80

Figure 3.12: Influence of temperature on 3251D PLA zero shear viscosity (±SD), η_0, as determined by experimental date fitting to the Carreau-Yasuda model....81

Figure 3.13: (a) Influence of the pressure profile on composite plate flexural strength (±SD) and (b) flexural modulus (±SD) with progressively higher fibre content. The black dashed line represents the theoretical composite plate strengths calculated by substitution of mean experimental matrix and fibre strengths in the rule of mixtures. The range of human cortical bone flexural strength is denoted by black dotted lines. 82

Figure 3.14: Representative DSC traces of a) cyclic Pressure and b) static pressure compression moulded composite plates. The inset isolates the area enclosed by the blue dashed line. 85

Figure 3.15: SEM cross sectional images of the (a) & (b) 0.15vf, (c) & (d) 0.25vf, (e) & (f) 0.35vf and (g) & (h) 0.45vf compression moulded composite plates manufactured by (left) static pressure and (right) cyclic pressure profiles, respectively. 88

Figure 3.16: Influence of the magnitude of cyclic pressure consolidation on the (a) flexural strength (±SD) and (b) flexural modulus (±SD) of PLA-PGF composites with 0.35 fibre volume fraction processed at 180°C. 90

Figure 3.17: Influence of the processing temperature on the (a) flexural strength (±SD) and (b) flexural modulus (±SD) of PLA-PGF composites with 0.35 fibre volume fraction consolidated with 40 bar cyclic pressure. 90

Figure 3.18: (left) Transverse plane SEM micrographs of 4.5 mm × 110 mm × 110 mm (thickness × width × length) compression moulded composite plates representative sections, from which 4.5 mm × 3 mm × 100 mm (thickness × width × length) composite blanks were cut and subsequently forged into 4 mm

× 80 mm (diameter × length) composite rods (rigth) with 0.15, 0.25, 0.35 and 0.45 fibre volume fractions.....93

Figure 3.19: Effect of uniaxial compression forging on the flexural (a) strength (±SD) and (b) modulus (±SD) of forged composite rods. The mechanical properties of the initial composite plates are indicated by black dashed lines. The solid columns represent the mechanical properties of the uniaxial compression forged rods. The mechanical properties of the rods forged from cyclic pressure-consolidated 'CP' composite plates are highlighted in red and those representative of rods obtained from static pressure-consolidated 'SP' composite plates are highlighted in blue. 95

Figure 3.20: Effect of plane strain forging on the flexural (a) strength (±SD) and (b) modulus (±SD) of forged composite rods. The mechanical properties of the initial composite plates are indicated by black dashed lines. The solid columns represent the properties of the plane strain composite forged rods. The mechanical properties of the rods forged from cyclic pressure-consolidated 'CP' composite plates are highlighted in red and those representatives of rods obtained from static pressure-consolidated 'SP' composite plates are highlighted in blue. 96

Figure 3.21: Cross sectional SEM images of as-forged 0.35vf composite rods forged via plane strain and uniaxial compression conditions, respectively. (a) Transverse cross section of a 0.35vf composite rod forged under plane strain conditions. (b) Magnified view of the region enclosed by a dotted box is shown in (a). (c) & (d) Longitudinal (*y-z* plane) cross sections of a plane strain and a uniaxial compression forged rod, respectively.....97

Figure 3.22: Transverse cross sectional images of composite plates and the respective plane strain forged rods fabricated using thin glass fibre mats: (a) & (b) composite plate and rod of the 0.35-CP-M series containing 20 thin glass fibre mats, and (b) & (d) composite plate and rod of the 0.45-CP-M series containing 25 thin glass fibre mats.....99

Figure 3.23: Variation of flexural properties of PGF-PLA forged composite rods and neat-PLA control rods during conditioning in PBS at 37°C: (a) Flexural strength (±SD) and (b) flexural modulus (±SD) degradation profiles. The profiles of the forged composite rods obtained from plates consolidated under cyclic pressure (CP) were denoted by solid lines, whereas the profiles of the forged composite rods obtained from plates consolidated under static pressure (SP) were denoted by dashed lines.....101

Figure 3.24: SEM images of the fracture surfaces of a representative neat-PLA rod prior immersion and a 0.35-CP-M forged composite rods at different conditioning time points in PBS at 37°C. (a) Macroscopic view of a fractured non-degraded neat-PLA rod. Magnified fracture surfaces of PBS conditioned samples at (b) day 0, (c) day 1, (d) day 3, (e) day 7, (f) day 15, (g) day 23 and (h) day 30, respectively.....103

Figure 3.25: (a) Water uptake (±SD) and (b) dry mass change profiles (±SD) for PGF-PLA plane strain forged composite rods and neat PLA control rods conditioned in PBS at 37°C. The inset of (a) shows the variation of pH (±SD) for the studied samples. The profiles of the forged composite rods obtained from plates consolidated under cyclic pressure (CP) are denoted by solid

lines, whereas the profiles of the composite rods obtained from plates consolidated under static pressure (SP) are denoted by dashed lines. 105

Figure 3.26: a) Evolution of the crystallinity content (±SD) for the PLA matrix in the PGF-PLA forged composite rods conditioned in PBS at 37°C and (b) variation of number average molecular weight, M_n, (±SD) of the PLA matrix in the composite rods with increasing conditioning time in PBS at 37°C. The profiles of the composite rods obtained from plates consolidated under cyclic pressure (CP) were denoted by solid lines, whereas the profiles of the composite rods obtained from plates consolidated under static pressure (SP) were denoted by dashed lines. 108

Figure 3.27: (a) Variation of feeder output (±SD) with feeder speed. (b) Influence of extrusion temperature on the pressure (±SD) measured at the crosshead die entry. 111

Figure 3.28: Variation of PLA-sheath mass per 80 mm produced with increasing haul-off speed. The PLA-sheath was extruded at 165°C using a screw speed of 30 rpm and a feeder output of 6.6 g. 111

Figure 3.29: Backscattered electron images of the transverse cross section of representative PGF-PLA composite rods with (a) 0.15, (b) 0.25, (c) 0.35 and (d) 0.45 fibre volume fractions fabricated through the consolidation of PLA-sheathed glass fibre bundles. Magnifications of selected regions enclosed by white dashed lines are also shown at the right of the respective rods. 113

Figure 3.30: Influence of fibre volume fraction on the (a) flexural strength (±SD) and (b) flexural modulus (±SD) of PGF-PLA composite rods manufactured through compression moulding of PLA-sheathed bundles of either annealed or as-drawn glass fibres. The ranges of human cortical bone flexural properties were denoted by the black dotted lines. 115

Figure 3.31: Variation of flexural properties of PGF-PLA compression moulded composite rods during conditioning in PBS at 37°C: (a) Flexural strength (±SD) and (b) flexural modulus (±SD). The flexural strength and modulus variation profiles of the composite rods manufactured from PLA-sheathed as-drawn fibre bundles were represented by open markers and dashed lines. The ranges of human cortical bone flexural properties were denoted by black dotted lines. 117

Figure 3.32: (a) Water uptake, m_G, (±SD) and (b) dry mass change, m_L, profiles (±SD) for bioresorbable composite rods manufactured through compression moulding of PLA-sheathed bundles of either annealed of as-drawn fibres conditioned in PBS at 37°C. The inset of (a) shows the pH variation (±SD) of the collected conditioning media for the studied composite rods. The profiles of the bioresorbable composite rods containing as-drawn fibres were denoted by open markers and dashed lines, whereas the profiles of the bioresorbable composite rods containing annealed fibres were denoted by solid markers and solid lines. 119

Figure 3.33: SEM images of the fracture surfaces of representative 0.35vf compression moulded composite rods reinforced with (right) annealed and (left) as-drawn phosphate glass fibres at (a) & (b) day 0, (c) & (d) day 1, (e) & (f) day 7, (g) & (h) day 15, (i) & (j) day 30, respectively, during conditioning in PBS at 37°C. The insets show the backscattered electron images of the

corresponding polished cross sections at the respective conditioning time points. 122

Figure 3.34: Representative DSC traces of as-drawn and annealed fibre reinforced compression moulded composite rods recorded during the second heating cycle once differences in thermal history have been eliminated. The inset shows a magnified view of the region enclosed by the blue dashed line. 126

Figure 3.35: (a) Evolution of the crystallinity content (±SD) for of the PLA matrix in the PGF-PLA compression moulded composite rods conditioned in PBS at 37°C and (b) variation of number average molecular weight, M_n, of the PLA matrix with conditioning time in PBS at 37°C for the bioresorbable compression moulded composite rods reinforced with either annealed or as-drawn glass fibres. The profiles of the bioresorbable composite rods containing as-drawn glass fibres were denoted by open markers and dashed lines, whereas the profiles of the bioresorbable composite rods containing annealed glass fibres were denoted by solid markers and solid lines. 127

Figure 4.1: Comparison of as-drawn glass fibres conditioned in (a) PBS and (b) deionised water during 15 days at 37°C. 136

Figure 4.2: Schematic description of the composte plate consolidation process under cyclic and static pressure. 143

Figure 4.3: (Left) Schematic of the structural changes observed in the reinforcing phosphate glass fibres throughout the forged composite rods degradation study. The glass hydrated layer is represented by the solid blue lines and the precipitate formations are illustrated by the red solid lines enclosing the yellow fibre cores. The PLA matrix is represented by the blue background. Water molecules absorbed by the PLA matrix are depicted by the dotted lines enclosing the water's chemical formula. Water adsorbed at the interface has been represented by dashed blue lines. (Right) Backscattered electron images of the polished cross sections of representative composite rods degraded in PBS at the specified conditioning time point. 157

Figure 4.4: Flow diagrams for the manufacture of fibre reinforced composite rods via (right) forging of preconsolidated composite blanks and (left) compression moulding of PLA-sheathed glass fibre bundles. 172

Figure 4.5: Comparison of the retention of a) flexural strength and b) flexural modulus of selected bioresorbable devices intended as orthopaedic implants, namely: i) 0.45vf compression moulded composite rod reinforced with as-drawn phosphate glass fibres (0.45vf-NA-CMCR), ii) 0.45v_f compression moulded composite rod reinforced with annealed phosphate glass fibres (0.45v_f-A-CMCR), iii) 0.45-CP-M plane strain forged composite rod (0.45-CP-MPSFR) iv) plane strain forged neat-PLA rod, v) phosphate glass fibre reinforced poly(lactic acid) (PGF-PLA) [17] vi) bioresorbable silica-based glass fibre reinforced poly(lactic acid) (SGF-PLA) [193], vii) self-reinforced poly(lactic acid) (SR-PLA) [369], and vii) random phosphate glass fibre reinforced poly(lactic acid) (RM-PGF-PLA) [215]. For clarity, only the best performing samples produced in this study were included. 183

Figure 5.1: Bioresorbable composite rods with structures unique to compression moulding of PLA-sheathed fibre bundles. PLA-matrix is

represented in blue and reinforcing phosphate glass fibres/particles are represented in yellow. 195

Figure 5.2: Exploded view of the pultrusion attachment assembly for the manufacture of semi-finished or finished bioresorbable pultruded composite products.....196

Figure 5.3: Cross section of the crosshead die in the pultrusion configuration. Fibres and molten PLA come into contact inside the impregnation chamber. The impregnated fibre bundles are then consolidated into the desired profile cross section inside the forming die. 196

Figure 5.4: Lateral cross section of the pultrusion attachment showing the pins a) perpendicular and b) aligned parallel to the extrusion axis. PLA melt is represented in blue and the fibre bundle is shown in yellow. 197

Figure 5.5: Top cross section of the pultrusion attachment showing the pins a) perpendicular and b) aligned parallel to the extrusion axis. PLA melt is represented in blue and the fibre bundle is shown in yellow. 198

List of Tables

Table 1.1: Bone mechanical properties 8

Table 1.2: Summary of the physical and mechanical properties of common metallic biomaterials in comparison to natural bone.....15

Table 1.3: Summary of properties for selected polymeric materials.....16

Table 1.4: Effect of processing temperature on the molecular weight of 90/10 PDLLA copolymer.....23

Table 2.1: Composition of the cyclic 'CP' and static pressure 'SP' compression moulded composite plates. 56

Table 2.2: Summary of PLA-sheathed glass fibre bundle production conditions and compression moulded composite rods composition. 60

Table 3.1: Summary of parameters used to confirm the target nozzle yield during fibre drawing at 1000°C. 69

Table 3.2: Summary of EDX analyses (±SD) conducted on P45Fe2 bulk glass polished surface and embedded glass fibres in the as-drawn and annealed conditions. 70

Table 3.3: Summary of physical properties of as-drawn 'NA' and annealed 'A' P45Fe2 glass fibres. 71

Table 3.4: Physical and mechanical properties (±SD) of the PLA-phosphate glass fibre reinforced composite plates constituent phases.....82

Table 3.5: Summary of PLA-PGF composite plates thermal properties consolidated with either static pressure 'SP' or cyclic pressure 'CP'. 86

Table 3.6: Summary of experimental fibre volume fraction and void content analysis (±SD) for composite plates consolidated with either static pressure 'SP' or cyclic pressure 'CP'. 87

Table 3.7: Summary of chromatography results (±SD) for the neat polymer at different stages and PLA in the composite plates fabricated in this study. 89

Table 3.8: Summary of experimental fibre volume fraction and void content analysis (±SD) for fibre reinforced composite plates with 0.35 fibre volume fraction manufactured with increasing consolidation cyclic pressure and processing temperature, respectively.....91

Table 3.9: Summary of reinforcing P45Fe2 glass fibres EDX analysis (±SD) at different conditioning time points.....102

Table 3.10: Thermal properties (±SD) of compression moulded composite plates 'P' and non-degraded plane strain forged composite rods 'R'. 106

Table 3.11: Summary of bare PLA-sheath production at 165°C. 110

Table 3.12: Summary of experimental volume fraction and void content analysis (±SD) for fibre reinforced composite rods fabricated via compression moulding of PLA-sheathed glass fibre bundles. 114

Table 3.13: Summary of EDX analysis conducted on the reinforcing P45Fe2 glass fibres in 0.35vf compression moulded composite rods at different conditioning time points. The time point at which the rods were recovered from solution is indicated by the number at the end of the sample code. 124

Table 3.14: Thermal properties (±SD) of non-degraded fibre reinforced composite rods fabricated via PLA-sheathed glass fibre bundle compression moulding. 125

Abbreviations and Nomenclature

45s5	46.1SiO_2·26.9CaO·24.4NaO·2.6P_2O_5 mol%
a	Weight of the sample in air
A	Annealed phosphate glass fibres
ATP	Adenosine Triphosphate
a.u.	Arbitrary units
b	Weight of the sample submerged in ethanol
BG	Bioglass
BS	British Standard
CMCR	Compression Moulded Composite Rod
CP	Cyclic Pressure
CT1	Type 1 Collagen
d	Fibre diameter
D	Bushing nozzle diameter
d_0	Fibre diameter measured prior immersion
DDR	Drawdown Ratio
d_i	Fibre diameter at the *ith* time point
DI	Deionised water
DSC	Differential Scanning Calorimetry
e	Elongation
E	Elastic modulus
E_C	Compressive modulus
E_S	Shear modulus
EDX	Energy Dispersive X–ray analysis
E_T	Tensile modulus
f	Extruder feeding rate
g	Gravitational acceleration
G'	Storage modulus
G''	Loss modulus
HA	Hydroxyapatite
IM	Intramedullary
ISO	International Standards Organization
L	Bushing nozzle length
LC	Liquid Chromatography
L/D	Extruder screw Length to Diameter ratio

$\dot{m}$	Bushing nozzle yield
M	Thin phosphate glass fibre mat
m_0	Initial composite rod mass
$M_{2/v}O$	Modifier oxide with valence ***v***
m_b	Bulk glass percentage mass loss
m_{bi}	Initial bulk glass mass
m_{bt}	Bulk glass mass at the *ith* day
m_B	Fibre bundle linear density
m_d	Composite dry mass at the *ith* time point
m_E	Estimated % mass loss
m_f	Phosphate glass fibre mass
m_G	Composite rod % water uptake
m_i	Initial mass of the glass fibre bundle
m_L	Composite rod % mass loss
m_{LF}	Glass fibre percentage mass loss
M_n	Number average molecular weight
m_m	Poly(lactic acid) mass
m_S	Poly(lactic acid) sheath linear density
m_t	Glass fibre bundle at the *ith* time point
m_w	Composite wet mass at the *ith* time point
M_w	Weight average molecular weight
M_z	Size average molecular weight
n	Number of specimens
NA	As-drawn phosphate glass fibres
NBOs	Non-Bridging Oxygens
P	Composite plate
P40Fe4	$40P_2O_5{\cdot}16CaO{\cdot}16Na_2O{\cdot}24MgO{\cdot}4Fe_2O_3$
P45Fe2	$45P_2O_5{\cdot}16CaO{\cdot}13Na_2O{\cdot}24MgO{\cdot}2Fe_2O_3$
P50Fe5	$50P_2O_5{\cdot}40CaO{\cdot}5Na_2O{\cdot}24MgO{\cdot}5Fe_2O_3$ mol%
PBS	Phosphate Buffered Saline
PCL	Polycaprolactone
PDLA	Poly(DL-lactide)
PEEK	Polyether Ether Ketone
PGA	Poly(glycolic acid)
PGF	Phosphate Glass Fibres
PLA	Poly(lactic acid)

PLLA	Poly-L-lactic acid
PMMA	Polymethylmethacrylate
PSFR	Plane Strain Forged Rod
PTFE	Polytetrafluoroethylene
$\mathbf{Q}^{i}$	Connectivity number
R	Composite rod
RM	Random Mat
S_B	Flexural strength
SBF	Simulated Body Fluid
S_C	Compressive strength
S_{cm}	Composite strength
SD	Standard Deviation
SEC	Size Exclusion Chromatography
SEM	Scanning Electron Microscope
S_f	Fibre strength
S_m	Matrix strength
SP	Static Pressure
SR	Self-Reinforced
S_S	Shear strength
S_T	Tensile strength
T	Temperature
TCP	Tricalcium Phosphate
T_f	Fictive temperature
T_g	Glass transition temperature
T_m	Melting temperature
TRIS	Tris(hydroxymethyl)aminomethane
t_S	PLA sheath thickness
T_X	Cold crystallisation peak temperature
T_{X0}	Crystallisation onset temperature
UD	Unidirectional
UHMWPE	Ultra-high Molecular Weight Polyethylene
v	Fibre drawing speed
$\dot{V}$	Volumetric yield
v_f	Fibre volume fraction
v_{HO}	Haul-off speed
w_m	Matrix mass fraction

w_f	Fibre mass fraction
x	Modifier oxide mol%
X	Crystallinity content
α	Thermal coefficient of expansion
ΔH_c	Cold crystallisation enthalpy
ΔH_m^0	Melting enthalpy for infinite size PLLA crystals
ε_z	Deformation in the z direction
η_0	Zero shear viscosity
η^*	Complex viscosity
λ	Wavelength
ρ	Density
ρ_a	Density of air
ρ_b	Density of ethanol
ρ_{ce}	Composite experimental density
ρ_{ct}	Composite theoretical density
ρ_f	Fibre density
ρ_m	Matrix density
ρ_{m0}	Density of amorphous PLA at 23°C
ρ_{mT}	Density of PLA at the processing temperature
σ	Glass surface tension
τ	Glass structure relaxation time
Ø	Diameter
ϕ_v	Percentage void content
ϕ_t	Maximum content of voids
ω	Oscillation frequency

I) Introduction

Femoral diaphyseal fractures are one of the most common long bone fractures affecting the lower extremities [1, 2]. Due to the high vascularity and volume of soft tissue associated with the femur, traumas in this region often require surgical intervention to prevent the displacement of bone fragments due to muscle traction [2].

Intramedullary 'IM' nails represents the best option to reduce and stabilise long bone fragments in virtue of the minor tissue tethering, and reduced infection risk associated with its surgical implantation [3, 4]. Furthermore IM nails are implanted at the bone neutral axis, being capable of sharing the load to a certain extent, instead of directing it around the fracture site as it happens with dynamic compression plates [5].

In spite of these benefits, current IM nails are metallic devices, and thus, they can elicit a series of detrimental conditions such as inflammatory cascades and bone atrophy secondary to stress shielding that arise from the large difference in mechanical properties between metallic materials and bone [6, 7].

Such issues are usually complicated by the disadvantage of requiring either permanent implantation or removal via secondary surgery after bone union has been achieved to alleviate the discomfort of metalware protruding into the soft tissue [6, 8]. The first option is generally selected in order to avoid the inherent health risks and costs associated with surgery [6]. This is, however, a less than optimal solution, since foreign bodies are areas for potential remote-site induced infection and can greatly complicate subsequent treatment should the same area become injured again [6, 9].

Bioresorbable composites fabricated from poly(lactic acid) 'PLA' and phosphate glass fibres 'PGF' have been described as a feasible solution for the shortcomings of bone fracture surgical reduction via metallic fixation [10]. Poly(lactic acid) is an aliphatic polyester that is known to ultimately degrade *in vivo* into naturally occurring lactic acid, which is subsequently metabolised via the tricarboxylic acid cycle into water and carbon dioxide [11].

Unlike silicate-based glasses, phosphate-based glasses can completely dissolve congruently in aqueous media through hydration and hydrolysis

reactions [12]. Their dissolution rate can be fine-tuned by simply adjusting the glass stoichiometry [13]. Furthermore, the controlled release of glass degradation by-products could stimulate specific cell metabolic processes involved in the regeneration of damaged bone tissue without prompting systemic toxicity [14]. The combination of bioactivity and biodegradability make PGF-PLA composites the optimum approach to encourage sound fracture healing and prevent risky revisionary surgeries for implant removal.

The concept validity has been supported by the fabrication of prospective PGF-PLA intramedullary composite rods with varied fibre architecture, fibre volume fraction and glass fibre composition [15-17]. Comprehensive analysis of continuous fibre reinforced composite rods with slowly dissolving fibres has clearly shown that the candidate implants possess mechanical properties even exceeding those of cortical bone and manage to retain them within an acceptable range for at least one month after immersion in aqueous medium [18].

The fundamental challenge with the processing of fibre reinforced thermoplastic composites is the high viscosity of the polymer melts which hampers the impregnation of the tightly packed fibre networks [19]. Moreover, the poor drapability of most thermoplastic preforms coupled with their lack of tackiness poses difficulties in their conformation to the mould cavity, especially in the presence of curved surfaces [20]. These complications have restricted the experimental manufacturing of continuous fibre reinforced biomedical composites featuring two-dimensional curvatures to solid-state forming or forging on account of the high up-front investment required to set up a pultrusion facility.

In spite of its versatility and simplicity, forging is labour intensive and process-induced defects, which drastically impair the composite mechanical performance, can be introduced as a result of the stresses generated during the stamping stage [21]. Furthermore, forging is a batch process with low production yields, making difficult the fabrication of the amount of samples necessary for the thorough characterisation of medical intended devices.

Accordingly, this study investigated on the efficient and effective manufacture of continuous phosphate glass fibre reinforced poly(lactic acid) composites with a particular focus on cylindrical rods. Current compression moulding and forging technologies process were revised and improved.

In addition, a new method for the fabrication of bioresorbable thermoplastic hybrid preforms and its subsequent consolidation into continuous fibre reinforced composite rods was developed. As in cable sheathing, a polymer sleeve is extruded through a crosshead die into which a phosphate glass fibre bundle is continuously fed. The polymer comes into contact with the glass fibre bundle outside of the pressurised die, avoiding stresses that might compromise the glass fibre integrity. In addition, the polymer sheath protects the glass fibres from abrasion and prevents them from interacting with the polymer quenching medium.

Such characteristics allow the high speed production (in the order of hundreds of meters per minute) of flexible PGF-PLA hybrid preforms comprising delicate and water soluble phosphate glass fibres in both the annealed and as-drawn condition. The preforms can be trimmed, stacked and consolidated into continuous or discontinuous fibre reinforced bioresorbable composite rods through compression moulding or other composite manufacturing technologies.

The relationship between processing, structure and properties of the composites produced by film stacking, solid state forming and compression moulding of polymer-sheathed fibre bundles was determined and their performances in simulated physiological conditions were compared.

II) Aims and Objectives

The aim of this project was to create a reproducible manufacturing process suitable for high-volume production of bioresorbable composites for fracture fixation applications, with a particular focus on rods for intramedullary nailing.

The main objectives can be summarised as follows:

i) Determination of the optimum conditions (bushing head and drawing temperature) for the metered production of phosphate glass fibres from cullet of the P45Fe2 composition ($45P_2O_5 \cdot 16CaO \cdot 13Na_2O \cdot 24MgO \cdot 2Fe_2O_3$).

ii) Characterisation and comparison of the degradation mechanism of annealed and as-drawn P45Fe2 phosphate glass fibres in aqueous media.

iii) Production of unidirectional phosphate glass fibre mats and PLA films with metered masses for the manufacture of continuous PGF-PLA unidirectional composites with four different fibre volume fractions via compression moulding.

iv) Evaluation of the effect of pressure profile and temperature during compression moulding on the mechanical properties of continuous PGF-PLA unidirectional composite plates with different fibre volume fractions.

v) Manufacture of continuous PGF-PLA unidirectional composite rods with four different fibre volume fractions via plane strain and uniaxial compression forging of preconsolidated PGF-PLA composite blanks and assessment of the effect of the deformation mode on the structure and mechanical properties of forged composite rods.

vi) Characterisation of the *in vitro* degradation behaviour of continuous PGF-PLA unidirectional composite rods manufactured via forging of preconsolidated composite blanks.

vii) Design of a crosshead extrusion die for the manufacture of thermoplastic hybrid preforms via PLA-sheathing of as-drawn and annealed phosphate glass fibre bundles and determination of the processing parameters (haul-off speed, screw speed, feeder output and extrusion temperature) for the metered production of PLA-sheathed fibre bundles with four different fibre volume fractions.

viii) Fabrication of continuous as-drawn and annealed phosphate glass fibre reinforced unidirectional composite rods with four different fibre volume fractions via compression moulding of PLA-sheathed fibre bundles.

ix) Comparison of the mechanical properties of continuous PGF-PLA unidirectional composite rods manufactured via forging of preconsolidated composite blanks and compression moulding of PLA-sheathed fibre bundles

x) Evaluation of the *in vitro* degradation behaviour of as-drawn and annealed fibre reinforced PGF-PLA unidirectional composite rods manufactured via compression moulding of PLA-sheathed fibre bundles and comparison with forged composite rods.

1 Literature Review

1.1 Bone: The Material

Bone provides mechanical support for joints, tendons and skeletal muscles while protecting vulnerable organs from external forces [22]. Furthermore, it acts as the principal reservoir for calcium, magnesium, phosphorus and sodium, playing an essential role in the maintenance of ion homeostasis [23].

Such functions are possible in virtue of bone's hierarchical structure spanning from the nanoscale to the macroscopic level (see Figure 1.1). At its lowest organisational level, human bone can be described as a polymer-matrix composite reinforced with approximately 0.5 volume fraction of nonstoichiometric nanosized hydroxyapatite 'HA' platelet crystals (E_{HA}=114 GPa) with dimensions of 2 nm × 25 nm × 50 nm (thickness × width × length, respectively), periodically distributed in a type I fibrous collagen matrix (E_{CT1}=1.2 GPa) [23-25].

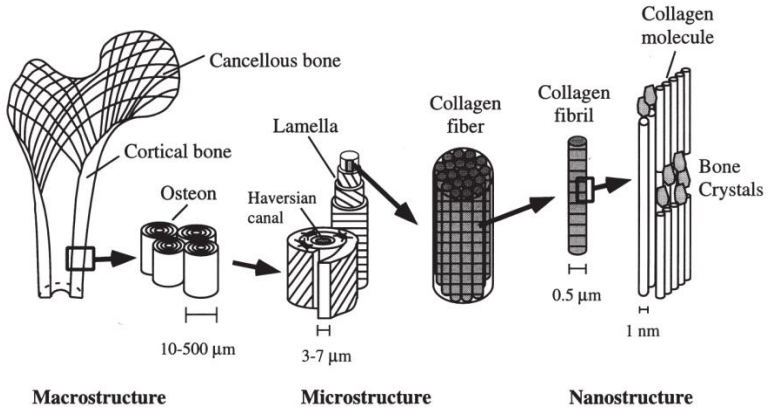


Figure 1.1: Hierarchical structure of bone [26].

Mineralised collagen fibres (cf. Figure 1.2) are unidirectionally packed in discrete sublayers that progressively rotate with respect to each other (in a plywood-like configuration) giving rise to individual lamellae (3–7 µm wide) [26, 27] which, based on their microstructural disposition and porosity content, can be classified as either cortical or trabecular bone.

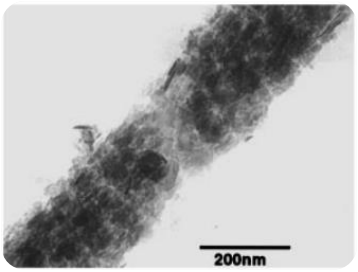


Figure 1.2: SEM image of a mineralised collagen fibre. The black regions represent the nanosized non-stoichiometric hydroxyapatite crystals [23].

In cortical bone, lamellae with alternating fibre orientation are organised in concentric cylinders (of about 3-8 sheets) around a central channel which encloses conjunctive tissue and blood vessels (the Harvesian canal), ultimately creating a hollow structure of about 200-250 μm in diameter known as osteon [26, 28]. This arrangement allows the transport of nutrients and confers the bones with anisotropic features on account of the alignment of osteons along the principal stress direction [26, 28].

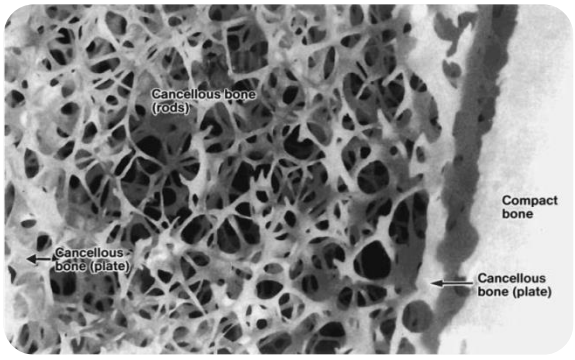


Figure 1.3: Photograph of a proximal tibia section showing an outer thin layer of cortical (compact) bone and the inner trabecular (cancellous) bone network comprising trabecular plates and rods. Network voids are filled with bone marrow in living specimens [22].

As shown by Figure 1.3, cancellous or trabecular bone is composed of an irregular framework of thin rods and plates (ranging from 50–300 μm in diameter), commonly regarded as trabeculae [22, 24]. Within the trabeculae, the lamellae are grouped in cylindrical structures, although in this case they do not contain an inner vascular cannel; instead, the individual rods nourish from the bone marrow that fills the interstices of the trabecular bone network [25, 26].

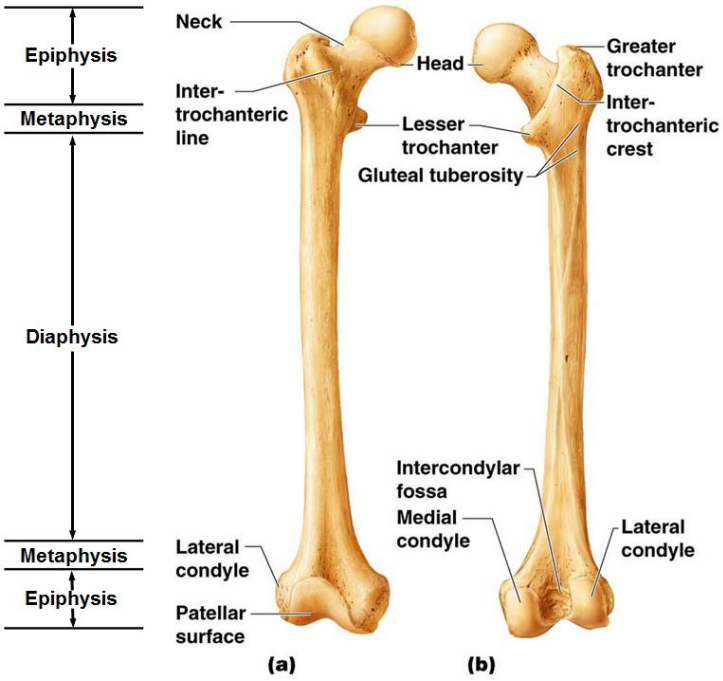


Figure 1.4: Schematic of the femoral bone structure.

The relative amounts of each type of bone depend on the anatomical location. Dense cortical tissue (1.8 $g \cdot cm^{-3}$ [26]) is the principal constituent of the diaphysis or midshaft region in long bones (femur, humerus, radius, tibiae, among others), whereas the short (carpal, tarsal, etc.) and flat bones (like the skull and ribs), in addition to the metaphyseal and epiphyseal regions of long bones, are composed of the highly porous trabecular bone lattice (0.2 $g \cdot cm^{-3}$ [26]) enclosed by two relatively thin cortical bone layers [23, 25].

The mechanical behaviour of bone is intimately related to the level of porosity [26]. Cortical bone displays higher strength and stiffness upon loading as evidenced by Table 1.1, where S and E denote strength and modulus, respectively. The T, C, B and S subscripts stand for the loading condition, namely, tensile, compression, flexural and shear, respectively. Experimental properties vary in function of biological factors (such as the donator's age, gender, physical condition, bone mineral phase content and amount of water), testing method and conditions. [25, 26].

Table 1.1: Bone mechanical properties, compiled from [22, 25, 26, 29-31].

Type of Bone	S_T (MPa)	E_T (GPa)	S_C (MPa)	E_C (GPa)	S_B (MPa)	E_B (GPa)	S_S (MPa)	E_S (GPa)
Cortical	35-283	7-30	100-240	14-34	35-238	5-23	50-75	3.1-3.7
Cancellous	7-20	0.4	1.5-38	0.01-1.5	1-9	0.05-0.34	-	-

Flexural properties are specially determinant since during routinary activities, bones, such as the femur, are mainly, but not exclusively, subjected to bending moments [32].

1.2 Bone Metabolism

Despite being a rigid frame supporting the locomotion apparatus, bone is not an inert structure but a highly vascularised dynamic entity that experiences changes throughout the entire organism's life in structural and volumetric terms [33]. This feature makes it capable of repairing damage product of the repeated cyclic loading associated with daily activities or even acute trauma (macroscale fracture) [34].

Bone can adapt in accordance to the prevailing loading circumstances via the modelling/remodelling cycle, conferring biomechanical advantage through the modification of its spatial distribution, in such way that bone strength is optimised without an excessive increase in cross section [35, 36].

This complex and tightly regulated process takes place through the synergetic interactions of bone's cellular machinery, essentially involving three kinds of bone lineage cells illustrated in Figure 1.5, viz.: i) osteoclasts, ii) osteoblasts and iii) osteocytes (terminally differentiated osteoblasts), cooperating in what is known as the basic multicellular unit (BMU) [37-39].

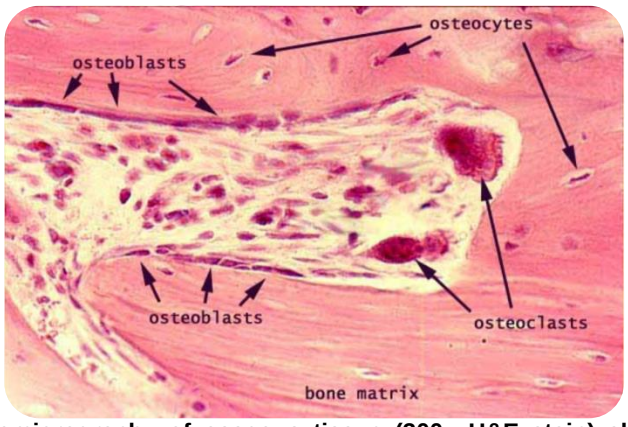


Figure 1.5: Photomicrography of osseous tissue (300x H&E stain) showing the three types of cells involved in bone remodelling, namely: i) giant multinucleated osteoclasts, ii) bone forming osteoblasts and iii) extracellular matrix-trapped osteocytes [52].

1.3 Bone Fracture

Bone is capable of withstanding substantial loads in a fair range of configurations [22]. Due to its microstructural nature, it is more vulnerable to

tensile strains, such that excessive stresses or high loading speeds result in bone fracture. In some cases bone fracture may occur below normal tolerance as a result of degenerative conditions that impair bone performance (e.g. anomalous bone remodelling), in which case the bone fracture is classified as pathological [40-42].

1.3.1.1 Femoral Diaphyseal Fractures

Due to the large blood vessels and soft tissue volume associated with the femoral bone, traumas within this region have proven to be specially challenging to treat. This circumstance is complicated by the combined muscle action that may cause fragment displacement [43]. Corrective medical procedures should be selected chiefly in terms of the degree of stability required, but keeping the disruption to the peripherial tissue and joints strictly to the minimum, so that the normal limb function is restored as effectively and quickly as possible.

1.3.2 Primary or Direct Bone Healing

If the fracture has been reduced and the fragments shielded against strain (such that no motion occurs under functional load) via a rigid fracture fixation device such as a lag screw or a dynamic compression plate, direct lamellar bone remodelling occurs without callus formation [1, 41]. Osteoclasts tunnel across the fracture line within a “cutting cone“ remodelling unit, immediately followed by osteoblasts, which lay down bone matrix, restoring the continuity of Harvesian systems as illustrated in Figure 1.6 [44, 45].

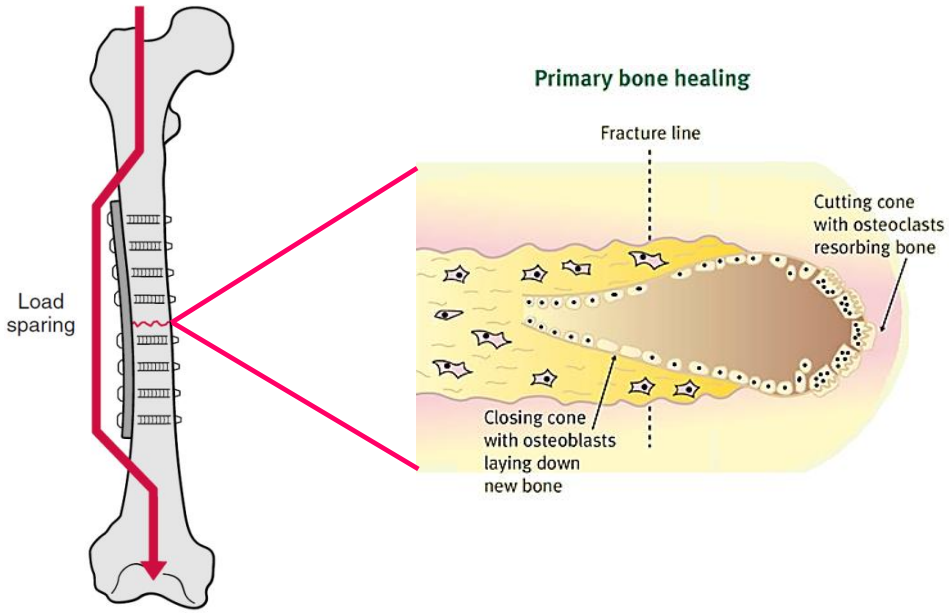


Figure 1.6: Schematic representation of primary fracture healing through "cutting cone" remodelling units, after fixation with a dynamic compression plate that deviates the force pathway, shielding the fracture site from stresses. Adapted from [2, 40].

1.3.3 Secondary or Indirect Fracture Healing

Secondary healing is characterised by the formation of callus (which bridges the bone fragments) and its eventual mineralisation into bone tissue through a series of cascade events [37, 46]. The process begins with haematoma formation at the fracture site, locally depriving bone tissue from nutritional support and consequently leading to bone necrosis and hypoxia, in turn stimulating in coagulation and acute inflammatory response [40, 47].

The cloth provides a temporary fibrin scaffold which matures into a loose aggregate of cells interspersed with capillaries (granulation tissue) through the proliferation of fibroblasts in the fibrin network, progressively reducing the strain at the fracture site. Eventually, the granulation tissue is replaced by a cartilaginous soft callus which in time develops into a woven bone or hard callus (composed of coarse collagen fibres interwoven in an irregular disposition) through endochondral ossification. Once solid union has been achieved, surplus bone tissue is gradually resorbed in function of the stress demands [48, 49].

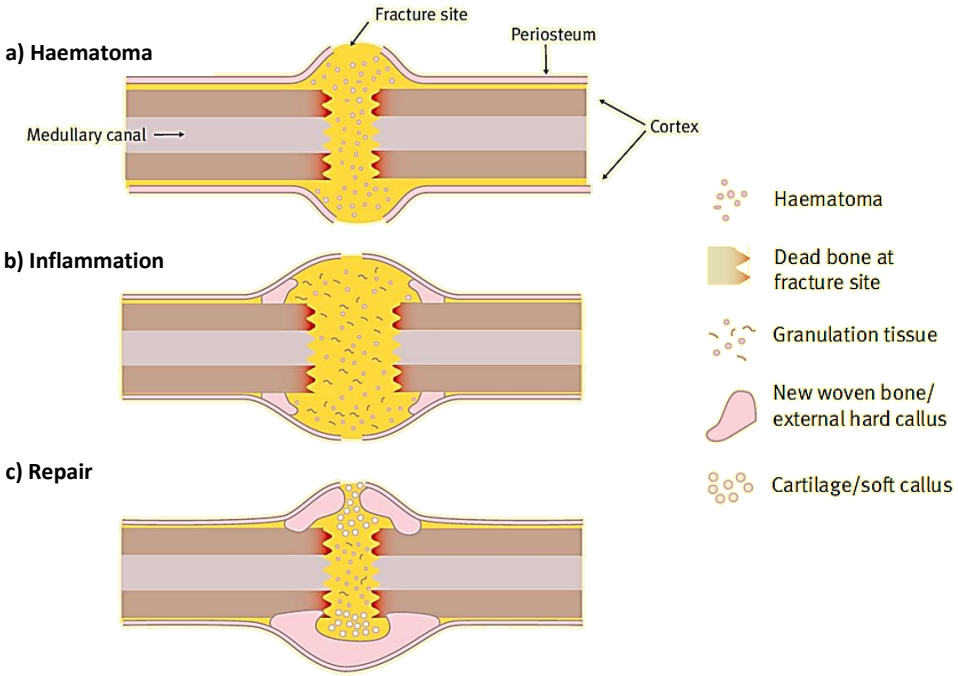


Figure 1.7: Schematic representation of the indirect fracture healing process, displaying the main stages towards stabilisation through callus formation viz.: a) haematoma formation and coagulation, b) acute inflammation and c) repair via callus development [40].

1.4 Fracture Management

The potential vascularity impairment after dissection and infection risk are arguments normally used against fracture fixation [1]. Nevertheless, the advances in the materials field coupled with enhanced surgical procedures have made operative treatment the standard medical procedure [1, 2].

In skilled hands, fracture fixation devices enable precise anatomical reconstruction and accurate control of the length, rotation and angulation of the bone fragments, in addition to early limb mobilization, avoiding the complications outlined before in §1.3.1 [1, 2].

1.4.1 Intramedullary Rods

Fracture stabilisation is guaranteed through the implantation of a range of orthopaedic implants. Intramedullary nailing 'IM' (Figure 1.8) stands out from similar fixation devices in virtue of the minimally invasive character of its surgical implantation [2, 50].

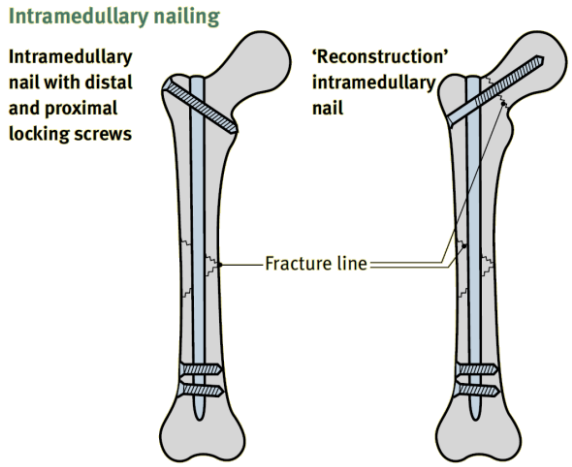


Figure 1.8: Intramedullary nail femoral bone fracture fixation and interlocking screws in the femoral neck [51].

The change from non-operative fracture reduction to IM nailing of femoral fractures roughly started in the 1950s after the development of the cloverleaf-shaped Küntscher steel nail. However, the technique only assumed its current relevance after its refinement through the combined application of interlocking screws (cf. Figure 1.8), extending to nearly all long bone treatment even with substantial fracture comminution [2, 52].

Unlike bone plates and external fixators (which involve rather aggressive dissection and further periosteal damage, increasing initial necrosis) intramedullary nailing requires only a minor incision to insert and manipulate a nail of around 13 mm of diameter for mature patients into the medullar cavity [2, 3]. In such way, the fracture haematoma is kept relatively undisturbed, preserving a favourable environment for fracture healing [2, 50].

Contrary to the rigid fixation provided by bone plates, which may result in bone atrophy and refracture at the originally affected site, IM nails may act as a load-sharing device, allowing limited amounts of micro-motion, encouraging callus bridging (cf. Figure 1.9) and ultimately reducing the extent of stress shielding [40, 41]. This fact is reflected in the low fracture reincidence observed following implant removal [4, 5].

The technique's main issue is the chronic pain caused by metalware protrusion into the soft tissue, frequently demanding for an additional intervention to alleviate patient distress [2, 53].

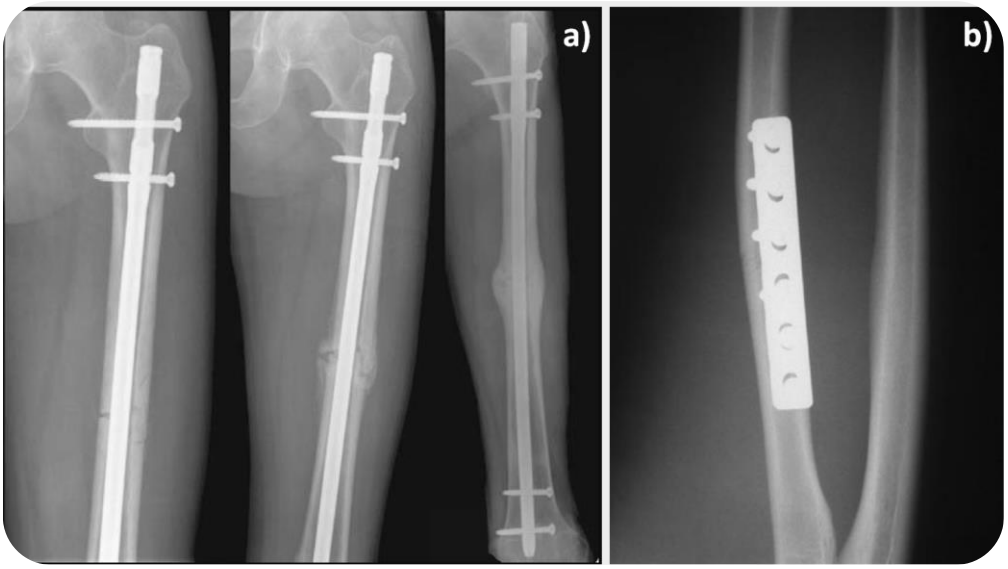


Figure 1.9: a) Radiographs of a mid-shaft femoral fracture treated with distally and proximally locked intramedullary nails, showing bone union progressing by secondary fracture healing with callus formation (from left to right). The third image in a) shows an external mineralised 'hard' callus, and a central cartilaginous 'soft' callus; b) radiograph of radial fracture reduction via compression plating, showing primary bone healing without the formation of a visible external callus. Adapted from [40, 41].

1.5 Biomaterials in Orthopaedics

1.5.1 Metallic Biomaterials

Within the range of engineering practices, medical disciplines call for superior materials capable of withstanding relatively large amplitudes of dynamic loading in addition to the aggressive in vivo environment where structural breakdown is unacceptable since failure may be life-threatening for the patient [7].

Metallic materials, chiefly stainless steels, cobalt and titanium alloys remain extensively used for orthopaedic applications in virtue of their high mechanical properties, which in conjunction with well-established processing technologies (e.g. casting, forging, machining and so forth), enable the easy fabrication of reliable long-term implants with intricate shapes for major load bearing applications, as illustrated in Figure 1.10 [6, 54].

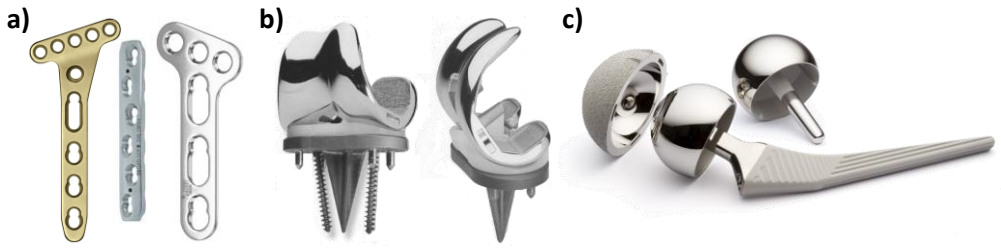


Figure 1.10: Common metallic implants used in the orthopaedics field; a) stainless steel dynamic compression plates, b) Vitalium (Co-Cr) alloy total knee replacement and c) titanium total hip replacement. Adapted from [55, 56].

Although metallic implants have shown undoubted success when used for fixation of bones and soft tissue, they are not well tolerated within the body due to the fundamental difference between human tissue and metallic implants as demonstrated in Table 1.2 [9, 57]. The range of values shown for density, $\boldsymbol{\rho}$, tensile strength, $\mathbf{S_T}$, compression strength, $\mathbf{S_C}$, elastic modulus, **E**, and elongation, **e**, arise from microstructural differences associated with the production method.

Since the load carried by the implant is proportional to the implant-bone stiffness ratio, the large difference in elastic modulus between metals and bone tissue results in reduced stimulation for new bone formation, shifting the bone remodelling balance towards resorption, and ultimately leading to bone mass loss. Bone atrophy caused by stress shielding following metallic fracture fixation is the most common cause of implant loosening and bone refracture [58, 59]. Additionally, metallic implants may release toxic ions and particles through corrosion and wear processes that lead to inflammatory cascades [9].

Table 1.2: Summary of the physical and mechanical properties of common metallic biomaterials in comparison to natural bone [31, 60-62].

Material	ρ (g·cm^{-3})	S_T (MPa)	S_C (MPa)	E (GPa)	e (%)
Cortical Bone	1.8-2.1	35-283	164-240	7-30*	1.07-2.10
316L	8.0	540-1000	480-620	193	30-40
Ti6Al4V	4.43	830-1172	896-1172	114	12-15
CoCrMo	8.3-9.2	900-1540	-	240	5-30
Mg (99.9%)	1.74	87-180	40-140	41	13±1.4
AZ91E	1.81	165-457	97-165	45	2.5-11.1

***The elastic modulus was obtained under tensile loading.**

1.5.1.1 Biodegradable Metallic Implants

More recently, magnesium and its alloys have attracted great attention for orthopaedics applications due their i) unique combination of physical properties, which closely resemble those of cortical bone (see Table 1.2) and

ii) their degradation in physiological environment, obviating the need for implant removal [63]. Furthermore, magnesium is essential for human cell metabolism with a daily consumption in the 250-300 mg per day and is the fourth most abundant cation (it is estimated that ~25g are stored in the human body, half of which is associated to bone tissue) [61, 63, 64].

Nevertheless, the rapid corrosion of magnesium in physiological conditions (pH 7.4-7.6, $[Cl^-]$=150 $mmol \cdot l^{-1}$ [62]) and its susceptibility to pitting corrosion at chloride concentrations above 30 $mmol \cdot l^{-1}$ [64] remains an issue. Additionally, the quick evolution of hydrogen gas during magnesium aqueous dissolution has ultimately prevented their successful implementation as orthopaedic implants [64-66].

1.5.2 Polymeric Biomaterials

Polymers have been extensively used in the biomedical field as a result of their wide range of mechanical properties (influenced by molecular weight, chain configuration and conformation, crystallinity and/or crosslinking density) and their ease of fabrication into complex morphologies [67-69]. Polymeric components can be obtained by extrusion, injection and compression moulding, solvent spinning or casting [70]. In some circumstances primary shaping may be followed by downstream machining into final parts [71, 72].

Table 1.3: Summary of properties for selected polymeric materials [69, 73-75].

Material	Degradation Time	S_T (MPa)	E_T (GPa)
UHMWPE	N/A	21	1
PEEK	N/A	139	8.3
PTFE	N/A	28	0.5
PMMA	N/A	21	4.5
Silicone	N/A	7.6	0.008
PLLA	>24	50-80	3-6
PCL	>24	20-35	0.2-0.4
PGA	6-12	60-80	7

Orthopaedically relevant non-degradable polymers include ultra-high molecular weight polyethylene ‘UHMWPE’ for the fabrication of acetabular cups in total hip arthroplasty, polymethylmethacrylate ‘PMMA’ as bone cement in total joint replacement and silicon for the replacement of small deceased joints. However, the role of polymers in hard tissue engineering has been

greatly limited by their poor mechanical strength in comparison to human cortical bone, as demonstrated in Table 1.3 [6, 68, 69].

1.5.2.1 Bioresorbable Polymers

Bioresorbable polymers are meant to be functional only during a specific period, eventually degrading *in vivo* [8]. First introduced in 1960 as sutures and rods for mandibular fracture repairs in dogs, bioresorbable polymers have been heavily investigated for tissue repair [71, 76]. Amongst these materials, the members of the polyester family namely poly(lactic acid) 'PLA' and poly(glycolic acid) 'PGA' deserve special consideration on behalf of their mechanical properties (see Table 1.3) [76].

Despite its higher strength and modulus in comparison to PLA, the quick degradation of pure PGA devices in aqueous environments have precluded a more extensive application in bone repair [77, 78]. Adverse tissue responses to PGA fixation implants, varying from erythematous papules to discharging sinus at the implant location (cf. Figure 1.11) have been reported in multiple clinical studies [79, 80].



Figure 1.11: Polymeric debris discharging sinus formed as a result of foreign-body reaction to a PGA screw. The sinus emerged 11 weeks after implantation [79].

These circumstances have made the slow degrading PLA subject of intensive research and development as revealed by the increasing number of studies dedicated to its manufacture, characterisation and modification [71, 76, 81-83]. The outcome of these efforts is the successful application of PLA as interference screws used in anterior cruciate ligament reconstruction, or PLA-based suture anchors for ligament attachment in shoulder and foot surgery [84]. PLA arrows and plugs are also been used in the fixation of the knee lesions and shoulder dislocations [71, 76, 84]. More recently bioresorbable implants for spinal surgery have been successfully manufactured [85]. Nonetheless, when it comes to fracture fixation devices, biopolymers do not

yet meet the criteria to be safely used as major load bearing implants by their own, since their low modulus will allow excessive movement at the fracture site, preventing solid union [75].

1.5.2.1.1 Poly(lactic acid)

PLA is a member of the aliphatic polyesters family derived from the conjugation of α-hydroxy acids [70]. Due to the atomic spatial distribution in its lactic acid basic building block, two optically active species can be differentiated (L or D-enantiomers) as illustrated in Figure 1.12 [83].

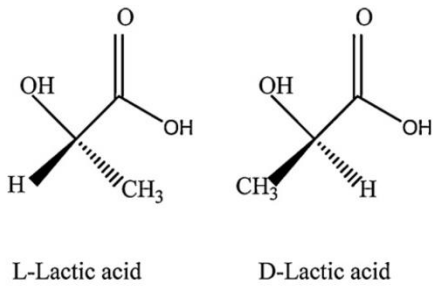


Figure 1.12: L- and D- enantiomers of (2-hydroxy propionic acid) or lactic acid [83].

The presence of both hydroxyl and carboxyl moieties in the lactic acid monomer enables its direct conversion into polyester via condensation [86]. However, in virtue of its reversible character, the ultimate molecular weight achievable by means of direct condensation is greatly limited by the complications arising from dehydration of the system in the late polymerisation stages (see Figure 1.13) [83, 86]. Hence, polyesters produced by lactic monomer condensation never exceed molecular weights of 10000 $g \cdot mol^{-1}$ [82, 83].

Nowadays, most of commercial PLA is produced via ring-opening polymerisation in which aqueous lactic acid is condensed into a low molecular weight oligomer and subsequently depolymerised via internal transesterification or 'back-biting' reaction into a lactic acid cyclic dimer or lactide [86, 87]. Finally, after vacuum melt purification, high molecular weight PLA (M_W>100000 $g \cdot mol^{-1}$) is produced [82, 83].

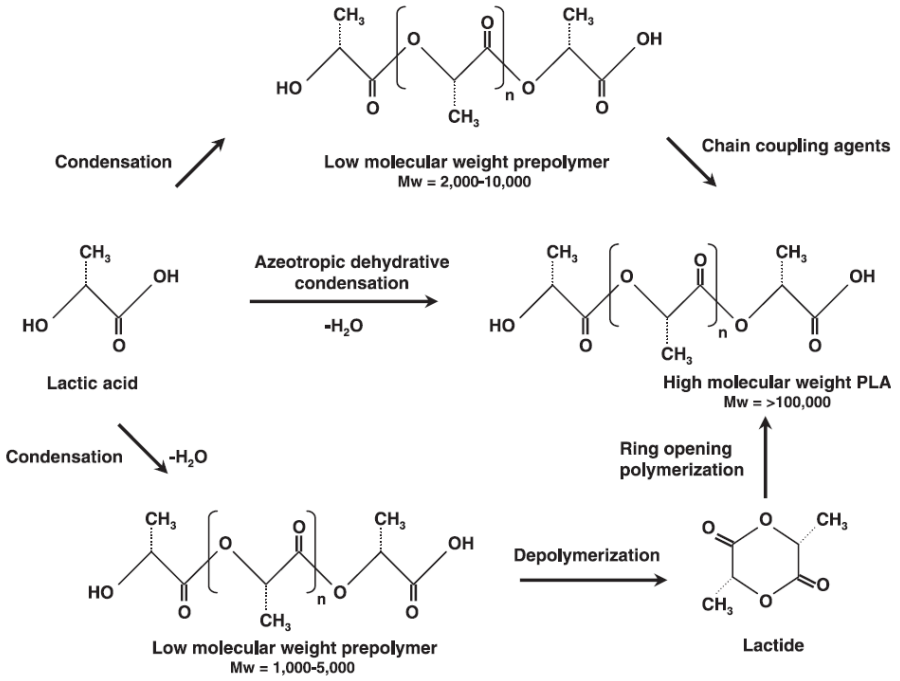


Figure 1.13: Polymerisation route of PLA from L- and D-lactic acid monomeric units [70].

1.5.2.1.2 Crystallisation of PLA

Poly(lactic acid) is a rigid thermoplastic that may be found in a semicrystalline or totally amorphous state, depending on the thermo-mechanical history and polymer stereopurity [82, 86]. Since most of physicochemical properties of PLA (including hardness, modulus, tensile strength, elastic modulus, hydrolytic degradation rate and melting point) are strongly linked to the crystallinity content, attainable crystallinity plays a crucial role in compositional selection [72, 84]. For instance, amorphous poly(DL-lactide) 'PDLA' has a modulus about 25% lower than semicrystalline poly(L-lactide) 'PLLA' and a degradation time spanning from 12 to 16 months, whereas for poly(L-lactide) the total *in vivo* resorption period is in the order of 3 to 5 years [73, 87].

It is possible for PLA to crystallise provided the content of a single optical species (either L-(+)- or D-(-)-isomer) is higher than 90%, [82, 86]. Optical impurities introduce defects in the crystalline arrangement, which hamper the molecular rearrangement necessary for crystal formation [82, 83]. As optical purity decreases (<90%), crystallization eventually becomes impossible [86, 88].

PLA has been found to crystallise in a range of morphologies spanning from spherulitic aggregates to hexagonal lamellar stacks [89]. Such a variety is explained by different nucleation and crystal growth rates associated with a particular temperature regime. Crystallisation from the melt at temperatures below 145°C results in the former, whereas heat treatment at higher temperatures produces the latter [86, 89].

As shown in Figure 1.14, spherulites are three-dimensional aggregates of minute crystalline units organised in a stacked lamellar arrangement with restricted amorphous regions in between, where the long axis of the lamellar crystal runs parallel to the spherulite radius [89].

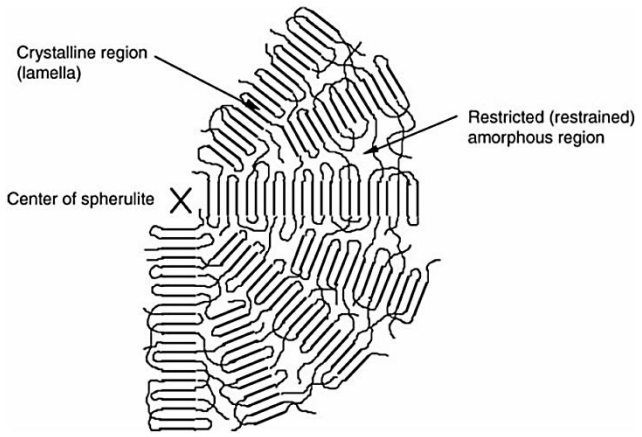


Figure 1.14: Schematic representation of a spherulite [90].

1.5.2.2 Hydrolytic Degradation of Poly(lactic acid)

PLA undergoes degradation in aqueous media by random hydrolytic cleavage of the labile ester group to form organic acid entities with carboxyl and hydroxyl end-groups as shown in Figure 1.15 [86]. The reaction leads to an overall decrease in the chain length and to acidification of the surrounding environment due to the increase of acidic carboxylic moieties in solution [91, 92].

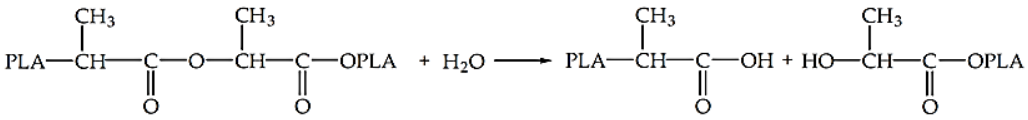


Figure 1.15: Hydrolytic cleavage of poly(lactic acid) chains [90].

Ester bond hydrolysis is influenced by intrinsic and extrinsic factors, namely molecular weight, residual monomer concentration, implant geometry,

temperature and location, among others, but the mechanism and degradation rate is mainly determined by the polymer crystallinity and the pH of the medium [84, 93].

The close dependence of PLA hydrolysis on the microstructure stems from the permeability difference between amorphous and crystalline regions [94, 95]. Since water molecules find more difficult to penetrate the compact crystalline domains, the amorphous parts of the polyester (which act as physical crosslinks between crystal blocks as illustrated in Figure 1.16) undergo hydrolysis preferentially due to the high concentration of hydrophilic carboxyl and hydroxyl groups which have been rejected from the lamellae packets into the amorphous domains during crystallisation [95]. The increased density of hydrophilic terminal groups hampers close packing of the polymer chains, ultimately deriving in a net increase in the water diffusion and enhanced degradation rate [95, 96].

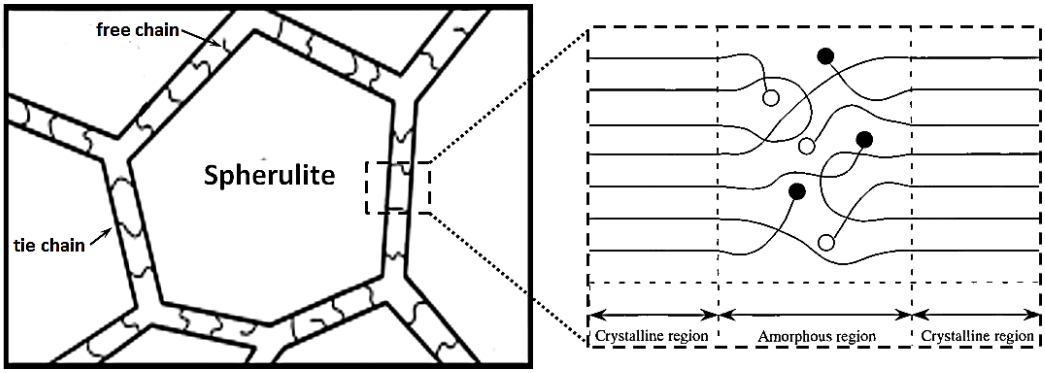


Figure 1.16: Schematic representation of the crystallite disposition in a semicrystalline PLA sample. The amplification of the region enclosed by dashed lines illustrates the high concentration of carboxyl and hydroxyl groups (closed and open circles, respectively) in the amorphous regions after their rejection from crystalline domains. Adapted from [95, 97].

Localised scission of tie chains at the inter- and intra-sphrerulite amorphous regions in semicrystalline specimens will result in a rapid and rather dramatic decrease of strength and elastic modulus of crystallized PLA [95, 96]. Once amorphous parts have been completely hydrolysed, degradation proceeds in the crystalline domains, although, at a significantly reduced rate [98].

Conversely, in fully amorphous samples at temperatures below T_g, each molecule is bound to numerous adjacent chains by either van der Waals forces or physical entanglement as depicted by Figure 1.17 [95]. The extent of ester bond cleavage in amorphous polymers will be considerable before a noticeable reduction in mechanical properties [96]. Splitting of PLA chains into

low molecular weight oligomers results in an increase in the concentration of hydrophilic chain ends [91]. Eventually, their concentration is high enough to significantly catalyse the hydrolytic cleavage of adjacent ester bonds [91, 92].

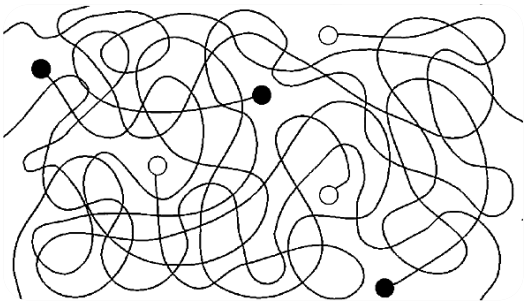


Figure 1.17: Schematic representation of the polymer chain arrangement in amorphous PLA products. Open circles represent carboxyl end-groups, while closed ones depict hydroxyl moieties. Adapted from [95].

Another parameter to be considered is the presence of ionic species in solution. Both acids and bases markedly increase polyester hydrolysis rate, however, the influence of H^+ becomes significant only in the degradation of polymers with molecular weights lower than $1.5x10^6$ $g \cdot mol^{-1}$ [90]. On the other hand, hydroxyl ions have been reported to actively engage in the cleavage of ester groups at the sample surface as described by Equation 1.1, independently of molecular weight [99]:

$$\mathrm{RCOOR'} + \mathrm{NaOH} \rightarrow \mathrm{RCOO^-} + \mathrm{Na^+} + \mathrm{R'OH} \qquad (1.1)$$

Only after the significant reduction in molecular weight, biological degradation of PLA can occur [72]. In contact with organic tissue, PLA residue becomes incorporated to the metabolic pathway of the tricarboxylic acid cycle (cf. Figure 1.18). The final products are adenosine triphosphate 'ATP', water and CO_2 that are excreted by the kidneys and lungs, respectively [73]. It should be noted that if the surrounding tissue cannot process the acidic by-products as fast as they are generated, an inflammatory response ensues [100]. On the other hand, undissolved crystalline debris can be attacked by the immune system, promoting osteolysis and implant loosening [75].

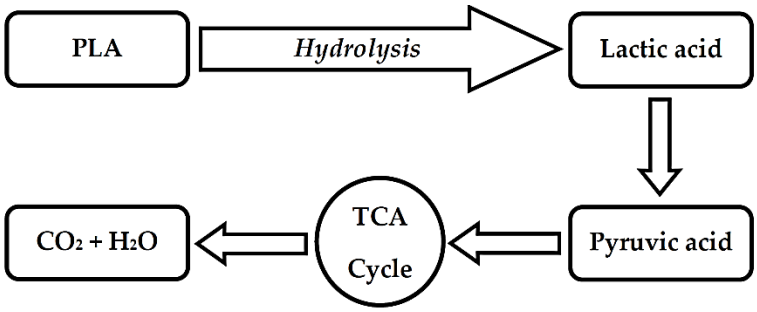


Figure 1.18: Simplified diagram of *in vivo* PLA degradation sequence [101].

1.5.2.3 Thermal Degradation of Poly(lactic acid)

Since most bioresorbable polymers have been synthesized by reversible polymerization reactions (cf. Figure 1.13), the temperature and high pressures generally employed in manufacturing processes can displace the equilibrium towards depolymerisation [71]. The thermal instability of poly(lactic acid) has been attributed to the labile proton in the CH group, whose contiguity to the ester moiety in the polymer backbone makes the carbonyl carbon–oxygen linkage highly reactive [102, 103].

PLA and PLA copolymers are known to undergo thermal degradation even at temperatures below the melting point, but the loss of molecular weight is dramatically accelerated when exposed to higher temperatures even for a short time as demonstrated in Table 1.4 [94, 104].

Table 1.4: Effect of processing temperature on the molecular weight of 90/10 PDLLA copolymer [93].

Initial Molecular Weight	M_w after 30 min at 160°C	M_w after 30 min at 190°C
151,000 (M_n)	102,000	84,000
255,000 (M_w)	160,000	104,000
285,000 (M_z)	204,000	142,000
470,000 (M_n)	354,000	228,000
562,000 (M_w)	362,000	223,000
950,000 (M_z)	650,000	390,000

Thermal decay of PLA can be attributed to a series of reactions, one of which will dominate provided specific processing conditions are met, namely: (i) zipper-like or backbiting depolymerization, (ii) oxidative, random main-chain scission, (iii) intermolecular transesterification, and (iv) intramolecular transesterification resulting in formation of monomers and low molar mass oligomers (lactides) [71, 105]. The rate of these reactions is enhanced by the

presence of impurities like residual catalysts and monomers, and active chain-end groups [105, 106].

Considering that PLA is usually processed within the 180-220°C temperature window, thermal degradation of PLA during melt processing can be mainly attributed to intramolecular transesterification [103]. The product of this reaction might be a lactide molecule, an oligomeric ring, or acetaldehyde plus carbon monoxide, depending on the site attacked by the nucleophilic oxygen as shown in Figure 1.19, [106].

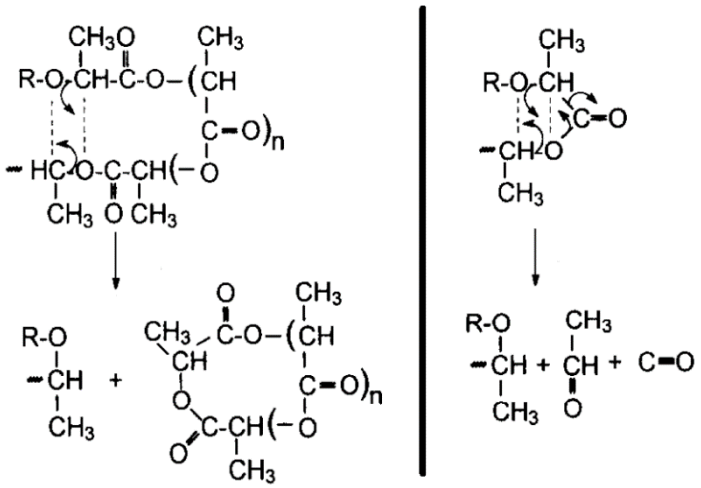


Figure 1.19: Intramolecular transesterification reaction pathways leading to the formation of oligomeric rings (left) and the production of acetaldehyde plus carbon monoxide (right). Adapted from [103].

PLA is a hygroscopic thermoplastic and quickly absorbs water up to its equilibrium swelling level after exposure to humid environments, further complicating PLA's high temperature degradation during processing [70, 106]. To prevent excessive polymer degradation, the material must be dried to moisture contents as low as 50 ppm for maximum retention of molecular weight. As reported previously, PLA drying for 24 hours at 80°C reduced the overall degradation by ~30% when processing above 200°C [71].

1.5.3 Ceramic Biomaterials

The natural presence of mineral deposits in bone extracellular matrix makes ceramic materials viable candidates for hard tissue replacement. Orthopaedic applications of these materials have been expanded ever since the use of calcium sulfate dehydrate (plaster of Paris) for bone grafting in 1892, with the advent of enhanced powder processing techniques [107, 108]. The use of bioinert ceramics in major loading components with surfaces in relative motion

has been demonstrated to reduce wear rate and debris release [109]. Furthermore, the implantation of ceramics in the human body is not compromised by corrosion and toxic ion leaching commonly observed for metallic prosthesis [110].

Major orthopaedical applications of bioinert ceramics (namely, alumina, zirconia and more recently yttria-stabilised zirconia) include femoral heads and acetabular cups for hip replacement and wear plates in prosthetic knees [75, 111].

Unfortunately, ceramic components may experience early fracture in virtue of their intrinsic brittleness as confirmed by several clinical reports [108]. Furthermore, due to lack of chemical bonding with organic tissue, these ceramics experiment foreign body reactions, utterly leading to their isolation within an acellular collagen capsule, which limits their application as a potential bone substitute [75, 107]. In addition, serious problems of stress shielding, resulting from the very high elastic modulus compared with human cortical bone have been observed in patients. This circumstance is aggravated in elder hosts with osteoporosis or rheumatoid arthritis issues and may cause implant loosening [6].

1.5.3.1 Bioactive and Bioresorbable Ceramics and Glasses

Bioactive and bioresorbable ceramics and glasses were conceived in response to the rejection response of the host tissue towards bioinert graft materials, which in extreme cases of extensive of tissue damage, may result in the amputation of the injured limb [112]. Bioactive materials present favourable surfaces for bone adhesion and bone ingrowth, whereas bioresorbable ones are gradually replaced by the host tissue as the material degrades with time [110]. Bone adhesion has been attributed to the formation of a hydroxycarbonate layer on the surface after initial dissolution [113]. Due to their compositional similarity with the mineral component of bone, the great majority of currently used bioactive materials are based on calcium phosphate products (mainly hydroxyapatite, and tricalcium phosphate ‘TCP’) and silicate-based glasses with sodium, calcium and phosphorous oxide substitutions [108, 110].

The most important applications of bioactive ceramics and glasses have been i) the coating of permanent orthopaedic metallic implants where strong anchoring with bone is required (namely, femoral stems for the hip joints and both the tibial and femoral components in prosthetic knees) and ii) as synthetic bone grafts in comminuted fractures [108, 112].

In contrast to crystalline ceramics, the composition of silicate-based bioactive glass systems is not limited by stoichiometry [114]. Therefore, the overall degradation rate of bioglass components (which in most of the cases describe a progressive change with silica substitutions) can be tailored to suit the patient needs [112].

This characteristic holds true for other glass forming systems including borate- and phosphate-based glass systems, which by their own merits, have spurred intensive research and development for their use in the human body.

1.5.3.1.1 Phosphate-based glasses

In contrast to bioactive ceramics and silicate-based glasses, phosphate glasses can completely dissolve in aqueous environments [115, 116]. The high flexibility of the phosphate glass network (attributed to the presence of a terminal oxygen in the PO_4 structural unit) broadens the glass forming compositional range in comparison to the more rigid silicate-based glass systems. Furthermore, unlike silicate-base bioactive glasses whose product range is greatly limited by their crystallisation tendency at the respective processing temperatures, phosphate glasses with biomedically relevant compositions can be readily manufactured into various geometries, including fibres and microspheres [117-119].

Phosphate-based glasses are composed of interconnected PO_4 units that result from the formation of sp^3 hybrid orbitals from its valence electrons ($3s^2 3p^3$) [120]. During hybridisation, the fifth electron is promoted to a 3d orbital where a strong π-bonding interaction with oxygen 2p electrons ensues, giving rise to a highly asymmetric tetrahedral structure [120, 121]. The occurrence of the double bond limits the network connectivity to a maximum of three bridging oxygens that link to neighbouring coordination polyhedra by corner-sharing [122].

The addition of network modifiers (generally members of the alkaline and alkaline earth family) results in the creation of two charged non-bridging oxygens 'NBOs'. Electrical neutrality is maintained via an associated metallic cation that sits in the interstices of the glass network [123].

Glass former oxide substitution leads to the progressive breakdown of the original network in favour of structure composed of chains, P_2O_7 dimers and ultimately isolated PO_4 tetrahedra [120]. Such structures are better described by the Q^i nomenclature where 'i' denotes the number of bridging oxygens linked to the central phosphorous atom as shown in Figure 1.20.

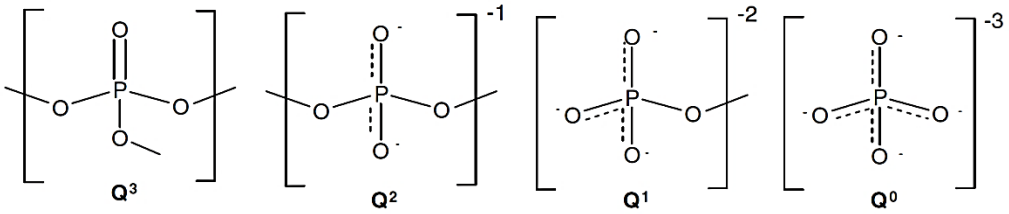


Figure 1.20: Structural units found in phosphate based glasses [120].

The relative amounts of these entities depend on the extent of modifier oxide substitution so that a good estimate of the glass structure can be made based solely on the composition [120]. This postulate is the rationale behind the most comprehensive classification of phosphate-based glass systems commonly represented by the generic expression $xM_{2/v}O–(1-x)P_2O_5$, where '*x*' stands for the total amount modifier oxide '$M_{2/v}O$' and the subscript ***v*** denotes the valance of the metal cation [120].

Ultraphosphate glasses ($0.50>x\geq0$): ultraphosphates span from the vitreous P_2O_5 (x=0) to glass compositions with exactly 50 mol% of modifier substitution. Accordingly, the 3-D interconnected structure, initially composed of exclusively Q^3 groups, gradually evolves into a series of entangled chains of Q^2 entities that might interact via ionic crosslinks with neighbouring chains provided the presence of polyvalent ions in the glass [120].

Metaphosphate glasses (x=0.50): the metaphosphate glass composition is represented by a single point at half of glass former content with a structure based entirely on Q^2 tetrahedra forming infinite long chains and/or rings. The chains and rings are may be linked by ionic bonds between various metal cations and NBOs when polyvalent oxides (e.g. Ca^{2+}, Sr^{2+}, Fe^{3+}, Ti^{4+}, etc.) are incorporated into the glass [120, 121].

Polyphosphate glasses (0.5<x<0.67): the unfeasible event of achieving exactly equal molar proportions of modifiers and glass former, makes the polyphosphate structures the most likely to prevail for modifier concentrations equal or greater than the theoretical P_2O_5 content. The polyphosphate domain is characterised by progressively shorter Q^2 chains terminated by Q^1 tetrahedra [120, 121].

Pyrophosphate or Invert glasses (0.67≤x≤0.75): the pyrophosphate composition marks the critical point where the "network" has been depolymerised enough to be exclusively composed by P_2O_7 dimers linked through ionic bonds between metallic cations and NBOs [120]. Further modifier addition will promote the dimer cleavage into isolated orthophosphate PO_4 units [120, 124].

Orthophosphate glasses (x=0.75): a point will be reached were all the covalent P-O-P bonds have been disrupted to be entirely replaced by ionic links between isolated PO_4 tetrahedral units and polyvalent cations [120].

Unlike singly charged alkaline metals, polyvalent modifier oxides (Mg^{2+}, Ca^{2+}, Fe^{3+}, Al^{3+} and Ti^{4+}, etc.) manage to dramatically improve glass stability and chemical durability, being capable to reduce the degradation rate over more than four orders of magnitude (from 10^{-4} to almost 10^{-10} $g \cdot cm^{-2} \cdot min^{-1}$) when incorporated to the glass system [13, 125, 126].

Such results were explained by the formation of ionic crosslinks between neighbouring NBOs of different chains by polyvalent cations in a way that resembles a metal chelate structure as illustrated by Figure 1.21 in the case of CaO substitution [120, 124].

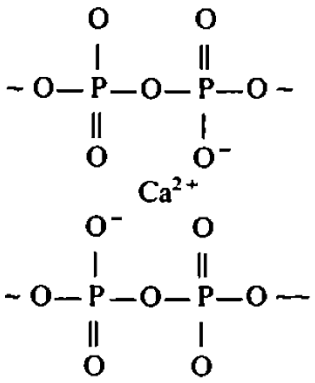


Figure 1.21: Ionic crosslinks between adjacent polymer-like phosphate chains [13].

The charge-to-size ratio of the modifier cation also plays an important role in determining the strength of the ionic crosslinks between two NBOs and the whole network [120, 121, 127]. It is expected that the substitution of a cation for another with higher charge-to-size ratio (small cations with higher valences) will result in a more rigid structure with stronger bonds [124]. This behaviour has been confirmed by the synthesis of glass systems containing Fe_2O_3 and TiO_2 with degradation profiles lower than those of the reference compositions containing monovalent cations [128-130].

1.5.3.1.2 Phosphate Based Glasses Solubility and Degradation

Water incorporated into the structure can also disrupt the phosphate network, thereby acting like a network modifier [120, 124]. Due to the asymmetry of the PO_4 tetrahedron (that impair the P-O-P bond stability) high P_2O_5 content glasses are prone to hydrolytic degradation, precluding the ultraphosphate compositions from direct application [125, 126].

Nevertheless, this apparent drawback offers the opportunity to tailor the degradation rate by replacing the highly hydrolysable P-O-P covalent bonds with the more resistant M-O-P ionic crosslinks, making the meta- and polyphosphate compositions of special interest [131]. Therefore, a significant amount of work has focused on the dissolution behaviour of complex phosphate glass systems, where the effect of multiple modifier oxides has been characterised [13, 125, 126, 130, 132].

It is generally accepted that phosphate glasses dissolve congruently in aqueous solutions without preferential leaching of their constituents. The dissolution process starts with the diffusion-controlled network hydration, during which a hydrated layer of glass is formed by the penetration of water molecules into the glass network and the subsequent disruption of ionic interchain linkages via NBOs ion exchange or hydration reactions [13, 124]. From the reaction presented in Figure 1.22, it is evident that the lower the pH of the medium, the more the equilibrium shifts towards the protonation of the NBO, giving rise to faster degradation rates in acidic media [125].

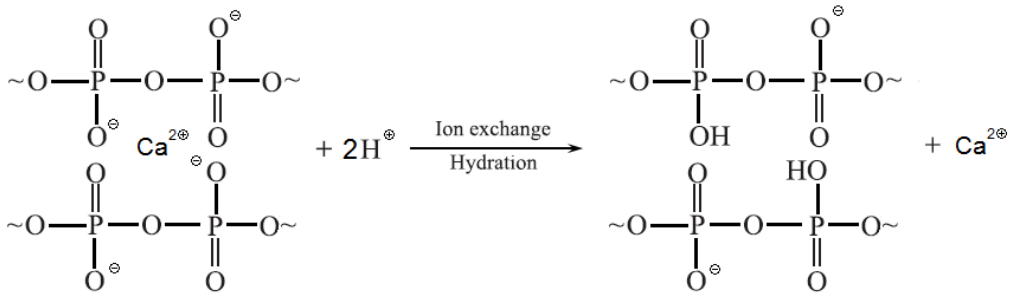


Figure 1.22: Ion-exchange reaction in which protons associate with NBO and crosslinking cations are released into solution [125].

Eventually all M-O-P bonds that link neighbouring phosphate chains at the glass-media interface are disrupted so that totally hydrated chains can detach from the surface and float into solution [13]. Once in solution, the P–O–P bonds in the hydrated chains are cleaved by the hydrolysis reaction as shown in Figure 1.23, leading to the production of acidic phosphate anions and the decrease of the leachate pH [125]. Kinetics of long phosphate chains hydrolysis are sluggish, making possible the use of techniques like chromatography to characterise the structure of pristine phosphate glasses from the analysis of the dissolution medium [133].

As glass dissolution proceeds, a point will be reached where the glass-media interface moves with identical velocity to the hydration front so that linear reaction kinetics dominate the glass dissolution behaviour [125].

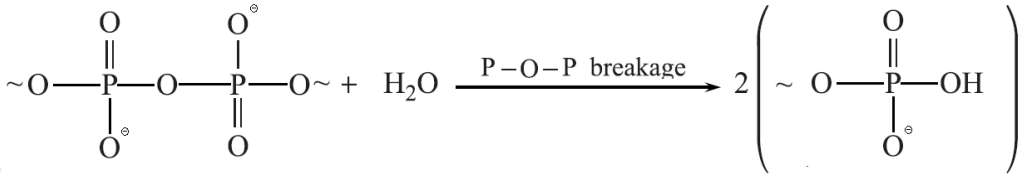


Figure 1.23: Hydrolytic cleavage of P-O-P bonds [125].

1.5.3.1.3 Phosphate Based Glasses Biocompatibility

Since the typical constituents of phosphate glasses are elements that naturally occur inside the body, it has been envisaged that these materials will benefit from a superior biocompatibility. Furthermore, interaction of the local cell environment with metallic ions selectively incorporated into the phosphate glass network and gradually released into the surrounding medium in the course of glass dissolution could have anti-inflammatory and antibiotic effects, as well as actively encourage osteo- and angiogenesis [14, 134].

The potential suitability of these glasses for their application in hard tissue regeneration has been assessed by incubation of human osteoblast cell lines on glass samples with mainly polyphosphate compositions [129, 135-137]. It was concluded that the biological response of these phosphate glass systems is strongly influenced by the dissolution behaviour.

Samples with lower dissolution rates supported higher numbers of viable cells, whereas rapidly degrading compositions presented reduced cell proliferation [136, 138]. The phenomena was explained by the excessive amount of ions released from the glass as a result of the dissolution process, coupled with the decrease in pH associated with the cleavage of P-O-P bonds, that have a deleterious effect on cells [136, 138]. Therefore it is expected that additions of modifier oxides known for their effect in reducing the degradation rate, result in significant improvements in the glass biocompatibility.

1.5.3.1.4 Phosphate Glass Fibres

Industrial production of glass fibres is conducted via melt-drawing, in which multiple hydrostatic pressure-driven jets of glass are attenuated by tensile stresses applied by a rotary drum [139]. Molten glass can only flow out of the nozzle if the hydrostatic pressure is greater than pressure associated with the glass surface tension (proportional to $4\sigma/D$, where σ is the glass surface tension and D is the orifice diameter) [140]. Once the weight of the glass drop under the nozzle exceeds the opposing surface energy, continuous fibre drawing (instead of the formation of discrete glass drops) can be conducted provided the application of tension to the glass jet [140].

The ability to produce fibres via attenuation of a jet of molten glass is primarily determined by the ratio of the glass viscosity to the glass surface tension; the higher this value the easier to draw fibres from a particular glass melt [140, 141]. For glasses with fibre-forming tendency, the viscosity-surface tension ratio usually falls within the 2.0-26.0 limits [140].

On the other hand, the capacity of drawing continuous fibre heavily depends on the crystallisation tendency of the glass, chemical and thermal uniformity and gas saturation, being the formation of crystals and gaseous inclusions the most frequent causes of filament breakage in the course of fibre production [140, 142]. Continuous glass fibres can also be produced via the glass rod

method, in which a glass preform is heated in between the glass transition and the onset of crystallisation temperature. However, due to its low efficiency, the glass rod method is limited to very specific compositions and applications (e.g. fibre production from refractory materials and optical fibres) [140, 142].

In general, the highly disrupted glass networks characteristic of compositions with large modifier oxides substitutions (especially monovalent alkaline cations which do not form ionic crosslinks between neighbouring phosphate chains) tend to crystallise more readily [12, 141]. Crystallisation tendency is strongly connected to the glass viscosity and glass structure since the small phosphate structural units (ortho- and pyrophosphate groups) in low viscosity glass melts can easily rearrange into crystalline aggregates at the processing temperature [12, 143, 144].

Conversely, phosphate-based glasses constituted from polymeric-like chains (namely poly- and metaphosphate glasses) present a lower tendency to crystallise as a result of the higher viscosity of such glass melts, in addition to the sterically inhibited rearrangement of long phosphate chains towards the denser crystalline structure [12, 145].

The field strength of the modifier cations has also been found to alter the crystallisation tendency. Inclusion of modifier cations with large field strength values resulted in a lower crystallisation tendency due to stronger ionic crosslinking between neighbouring phosphate units [12, 144]. Alternatively, the crystallisation tendency can be reduced merely by increasing the number of components in the glass melt, thereby increasing the entropy of mixing and the energy barrier for atomic diffusion, making quaternary and quintenary highly suitable for fibre drawing [12, 115, 146].

The extreme cooling rates (~10^6 $K \cdot s^{-1}$) experienced during glass fibre production results in the freezing of a more open liquid-like structure with higher volume in comparison to that associated with slowly cooled bulk glasses as illustrated in Figure 1.24 [147, 148]. Glass structure can be characterised in terms of the disposition of the atoms in the supercooled liquid frozen at a certain fictive temperature T_f, which corresponds to the intersection of the extrapolated liquid and glass volume lines as illustrated in Figure 1.24

[148]. The higher the cooling rate, the higher the fictive temperature and the more open the structure of the resulting glass.

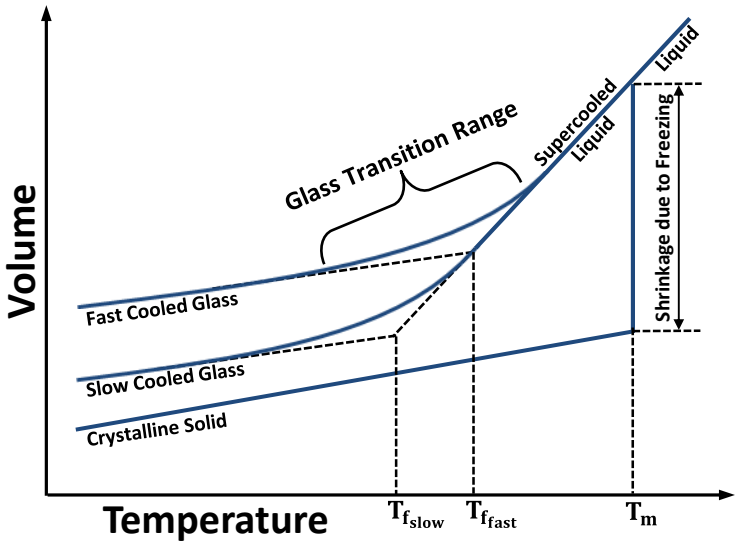


Figure 1.24: Effect of cooling rate on the volume of a glass forming melt. Adapted from [148].

The application of tensile stresses in the course of fibre drawing causes the orientation of structural units along the fibre axis and defects created during fibre drawing or glass synthesis (striae, microbubbles and inhomogeneous domains) as suggested by birefringence measurements [149, 150]. As the temperature approximates to the glass transition region, stress relaxation is hindered by the exponential increase in viscous resistance, locking the glass structural units in their oriented positions [148].

The orientation of both phosphate chain molecules and defects parallel to the fibre axis in phosphate glass fibres has been suggested to greatly contribute to the strength differences observed between glass fibres and bulk samples [147, 149-151]. Strong anisotropic features have been noticed in glasses with structures comprising mainly long phosphate chains (i.e. glass compositions close to the metaphosphate range) substituted with modifier cations weakly bonded to oxygen so that molecular alignment is not hampered by strong ionic interactions between neighbouring chains [149, 150, 152].

In addition to fibre strength, structural alterations caused by the thermal (hyperquenching) and mechanical history (drawing stresses) result in the variation in physicochemical properties between glass fibres and bulk glass,

including, but not limited to, elastic modulus, refractive index, density, degradation rate and thermal expansion [149, 150, 153, 154].

It should be noted that the stress-induced anisotropic structure frozen into glass fibres is highly unstable and it can be quickly relaxed at relatively low temperatures (in the order of 0.5 T_g) through local structural rearrangements driven by vibrational dynamics upon heat treatment [147, 155]. On the other hand, relaxation of the hyperquenched structure (also referred to as enthalpy relaxation) requires the rearrangement of the entire glass network via bond switching, and thus demands for higher annealing temperatures and/or annealing times [147, 149, 155].

1.5.3.1.5 Phosphate Glass Fibres Dissolution

Phosphate glass fibres dissolve at a significantly higher rate vis-à-vis the corresponding bulk glass on account of the larger surface area in contact with the conditioning media [127, 156, 157].

Alteration layers in the form of peripheral shells (see Figure 1.25) have been observed to form in the course of phosphate glass fibres *in vitro* degradation in static and dynamic conditions and different types of conditioning media (deionised water, SBF, TRIS and PBS), however, no consensus has been reached with respect to the nature of such structures [115, 158-162].

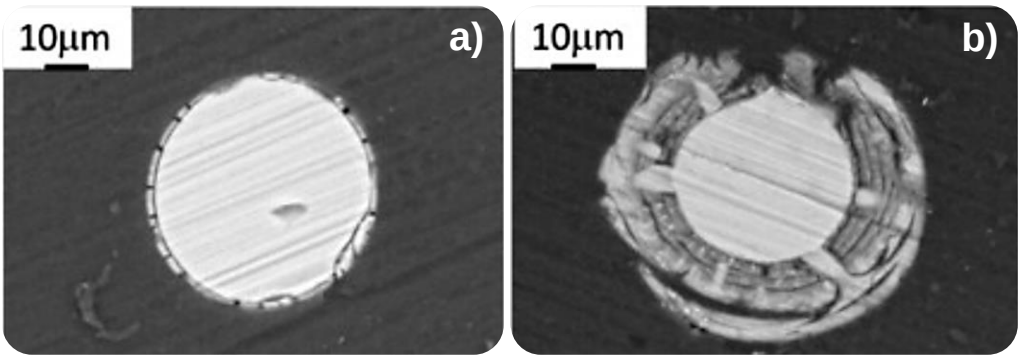


Figure 1.25: Cross section SEM images of $50P_2O_5{\cdot}40CaO{\cdot}10NaO_2$ mol% phosphate glass fibres after a) 6 h and 72 h of SBF conditioning [161].

On the one hand, such formations have been attributed to the detachment of a hydrated layer with chemical properties different to those of the fibre core [146, 158, 160, 162]. The difference in chemical properties was suggested to arise from the formation of a chemically stable outer layer in which phosphate structural units were frozen in highly oriented positions as a result of the extreme cooling rates experienced by the surface during fibre drawing [160].

On the other hand, the origin of the core-shell structure was explained by the precipitation of calcium-phosphate phases following the saturation of the conditioning media with glass corrosion by-products [127, 161].

1.5.4 Polymer-matrix Reinforced Composite Biomaterials

Despite their exceptional biocompatibility and strength, bioactive and bioresorbable ceramics and glasses are limited by their inherent brittleness, whereas polymers lack of the required mechanical properties to provide sound support to the injured limb during fracture reduction.

Composites offer the opportunity to overcome the shortcomings of homogeneous materials. Dispersion of ceramic reinforcements in a polymeric matrix exploits their mechanical and bioactive traits while securing the toughness and manufacturability of plastics.

The use of composite materials as orthopaedic devices seems more pertinent ever since human tissues are essentially composites with anisotropic properties relying on the volume and structural arrangements of their constituents [69].

Furthermore, composite materials benefit from an unmatched design flexibility since their mechanical properties can be easily tailored by controlling i) the mechanical properties of the individual constituents, ii) the relative amounts of the dispersed and/or continuous phases (volume fraction) iii) reinforcement aspect ratio (continuous or discontinuous reinforcements) iv) reinforcement orientation with respect to the main loading direction (only applicable when the reinforcing phase has a dimension significantly larger with respect to the others as in fibrous reinforcement). Intimate contact between the constituents is critical for effective transfer of stresses from the soft matrix to the stiff ceramic reinforcement, otherwise a significant reduction in mechanical properties will be ensued in the final composite parts [163, 164].

1.5.4.1 Thermosets and Thermoplastic Polymer Matrices

At its most basic level, polymer-matrix composite materials are classified in terms of the physicochemical nature of the matrix as thermoset and thermoplastic reinforced composites. The specifics of the manufacturing

processes vary in function of the characteristics of the respective polymer matrix and reinforcements used [165].

Thermoplastics are high molecular weight polymers whose chains associate through relatively weak van der Waals forces that can be easily overcome by the thermally excited polymer chains [166].

Alternatively, thermosetting polymers are constituted from long chains strongly crosslinked via covalent bonds, forming a three dimensional network once curing has been completed. Unlike thermoplastic composites, thermosets do not melt upon heating but undergo thermal degradation since the energy necessary to disrupt the bonds between the chains for them to move relative to each other is equal to the energy required to cleave the bonds within the polymer backbone itself [166, 167].

The great majority of structural composite components are manufactured from thermosetting resins on account of their low viscosities (typically under 100 mPa·s), which facilitates full impregnation of the reinforcement during processing [168]. Nevertheless, the presence of potentially toxic monomers, catalysts and additives has severely limited the applications of thermoset reinforced composites in the biomedical field to mainly dental restoration [69, 169, 170].

Unlike thermosets, thermoplastics are fully polymerised at the time of processing and are considered to be free from the biocompatibility complications associated with potentially harmful leachates [69]. Furthermore, the fabrication cycles of thermoplastic composites are significantly shorter (usually less than an hour) and simpler with respect to thermosets (frequently in excess of 6 hours), which may require, degassing, preheating and cooling under vacuum in addition to lengthy curing times under high temperature and pressure [171]. Also, thermoplastic composites can in theory be reshaped as required at the time of surgery to fit the patient's anatomy [69, 171]. Nevertheless, the high viscosities of thermoplastic melts (100-1000 Pa·s [172]) pose technological challenges to the manufacture of high quality composite parts.

1.5.4.2 Manufacture of Reinforced Thermoplastic Composites

The manufacturing techniques and processing variables of thermoplastic composites are greatly influenced by the morphology and scale of the reinforcement. Particle (micron and even nanosized) and short fibre (0.5-3 mm) reinforced thermoplastic composites can be compounded via twin mill rollers and single or twin screw extruders [173-175]. The extruder can be part of an injection moulding line, in which an accurately sized shot of fibre filled polymer is rapidly forced through a small gate into a split mould through the action of a reciprocating screw. Alternatively the filler compound can be pelletized and subsequently processed via compression moulding [173, 176].

The shear forces involved in fibre-polymer compounding for short and particle reinforced thermoplastic composites would result in the attrition of continuous fibres and the loss of the mechanical advantage obtained by embedding high aspect ratio reinforcements [176-178]. Therefore, the processing of continuous fibre reinforced thermoplastic composites is limited to low-shear manufacturing methods, namely i) compression moulding, ii) pultrusion and iii) thermoforming [173, 179, 180].

Traditionally, continuous fibre reinforced thermoplastic composites are manufactured by stacking alternate layers of fibre mats and polymer films inside a mould cavity. Composite consolidation takes place by heating the mould to a temperature at which the molten polymer presents a viscosity low enough to percolate through the dense fibre network upon pressure application [173, 179]. The extent of polymer penetration into the fibrous structure is directly proportional to the magnitude of the applied pressure and fibre network permeability, and inversely varies with polymer viscosity and thickness of the fibrous structure as stated in Darcy's Law [173, 181]. Fibre network permeability decreases with applied pressure, and so excessive consolidation pressures should be avoided [164, 182].

The poor drapability of most of thermoplastic preforms coupled with their lack of tackiness poses difficulties in their conformation to the mould cavity, and is particularly difficult in the presence of curved surfaces [20]. These complications have restricted the manufacturing of continuous fibre reinforced thermoplastics featuring two-dimensional curvatures to pultrusion and post-process shaping methods like thermoforming.

Composite profiles with constant cross section can be consolidated and shaped in a single operation by continuously pulling reinforcing fibres impregnated with a thermoplastic matrix through a die with the desired shape [173, 183, 184]. The main disadvantage of thermoplastic pultrusion is the low processing speed required to achieve adequate impregnation of fibre bundles, which increases the product cost and reduces its commercial relevance [184, 185]. In addition, there is a risk of stagnation within the polymer melt container and fibre breakage frequently occurs due to the high tensile stresses developed consequent to the contact with multiple spreading pins which are indispensable for the fibre bundle impregnation [186].

To circumvent the fibre wetting issues encountered during continuous melt impregnation, the fibre and the matrix can be assembled into intermediate hybrid entities that can be used as a raw material in thermoplastic pultrusion (see Figure 1.26) [179, 180, 185]. Hybrid preforms reduce the path that the polymer melt has to displace to fully impregnate the fibres by bringing the composite constituents to intimate contact [184]. Powder impregnated tows, commingled yarns and pre-consolidated tapes are the three most important concepts used in industry for the fabrication of hybrid preforms [173, 186]. However, the polymer has to be either ground into very small particles as in powder impregnation or spun into fibres (preferably of the same size as the reinforcing filaments) for commingled products [180, 184, 185]. Only then, the matrix can be intimately combined with the reinforcing fibres. In the case of preconsolidated tapes, heated fibre rovings are spread and partially impregnated with polymer by means of a crosshead die designed to produce a flat shape [173, 185].

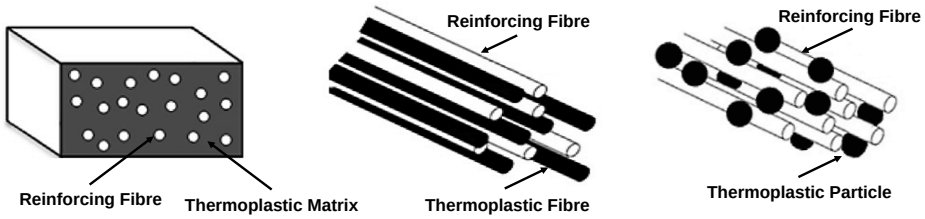


Figure 1.26: Commercially available thermoplastic hybrid preforms. Adapted from [185].

These additional steps of reshaping and combining augment the cost of hybrid preforms and increase the overall cycle time for the production of the final reinforced thermoplastic product. Furthermore, the spreading of the fibres through pins or air jets during physical blending, damages the fibres,

precluding the processing of fine and delicate filaments [179]. In addition, high residual stresses that may induce cracks and ultimately delamination due to the quick cooling experienced by thermoplastic pultruded products remains issue [185, 187].

Two- or three-dimensional thermoplastic composites can also be manufactured via forging which consists in the stamping of pre-consolidated thermoplastic composite products [173]. Off-axis components with varied cross sections in the length direction can be manufactured from flat laminates through these means. In spite of its versatility and simplicity, the method is labour intensive and process-induced defects which drastically impair the composite mechanical performance can be introduced as a result of the stress state generated during the stamping stage [21, 188].

1.5.4.3 PLA-based Bioresorbable Composites

In order to prevent the medical complications of rigid fracture fixation, the mechanical properties of the fixation device should decrease in a controlled fashion ideally matching the bone healing rate so that robust bone union is favoured by the increasing mechanical stimulation. To meet this need, the manufacture of fully bioresorbable composites as an alternative to metallic implants is being heavily investigated [18, 189-195].

Fracture fixation devices constituted from bioresorbable polymers and bioresorbable ceramic/glass reinforcements confer major advantages over metallic implants, including: i) obviation of surgical removal, ii) release of chemical species from ceramic/glass dissolution that can elicit favourable cell responses and buffer large pH variations caused by polymer hydrolysis and iii) prevention of bone atrophy by initially matching bone mechanical properties and gradually transferring load to the healing tissue upon degradation [14, 196].

Bioresorbable composites based on aliphatic polyesters can be manufactured through conventional melt impregnation techniques. However, on account of the hydrolytic sensitivity of the ester linkage, the temperature cycle has to be carefully controlled to prevent large molecular weight reductions during processing [197, 198].

1.5.4.4 PLA-based Bioresorbable Composites with Discontinuous Reinforcements

Since 1990 biodegradable composites have been fabricated by incorporating different bioactive fillers into a PLA matrix, being synthetic HA, TCP and silicate-based 45S5 Bioglass® 'BG' ($46.1SiO_2 \cdot 26.9CaO \cdot 24.4NaO \cdot 2.6P_2O_5$ mol%) the most studied systems on behalf of their osteoinductive behaviour [69, 199, 200]. In theory, the addition of the stiffer and stronger ceramics (E_{BG}=35 GPa & S_{BG}=500 MPa [201]; E_{HA}=114 GPa & S_{HA}= 685 MPa [201, 202]; E_{TCP}=21 GPa & S_{TCP}= 315 MPa [203], where E is the elastic modulus and S stands for the compressive strength), provided a homogeneous dispersion, should enhance the PLA mechanical properties, ever since the strengthening effects of these phases have been documented in alternative polymeric matrices at high volume fractions ($v_f \geq 0.40$) [204-206].

BG-PLA composites have been fabricated through extrusion compounding followed by compression moulding [207-209]. The addition of Bioglass® particles resulted in decreases in strength, elastic modulus and strain with respect to the neat polymer. Increasing content of BG particles lead to in further decreases in the mechanical properties, i.e., the composites became weaker and more brittle as the BG particle volume fraction was increased [207-209]. Incorporation of Bioglass® particles impaired the elastic modulus and the bending and shear strength of the PLA-based composites even in those cases where the matrix was self-reinforced by hot solid-state axial orientation in a die-drawing process [210].

The decrease in elastic modulus and strength was attributed to a poor glass/polymer interface (see Figure 1.27) and porosity stemming from gas generation during extrusion [208, 209]. Moreover, poly(α-hydroxyesters) matrices experience accelerated thermal degradation during melt processing even at rather low temperatures (150°C) in the presence of BG particles as evidenced by the development of a yellowish tone in PLA and later confirmed by size exclusion chromatography 'SEC' [207, 208].

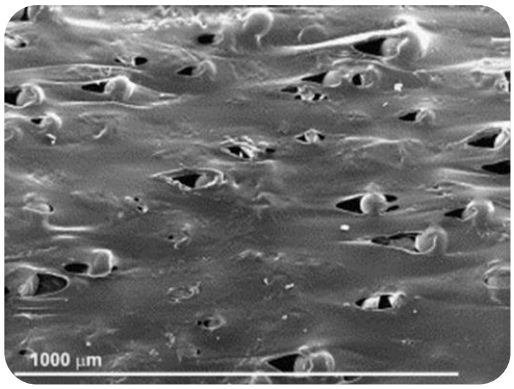


Figure 1.27: Distribution of bioactive glass spheres in a PLA matrix with 40 wt% of filler. No adhesion was observed between the polymer and BG spheres [208].

The post-processing molecular weight of neat PLA corresponded to the ~85% of its original value. The addition of 0.02 volume fraction of BG particles resulted in a decrease in molecular weight in excess of 70% with respect to the as-received PLA [207]. It was suggested that the presence of $Si\text{-}O^-$ entities at the particle surface (created as a result of the interaction of the hydrophilic glass particles with environmental moisture) catalysed polymer chain scission at the filler–matrix interface [207].

Similarly TCP was identified as a non-viable reinforcement for PLA-based composites fabricated via melt processing methods [196, 211-213]. As shown in Figure 1.28, the poor adhesion between PLA and the ceramic particles resulted in a weak interface where voids can develop and subsequently nucleate or interact with a growing crack.

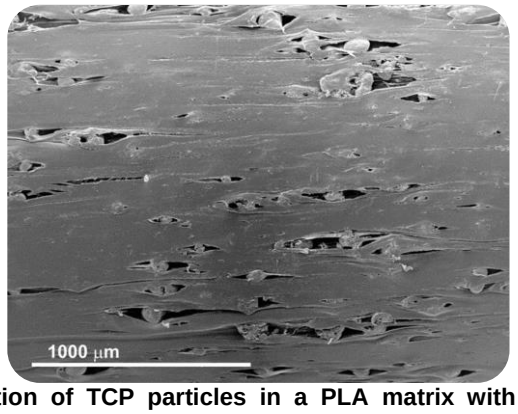


Figure 1.28: Distribution of TCP particles in a PLA matrix with 20 wt% of filler. No adhesion is observed between the polymer and TCP particles [196].

Furthermore, the incorporation of TCP resulted in the decrease of PLA molecular weight with respect to the neat polymer. It should be noted, however, that despite their detrimental effect on the mechanical performance of neat-PLA and initial molecular weight, the release of PO_4^{3-} ions from TCP dissolution prevented the acidification of the medium by neutralising protons

evolved during the hydrolysis of ester linkages in the course of *in vitro* degradation studies [196, 207].

Discontinuous phosphate glass fibres have been used to reinforce PLA compression moulded plates [214]. In spite of the poor interfacial fibre-matrix adhesion (as evidenced by the clean fibre surfaces free from any matrix residue in Figure 1.29), embedment of random discontinuous phosphate glass fibres in PLA via compression moulding resulted in significant increases in strength and elastic modulus with respect to the neat-PLA control samples [194, 215-217]. The mechanical properties of the composites gradually increased leading to a plateau with further fibre addition, reaching flexural strength and flexural modulus values of ca.120 MPa and ca. 10 GPa for a 0.45 fibre volume fraction composite, respectively [215].

In contrast to particle reinforced composites, the significant increases in strength and modulus in random mat discontinuous phosphate glass fibre reinforced PLA composites can be attributed to the higher aspect ratio of the fibres with respect to discrete particles, which present a larger surface area for the matrix to interact with.

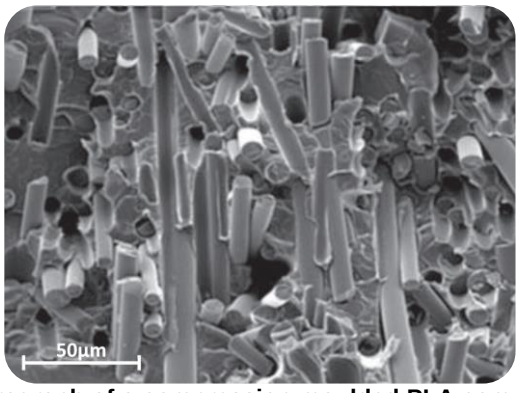


Figure 1.29: SEM micrograph of a compression moulded PLA composite plate reinforced with 10 mm phosphate glass chopped fibres [216].

The incorporation of HA particles into PLA through conventional melt processing methods has been shown to enhance the elastic modulus and biocompatibility at expense of the strength as a result of the poor interfacial bonding between the hydrophilic reinforcement and the hydrophobic matrix [218-221]. A better contact between the composite constituents can be achieved by forcing the solid-state polymer matrix into the surface discontinuities of the HA particles via a solid-state forming process referred to as forging [196, 207].

Rods and plates manufactured via forging showed the highest mechanical properties among discontinuously reinforced composites, reaching a flexural strength of approximately 270 MPa and a flexural modulus of 12 GPa for a particle volume fraction of 0.32. The excellent mechanical properties were ascribed to the microanchoring (mechanical interlocking) between the HA particles and the PLA matrix in addition to the complex crystal orientation achieved by forging. More importantly, the strength values were retained at levels over 200 MPa for over 6 months. However, the remarkable properties of HA-PLA forged composites depended on the high crystallinity content of the samples, which initially were close to 50%, reaching values of 60% after a 6 months degradation period [222]. Slowly resorbing PLA crystalline residue has been observed to trigger foreign body reactions and osteolysis during in vivo degradation studies [212, 223]. Furthermore, the reported moduli still fall short from the optimum values, which for safety reason should exceed those of cortical bone.

1.5.4.5 PLA-based Bioresorbable Composites with Continuous Reinforcements

The high availability of standard or near standard methods to manufacture particulate and short fibre reinforced composites has overshadowed the superior mechanical performance of continuous fibres as evidenced by the number of publications committed to the processing of discontinuously reinforced composites [204-206, 208, 209, 211]. Continuous reinforcement demands careful handling and low shearing processes to prevent damaging the delicate fibres. Such a requisite is incompatible with mass production technologies like conventional extrusion and injection moulding that force the melt through a narrow bore and depend on high shearing forces to achieve homogeneous reinforcement dispersion [106, 224].

This circumstance leaves compression moulding and pultrusion as the only methods capable of producing finished or semi-finished thermoplastic composite products [106, 224]. However, due to the elevated up-front investment required to set up a pultrusion facility [225] along with the poor drapability and tackiness of thermoplastic preforms (which hamper their conformation to curved surfaces [226], an overwhelming majority of investigations featuring experimental continuous fibre reinforced bioresorbable

composites employed some form of compression moulding for the manufacture of mainly plate-like products [193-195, 215, 227].

1.5.4.5.1.1 Fully Bioresorbable Continuous Fibre Reinforced-PLA Composite Plates

The benefits conferred by the use of continuous fibres over discontinuously reinforced composites have been confirmed for PLA-PGF composites in previous works [15-17, 227]. Samples fabricated by compression moulding of PLA films and unidirectional 'UD' mats reported flexural strength and modulus values approximately two times greater than their short fibre reinforced counterparts for equivalent fibre volume fractions [15, 16]. This was attributed to a larger matrix/fibre interfacial area in long fibre reinforced composites, allowing the polymer to transfer more efficiently the load to the reinforcement in addition to the reduction of fibre end effects [227-229].

More importantly the properties of the composites coincided and even surpassed the target upper-limit cortical bone properties achieving flexural strengths in the range of 250-325 MPa and moduli averaging 25 GPa [15, 16]. However it must be noted that large standard deviations were observed in these studies as a result of the poor control over the manufacturing process and the low number of specimens tested (3 maximum), emphasising the low-yield and lack of reproducibility of the methods used [15, 16, 227].

A quick deterioration of the mechanical properties in excess of 30% with respect to the initial strength and modulus was frequently observed during the first 3 days of PGF-PLA composite plate samples conditioning in aqueous media [215, 230, 231]. The strength and modulus continued to decrease with further conditioning time until reaching a plateau at approximately day 15, matching the values of control neat-PLA samples [215, 230]. In some cases the mechanical properties were observed to bypass the control values and continued to decrease for the remainder of the study [232].

The velocity at which the mechanical properties of the composite decreased during conditioning in aqueous medium, especially the elastic modulus, was observed to depend on the fibre degradation rate. Slowly dissolving phosphate glass fibres with higher substitutions of iron and boron oxides where seen to retain the mechanical properties for longer periods in comparison to fibres with

higher dissolution rates containing only alkaline and alkaline earth cations [231-233].

The quick loss of mechanical properties after immersion in aqueous solution was attributed to the disruption of the fibre-matrix interface by capillary water, impairing stress transfer to the reinforcing fibres [215, 231]. The pH of the conditioning medium was observed to decrease in the course of the composite degradation study as a result of fibre dissolution and the formation of acidic species from phosphate chains hydrolysis [18, 215, 232].

Treatment of fibres with coupling agents, namely, 3-aminopropyltriethoxy silane and sorbitol ended PLA oligomers, resulted in significantly higher strength and modulus values due to the formation of a chemical bonding between the matrix and the fibres in compression moulded PGF-PLA plates. However, the composites still exhibited important losses in mechanical properties after immersion in aqueous solution, reaching values close to the PLA control by day 15 [230].

Continuous fibre reinforced PLA composite plates with flexural strengths exceeding 700 MPa have been manufactured via compression moulding of preimpregnated silicate-based glass fibre cords with nominal compositions containing SiO_2 in excess of 67 wt% for ease of fibre drawing. Sizing was added in the course of fibre drawing as a water-based dispersion of 3-glycidoxypropyltriethoxysilane and polycaprolactone as a compatibiliser to improve the adhesion of the silicate-based glass fibres to the PLA matrix. A continuous reduction of both the modulus and strength was observed throughout the entire 22-weeks study.

Strength and modulus reductions in excess of 60% and 30% were observed after 2 weeks of conditioning in SBF. However, on account of the extreme mechanical properties and the low dissolution rate of the silicate-based glass fibres used, the modulus and the flexural strength of the composite plates decreased below the range of mechanical properties of bone after 13 and 9 weeks, respectively for the best performing samples fabricated. Although silicate-based glasses readily form HA-like surface layers and bond to bone, they are rarely fully resorbed [234-236]. Therefore, a portion of pristine core glass is often found after years of implantation [235, 237, 238]. Furthermore,

silicate-based glasses with composition containing SiO_2 in concentrations greater than 65 wt% have identified as effectively bioinert and implantation might result in scar tissue encapsulation [114].

1.5.4.5.1.2 Fully Bioresorbable Continuous Fibre Reinforced-PLA Composite Rods

In order to expand the applicability of fully bioresorbable continuous fibre reinforced composites and encompass the full spectrum of fixation devices, alternative geometries other than simple flat shapes and the methods by which they are produced need to be investigated.

As mentioned in §1.5.4.2, there are a range of complications in the production of high quality reinforced composites in configurations other than simple flat plates, specifically cylindrical rods, which are directly associated with the continuous nature of the fibres and the lack of tackiness and drapability of conventional thermoplastic preforms [226, 239, 240].

Such complications have limited the study of manufacturing of continuous fibre reinforced bioresorbable composites rods to a handful of publications focused on the forging of preconsolidated composite blanks [226, 239, 240]. Fully resorbable cylindrical composite rods were fabricated by solid state forming of continuous phosphate glass fibre reinforced-PLA rectangular bars with dimensions of 4.5 mm × 3.05±0.05 mm × 100 mm (thickness x width x length) at 90-100°C. The rectangular bars were machined from compression moulded plates manufactured via laminate stacking of PLA films and unidirectional phosphate glass fibre mats. Reasonable values of flexural strength (240 MPa) and modulus (25 GPa) were obtained for rods with a fibre volume fraction of 0.37±0.02. The higher mechanical properties of the rods in comparison to those of previously reported plates with similar fibre content were attributed to the orientation of the PLA chains in the rod axis as a result of viscous flow during forging [15].

Retention of mechanical properties was observed to depend on the composition of the glass fibres. The strength of composite rods containing fast degrading fibres with a composition of $50P_2O_5{\cdot}40CaO{\cdot}5Na_2O{\cdot}24MgO{\cdot}5Fe_2O_3$ mol% (P50Fe5) continuously decreased, finally reaching values below 50 MPa after 28 days in PBS solution at 37°C. Alternatively, rods reinforced with slowly degrading glass fibres with P40Fe4 composition

($40P_2O_5 \cdot 16CaO \cdot 16Na_2O \cdot 24MgO \cdot 4Fe_2O_3$) presented values close to 100 MPa up to 42 days, finally decreasing to ca. 75 MPa by day 63.

The effect of conditioning in elastic modulus was lower with respect to flexural strength. The modulus of the composite rods reinforced with P50Fe5 fibres remained within the range of human cortical bone (>10 GPa) for 28 days. On the other hand, the modulus of the composite rods with P40Fe4 fibres remained above 10 GPa for 63 days.

In contrast to particulate reinforced composites, the deformation response of long fibre thermoplastics during forging is directionally dependent due to their orthotropic properties [165]. Furthermore, the heterogeneous nature of fibre reinforced composites implies a non-uniform through-thickness strain and stress distribution, which may lead to materials instabilities during processing. In spite of this, no evaluation of the effect of forging on the fibre reinforced composite physical properties nor the effect of initial composite structural features on the final forged product was conducted in [15, 18, 190, 231].

The manufacture of defect-free composite products with predictable performances is critical for load-bearing components, particularly for orthopaedic devices where premature failure due to forging induced defects can be catastrophic. Accordingly, it is essential to thoroughly investigate the effects of processing variables on the structure and performance of composite forged products so that optimum conditions can be implemented during part production to meet the end-application requirements.

2 Materials and Methods

2.1 Glass Synthesis

Glass of the composition $45P_2O_5 \cdot 16CaO \cdot 13Na_2O \cdot 24MgO \cdot 2Fe_2O_3$ mol% (elsewhere referred to as P45Fe2) was synthesised from reagent grade NaH_2PO_4, $CaHPO_4$, $FePO_4 \cdot 2H_2O$, P_2O_5 and $MgHPO_4 \cdot 3H_2O$ powder precursors (Sigma Aldrich, UK) mixed into a Pt/5%Au crucible (Birmingham Metal Co., UK). The crucible was placed in a furnace for 30 min at 350°C for moisture removal and then transferred to a furnace preheated at 1150°C for 90 min. Finally, the melt was poured onto a steel plate and left to cool to room temperature.

2.2 Melt-drawn Fibre Production and Fibre Heat Treatment

Phosphate glass fibres were manufactured by continuously drawing molten P45Fe2 glass onto a spinning drum with adjustable speed from a single nozzle Pt-10%Rh bushing (Birmingham Metal Co., UK) loaded with a specified amount of glass cullet using an in-house melt-drawing facility. Glass fibres were collected in the form of discrete bundles or non-woven unidirectional glass fibre mats as required by the respective fibre reinforced composite manufacturing method.

The volumetric yield, $\dot{V}$, in $cm^3 \cdot s^{-1}$ through the bushing nozzle can be estimated according to the Hagen-Poiseuille equation [241]:

$$\dot{V} = \left(\frac{\pi g}{128}\right)\left(\frac{\rho h D^4}{\mu L}\right) \quad (2.1)$$

where g is the gravitational acceleration in $cm \cdot s^{-2}$, ρ is the density of the glass at the processing temperature in $g \cdot cm^{-3}$, h is the head of bushing in cm (height of glass above the nozzle), D is the nozzle diameter in cm, μ is the dynamic viscosity of the glass at the processing temperature in poise and L is the nozzle length in cm.

The nozzle yield in $g \cdot s^{-1}$, $\dot{m}$, is related to the volumetric yield through Equation (2.2):

$$\dot{m} = \rho \dot{V} \quad (2.2)$$

Drawing conditions (melt temperature and bushing head) were carefully controlled to achieve the intended nozzle yield (ca. 1 g·min^{-1} or 0.017 g·s^{-1}) for the accurate collection of the required amount of glass fibre as specified by the target composite fibre volume fraction, $\mathbf{v_f}$, during composite manufacturing.

Being the flow rate through the nozzle independent of the drawing speed [241], the diameter of phosphate glass fibres drawn at different speeds were measured via SEM (cf. §2.10) and substituted in Equation (2.3) [241] for nozzle yield verification:

$$\dot{m} = \left(\frac{\pi d_1^2}{4}\right) v_1 \rho = \left(\frac{\pi d_2^2}{4}\right) v_2 \rho = \left(\frac{\pi d_n^2}{4}\right) v_n \rho \qquad (2.3)$$

where d_1, d_2, and d_n are the diameters in cm of the fibres drawn at speeds v_1, v_2 and v_n in cm·min^{-1}, respectively.

As-drawn fibre bundles were laid down straight on aluminium trays for heat treatment within a convection oven. The temperature was increased to 200°C at 20°C·min^{-1} followed by a 5°C·min^{-1} ramp to 460°C. The fibre bundles were isothermally held at this temperature for 60 minutes before cooling back to room temperature at 5°C·min^{-1}.

2.3 X-ray Diffraction

X-ray powder diffraction scans were performed on i) as-quenched glass, ii) as-drawn glass fibres and iii) annealed glass fibres. Samples were first ground to fine powder in an agate mortar and mounted into purpose-built holders for analysis at standard temperature and pressure conditions in a Siemens D500 diffractometer, configured in a Bragg-Brentanno geometry, using Cu Kα radiation (λ=1.5418 A°) in the 2θ range of 10–70°. Scans were performed using a step size of 0.02° 2θ every second. The X-ray tube was operated at 40 kV and 25 mA.

2.4 Glass Density Measurements

Bulk glass and as-drawn glass fibre density measurements were obtained via use of an AccuPycTM 1330 Pycnometer (with a precision of 0.1%) calibrated using a standard steel sphere. The analysis was repeated 10 times and the mean value was used for the relevant calculations.

2.5 Single Fibre Tensile Test

The tensile properties of 60 fibres with a gauge length of 25 mm in both the annealed and as-drawn condition were evaluated through uniaxial tensile test of individual filaments using a LEX810 Tensile Tester according to standard BS ISO11566. The fibres were randomly selected from bundles in the respective condition. Prior to testing, the fibre diameter was determined with a Mitutoyo Series 544 LSM-500S Laser diameter gauge.

Evaluation of the tensile strength was conducted using Weibull's statistics assuming a uniform distribution of independent flaws. Weibull parameters were calculated using Minitab® 15 (version 3.2.1).

2.6 Glass Thermal Analysis

The thermal properties of as-drawn and annealed glass fibres, in addition to as-quenched glass were determined via a DSC Q600 (TA Instruments , USA). Approximately 30 mg of sample (in powder form for glass fibres and as a chunk for as-quenched glass) were loaded into platinum pans and heated under argon gas flow of 100 $cm^3 \cdot min^{-1}$ from 25 °C to 1200°C at a rate of $20°C \cdot min^{-1}$. A 5 min isothermal hold was allowed before cooling at a rate of $20°C \cdot min^{-1}$ back to 25°C. The equipment was allowed to equilibrate at this temperature before resuming a subsequent run with the same parameters as those previously described.

2.7 Glass Viscosity Measurements

High temperature viscosity (800-110°C) of P45Fe2 glass was determined using a Brookfield DV-III rotational viscometer (UTRA, USA). The viscosity was determined by evaluation of the shear stress exerted by the molten in response to a cylindrical platinum spindle rotating at a predetermined shear rate.

2.8 *In Vitro* Phosphate Glass Dissolution Studies

2.8.1 Phosphate Bulk Glass Dissolution Study

Bulk glass dissolution study was conducted on cylindrical samples (10 mm in diameter and 10 mm in height) cut from glass rods prepared by casting molten glass into a graphite mould preheated at 460°C for 54 days. The mould was held at this temperature for an hour and then slowly cooled to room

temperature to prevent the formation of residual stresses. The specimens were placed into vials containing 30 ml of phosphate buffered saline 'PBS' (pH 7.42±0.1), in accordance with degradation standard test conditions (specified in ISO 10993–13:2010) and kept in an oven set at 37 °C to simulate physiological conditions. At different time points the three samples were removed from the solution and their masses were measured using a 5 decimal point sensitive balance (Sartorius CP 225D). The bulk glass percentage mass loss at the *i*th time point, $m_b(t)$, was determined through Equation (2.4).

$$m_b(t) = 100 \times \frac{m_{bt} - m_{bi}}{m_{bi}} \quad (2.4)$$

where m_{bi} and m_{bt} are the sample masses at the initial and *ith* day, respectively. Once the measurements were taken, the specimens were returned to their vials with fresh PBS solution.

2.8.2 Phosphate Glass Fibre Dissolution Studies

The dissolution behaviour of bare annealed and as-drawn fibres was investigated by individually conditioning 80 mm bundle segments of approximately 400 mg in glass vials filled with 40 ml of either of phosphate buffered saline (PBS, pH 7.5±0.05) or deionised water (DI, pH 6.6±0.2) maintained at 37°C for up to 30 days, in accordance to BS EN ISO 10993-13 (2010). Three fibre bundle specimens of each fibre type were recovered from solution at days 1, 3, 7, 15, 23, and 30. Throughout the study, the conditioning media was collected and replaced with fresh solution twice a week using the device shown in Figure 2.1. Briefly, a 10 µm square piece of nylon mesh was stretched across the top of the sample vials by means of a threaded plastic lid in which a hole was made. The top of a 60 ml plastic syringe barrel was then fitted on top of the sample vial. A rubber O-ring was placed inside of the severed syringe barrel to create a seal at the interface between the vial and the syringe barrel. Subsequently, the barrel-fitted sample vial and a 60 ml syringe were locked at the respective ports of a 3-way stopcock as shown in Figure 2.1. The discharge port was blocked as illustrated in Step 1 in Figure 2.1 and the plunger was pulled to extract the medium through the nylon mesh. Afterwards, the sample port was blocked as shown Step 2 in Figure 2.1 and the conditioning media was collected through the discharge port for analysis. The discharge port was then blocked again and deionised water was injected and then extracted again following the procedure described in Step 1 to

eliminate residual soluble salts. Finally, the sample vial was either i) refilled with fresh PBS solution as shown in Step 3 in Figure 2.1, if the dissolution study was to be continued or ii) evacuated from liquid and dried inside a vacuum oven at 50° C until constant weight was achieved. Dried samples were weighed using a digital balance of 0.01 mg resolution. The glass fibre percentage mass loss, m_{LF} (t), at the ith time point was determined through Equation (2.5) [115]:

$$m_{LF}(t) = 100 \times \frac{m_t - m_i}{m_i} \qquad (2.5)$$

where m_i is the initial mass of the glass fibre bundle prior immersion in the respective conditioning media and m_t is the mass of the glass fibre bundle at the ith time point after vacuum drying at 50° C.

The pH of the media collected from both bulk glass and glass fibre degradation studies was monitored using a bench-top pH meter (Metler Toledo S220 SevenCompactTM) sequentially calibrated using four standard buffer solutions (pH 2.0, 4.0, 7.0 and 10.0).

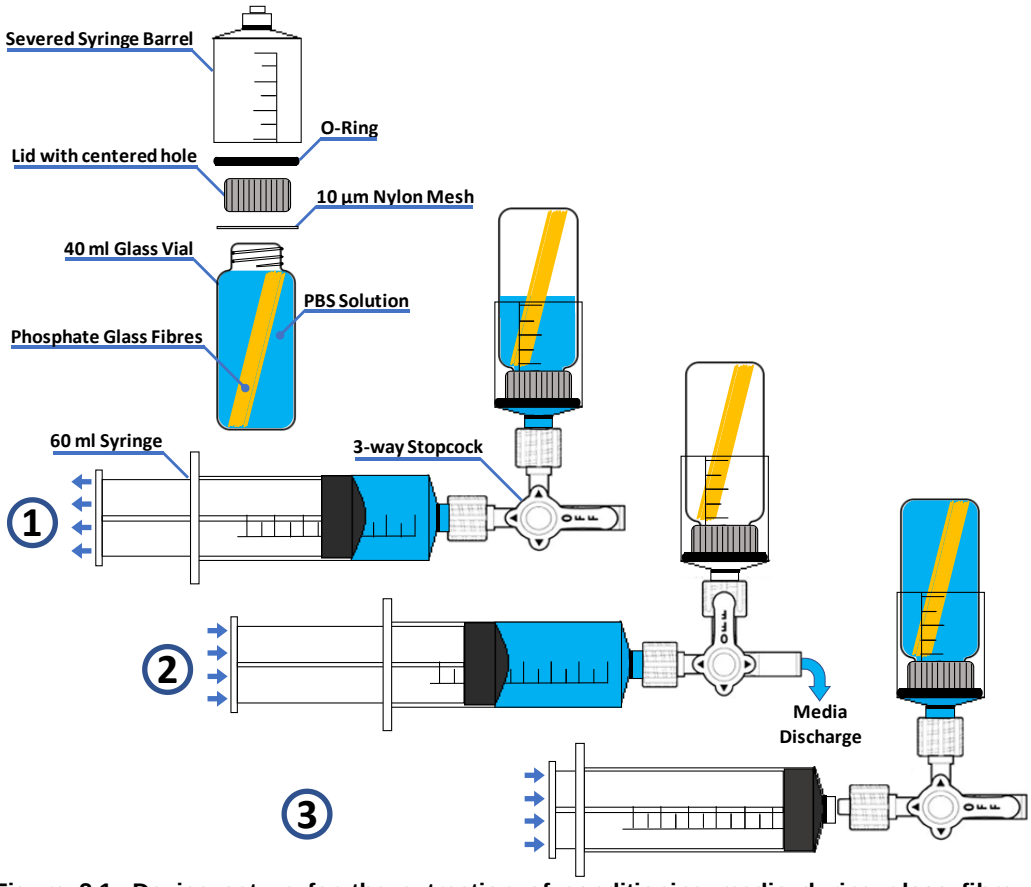


Figure 2.1: Device set-up for the extraction of conditioning media during glass fibre dissolution studies.

2.9 Energy Dispersive X-ray (EDX) Analysis

The chemical composition of the glass used in this study was evaluated by Energy dispersive X–ray analysis (EDX). Compositional analysis was conducted on epoxy resin embedded samples (e.g. glass rods, glass fibres and fibre reinforced composites) ground and polished using ethanol as lubricant. The samples were cleaned and dried with air spray and coated with a thin carbon layer by vacuum evaporation. At least three sites of interest for each degradation time point were characterised via EDX spot analysis with an Oxford Instruments ISIS 300 series equipment attached to a Phillips XL-30 scanning electron microscope using ZAF quantitative analysis. The system was operated with an accelerating voltage of 20 kV and an analysis time of 30 seconds. The working distance was adjusted to 10 mm.

2.10 Scanning Electron Microscopy (SEM)

The morphology of the fibres and the composites produced in this study were studied and compared by means of SEM. The respective samples were fixed onto aluminium stubs with conductive carbon sticky tabs and sputter coated (Agar Sputter Coater) with platinum for examination using a Philips FEI XL-30 scanning electron microscope with an accelerating voltage of 10 kV in secondary electron mode. For composite cross sectional analysis, samples were mounted in epoxy resin, ground and polished using ethanol as a lubricant.

The diameters of at least 30 different fibres in both annealed and as-drawn conditions were measured at each time point via SEM during the bare fibre degradation study. The estimated % mass loss, m_E, of both annealed and as-drawn fibres was calculated according to Equation (2.6):

$$m_E = 100 \times \left(1 - \left(\frac{d_i}{d_0}\right)^2\right) \qquad (2.6)$$

where d_0 and d_i are the fibre diameters measured prior immersion in the respective conditioning media and at the *i*th time point.

2.11 Fibre Reinforced Composite Plate Manufacturing via Laminate Stacking

Unidirectional composites of four different nominal volume fractions, v_f, (see Table 2.1) were manufactured by alternately stacking unidirectional mats of as-drawn phosphate glass fibres and PLA films inside a purpose-built compression moulding tool with a 4.5 mm × 110 mm × 110 mm (thickness × width × length) cavity (see Figure 2.2). The mould was designed such that the bottom plate could be exchanged for a thicker or thinner one to control the thickness of the moulded part and to easily extract the final product.

Unidirectional phosphate glass fibre mats were manufactured by drawing fibre at 18 $m \cdot s^{-1}$ onto a traversing drum at a nozzle yield of approximately 1 $g \cdot min^{-1}$. The fibres were sprayed to prevent fibre misalignment using a 5g/100 ml PLA-Chloroform solution (Resin Ingeo 3251D NatureWorks®). Following a 2 h period for the complete evaporation of the chloroform, the mat was cut into 121 cm^2 square pieces and stored in a vacuum oven for subsequent processing.

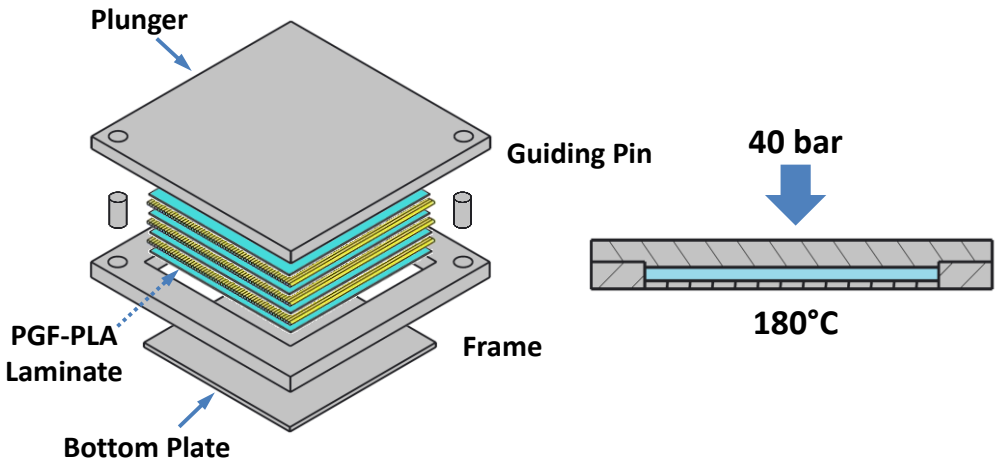


Figure 2.2: (right) Exploded view of the purpose-built compression moulding tool and (left) transverse cross section of the compression moulding tool assembly during the consolidation stage.

The masses of the mats used for the fabrication of composites with different fibre volume fractions are listed in Table 2.1. PLA films of *ca.* 0.3 mm in thickness were fabricated by pressing 4.5 g batches of PLA resin pellets (Resin Ingeo 3251D NatureWorks®). The PLA pellets were dried in a vacuum oven at 50°C for at least 24 h prior use and were then placed between two

PTFE covered aluminium plates. The plates were then transferred to a hydraulic press preheated to 185°C. The pellets were held at this temperature for 5 min before compressing at 3 bar for 10 s. Finally the plates were then moved to a second press set at the same pressure for cooling. The PLA films were then trimmed, bagged and stored in a vacuum oven until required for further composite plate manufacturing.

Once loaded, the mould was placed in a hydraulic press at 180 °C for 10 min. Immediately after, the pressure was alternated between 40 and 0 bar for 1 min to assist the evacuation of air trapped during the lay-up, followed by consolidation for 9 min according to two different pressure schemes illustrated in Figure 2.3: a) static pressure 'SP' (pressure held constant at 40 bar throughout the entire 9 min period) and, b) cyclic pressure 'CP' (pressure cycled for 1.5 min towards the end of the consolidation stage). Finally the system was cooled under constant pressure to prevent cavitation from crystallisation or thermal shrinkage of the polymer melt.

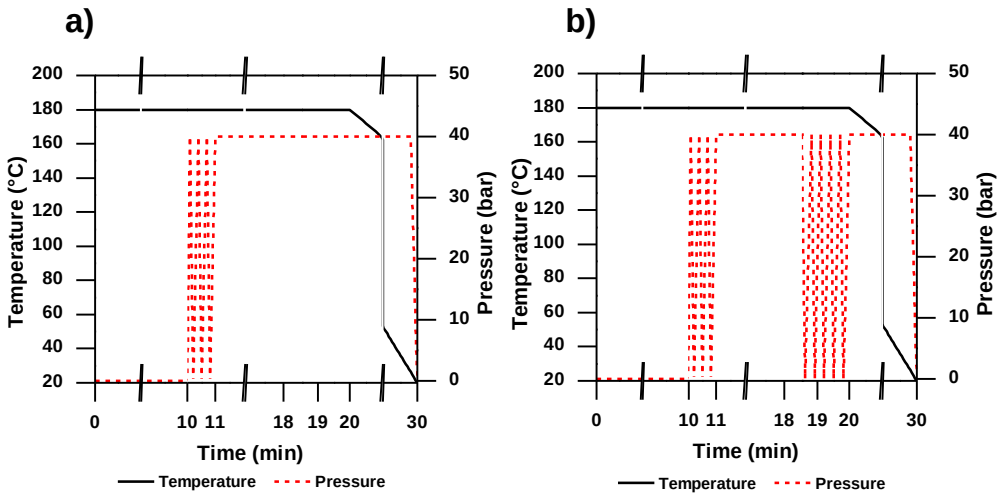


Figure 2.3: Schematic representation of the nominal temperature and pressure processing schemes for the PLA-PGF composites: a) static pressure and b) cyclic pressure case.

For each nominal fibre volume fraction in the respective series, at least two composites were fabricated. In addition, pure PLA plates were fabricated from film laminates as control samples.

Table 2.1: Composition of the cyclic 'CP' and static pressure 'SP' compression moulded composite plates.

Sample Codes	v_f Nominal	PLA mass (g)	No. of Films	Film mass (g)	PGF mass (g)	No. of mats	Mat mass (g)
PLA-plate	0	67.31	10	6.7	-	-	-
0.15-CP/SP	0.15	57.21	17	3.4	21.35	16	1.3
0.25-CP/SP	0.25	50.48	15	3.4	35.58	14	2.5
0.35-CP/SP	0.35	43.75	13	3.4	49.81	12	4.2
0.45-CP/SP	0.45	37.02	11	3.4	64.04	10	6.4
0.35-CP-M	0.35	43.75	21	2.1	49.81	20	2.5
0.45-CP-M	0.45	37.02	26	1.4	64.04	25	2.5

The effect of processing variables on the cyclic pressure-assisted manufacture of fibre reinforced composite plates was investigated through the manufacture of two additional series of composite plates with fixed 0.35 fibre volume fraction. In one of these series, composite plates were processed under 40 bar of consolidating cyclic pressure at 180°C, 190°C, and 200°C, respectively, whereas the second composite plate group was produced under 30 bar, 40 bar, 50 bar and 60 bar of cyclic pressure consolidation maintaining the temperature at 180°C.

2.12 Fibre Reinforced Composite Rod Manufacturing via Forging

The thermomechanical response of unidirectional fibre reinforced composites was investigated by forging composite blanks of 4.5 mm × 3.05±0.05 mm × 100 mm (thickness × width × length) cut along the fibre direction of square composite plates (fabricated as previously described in §2.11) using a band saw. The rough band saw finish was finely adjusted by grinding with sand paper.

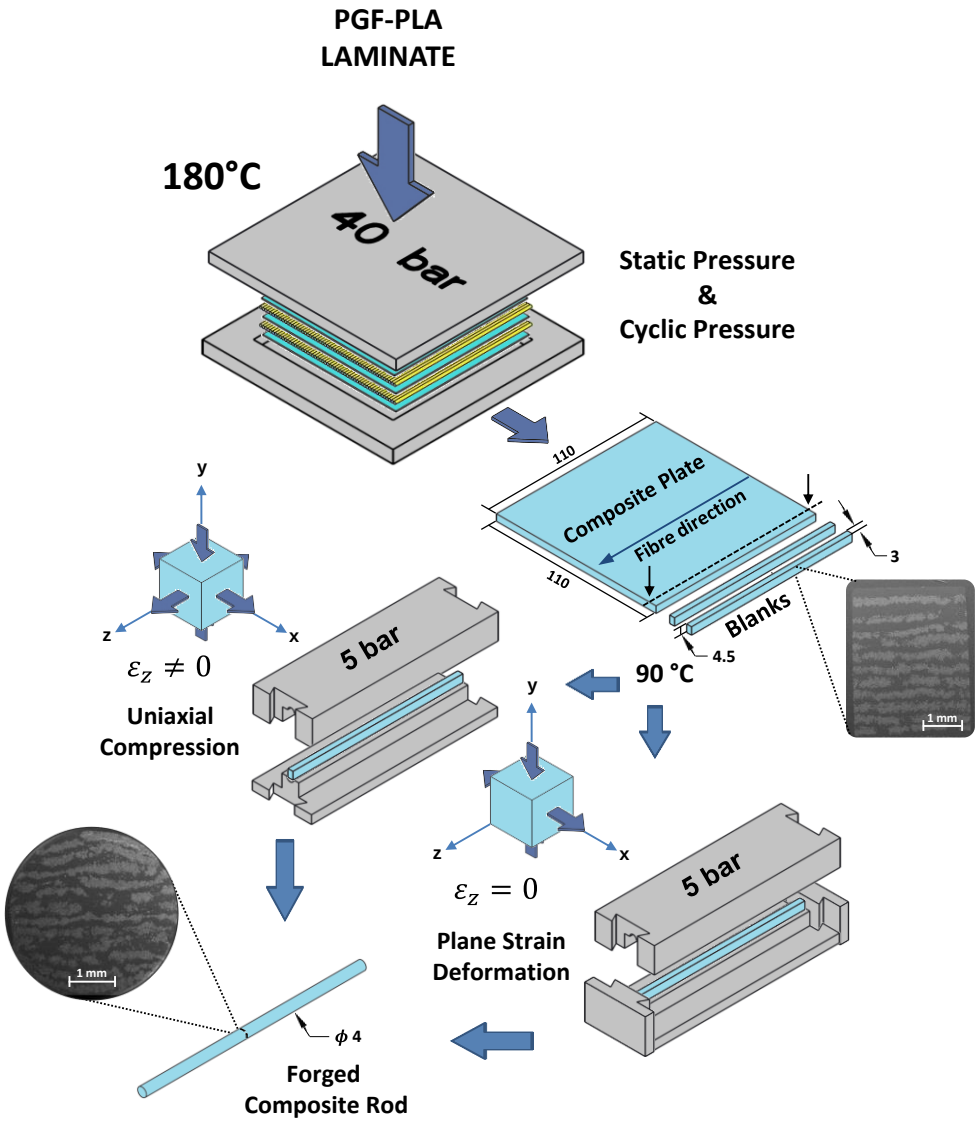


Figure 2.4: Manufacturing cycle for composite forged rods. Composite plates were consolidated through either static or cyclic pressure compression moulding. The 4.5 mm × 110 mm × 110 mm plates (thickness × width × length) were then sectioned along the fibre direction into 4.5 mm × 3 mm × 110 mm rectangular blanks (SEM cross sectional view is shown in the inset) and forged at 90°C under 5 bar pressure into cylindrical rods (SEM cross sectional view is shown in the inset) using two die configurations, namely: i) the blank was constrained in the fibre direction to produce a 4 mm rod under plane strain conditions and ii) the blank was free to deform in the fibre direction to produce a 4 mm rod under uniaxial compression.

A forging tool with a 4 mm cylindrical channel was designed so that two common plastic deformation modes could be investigated by changing the die configuration as shown in Figure 2.4. In plane-strain 'PS' deformation, both ends of the die channel were blocked to confine the plastic flow ($\boldsymbol{\varepsilon_z}$=0) to the plane transverse to the fibre direction (***x-y*** plane) as indicated by the blue arrows in the right hand side of Figure 2.4, whereas in uniaxial compression 'UC' the composite was free to deform in three orthogonal directions ($\boldsymbol{\varepsilon_z}\neq$0) as indicated by the blue arrows in the right hand side of Figure 2.4.

Composite blanks (see upper inset in Figure 2.4) were loaded in the respective die assembly as described earlier, and placed inside a convection oven preheated at 210°C for 10 minutes, allowing the system to reach a temperature range (90-100°C) suitable for plastic flow of reinforced-PLA as reported in [15, 18, 222, 231]. The die was then transferred to a press heated to 90°C and compressed isothermally under 5 bar pressure for 30 s. The pressure was released and finally, the die was cooled in a cold press with matching pressure settings during 5 minutes.

2.13 Fibre Reinforced Composite Rod Manufacturing via Consolidation of PLA-sheathed Phosphate Glass Fibre Bundles

2.13.1 Production of Bare PLA-sheaths via Tubing-type Crosshead Extrusion

The production of PLA-sheathed fibre bundles was investigated by carrying out experiments using a purpose-built crosshead die. As shown in Figure 2.5, the die was designed with multiple interchangeable parts to be able to explore different configurations and even future modifications with tailor-made attachments.

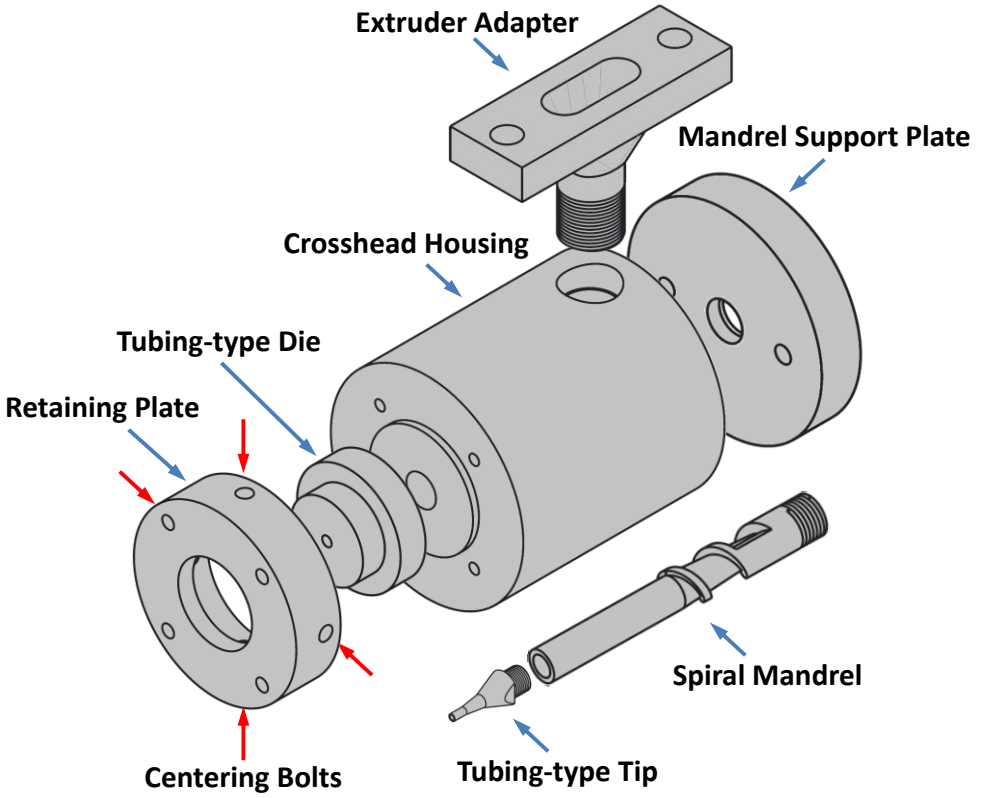


Figure 2.5: Exploded view of the crosshead tubing-type configuration used for PLA-sheathing of phosphate glass fibre bundles.

Experiments reported henceforth were conducted using the tubing configuration (cf. Figure 2.5) of the crosshead die, in which a layer of molten PLA was extruded through the annular space created by a Ø 3 mm cavity tubing-type die coupled with a Ø 1.8 mm tubing-type tip axially supported by a mandrel. A simple helical groove was cut in to the mandrel to assist the uniform distribution of polymer melt around the mandrel. Centering bolts in the retaining plate (indicated by the red arrows in Figure 2.5) allowed the adjustment of the tubing-type die axial position to obtain a uniform sheath thickness around the fibre bundle. PLA pellets (Ingeo 3251D NatureWorks®) were dispensed by a single screw volumetric feeder with a variable speed control. The extruder feeding rate, ***f***, was determined by sampling collections of PLA pellets during 5 minutes at the exit of the volumetric feeder set at the respective speed. Prior to each collection, the feeder was loaded with 1 kg of PLA pellets.

The extruder temperature distribution was controlled by means of cartridge heaters lodged in five different zones along the extruder barrel. The crosshead assembly was completed with a band heater to prevent polymer solidification inside the die during extrusion. For the sake of simplicity, the temperature controllers were all set at the same temperature reported in the following.

Molten PLA was continuously pumped to the crosshead die via a 21 mm twin-screw extruder (Rondol, Strasbourg, France) with a 30:1 L/D screw ratio and variable speed controller. Pressure at the crosshead die entry was monitored by an in-line pressure transducer. The sheathing line was driven by a flat belt caterpillar haul-off unit with a precision speed control (0-50 $m \cdot min^{-1}$). The extrudate was quenched by means of an in-line water cooling trough as illustrated in Figure 2.6. The PLA pellets were vacuum-dried for at least 24 h at 50°C prior extrusion.

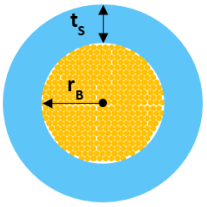
Optimum sheathing conditions were determined through the extrusion of a series of bare PLA tubes with varying i) feeding rate, ii) screw speed, iii) haul-off speed and iii) processing temperature. Extrudate was collected for 1 minute at the specified conditions and the sample mass was registered. The operation was repeated four times.

2.13.2 Production of PLA-sheathed Fibre bundles via Tubing-type Crosshead Extrusion

Continuous rovings of fibres in the annealed and as-drawn condition were assembled by locally applying a 5 g/100 ml PLA-Chloroform solution (Ingeo 3251D NatureWorks®) with a syringe at the meeting ends of the respective type of fibre bundles. The rovings were then fed at the back of a crosshead die of the tubing type with the assistance of a thin metallic wire for subsequent PLA sheathing. PLA melt was continuously supplied at a constant rotation speed of 30 rpm by a 21 mm twin-screw extruder (Rondol, Strasbourg, France) with a 30:1 L/D ratio coupled with a tubing type crosshead die with a tip diameter of Ø 1.8 mm and a die cavity of Ø 3 mm. PLA pellets were vacuum-dried for at least 24 h at 50°C prior extrusion. The temperature of the five barrel zones including the crosshead die temperature was fixed at 165°C to minimise PLA thermal degradation during extrusion. The PLA pellets Ingeo 3251D NatureWorks®) were dispensed by a single screw volumetric feeder set at ~6.6 g·min^{-1}. Abrasion damage and interaction of the hydrophilic phosphate glass fibres with the quenching medium was prevented by the protective PLA sheath. Finally, the hybrid preform was collected by a take-up device, demounted, chopped in to 80 mm segments and stored in a vacuum oven at 30°C until needed.

The thickness of the PLA sheath, $\mathbf{t_S}$, which corresponded to a PLA sheath linear density, $\mathbf{m_S}$, was metered by adjusting the haul-off speed, $\mathbf{v_{HO}}$, as determined by a series of tube extrusion experiments (cf. §2.13.1), as detailed in Table 2.2.

Table 2.2: Summary of PLA-sheathed glass fibre bundle production conditions and compression moulded composite rods composition.



v_f	r_B (mm)	t_S (mm)	m_B (g·m^{-1})	m_S (g·m^{-1})	Segments per Rod	m_m (g)	m_f (g)	v_{HO} (m·min^{-1})	DDR
0.15	0.019	0.373	0.225	0.603	22	1.063	0.396	11	9.4
0.25	0.025	0.351	0.389	0.553	21	0.938	0.661	12	10.2
0.35	0.029	0.315	0.524	0.460	22	0.813	0.923	14	12.3
0.45	0.029	0.250	0.524	0.303	28	0.688	1.189	22	18.7

PLA coating dimensions required to conform to the target volume fraction were estimated on the assumption that: i) all the fibres in the bundle had circular cross sections with the same diameter and that ii) the fibres were packed in a hexagonal lattice. The respective drawdown ratios, DDR, (ratio of the cross sectional area of the annular region inside the die to the cross

sectional area the PLA sheath) for the production of the PLA sheaths were also included in Table 2.2.

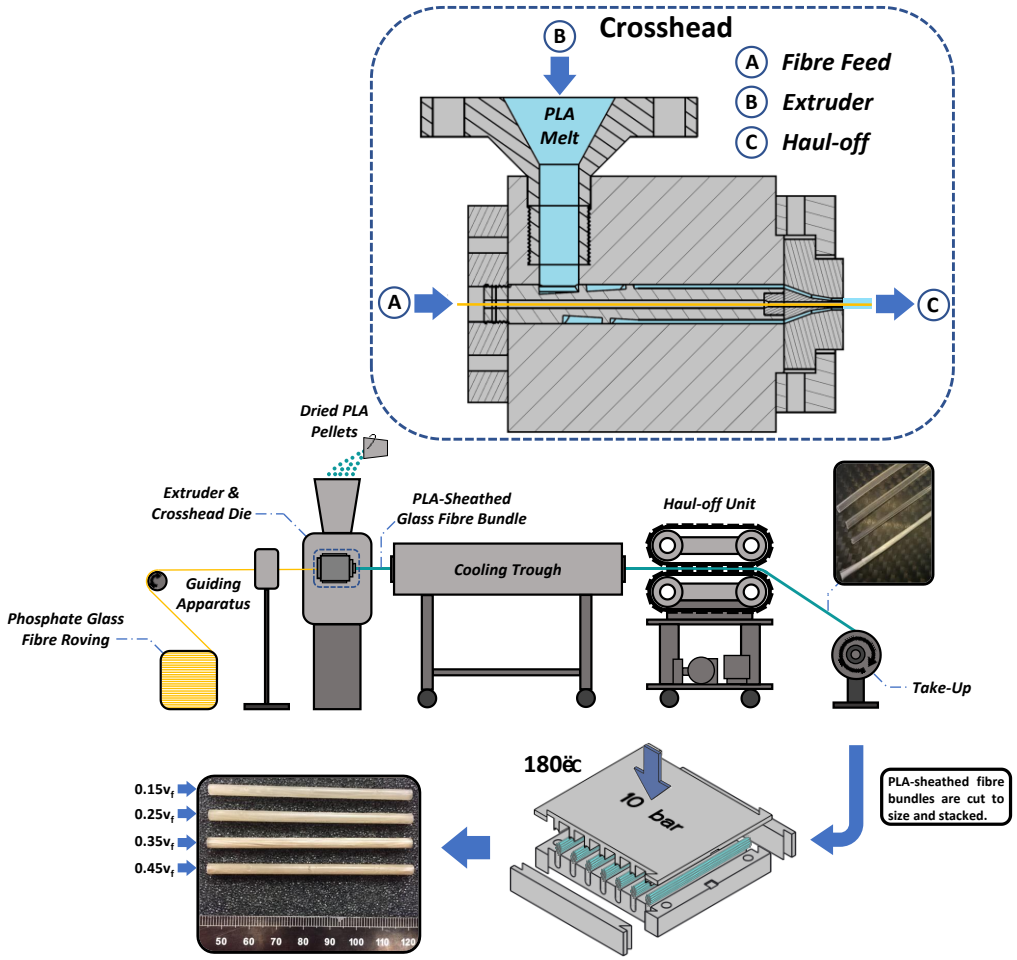


Figure 2.6: Manufacturing cycle of phosphate glass fibre-reinforced bioresorbable composite rods produced via compression moulding of PLA-sheathed glass fibre bundles.

2.13.3 Manufacture of Fibre Reinforced Composite Rods via Compression Moulding of PLA-sheathed Fibre Bundles

Continuous PLA-sheathed bundles of as-drawn and annealed fibre were chopped into 80 mm segments. Before use, the preforms were weighted and vacuum dried at 50°C for at least 24 h. Subsequently, the required number of segments (cf. Table 2.2) was loaded into a purpose-built multi-cavity split mould (cf. Figure 2.6) for the simultaneous production of seven Ø 4mm × 80 mm (diameter × length) unidirectional continuous fibre reinforced composite rods. The multi-cavity mould was placed in a hydraulic press at 180°C for 10 min. Immediately after, 10 bar consolidation pressure was statically applied for

5 minutes. Afterwards, the system was then cooled under constant pressure. Two series of bioresorbable composite rods, namely annealed and non-annealed were manufactured with four different fibre volume fractions as detailed in Table 2.2.

2.14 PLA Rotational Viscosity Measurements

Dynamic linear viscoelastic measurements were conducted using a stress-controlled Physica MCR 501 rotational rheometer (Anton Paar, Austria). PLA pellets (Ingeo 3251D NatureWorks®) were confined within a 1 mm gap between two Ø 25 mm plates. Sweeps spanning frequencies from 0.1 s^{-1} to 100 s^{-1} in 16 logarithmically spaced measurement points were carried out in the linear viscoelastic regime at temperatures in the range of 170-200°C at a strain limited to 1% to prevent the destruction of the polymer structure during the measurements. The temperature was controlled through a convection temperature attachment which covered the parallel plates. Zero shear viscosity values at the respective temperatures were determined by fitting the experimental data to the Carreau-Yasuda viscosity curve model function designed to describe pseudoplastic flow with asymptotic viscosities at zero and infinite shear rates for unlinked and unfilled polymers.

2.15 Void Content Determination

Due to the hygroscopic nature of both fibres and PLA, composite samples were conditioned in a vacuum oven at 40 ºC to remove any absorbed moisture until constant weight was achieved. The percentage void content, φ_v, of the composite samples was measured by the standard loss on ignition method ASTM D-2734-16 using a minimum of three samples in accordance with Equation (2.7) [242]:

$$\varphi_v = 100 \times \frac{(\rho_{ct} - \rho_{ce})}{\rho_{ct}} \tag{2.7}$$

where ρ_{ce} stands for the sample experimental density and ρ_{ct} is the composite theoretical density given by Equation (2.8) [242],

$$\rho_{ct} = \frac{1}{{}^{w_m}/_{p_m} + {}^{w_f}/_{p_f}} \tag{2.8}$$

w_m and w_f represent the matrix and glass fibre mass fraction and p_m and p_f denote the fibre and matrix density.

The experimental density of the composite samples, ρ_{ce}, was determined in accordance with the standard ASTM D-792, from the weight difference of samples in air and ethanol at 23°C, as shown by Equation (2.9) [243]:

$$\rho_{ce} = \frac{a}{a-b}(\rho_b - \rho_a) + \rho_a \qquad (2.9)$$

where ***a*** and ***b*** are the weight of the sample in air and submerged in ethanol, respectively and ρ_b and ρ_a are the density of ethanol and air at the operating temperature (0.789 g·cm^{-3}and 0.0012 g·cm^{-3} at 23°C respectively). The weight of the immersed sample was averaged over four measurements and used in Equation (2.9).

After volatilisation of the organic component, the real volume fraction was calculated using Equation (2.10) according to ASTM D2584-11 [244]:

$$v_f = \frac{{}^{w_f}/_{p_f}}{{}^{w_m}/_{p_m} + {}^{w_f}/_{p_f}} \qquad (2.10)$$

The maximum content of voids in the fibre reinforced composites created as a result of polymer deprivation inside the mould cavity during cooling, φ_t, was calculated by adapting Equation (2.7) on the assumption that the volume of the composite samples does not change as a result of the presence of voids (the voids are closed and are not accessible to an external fluid):

$$\varphi_t = 100 \times \frac{m_m\left(1 - \frac{\rho_{m_T}}{\rho_{m_0}}\right)}{m_f + m_m} \qquad (2.11)$$

where m_m and m_f are the required masses of the matrix and the fibre in accordance with the intended volume fraction (cf. Table 2.2) and ρ_{m0} is the density of amorphous PLA at 23°C used in this study (1.249 g·cm^{-3} according to the provider specifications). The density at the processing temperature, ρ_{mT}, was estimated via Equation (2.12) [245]:

$$\rho_{m_T} = \frac{\rho_{150°C}}{1+\alpha(T-150)} \quad (2.12)$$

where $\rho_{150°C}$=1.1452 g·cm^{-3}, α is the thermal coefficient of expansion of PLA (7.4×10^{-4}°C^{-1} at temperatures higher than 150°C) and T is the processing temperature in degree Celsius.

2.16 Fibre reinforced Composite Rod *In Vitro* Degradation Study

Composite rods of four different volume fractions fabricated via forging and compression moulding of PLA-sheathed fibre bundles, respectively and neat-PLA forged specimens of 80 mm (length) × 4±0.1 mm (diameter) were individually conditioned in glass vials filled with 40 ml of phosphate buffered saline (PBS, pH 7.5±0.05) maintained at 37°C for up to 30 days, in accordance with the standard BS EN ISO 10993-13 (2010). Three parallel specimens were prepared for each in vitro time point, up to which, the degradation medium was collected and replaced with fresh solution twice a week. The pH of the collected media was monitored as described in §2.8. The relevant samples were recovered from solution at day 1, 3, 7, 15, 23, and 30, blot dried to remove excess moisture, and weighed using a digital balance of 0.01 mg resolution. The samples were then immediately mounted in a fixture for flexural test in wet conditions as described in §2.17.

Tested specimens were then vacuum-dried at 40°C until constant weight was achieved. The % mass loss, $m_L(t)$, and the % mass gain due to water uptake, $m_G(t)$, at the ith time point were determined through Equation (2.13) and (2.14) [246]:

$$m_L(t) = \frac{m_d - m_0}{m_0} \times 100\% \quad (2.13)$$

$$m_G(t) = \frac{m_w - m_d}{m_d} \times 100\% \quad (2.14)$$

where m_0, is the initial mass of the rods before immersion in PBS and m_w, m_d, are the sample masses at the ith time point in the wet condition and after drying in vacuum at 40° C.

2.17 Flexural Testing

Flexural properties of the composite plates were evaluated through 3-Point bending test (n=3) using a Hounsfield Series S testing machine with a crosshead speed of 1 mm·min^{-1}, and a 5 kN load cell according to BS EN ISO 14125:1998+A1:2011. The mechanical competence of the composite rods was evaluated by means of 3-Point bending test conducted in a Bose ElectroForce® Series II 3330 test instrument (in agreement with BS ISO 3597-2:2003) fitted with a 1 kN load cell at a crosshead speed of 1 mm·min^{-1}. Tests were conducted in triplicate. A temperature controlled water bath enclosing the sample loading rig was mounted for sample testing in wet conditions. The sample rig was fully submerged in PBS during testing. The PBS solution was heated up to 37°C and allowed to stabilise before testing.

2.18 Differential Scanning Calorimetry (DSC)

The thermal properties of the polymer matrix in the phosphate glass fibre reinforced composites were determined using a DSC Q10 (TA Instruments). Prior to use, the equipment was calibrated with mercury and indium standards. Thin slices obtained from the transverse plane of the composite samples with a diamond saw, were sealed in aluminium pans and probed under nitrogen flow of 50 cm^3·min^{-1} from 30°C to 190°C at a rate of 5°C·min^{-1}. A 5 min isothermal hold was programmed before cooling back to 30°C at a rate of 20°C·min^{-1}. The equipment was allowed to equilibrate at this temperature before resuming a second run with the same parameters as those previously described.

On account of the fibre content, the mass of the composite slices was adjusted according to their experimental volume fraction to maintain a constant polymer matrix mass at ca. 10 mg. The samples were dried under reduced pressure for 48 h (0.01 mbar) at 30°C and stored in a desiccator until use. The DSC traces were analysed using TA instrument universal analysis 2000 software version 4.3A. The crystallinity content ‘X’ of the samples was evaluated using Equation (2.15) [247]:

$$X = \frac{100\%(\Delta H_m - \Delta H_c)}{\Delta H_m^0} \qquad (2.15)$$

where ΔH_m and ΔH_c are the melting and cold crystallisation enthalpies, respectively, and ΔHm^0 is the reference melting enthalpy for PLLA crystals having an infinite size (93.6 J· g^{-1}) [247].

2.19 Advanced Polymer Chromatography (APC)

Changes in PLA molecular weight were evaluated by size exclusion chromatography. A Waters ACQUITY advanced polymer chromatography (APC™) system equipped with a refractive index 'RI' detector was used. Separation was achieved by three columns connected in series, namely: i) Waters Aquity APC XT 900 (2,000,000–300,000 g·mol^{-1}), ii) Waters Aquity APC XT 450 (400,000-20,000 g·mol^{-1}), and iii) Waters Aquity APC XT 125 (30,000-1,000 g·mol^{-1}), each having 4.6 mm internal diameter and 150 mm length. Chloroform was used as the isocratic mobile phase with a flow rate of 0.4 ml/min at 30°C. The calibration curve was obtained by using 3 different monodisperse polystyrene standards (Waters ReadyCal Kit). Samples were prepared by dissolving the neat polymer and composite samples in chloroform to a concentration of 1.7 mg/ml. The polymer solutions were filtered through a 13mm 0.45 µm PTFE syringe filter into LC certified glass vials. The injection volume was set to 300 µl.

3 Results

3.1 Characterisation and *In Vitro* Degradation Studies of Bioresorbable Bulk Glass and Fibres of the $45P_2O_5{\cdot}16CaO{\cdot}13Na_2O{\cdot}24MgO{\cdot}2Fe_2O_3$ mol% Composition

As shown in Figure 3.1a, translucid and brownish glass samples of the polyphosphate composition $45P_2O_5{\cdot}16CaO{\cdot}13Na_2O{\cdot}24MgO{\cdot}2Fe_2O_3$, without visible crystallisation signs, were successfully obtained by melt-quenching. Figure 3.1b shows freshly drawn phosphate glass fibres. The density of the glass fibres (2.643±0.005 $g{\cdot}cm^{-3}$) was 1% lower than the value obtained for the bulk glass (2.762±0.001 $g{\cdot}cm^{-3}$).

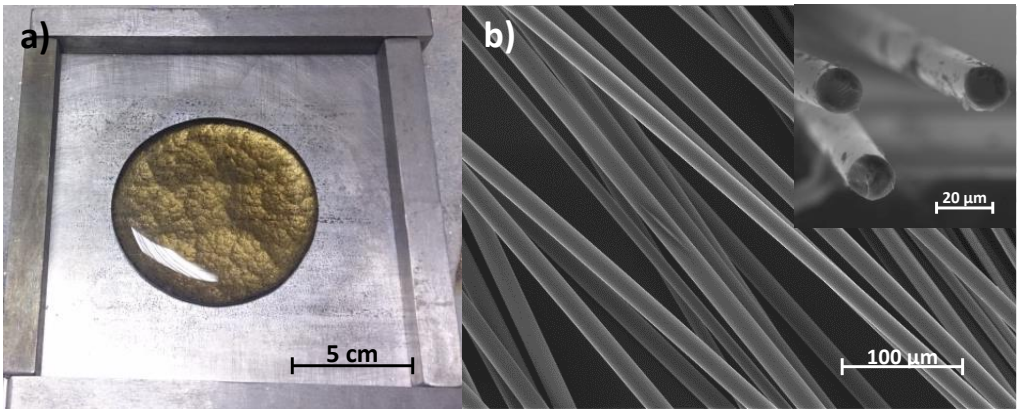


Figure 3.1: (a) Melt-quenched P45Fe2 bulk glass and (b) melt-drawn glass fibres.

3.1.1 Glass Viscosity

Figure 3.2a shows the P45Fe2 glass viscosity changes in the 800-1100°C temperature range. It was observed that the viscosity steadily decreased with increasing temperature in the solicited range as illustrated by Figure 3.2a.

3.1.2 Melt-drawn Fibre Production

Figure 3.2b summarises the variation in temperature of a region close to the bushing nozzle against the set temperature of the oven. The actual temperature of the bushing nozzle (assumed to be equal to the temperature of the glass during fibre drawing) was considerably lower than the set temperature of the furnace (approximately 100°C). The difference in temperatures was noted to decrease as the set temperature was raised.

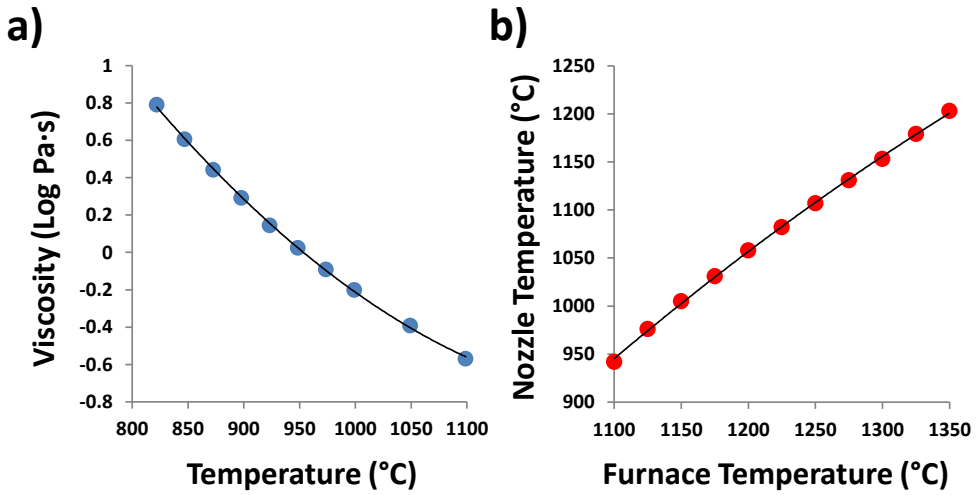


Figure 3.2: (a) Influence of the temperature on the viscosity of P45Fe2 glass. (b) Differences in the furnace set temperature and the temperature measured in a region close to the bushing nozzle.

By setting the nozzle yield to 1 g·min^{-1} (for easy reference during fibre collection) and substituting the respective dimensional values of the bushing in Equation 2.1, it was determined that fibre drawing should be conducted at a temperature around 1000°C (equivalent to a furnace set temperature of 1150°C and a viscosity value of ca. 630 Poise) with an initial glass cullet load of ca. 300 g.

Being the flow rate through the nozzle independent of the drawing speed, the accuracy of the selected processing variables (bushing head and drawing temperature), can be determined by the evaluation of the effect of drawing speed in fibre diameter. As shown in Figure 3.3, the diameter of the glass fibres decreased monotonically with increasing drawing speed.

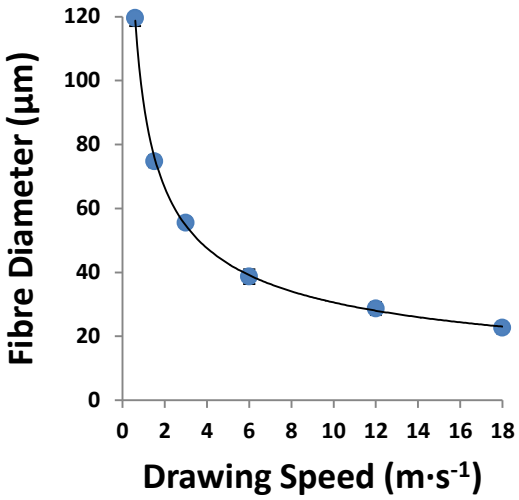


Figure 3.3: Influence of drawing speed on the diameter (±SD) of fibres drawn at 1000°C with a glass load of approximately 300 g.

Drawing speeds and the corresponding fibre diameters were substituted in Equation 2.3 and the result are summarised in Table 3.1. Within experimental error, the estimated values were reasonably close to the intended nozzle yield at 1000°C. During subsequent fibre production it was noted that changes in the bushing head were negligible for short drawing periods (in the order of 60 minutes), so that no changes in the set temperature were necessary.

Table 3.1: Summary of parameters used to confirm the target nozzle yield during fibre drawing at 1000°C.

Drawing Speed ($m \cdot s^{-1}$)	Drawing Speed ($cm \cdot min^{-1}$)	Fibre Diameter (μm)	Fibre Diameter (cm)	$\dot{m}$ ($g \cdot min^{-1}$)
0.6	3600	119.7	0.01197	1.07
1.5	9000	74.8	0.00748	1.04
3	18000	55.6	0.00556	1.15
6	36000	38.7	0.00387	1.12
12	72000	28.7	0.00287	1.23
18	108000	22.7	0.00227	1.15

3.1.3 X-ray Glass Powder Diffraction

Figure 3.4 shows the powder X-ray diffraction patterns of the phosphate bulk glass and the phosphate glass fibres in the as-drawn and annealed condition. No discrete diffraction peaks were noted in the diffraction patterns. All the samples, presented an amorphous halo centred in the 15-39° 2θ range.

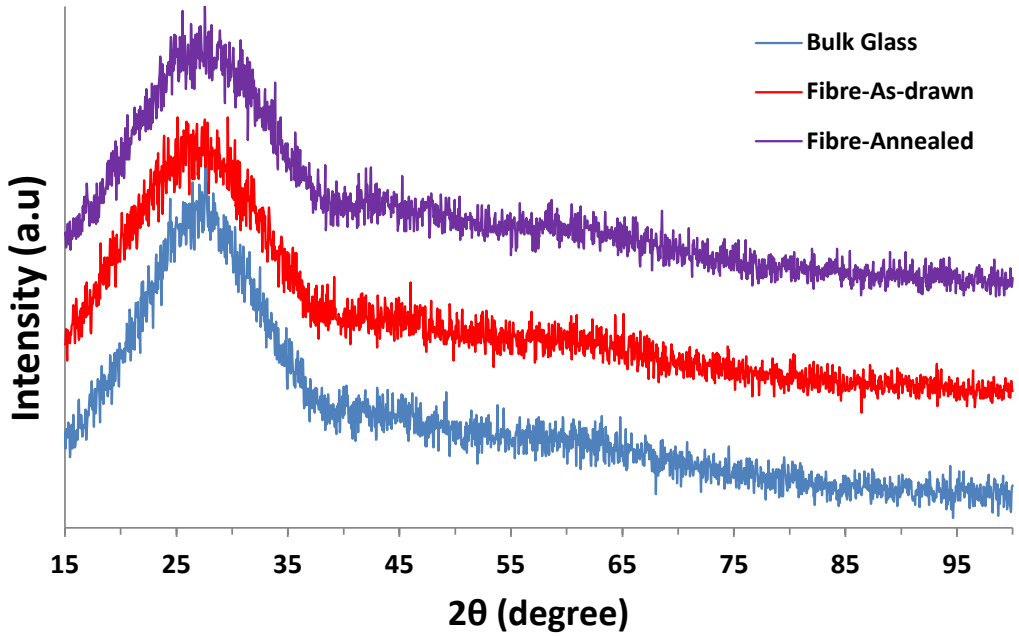


Figure 3.4: Powder X-ray diffraction patterns of P45Fe2 bulk glass and glass fibres in the as-drawn and annealed condition.

3.1.4 Glass Compositional EDX Analysis

Table 3.2 summarises the EDX compositional analyses conducted on both the polished surface of the bulk glass and embedded glass fibres in the as-drawn and annealed conditions. P45Fe2 theoretical composition was included for comparison purposes. It can be seen that within experimental error, the compositions of all the samples analysed were in good agreement with the theoretical composition

3.1.5 Glass Thermal Analysis

DSC thermograms of the bulk glass and both types of fibres are shown in Figure 3.5. No differences in the thermal behaviour of the samples could be detected during the second run (the samples only presented a glass transition in the same region as in the first run) and therefore are not presented here.

Table 3.2: Summary of EDX analyses (±SD) conducted on P45Fe2 bulk glass polished surface and embedded glass fibres in the as-drawn and annealed conditions.

Sample	Mol% of Na_2O	Mol% MgO	Mol% P_2O_5	Mol% CaO	Mol% Fe_2O_3
P45Fe2	13.0	24.0	45.0	16.0	2.0
Bulk Glass	12.7±0.4	22.9±0.4	47.5±0.2	14.7±0.5	1.8±0.1
Fibre-A	13.2±0.1	25.2±0.1	44.4±0.1	15.5±0.2	1.8±0.03
Fibre-NA	12.8±0.1	24.8±0.1	44.8±0.1	15.8±0.1	1.8±0.03

In all cases a single glass transition, $\mathbf{T_g}$, could be observed at temperatures in the vicinity of 460°C. Two crystallisation events could be observed in the glass fibre curves: i) a weak crystallisation peak, $\mathbf{T_{X1}}$, centred at 571°C for both annealed and as-drawn fibres followed by an intense and narrow crystallisation peak, $\mathbf{T_{X2}}$, centred at 664°C and 671°C for the annealed and as-drawn glass fibres respectively. A single broad crystallisation centred at 713°C was observed in the bulk glass sample. In correspondence to the two crystallisation peaks, a shoulder was noticed on the left side of the glass fibre melting peaks. The melting peaks, $\mathbf{T_m}$, were centred at 839°C and 840°C for the annealed and as-drawn glass fibres, respectively. No such shoulder was observed in the also asymmetric melting peak of the bulk glass at 841°C.

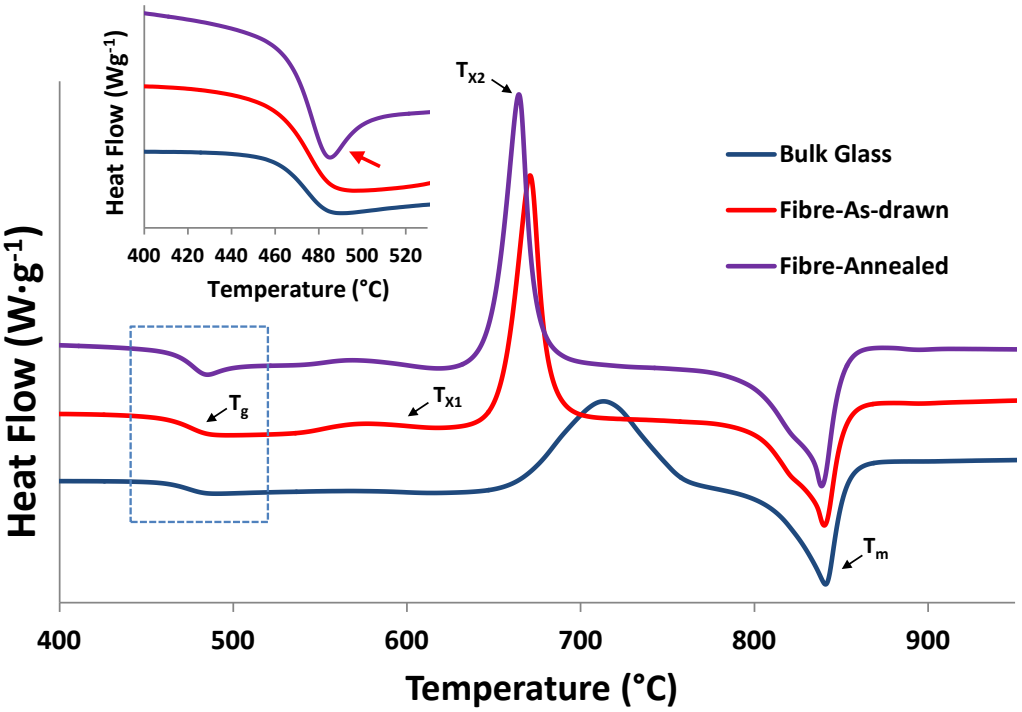


Figure 3.5: DSC thermograms of P45Fe2 bulk glass and glass fibres in the as-drawn and annealed condition. The inset shows a magnification of the region highlighted by the dashed blue line.

Closer examination of the glass transition region of the glass samples, revealed the presence of endothermic event in the single case of the annealed glass fibres (denoted by the red arrow in the inset of Figure 3.5).

3.1.6 Single Fibre Tensile Test

The results of the single fibre tensile test are presented in Table 3.3 along with other physical properties of the phosphate glass fibres used in this study. It was observed that as a result of annealing, the tensile strength of the phosphate glass fibres was significantly reduced to approximately 50% of the as-drawn (non-annealed) fibre strength. No significant changes were noted with respect to the tensile modulus ($p > 0.05$). In addition, the strain that the annealed fibres could tolerate before fracture was also reduced by over 50% with respect to the as-drawn fibres.

Table 3.3: Summary of physical properties of P45Fe2 as-drawn 'NA' and annealed 'A' glass fibres.

Sample Code	Structure	Tg (°C)	Tx_1 (°C)	Tx_2 (°C)	T_m (°C)	Strength (MPa)	Modulus (GPa)	Break Strain (%)
PGF-NA	Amorphous	462±2	571±1	671±1	840±0.4	820±190	56.6±14	0.72±0.16
PGF-A	Amorphous	464±3	571±2	664±2	839±0.5	444±117	63.3±12	1.56±0.30

3.1.7 Phosphate Bulk Glass *In Vitro* Degradation

Figure 3.6a shows the results of the cumulative degradation analysis performed in the bulk glass. The test was conducted in phosphate buffered saline at 37°C to simulate the physiological environment. The % mass loss of the bulk glass increased with conditioning time reaching a maximum of 1.09 % mass loss at day 54. Two events were observed to occur throughout the degradation study. During the first 5 days the data points described a decelerating behaviour best consistent with a $t^{1/2}$ model. In the second stage, the samples were observed to describe % mass loss profile consistent with cero order kinetics. As shown in Figure 3.6a, through linear regression of the second stage of the bulk glass dissolution curve it was estimated that the degradation rate for the P45Fe2 bulk glass was 4×10^{-8} $g\cdot cm^{-2}\cdot h^{-1}$. The pH variation in the media collected during the bulk glass degradation study is illustrated in Figure 3.6b. The pH of the collected media did not presented significant variations ($p>0.05$), remaining within a ±0.1 range of the initial pH value (7.42±0.1) throughout the entire study.

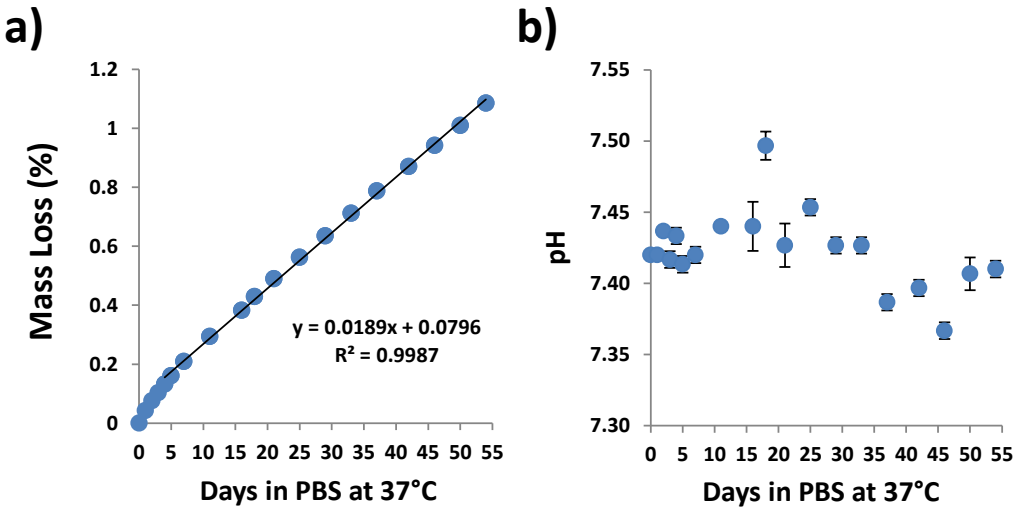


Figure 3.6: (a) % Mass loss profile (±SD) for P45Fe2 bulk glass conditioned in PBS at 37°C and (b) pH variation of the media collected from the bulk glass degradation vials.

3.1.8 Phosphate Glass Fibre *In Vitro* Degradation

3.1.8.1 Effect of Conditioning Time on Phosphate Glass Fibre Morphology

Morphological changes experienced by annealed and as-drawn P45Fe2 fibres during immersion in PBS at 37°C are shown in the left and right columns of Figure 3.7, respectively. It can be observed that at day 0 both fibre types presented pristine surfaces. After one day of conditioning, flake-shaped debris

could be observed on the surface of the as-drawn (non-annealed) fibres. Further conditioning time resulted in the growth of such residues around the as-drawn fibres which became continuous tube-like structures surrounding a progressively contracting core. No such flake-shaped debris or tube-like structures could be observed on the surface of the annealed glass fibres at any time point. However, at day 23 and 30, multiple particles started to develop on the surface of some annealed fibres as shown by Figure 3.7g and Figure 3.7i.

Morphological changes experienced by annealed and as-drawn P45Fe2 fibres as a result of deionised water conditioning at 37°C are shown in the left and right columns of Figure 3.8, respectively. In similitude to the fibre degradation studies conducted in PBS, the formation of flake-shaped debris could be observed on the surface of as-drawn fibres. However, such formations were only evident at day 15, in contrast to PBS conditioning in which debris was noted at day 1. Furthermore, these residues never developed into the continuous the tube-like structures observed at day 15 in PBS conditioning. Localised degradation similar to pitting corrosion was observed to have occurred in some of the as-drawn fibres conditioned in deionised water from day 15 onwards (cf. Figure 3.8h). No exogenous formations were noted during the deionised water degradation studies of annealed fibres.

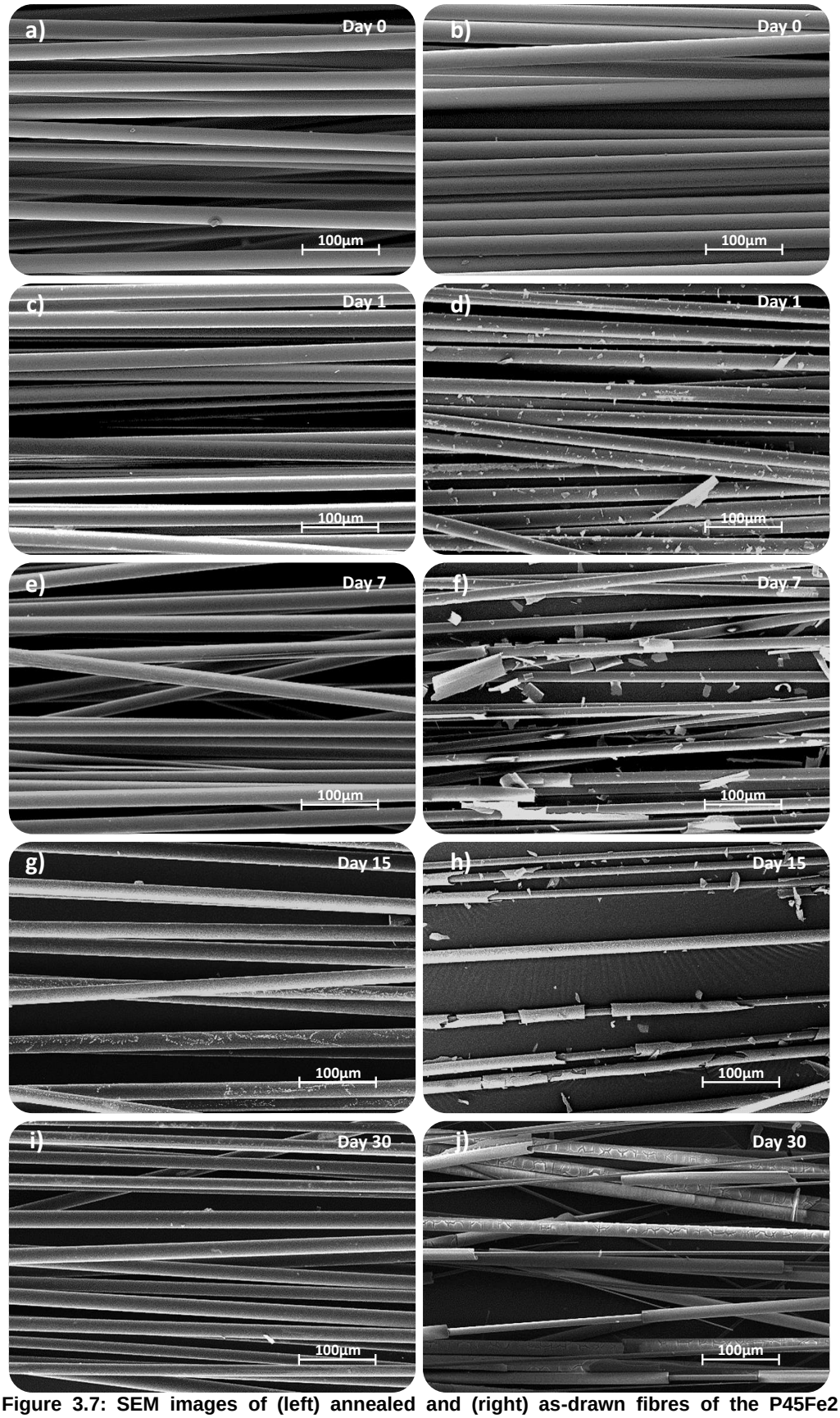


Figure 3.7: SEM images of (left) annealed and (right) as-drawn fibres of the P45Fe2 composition, respectively, at (a) & (b) day 0, (c) & (d) day 1, (e) & (f) day 3, (g) & (h), day 15 and (i) & (j) day 30 of immersion in PBS at 37°C.

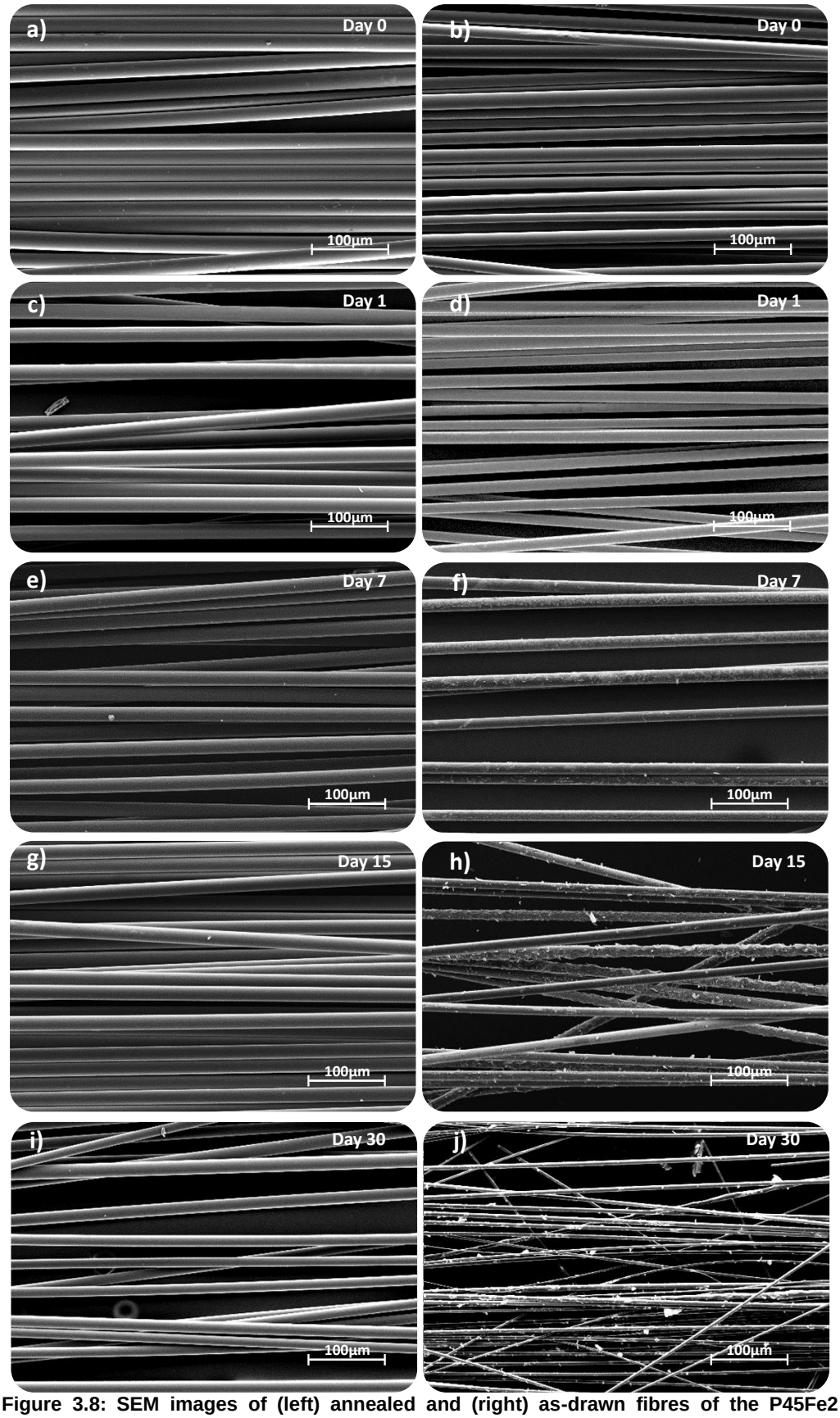


Figure 3.8: SEM images of (left) annealed and (right) as-drawn fibres of the P45Fe2 composition, respectively, at (a) & (b) day 0, (c) & (d) day 1, (e) & (f) day 3, (g) & (h), day 15 and (i) & (j) day 30 of immersion in deionised water at 37°C.

3.1.8.2 Effect of Conditioning Time on Phosphate Glass Fibre Mass

Figure 3.9a shows the % mass loss, m_{LF}, profiles of the annealed (purple circles) and as-drawn (red circles) P45Fe2 fibres conditioned in deionised water 'DI' (open circles and dashed lines) and PBS (solid circles and solid lines) respectively at 37°C. The % mass loss for annealed fibres conditioned in both deionised water and PBS was directly proportional to the conditioning time, reaching ca. 38% and 34% mass loss, respectively at day 30. On the other hand, the % mass loss of as-drawn fibres conditioned in both deionised and PBS followed a decelerating behaviour with increasing dissolution time.

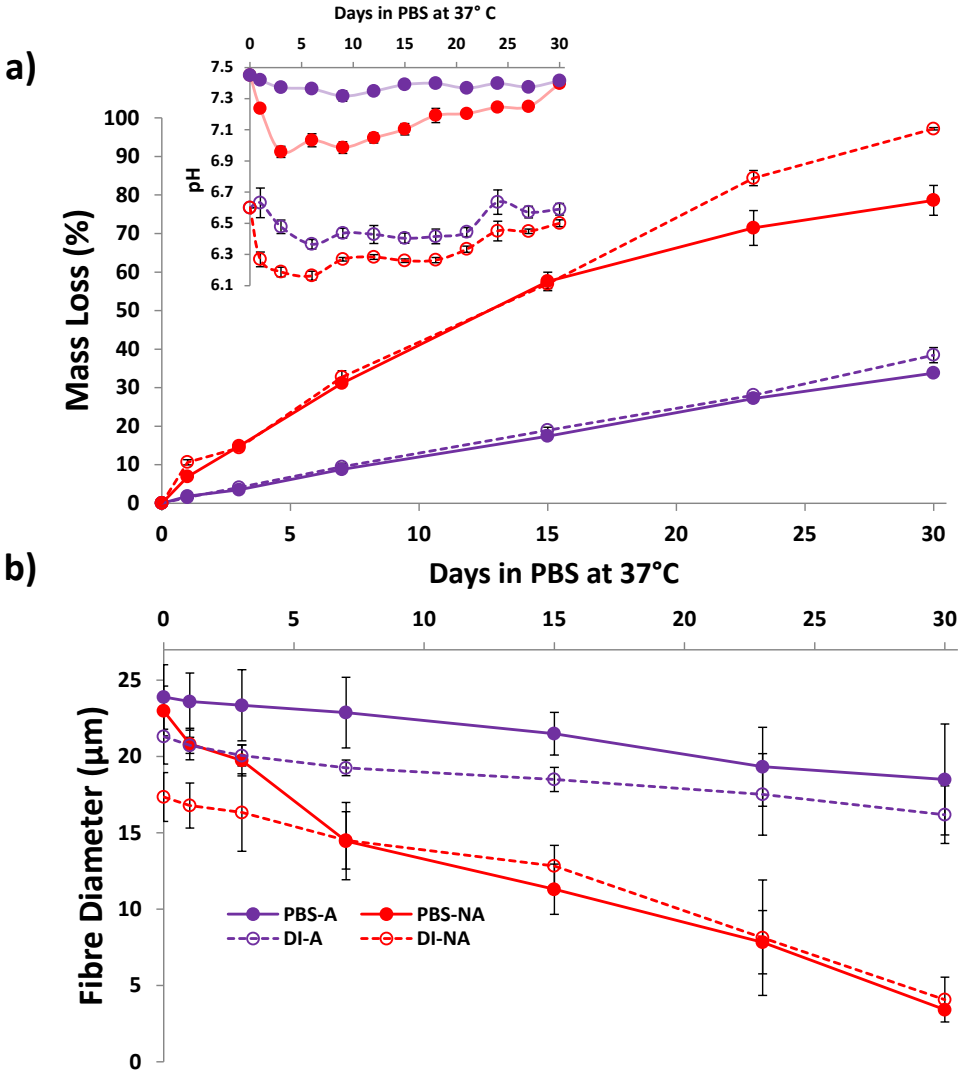


Figure 3.9: (a) % Mass loss, m_{LF}, (±SD) and (b) fibre diameter (±SD) variation for annealed (purple markers and purple lines) and as-drawn fibres (red markers and red lines) conditioned in deionised water 'DI' and PBS at 37°C, respectively. The inset of (a) shows the variation (±SD) of the conditioning media collected from as-drawn and annealed fibres. The % mass loss and the fibre diameter variation profiles for PBS conditioning were denoted by solid markers and solid lines, whereas the % mass loss and fibre diameter variation for deionised water conditioning were denoted by open markers and dashed lines.

At each time point the as-drawn fibres in both deionised water and PBS presented a much higher % mass loss with respect the annealed fibres, reaching a ca. 97% and 73% mass loss, respectively at day 30. It should be noted that for both as-drawn and annealed fibres, the % mass losses were greater in deionised water with respect to PBS.

3.1.8.3 Effect of Conditioning Time on Phosphate Glass Fibre Dimensions

The corresponding reduction in fibre diameter for both annealed and as-drawn fibres in deionised water and PBS as measured from SEM analysis is presented in Figure 3.9b. The diameters reported for the as-drawn fibres in PBS were obtained from the measurement of inner fibre cores exposed by the rupture of the enclosing shells (shown in the right column of Figure 3.7). As in the case of % mass loss, the variation in annealed fibre diameter in both deionised water and PBS described a linear trend, although with a negative slope. Similar to the corresponding % mass loss, the reduction in diameter of the as-drawn fibres in PBS followed a decelerating behaviour as dissolution time increased. In contrast, the reduction in diameter of as-drawn fibres conditioned in deionised water was directly proportional to the conditioning time.

3.1.8.4 Effect of Conditioning Time on the pH of Phosphate Glass Fibre Conditioning Media

The deionised water and PBS pH variation during phosphate glass fibre dissolution followed during 30 days is displayed in the inset of Figure 3.9a. It can be seen that the pH of the PBS where annealed fibres were immersed decreased slightly reaching a value of pH 7.32 at day 9. From this point onwards the PBS pH roughly stabilised at around pH 7.4 for the remainder of the study. In contrast, the pH of the PBS collected from vials with as-drawn glass fibres presented a sudden decrease, reaching values as low as ca. 6.9 by day 3. The pH of the PBS stabilised at this region up to day 9 to then progressively increase towards the as-prepared pH of PBS.

The pH of fresh deionised water was lower with respect to the as-prepared PBS as stated in §2.8.2. The pH of the deionised water collected during the glass fibre degradation study followed a similar behaviour to PBS. A slight decrease from pH 6.6 to ca. pH 6.3 during the first 9 days, followed by a 21 day stabilisation period and a finally increase towards fresh deionised water

pH values was observed for annealed fibre conditioning. The pH profile of the as-dawn fibre conditioning media resembled that of the annealed fibres, although shifted towards more acidic values. The initial deionised water pH decreased to around 6.15 and stabilised in this region to finally increase towards fresh deionised water pH readings.

3.1.8.5 Effect of Conditioning Time on Phosphate Glass Fibre Estimated Mass

The estimated mass losses, m_E, calculated from glass fibre diameter reduction of both annealed (purple markers) and as-drawn (red markers) fibres in deionised water (open markers and dashed lines) and PBS (solid markers and lines) are illustrated in Figure 3.10. For annealed fibres, the estimate % mass loss in both deionised water and PBS approximated reasonably well the corresponding % mass losses presented in Figure 3.9a, reaching 42% and 40%, respectively, at day 30 in comparison to the respective 34% and 38% mass losses.

The % mass loss estimate for as-drawn fibres conditioned in PBS was much greater than the corresponding value calculated from mass differences, reaching ca. 98% by day 30 in comparison to ca. 73%, respectively. On the other hand, the estimated % mass loss for as-drawn fibres conditioned in deionised water was in good agreement at all time points with the behaviour presented in Figure 3.9a. At day 30 the estimated % mass loss in deionised water was 95% which approximated well the 97% calculated from mass differences. The estimated % mass loss for as-drawn fibres in deionised water described a linear behaviour in contrast to the decreasing trend of the corresponding fibre and conditioning media in Figure 3.9a.

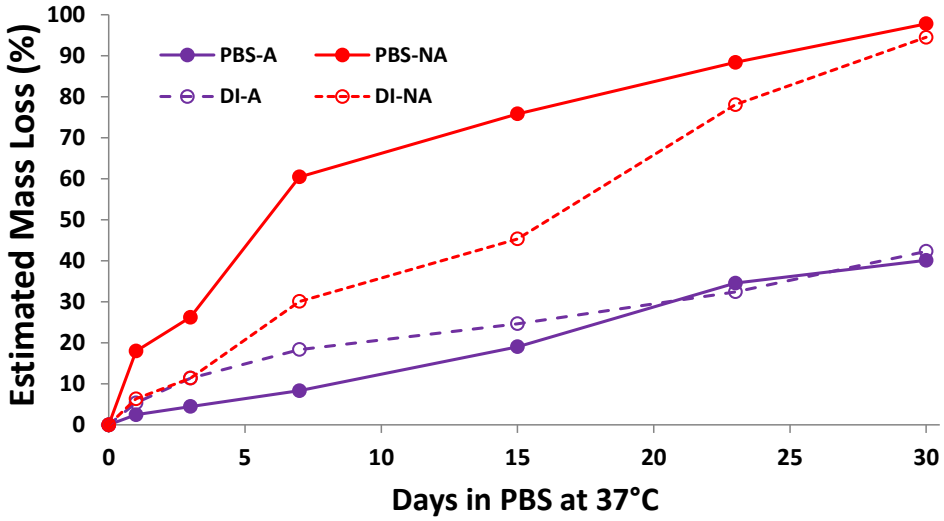


Figure 3.10: Estimated % mass loss, m_E, as calculated from diameter reduction of as-drawn (red markers) and annealed (purple markers). The estimated % mass loss profiles for PBS conditioning were denoted by solid markers and solid lines, whereas the corresponding values for deionised water conditioning were denoted by open markers and dashed lines. The open purple circles and open red squares represent the estimated % mass loss for annealed and as-drawn fibres, respectively.

3.2 Manufacture of Fully Bioresorbable Fibre Reinforced PGF-PLA Composite Plates via Cyclic Pressure-assisted Compression Moulding

3.2.1 PLA Rotational Viscosity

Figure 3.11 shows the results of the dynamic linear viscoelastic measurements conducted on 3251D commercial grade PLA under a shear strain of 1%. The frequency, ω, dependence of the storage, G', and loss modulus, G'', along with the complex viscosity, η*, of PLA at 180°C is presented in Figure 3.11a. The storage modulus approached but never exceeded the magnitude of the loss modulus as the oscillation frequency was increased. No crossover was observed over the entire frequency range examined. The complex viscosity seemed to be independent of the oscillation frequency. Excepting at 170°C, where the storage and loss modulus curves almost superpose each other, similar results were obtained at the additional test temperatures and therefore are not shown here.

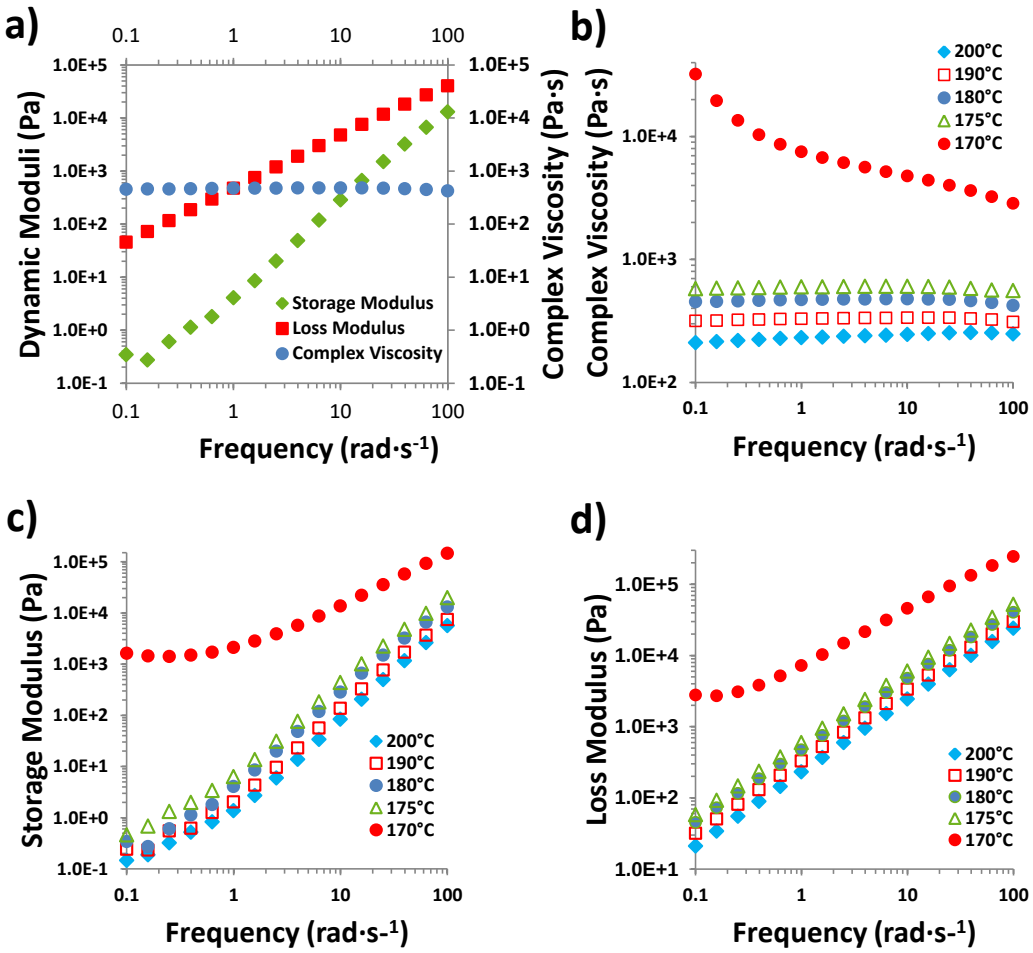


Figure 3.11: Dynamic linear viscoelastic measurements conducted on 3251D PLA. (a) Influence of oscillation frequency, ω, on the storage modulus, G', loss modulus, G'', and complex viscosity, η*, of PLA at the reference temperature of 180°C. (b), (c) & (d) Evolution of the complex viscosity, storage and loss modulus of 3251D PLA with oscillation frequency at different test temperatures, respectively.

Figure 3.11b presents the influence of both temperature and oscillation frequency on PLA complex viscosity. Excluding the 170°C case, where the viscosity exponentially increased as the solicitation frequency decreased, PLA complex viscosity was independent of the oscillation frequency, regardless of the test temperature. Samples tested at 200°C showed the lowest complex viscosity (ca. 240 Pa·s). The complex viscosity progressively shifted toward higher values as the test temperature was decreased, reaching ca. 590 Pa·s at 175°C. Further decreases in temperature resulted in substantial displacement (by over a decade) of the complex viscosity curve towards higher values.

As shown in Figures 3.11c the storage modulus increased monotonically as the oscillation frequency was raised with a scaling factor of approximately $G' \sim \omega^2$. The G' curves were displaced towards higher values as the test temperature was decreased. A sudden deviation of the observed scaling

relation was noted when the test temperature was decreased to 170°C. Likewise, the loss modulus increased alongside frequency, but with scaling factor of approximately G''~ω. As shown in Figure 3.11d, the G'' curves shifted towards higher values as the test temperatures was decreased. A sudden displacement of the loss modulus curve when the temperature was decreased to170°C was also observed.

Figure 3.12 shows the influence of temperature on the PLA zero shear viscosities, η_0, (determined by fitting of the dynamic experimental data to the Carreau-Yasuda model for unlinked and unfilled polymers). The viscosity decreased with increasing temperature, being 234 Pa·s the lowest η_0 value measured at 200°C. No results are reported for 170°C since the model predicted an infinity value of viscosity at this temperature.

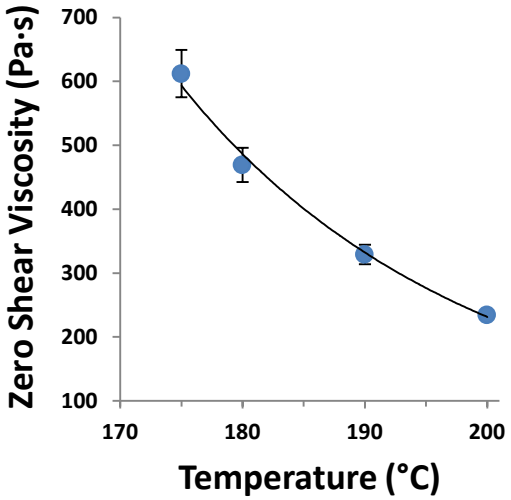


Figure 3.12: Influence of temperature on 3251D PLA zero shear viscosity (±SD), η_0, as determined by experimental date fitting to the Carreau-Yasuda model.

The mechanical and physical properties of the composite plate constituent phases, used in the relevant fibre volume fraction calculations, were compiled in Table 3.4. Figure 3.13a and 3.13b illustrate the flexural properties of the composite plates manufactured via the different pressure profiles as detailed in §2.11.

Table 3.4: Physical and mechanical properties (±SD) of the PLA-phosphate glass fibre reinforced composite plates constituent phases.

Properties	Phosphate Glass Fibre	Poly(lactic acid)
Density (g·cm^{-3})	2.640±0.005	1.250±0.002
Tg (°C)	462±2	58.2±0.3
Tm (°C)	840±0.4	170.7±0.2
Strength (MPa)	700±250	75±3
Modulus (GPa)	61±5	3.3±0.4
Elongation at Break (%)	1.5±0.7	3.5±0.3

3.2.2 Compression Moulded PGF-PLA Composite Plates Flexural Properties

The flexural properties of both composite plate series greatly exceeded those of PLA alone (75±3 MPa for flexural strength and 3.3±0.4 GPa flexural modulus, respectively). Flexural strengths of the CP-composite plates closely followed a linear trend directly proportional to fibre volume fraction as shown in Figure 3.13a.

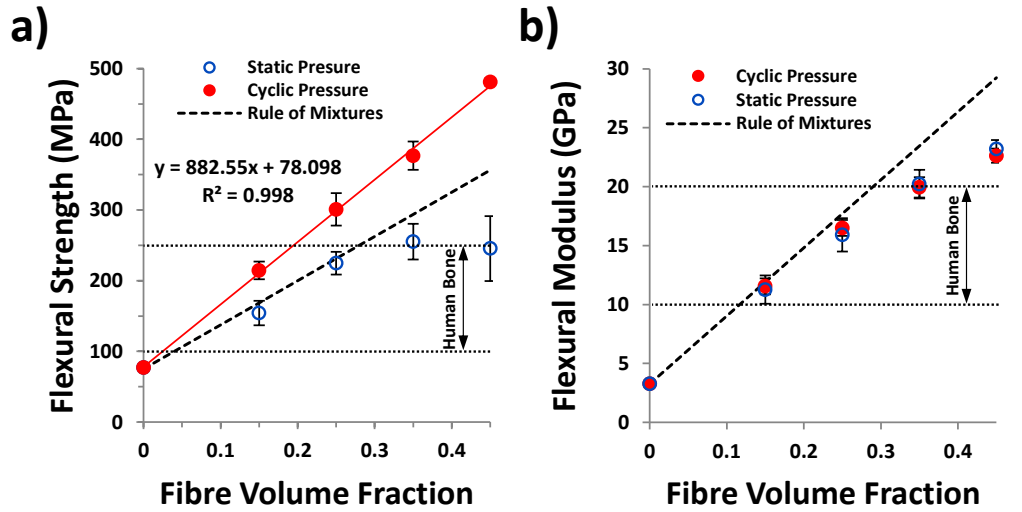


Figure 3.13: (a) Influence of the pressure profile on composite plate flexural strength (±SD) and (b) flexural modulus (±SD) with progressively higher fibre content. The black dashed line represents the theoretical composite plate strengths calculated by substitution of mean experimental matrix and fibre strengths in the rule of mixtures. The range of human cortical bone flexural strength is denoted by black dotted lines.

For all volume fractions, the strength values of the CP-composite plates significantly surpassed those of the SP-series; the difference being more pronounced the higher the fibre volume fraction. This was clearly evident for the 0.45v_f samples, where a 250 MPa difference was observed to separate the respective mean strength values of both composite plate series.

For comparison purposes, the strength values of a PLA-PGF composite plate series were calculated by substitution of the mean experimental strengths of

the constituent phases (cf. Table 3.4) using the Rule of Mixtures, expressed by equation (3.1) [165]:

$$S_{cm} = S_f v_f + S_m(1 - v_f) \quad (3.1)$$

where $\boldsymbol{S_{cm}}$, $\boldsymbol{S_f}$ and $\boldsymbol{S_m}$ are the composite plate, fibre and matrix strengths, respectively. The results were graphically illustrated by the black dashed line in Figure 3.13a.

The strength profiles for the $0.15v_f$ and $0.25v_f$ static pressure composite plate samples approximated well the predicted Rule of Mixtures curve. However, from $0.25v_f$ onwards, further increases in fibre content did not result in a strength improvement as estimated, but instead deleteriously impacted the consistency of the strength values as shown by the large standard deviation values attained.

On the other hand, the strengths of the cyclic pressure composite plates exceeded the values predicted by the rule of mixtures curve in all cases and described a well-defined linear trend with a greater slope.

An estimate of the effective strength of both matrix and fibres in the CP-composite plate series can be gained by rewriting Equation (3.1) into the slope-y intercept form of a linear equation with $\boldsymbol{v_f}$ as the independent variable and S_m as the y-intercept:

$$S_{cm} = v_f(S_f - S_m) + S_m \quad (3.2)$$

By equating the slope and y-intercept values of the best fitting line describing the trend of the CP-composite plate strengths (solid red line in Figure 3.11a) to the corresponding terms in (3.2), values of ca. 77 MPa and ca. 973 MPa were obtained for the matrix and fibre effective strength respectively in the cyclic pressure-composite system.

The matrix strength value at the ordinate intercept was found to be similar to the experimental strength of PLA (75±3 MPa) as shown in Table 3.4.

However, the effective fibre strength was found ca. 40% higher than the experimental fibre strength value associated with the SP series.

As shown by Figure 3.13b, no significant differences ($p>0.05$) in the modulus values were observed between the CP and SP-composite plate series. The elastic modulus increased monotonically with fibre volume fraction. It was observed that the $0.15v_f$ and $0.25v_f$ samples complied with the rule of mixtures applied to modulus, however for the higher fibre volume fractions, namely 0.35 and 0.45, the modulus diverged to lower values.

3.2.3 PGF-PLA Compression Moulded Composite Plates Thermal Analysis

Representative DSC traces obtained during the second heating cycle for the composites plates are depicted in Figure 3.14. Four features can be readily distinguished in the DSC thermograms: i) a glass transition phenomenon T_g, ii) a cold crystallisation peak (denoted by both peak maximum temperature, T_{X1}, and crystallisation onset T_{X0},) iii) a polymorphic transition peak (denoted by T_{X2}) and iv) an endothermic peak (characterised by T_m) associated with the melting of crystalline phases.

In addition to the respective values of the characteristic temperatures previously described, the enthalpies of melting, ΔH_m, and crystallisation of both peaks, ΔH_{X1}, and ΔH_{X2}, are also listed in Table 3.5, along with the crystallinity content, X, of the composite plates (calculated as stated in §2.18). No distinctive features could be observed in the DSC traces upon cooling.

In the cyclic pressure composite plate series, the most noticeable changes observed following the incorporation of fibres into the polymer matrix were: i) the contraction of both the melting and the cold crystallisation peak roughly at the same rate, resulting in a constant and rather low crystalline content throughout the composite plate series, (cf. Table 3.5), ii) the broadening of the crystallisation peak as a result of the evolution of a shoulder which appeared to intensify as the fibre volume fraction increased, and iii) the progressive shift of the crystallisation peak towards lower temperatures as the fibre volume fraction increased.

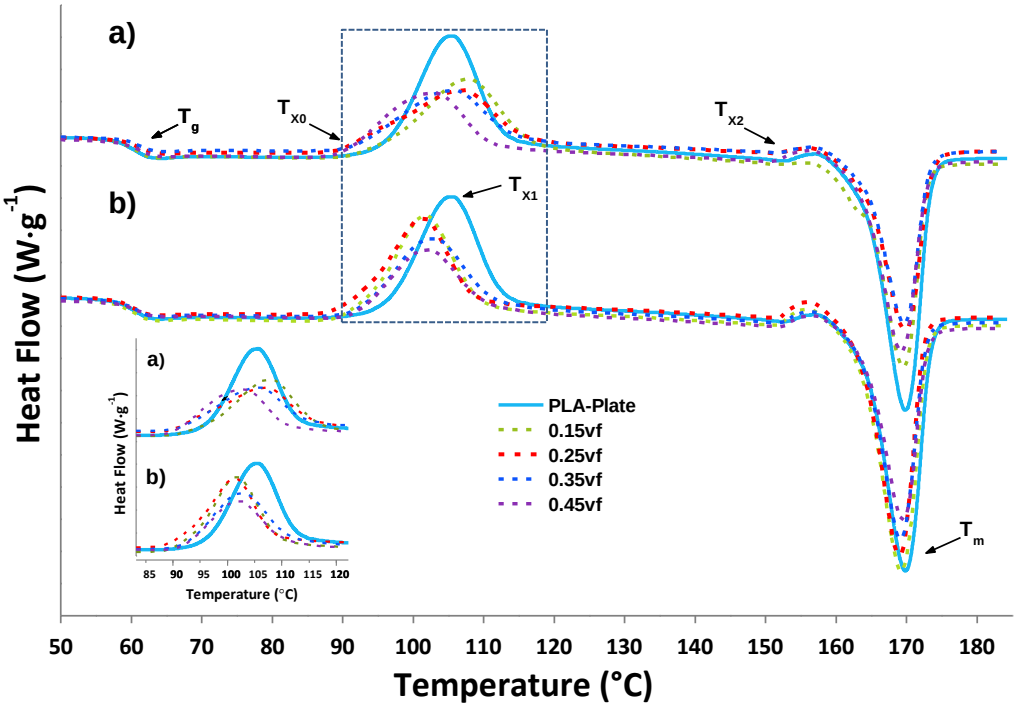


Figure 3.14: Representative DSC traces of a) cyclic Pressure and b) static pressure compression moulded composite plates. The inset isolates the area enclosed by the blue dashed line.

The melting and the cold crystallisation peaks for the SP-composites plate series also changed upon fibre addition in similar fashion to that previously described for the CP-series, but to a lesser extent. Both the onset and the maximum peak temperature shifted to lower temperature upon fibre addition. No significant changes in the glass transition temperature were found.

To rule out the possible effect of molecular weight decrease on the PLA crystallisation, the thermal cycle described in §2.18 was repeated in selected samples up to four times. No significant differences could be found between these complementary runs.

Table 3.5: Summary of PLA-PGF composite plates thermal properties consolidated with either static pressure 'SP' or cyclic pressure 'CP'.

Cycle	Sample	T_g (°C)	T_{X0} (°C)	T_{X1} (°C)	T_{X2} (°C)	T_m (°C)	ΔH_m ($J \cdot g^{-1}$)	ΔH_{X1} ($J \cdot g^{-1}$)	X (%)
	PLA-Plate	58.5	96.4	105.2	157.0	169.8	44.01	43.56	0.48
	0.15-CP	58.6	95.0	108.1	156.3	169.6	37.03	36.89	0.15
	0.25-CP	59.5	91.0	107.1	156.3	169.8	33.47	33.30	0.18
	0.35-CP	59.6	91.6	106.2	156.9	169.7	30.22	30.08	0.15
2	**0.45-CP**	59.7	90.5	105.6	156.7	170.0	28.64	27.47	1.25
	0.15-SP	58.5	93.1	101.9	156.3	169.3	41.15	39.39	1.88
	0.25-SP	58.4	92.0	101.2	156.3	170.0	38.71	36.93	1.90
	0.35-SP	59.2	92.3	102.8	156.9	170.2	35.05	32.89	2.31
	0.45-SP	59.1	92.2	102.3	156.9	169.5	30.72	28.38	2.50
	PLA-Plate	62.4	95.6	106.2	157.5	171.5	45.49	43.24	2.40
	0.15-CP	62.8	93.6	109.9	156.0	170.9	37.94	35.88	2.20
	0.25-CP	60.7	88.9	109.1	155.8	171.0	33.88	29.75	4.41
	0.35-CP	60.0	88.2	104.4	155.4	170.0	31.04	25.91	5.48
1	**0.45-CP**	58.7	87.4	104.2	155.8	170.1	29.49	25.09	4.70
	0.15-SP	61.2	92.8	103.6	156.7	170.4	41.62	37.03	4.90
	0.25-SP	64.0	90.4	102.6	156.4	170.4	38.88	32.51	6.81
	0.35-SP	61.9	90.7	103.8	156.6	170.6	34.76	29.46	5.66
	0.45-SP	61.6	90.4	102.27	156.23	169.64	30.81	23.85	7.44

3.2.4 PGF-PLA Compression Moulded Composite Plates Void Content Analysis

The results of the composite void content analysis conducted through comparison of the experimental and theoretical density values were outlined in Table 3.6. With the exception of the $0.45v_f$ SP specimens (where a threefold increase in void content was estimated in comparison to the corresponding CP composite plate samples) low void-content (φ_v<1%) composite plate specimens were achieved for both pressure profiles. The void content proved not to be dependent on the manufacturing method up to $0.35v_f$, with only a minor tendency for pressure cycling to produce composites with less content of voids.

Table 3.6: Summary of experimental fibre volume fraction and void content analysis (±SD) for composite plates consolidated with either static pressure 'SP' or cyclic pressure 'CP'.

v_f Nominal	Pressure Profile	v_f Experimental	φ_v(%)
0.15	**SP**	0.15 ± 0.01	0.37± 0.02
	CP	0.16 ± 0.01	0.32± 0.03
0.25	**SP**	0.24 ± 0.02	0.25± 0.02
	CP	0.260 ± 0.004	0.14± 0.05
0.35	**SP**	0.34 ± 0.03	0.54±0.15
	CP	0.360 ±0.003	0.54± 0.13
0.45	**SP**	0.45 ±0.01	1.90± 0.60
	CP	0.46 ± 0.01	0.73± 0.04

3.2.5 Compression Moulded PF-PLA Composite Plates SEM Cross Sectional Analysis

Figure 3.15 shows the cross section of the composite plates fabricated via static (left) and cyclic (right) pressure profiles. No significant differences were observed between the cross sectional images of the $0.15v_f$ and $0.25v_f$ samples fabricated under different pressure conditions.

The difference in the effect of the type of consolidating pressure was more evident as the thickness of the fibre preform increased alongside fibre volume fraction (cf. Table 2.1). In the case of the $0.35v_f$ specimens (obviating the crack resultant of flexural testing that propagated through the interface between the polymer and the fibre in the upper part of Figure 3.15f) a marginally higher number of voids can be observed in the SP specimen (Figure 3.15e).

Only a few voids were observed in the $0.45v_f$ CP cross section image in Figure 3.15h, whereas large areas with voids were present at the centre of the fibre layers in the $0.45v_f$ SP sample fabricated under static pressure (Figure 3.15g). Voids were concentrated at the interstices between the fibres mainly at the centre of the UD fibre mats. No defects could be seen in the polymer rich zones amongst the plies.

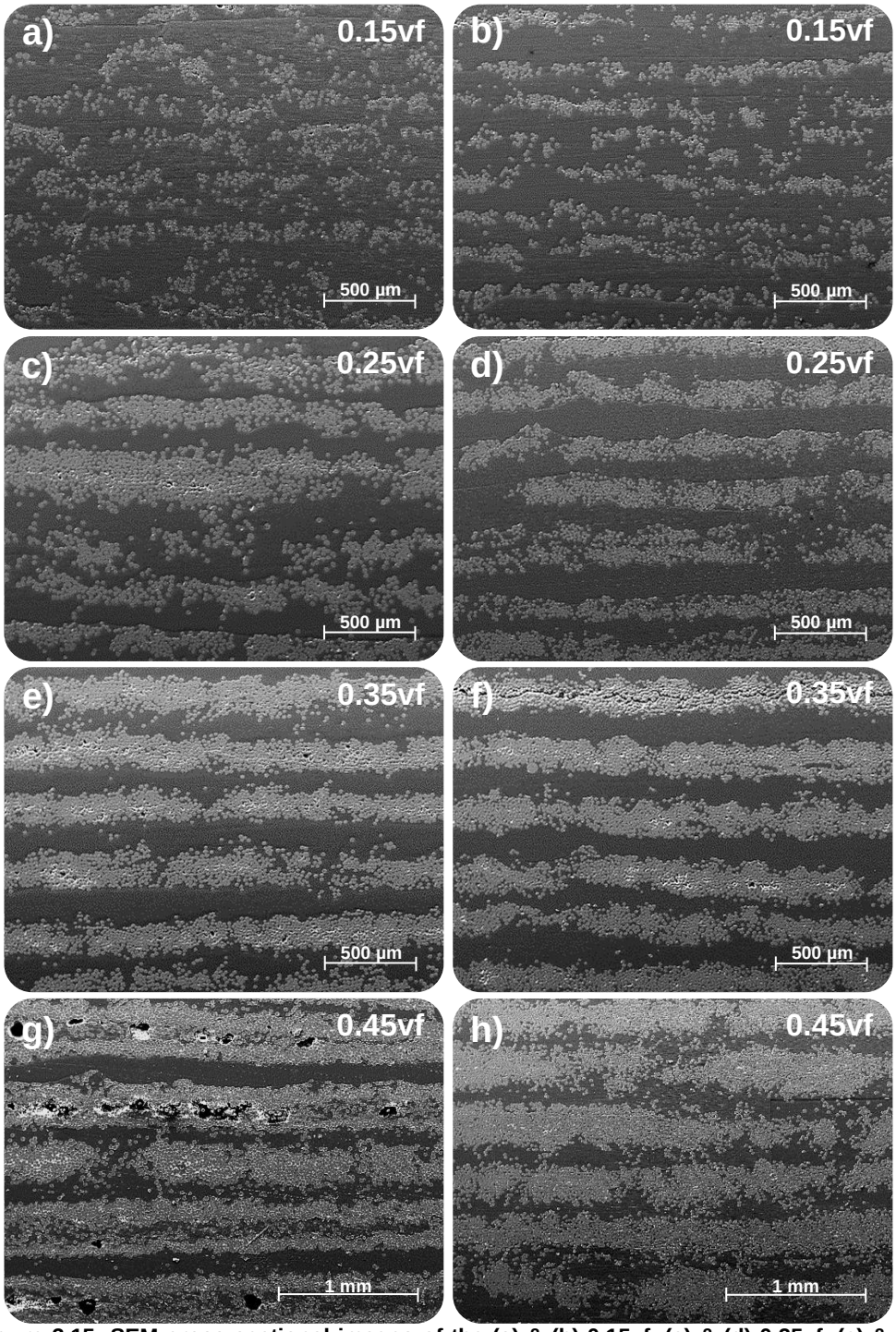


Figure 3.15: SEM cross sectional images of the (a) & (b) 0.15vf, (c) & (d) 0.25vf, (e) & (f) 0.35vf and (g) & (h) 0.45vf compression moulded composite plates manufactured by (left) static pressure and (right) cyclic pressure profiles, respectively.

3.2.6 Compression Moulded PGF-PLA Composite Plates GPC Analysis

The molecular weight distribution results are shown in Table 3.7. The number average M_n, weight average M_w, the *Z*-average molecular weight M_z, and the calculated polydispersity index $Đ_M$, are shown for the polymeric matrix in the

PLA-PGF composites at different stages during the manufacturing processes and fibre content. The molecular weight results for both pressure profiles were found identical within experimental error and thus generic molar masses for the composites plates are reported in the following.

Table 3.7: Summary of chromatography results (±SD) for the neat polymer at different stages and PLA in the composite plates fabricated in this study.

Sample	M_n (gmol^{-1})	M_w (g·mol^{-1})	M_z (g·mol^{-1})	$Đ_M$
Virgin	121000 ± 700	158000 ± 1000	216000 ± 1500	1.311
Film	116000 ± 800	154000 ± 1100	212000 ± 1600	1.325
Plate	115000 ± 1900	155000 ± 460	213300 ± 350	1.340
15v_f	115300 ± 700	150000 ± 1000	203000 ± 1700	1.302
25v_f	113100 ± 1000	146500 ± 750	195000 ± 3000	1.300
35v_f	104000 ± 2000	135000 ± 2000	179000 ± 800	1.300
45v_f	97000 ± 600	121000 ± 500	153000 ± 800	1.250

From the data presented in Table 3.7 it can be appreciated that the molecular weight tends to decrease steadily throughout the sequential processing steps of laminate compression moulding. Furthermore the fibre content seems to have a deleterious effect on the molar mass during melt processing since the higher the volume fraction, the lower the molecular weight. The polydispersity index roughly maintained constant during sequential processing steps and for different fibre volume fractions.

3.2.7 Effect of Processing Variables on Cyclic Pressure-assisted PGF-PLA Composite Plate Compression Moulding

3.2.7.1 Effect of Varying Pressure on Cyclic Pressure-assisted PGF-PLA Composite Plate Compression Moulding

To evaluate the effect on the processing variables on the mechanical performance of PLA-PGF composite plates, samples with 0.35 fibre volume fraction were fabricated with increasing magnitude of cyclic pressure consolidation and increasing processing temperature. Figure 3.16 presents the influence of cyclic pressure consolidation magnitude on the mechanical properties of fibre PLA-PGF reinforced composite plates. Four different consolidating pressures, spanning from 30-60 bar, in 10 bar increments were evaluated. Composite plates consolidated at 30 bar cyclic pressure presented the lowest flexural strength (ca. 286 MPa) which was comparable to the strength of the composite plates with matching volume fraction consolidated under 40 bar of static pressure (cf. Figure 3.13a). A 30% increment in flexural

strength was observed by upon increasing the consolidating pressure by 10 bar as shown in Figure 3.16a. Further increases in pressure led to a progressive decrease in the flexural strength of the composite plates.

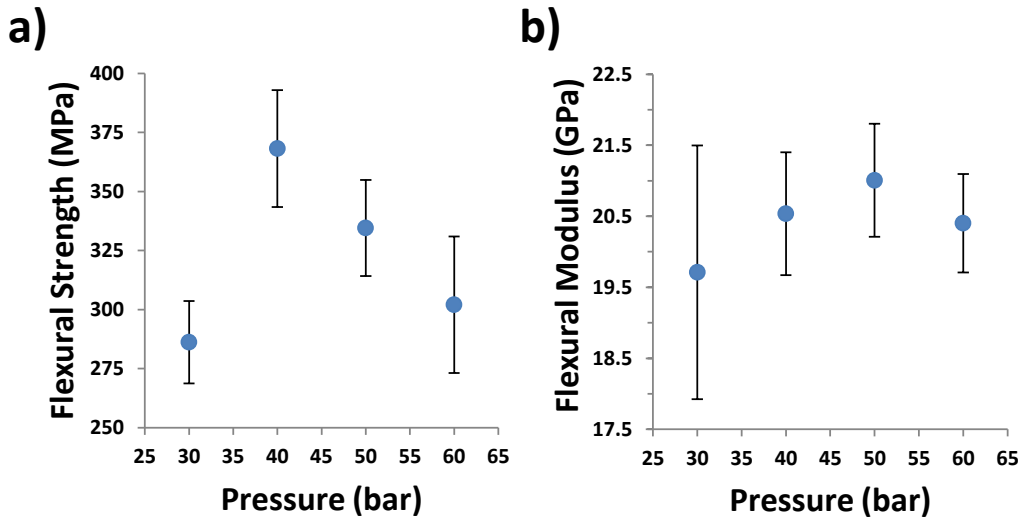


Figure 3.16: Influence of the magnitude of cyclic pressure consolidation on the (a) flexural strength (±SD) and (b) flexural modulus (±SD) of PLA-PGF composites with 0.35 fibre volume fraction processed at 180°C.

As shown in Figure 3.16b, no significant differences ($p>0.05$) in the flexural modulus of the composite plates were noticed across the spectrum of consolidating pressures used.

3.2.7.2 Effect of Varying Temperature on Cyclic Pressure-assisted PGF-PLA Composite Plate Compression Moulding

Figure 3.17 shows the effect of processing temperature on the mechanical properties of fibre reinforced composite plates.

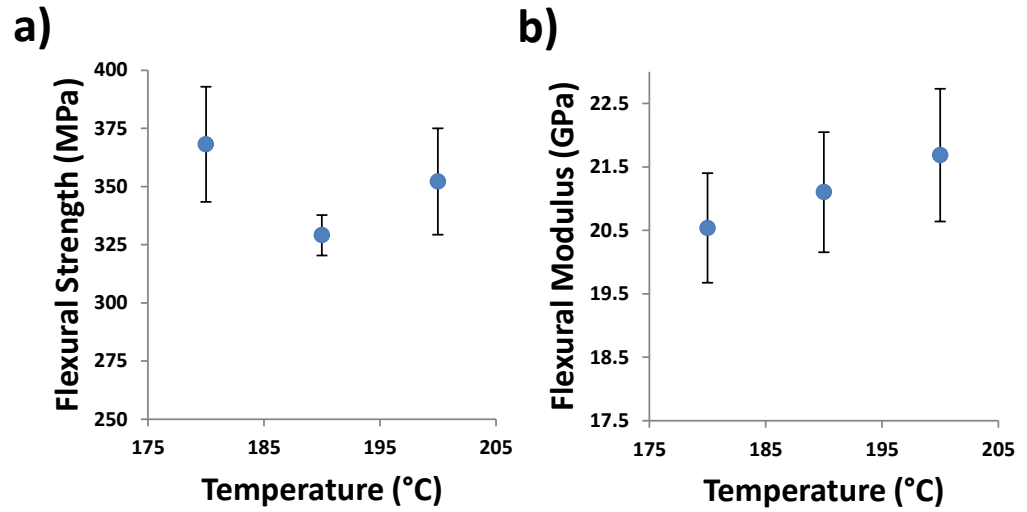


Figure 3.17: Influence of the processing temperature on the (a) flexural strength (±SD) and (b) flexural modulus (±SD) of PLA-PGF composites with 0.35 fibre volume fraction consolidated with 40 bar cyclic pressure.

Three different temperatures, spanning from 180-200°C, in 10°C increments were evaluated. No significant differences ($p>0.05$) were noted in either flexural strength (Figure 3.17a) or flexural modulus (Figure 3.17b).

3.2.7.3 Effect of Varying Pressure and Temperature on Compression Moulded PGF-PLA Composite Plates Void Content and Fibre Volume Fraction

Table 3.8 summarises the results of the void content and experimental fibre volume fraction analysis conducted on fibre reinforced composite plates with 0.35 fibre volume fraction consolidated with increasing cyclic pressure magnitude and increasing processing temperatures, respectively. No significant differences in thickness ($p>0.05$ in all cases) with respect to the reference plate fabricated at 180°C were noted in the plates fabricated at 180°C with varying cyclic pressure magnitude.

On the other hand, the thickness of the fibre reinforced composite plates manufactured at different temperatures, progressively decreased as the temperature was raised in increments of 10°C from the reference temperature. The difference in thickness with respect to the 180°C composite pate (ca. 5% thickness reduction) was significant ($p<0.05$) in the case of fibre reinforced composite plate fabricated at 200°C.

Within experimental error, the experimental volume fraction of the composite plates fabricated at different pressure and temperature was in good agreement with the intended 0.35 fibre volume fraction.

Table 3.8: Summary of experimental fibre volume fraction and void content analysis (±SD) for fibre reinforced composite plates with 0.35 fibre volume fraction manufactured with increasing consolidation cyclic pressure and processing temperature, respectively.

Pressure (bar)	Temperature (°C)	Thickness (mm)	v_f Experimental	φ_v (%)
30	**180**	4.46±0.05	0.360±0.003	0.69±0.06
40		4.54±0.03	0.38±0.02	0.31±0.02
50		4.48±0.09	0.37±0.03	0.18±0.07
60		4.42±0.08	0.36±0.02	0.31±0.09
40	**190**	4.44±0.09	0.36±0.04	0.003±0.013
40	**200**	4.34±0.08	0.38±0.03	0.44±0.06

In all cases, low void contents ($\varphi_v<1\%$) were estimated for the $0.35v_f$ pressure and temperature composite plate series. The composite plate consolidated with 30 bar cyclic pressure presented the highest void content of the

composite plates in the $0.35v_f$ pressure-series, whereas the composite plate fabricated at 200°C presented the highest void content in the $0.35v_f$ composite plate temperature-series.

3.3 Effect of Forging on Mechanical Properties and *In Vitro* Degradation of Fully Bioresorbable Fibre Reinforced PGF-PLA Composite Rods

3.3.1 Forged Composite Rods SEM Cross Sectional Imaging

Uniaxial compression and plane strain forged rods with dimensions of 4 mm × 80 mm (diameter × length) were manufactured via thermomechanical deformation of 4.5 mm × 3 mm × 100 mm (thickness × width × length) composite blanks (machined from 4.5 mm × 110 mm × 110 mm compression moulded composite plates) as detailed in §2.12.

Figure 3.18 shows representative SEM images of the transverse cross section of cyclic pressure-assisted compression moulded composite plates with 0.15, 0.25, 0.35 and 0.45 fibre volume fractions (left column) from which composite blanks were cut and subsequently shaped into cylindrical rods (right column) via plane strain forging.

No changes in fibre distribution or alignment were noticed in the transverse plane regardless of the fibre volume fraction of the composite blank. The fibre layers (particularly in the outermost region) were forced inwards to accommodate to the cylindrical mould cavity in all cases. Analogous observations were made for transverse cross sections of the complementary rods series, i.e., those fabricated via plane strain forging of static pressure compression moulded composite plates and uniaxial compression forging of static and cyclic pressure assisted compression moulded plates, and therefore, are not presented here.

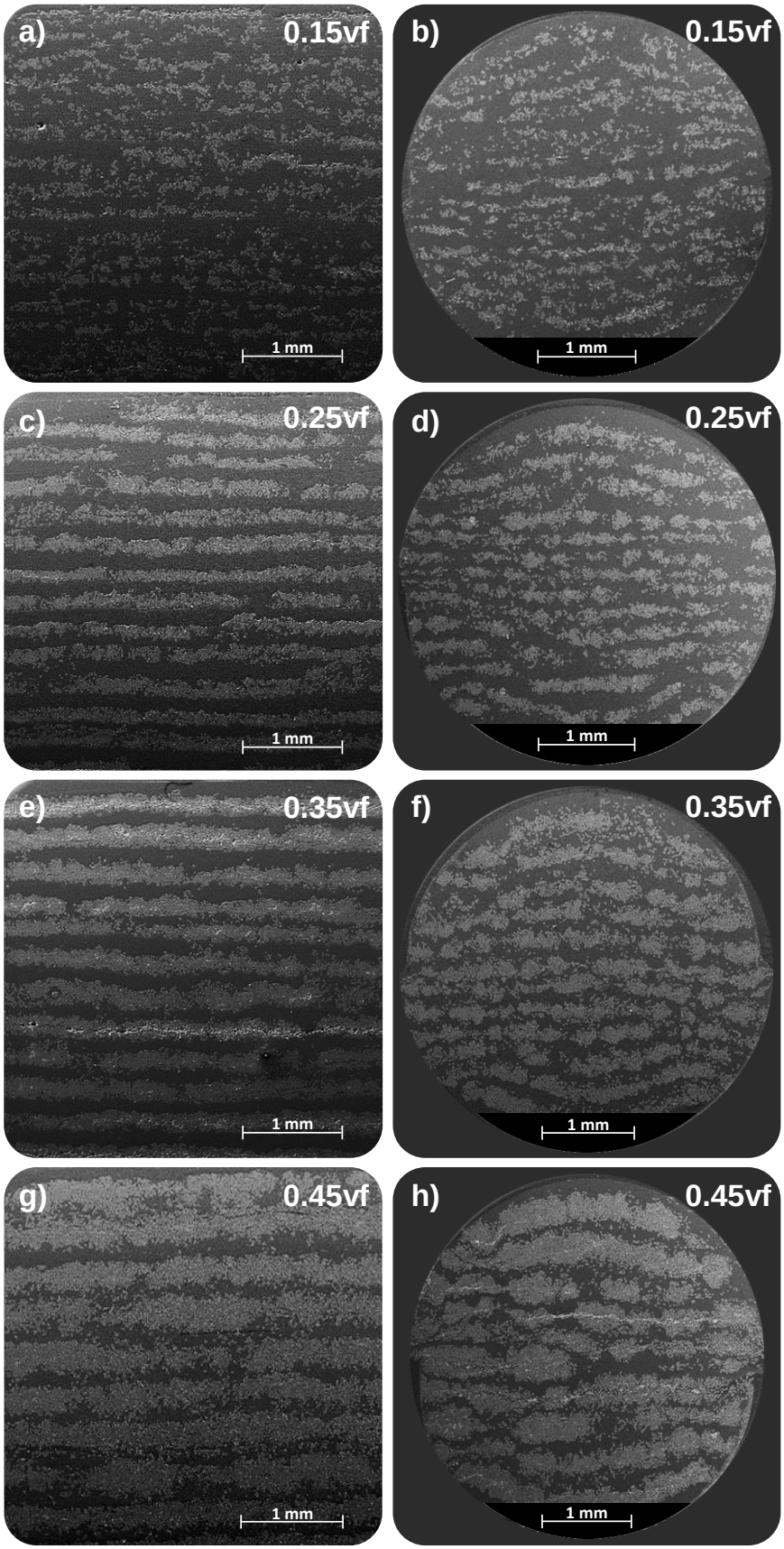


Figure 3.18: (left) Transverse plane SEM micrographs of 4.5 mm × 110 mm × 110 mm (thickness × width × length) compression moulded composite plates representative sections, from which 4.5 mm × 3 mm × 100 mm (thickness × width × length) composite blanks were cut and subsequently forged into 4 mm × 80 mm (diameter × length) composite rods (right) with 0.15, 0.25, 0.35 and 0.45 fibre volume fractions.

3.3.2 Effect of Forging on PGF-PLA Composite Rods Flexural Properties

The mean flexural properties of three 4.5 mm × 15 mm × 90 (thickness × width × length) test coupons obtained from the 4.5 mm × 110 mm × 110 mm composite plates are represented by the columns with dashed lines in Figures 3.19 and 3.20. The properties of the test coupons were considered to be representative of the entire composite plate. The mechanical properties of the Ø 4mm composite rods manufactured by forging 4.5 mm × 3 mm × 100 mm blanks (machined from the rest of the composite plates) under uniaxial compression and plane strain conditions are represented by the solid columns in Figure 2 and 3, respectively. The CP (cyclic pressure) and SP (static pressure) notations in the said figures were used to denote the specifics of the pressure scheme used during the composite plate compression moulding as stated in §2.11. The columns representing the mechanical properties of the rods obtained from composite plates consolidated under cyclic pressure have been highlighted in red, and those obtained from static pressure consolidated plates were highlighted in blue.

From Figure 3.19 and 3.20 it can be seen that the strength of cyclic pressure consolidated composite plates exceeded those manufactured using static pressure for all the volume fractions studied. The $0.15v_f$, $0.25v_f$, $0.35v_f$, and $0.45v_f$ plates consolidated under cyclic pressure were approximately 37%, 34%, 43%, and 92% stronger than those consolidated under conventional static pressure, respectively. No significant differences in flexural modulus resulting from the different consolidation pressure schemes could be observed. The strength and modulus of the composite plates consolidated using cyclic pressure increased in direct proportion to the fibre volume fraction.

3.3.2.1 Effect Uniaxial Compression Forging in PGF-PLA Composite Rods Flexural Properties

After uniaxial compression forging, the composite samples experienced an extension in the z-direction of 10%, which matched the reduction in cross sectional area, calculated as the ratio of the cylindrical rod (ca. 12.57mm^2) and the composite blank (ca. 13.725 mm^2) cross sectional areas.

Both the strength and modulus of the neat-PLA rod increased slightly in relation to the mechanical properties of the neat-PLA plate by 35% and 17%,

respectively, as a result of uniaxial compression forging. However, the flexural properties of the forged composite rods were, in all the cases, considerably lower than those of the equivalent composite plates, regardless of the pressure scheme used during the composite plate consolidation stage. It was also observed that the reduction in forged composite rod strength was considerably higher than the reduction in modulus as the sample volume fraction increased. No data has been reported for the $0.45v_f$ uniaxial compression forged composite rods since these samples completely delaminated at their middle plane during the demoulding stage.

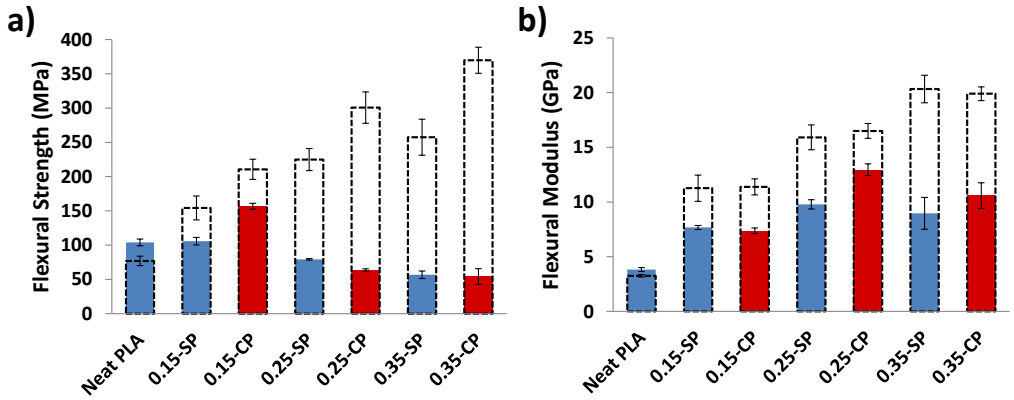


Figure 3.19: Effect of uniaxial compression forging on the flexural (a) strength (±SD) and (b) modulus (±SD) of forged composite rods. The mechanical properties of the initial composite plates are indicated by black dashed lines. The solid columns represent the mechanical properties of the uniaxial compression forged rods. The mechanical properties of the rods forged from cyclic pressure-consolidated 'CP' composite plates are highlighted in red and those representative of rods obtained from static pressure-consolidated 'SP' composite plates are highlighted in blue.

3.3.2.2 Effect Plane Strain Forging in PGF-PLA Composite Rods Flexural Properties

The effect of plane strain forging on the mechanical properties of forged composite rods in comparison to the composite plates is shown in Figure 3.20. No significant changes in the strength or modulus of the neat PLA, $0.15v_f$, and $0.25v_f$ forged rod specimens were observed with respect to the composite plates.

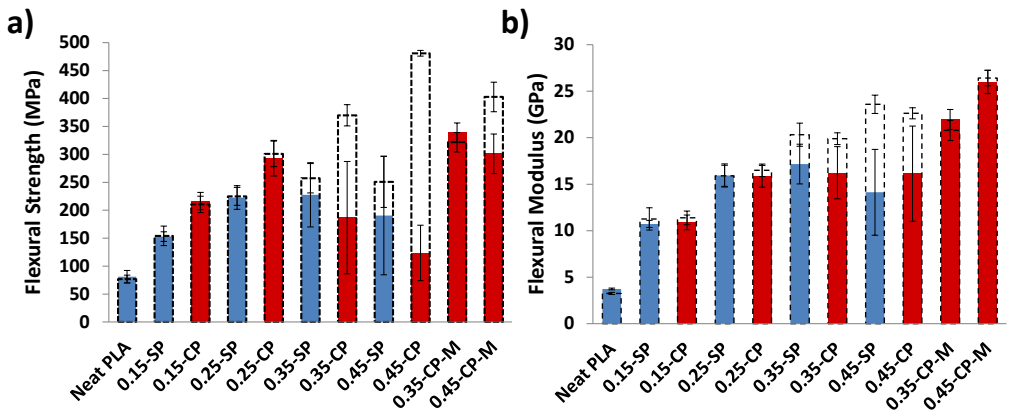


Figure 3.20: Effect of plane strain forging on the flexural (a) strength (±SD) and (b) modulus (±SD) of forged composite rods. The mechanical properties of the initial composite plates are indicated by black dashed lines. The solid columns represent the properties of the plane strain composite forged rods. The mechanical properties of the rods forged from cyclic pressure-consolidated 'CP' composite plates are highlighted in red and those representatives of rods obtained from static pressure-consolidated 'SP' composite plates are highlighted in blue.

Plane strain forged rods fabricated from cyclic pressure-consolidated composite plates remained considerably stronger than those forged from the static pressure-consolidated plates. On the contrary, the mechanical performance of the $0.35v_f$ and $0.45v_f$ was considerably impaired by plane strain forging, regardless of the pressure scheme implemented during plate consolidation.

The extent of the decrease in flexural strength was significantly greater for the composites rods forged from plates consolidated via cyclic pressure, which experienced in average a 50% and 75% reduction with respect to the composite plates for the 0.35-CP and 0.45-CP sample sets, respectively. In contrast, the forged composite rods obtained from static pressure consolidated plates with matching fibre content presented a reduction of 12% and 25% in flexural strength, respectively. The reduction in both flexural strength and modulus was noted to be greater for the rods with 0.45 fibre volume fraction. In spite of the lower decrease in strength for the forged composite rods manufactured from static pressure composite plates, the standard deviation from the average values for the said samples was markedly high (ca. 25% and 55% of the $0.35v_f$ and $0.45v_f$ forged composite rod mean strength, respectively) as shown in Figure 3.20.

3.3.3 Effect of Forging on PGF-PLA Composite Rods Structure

Figure 3.21 summarises the results of comprehensive structural examination of the composite rods forged under plane strain and uniaxial compression deformation conditions. It was noticed that intra-laminar cracks were nucleated preferentially at the middle plane of 0.35 and 0.45 fibre volume fraction composite rods during plane strain forging. Figure 3.21a illustrates the transverse cross section of a $0.35v_f$ plane strain forged composite rod and Figure 3.21b presents the magnified view of the region enclosed by the dotted box in Figure 3.21a. A couple of cracks extending from the parting line region can be clearly seen in Figure 3.21b. No significant differences were observed between samples with the same fibre volume fraction consolidated under different pressure schemes and therefore no distinction has been made in the images in Figure 3.21.

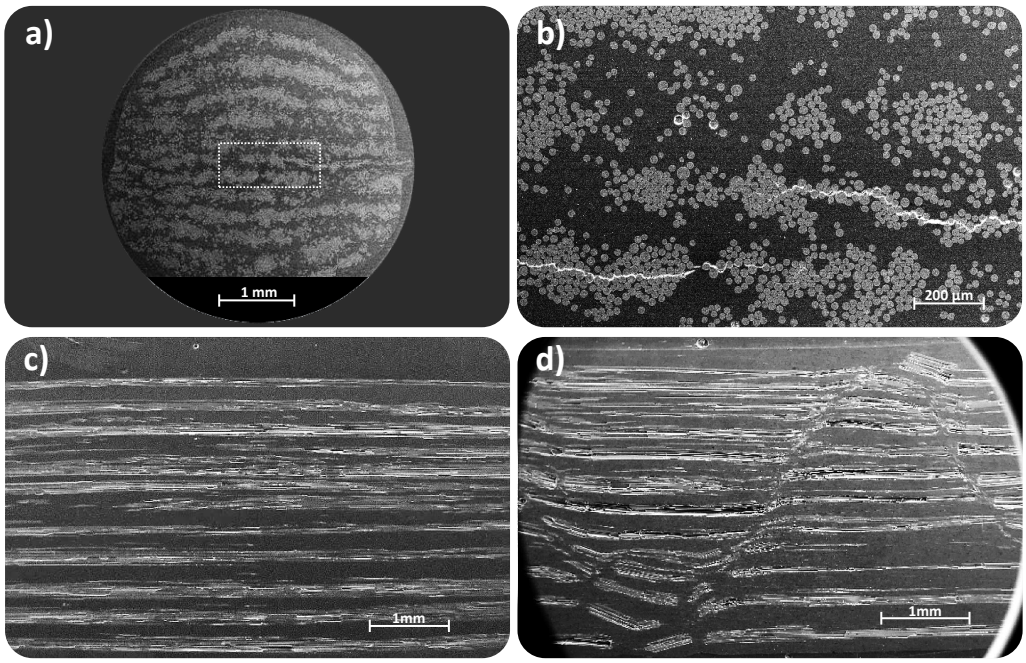


Figure 3.21: Cross sectional SEM images of as-forged 0.35vf composite rods forged via plane strain and uniaxial compression conditions, respectively. (a) Transverse cross section of a 0.35vf composite rod forged under plane strain conditions. (b) Magnified view of the region enclosed by a dotted box is shown in (a). (c) & (d) Longitudinal (*y-z* plane) cross sections of a plane strain and a uniaxial compression forged rod, respectively.

Sections along the longitudinal direction of a $0.35v_f$ plane strain and a uniaxial compression forged rods are presented in Figures 3.21c and 3.21d, respectively. As shown in Figure 3.21c, fibre alignment and fibre integrity were preserved seemingly undisturbed by confining the plastic deformation to the ***x-y*** plane in plane strain forging. Conversely, in uniaxial compression forging,

the fibres were observed to have fractured in a sinusoidal fashion as illustrated in Figure 3.21d.

3.3.4 Effect of Glass Fibre Mat Thickness on the Properties of PGF-PLA Composite Rods Fabricated via Forging

To evaluate the effect of the glass fibre mat thickness on the properties of the forged rods, two additional sets of composite plates (0.35-CP-M and 0.45–CP-M), were manufactured by stacking a greater number of thinner PLA films and glass fibre mats as indicated in Table 2.1, and subsequently forged under plane strain conditions. The transverse cross sections of the composite plates and the corresponding forged composite rods with 0.35 and 0.45 fibre volume fractions fabricated using thin glass fibre mats are shown in Figure 3.22. The composite plates fabricated using thinner mats showed a better reinforcement distribution for both the plate and the forged composite rod in comparison with the specimens obtained using thicker fibre mats (cf. Figure 3.18 and Figure 3.22).

As shown by the respective columns in Figure 3.20a and 3.20b, the flexural strength and modulus of the 0.35-CP-M composite plate were maintained in the plane strain forged rod specimen. No significant changes ($p>0.005$) in the modulus of the 0.45-CP-M plane strain forged rod samples were observed. However, a 25% decrease in flexural strength was observed for the forged composite rods, effectively reducing their strength below the 0.35-CP-M composite plate and rod samples mean value.

This reduction was smaller than that observed for the composite rods forged from thick glass mat composite plates. It should be noted that contrary to the expectation, the composite plates fabricated from thinner glass fibre mats presented a lower flexural strength than those constructed from thick mats and consolidated under the same pressure scheme as demonstrated by Figure 3.20a. The flexural strengths of the 0.45-CP-M and the 0.35-CP-M thin glass fibre mat composite plates were 16% and 13% lower than those of the 0.45-CP and the 0.35-CP thick glass fibre mat composite plates.

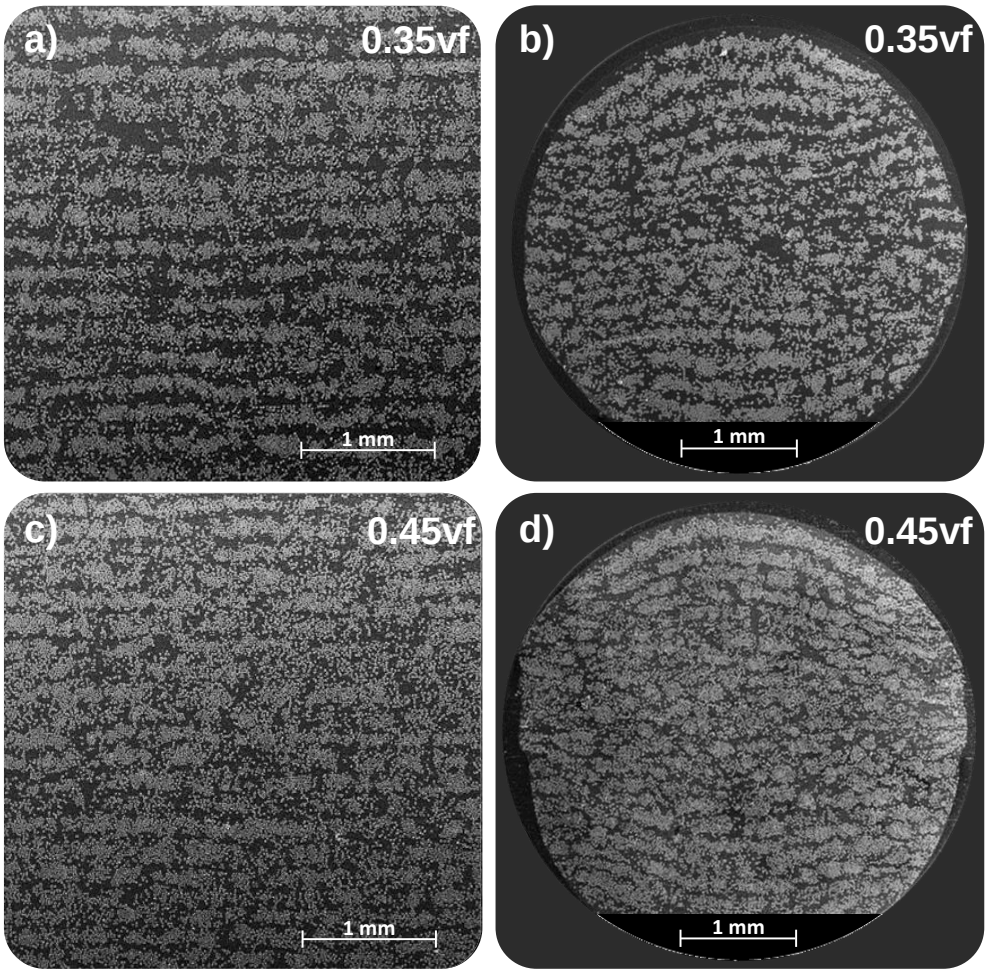


Figure 3.22: Transverse cross sectional images of composite plates and the respective plane strain forged rods fabricated using thin glass fibre mats: (a) & (b) composite plate and rod of the 0.35-CP-M series containing 20 thin glass fibre mats, and (b) & (d) composite plate and rod of the 0.45-CP-M series containing 25 thin glass fibre mats.

No significant differences ($p>0.05$) were observed between the flexural moduli of the 0.35-CP-M composite plate and the plates fabricated from thick glass fibre mats and consolidated through static and cyclic pressure respectively. However, the 0.45-CP-M fibre reinforced composite plate showed a significant increase ($p<0.05$) in excess of 10% with respect to the moduli of the thick mat-composite plates consolidated through static and cyclic pressure, respectively.

3.3.5 In Vitro Degradation of PGF-PLA Composite Rod Fabricated via Forging

3.3.5.1 Effect of Conditioning Time on the Mechanical Properties of PGF-PLA Composite Rods Fabricated via Forging

To discriminate the effect of conditioning in PBS at 37°C in the rod mechanical properties from that of forging induced defects, degradation studies were conducted on plane strain forged composite rod samples whose strength and modulus standard deviation was not greater than 15% of the mean value. In

spite of their narrow distribution of mechanical properties, no degradation studies were conducted on uniaxial compression forged rods since, aside from the $15v_f$ sample set, the mechanical properties of the complementary volume fractions of this series did not exceed the range of values reported for cortical bone, rendering them unsuitable for load bearing applications.

Figure 3.23 demonstrates that exposure to aqueous environment impaired the mechanical performance of the forged composite rods. The extent of the reduction in mechanical properties increased alongside fibre content. After just 1 day of exposure, except for the 0.15-SP specimens, the forged composite samples lost over 50% of their initial flexural strength regardless of the impregnation quality, with a maximum loss of ca. 70% observed for the 0.45-CP-M composites (which became the weakest specimens for the remaining time points). In the case of the neat PLA and the 15-SP specimens, the reduction in flexural strength was, in both cases, ca. 40% after 1 day of immersion in the degradation media.

Following day 1, the strength values of the neat-PLA forged rod plateaued at ca. 45 MPa for the remainder of the study. In the case of the forged composite rods, the loss in flexural strength continued for the $0.15v_f$ and $0.25v_f$ samples, finally matching the neat-PLA forged rod strength values by day 15, remaining unchanged throughout the rest of the study. On the other hand, the 0.35-CP-M and the 0.45-CP-M composite rod specimens lost the fibre reinforcing effect by day 7, and stabilised close to neat-PLA forged rod strength values for the remaining time points.

The flexural modulus was also deleteriously affected by immersion in aqueous medium. The decrease in modulus at day 1 was considerably lower than the reduction in flexural strength. The 0.45-CP-M samples experienced the greatest decrease with a ca. 40% of the initial modulus value. In the other cases, including the forged neat-PLA rod specimens, the forged composite rods showed a decrease of ca. 20% of the initial values regardless of the consolidation pressure scheme implemented.

Following a short period of stabilisation (between days 1 and 3), the modulus of the forged composite rods decreased gradually up to day 15 at values slightly higher than those of the forged neat-PLA rod.

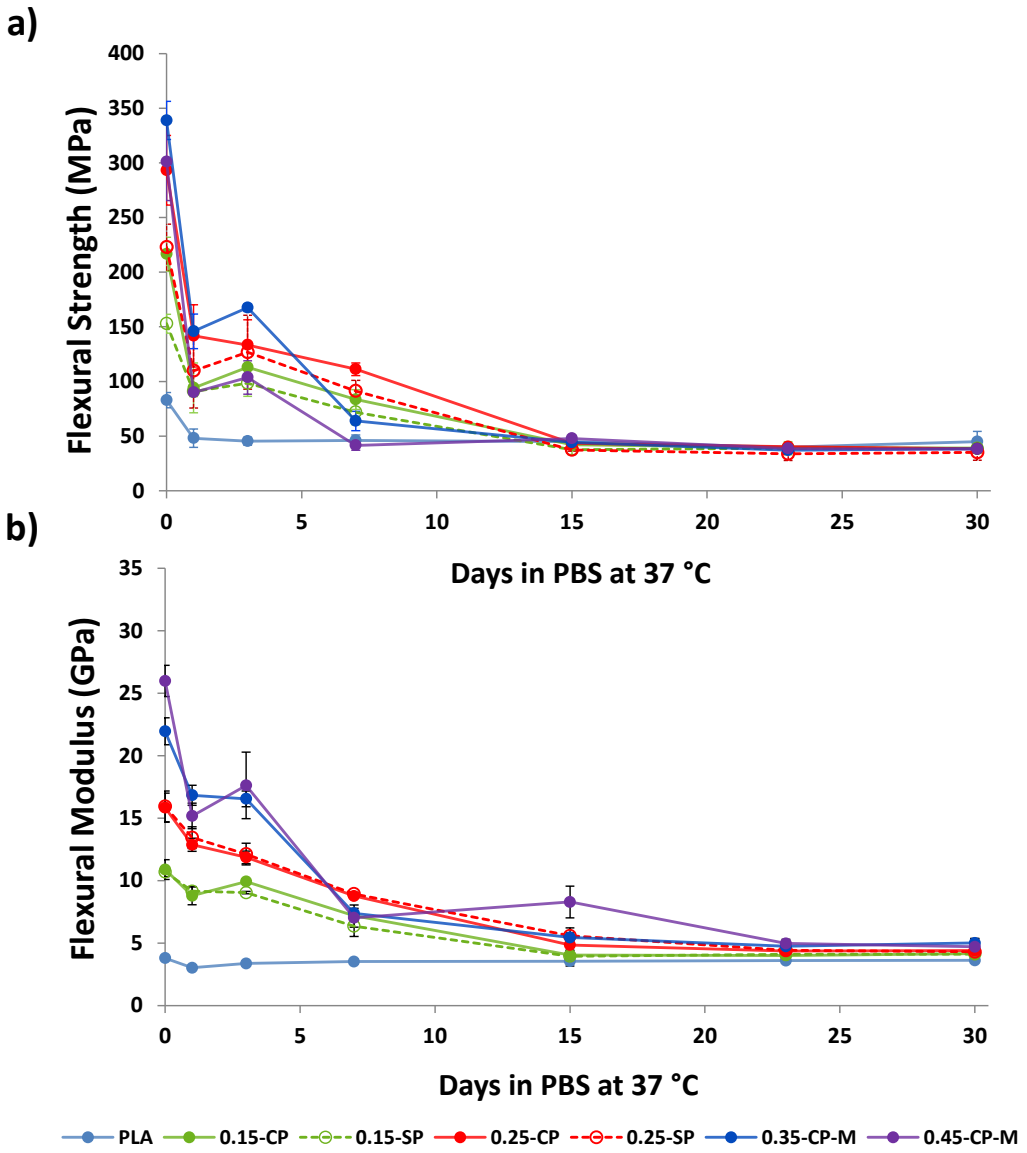


Figure 3.23: Variation of flexural properties of PGF-PLA forged composite rods and neat-PLA control rods during conditioning in PBS at 37°C: (a) Flexural strength (±SD) and (b) flexural modulus (±SD) degradation profiles. The profiles of the forged composite rods obtained from plates consolidated under cyclic pressure (CP) were denoted by solid lines, whereas the profiles of the forged composite rods obtained from plates consolidated under static pressure (SP) were denoted by dashed lines.

3.3.5.2 Effect of Conditioning Time on Reinforcing Fibre Structure in PGF-PLA Composite Rods Fabricated via Forging

Figure 3.24 shows representative SEM images of the fracture surface of a forged neat-PLA rod prior immersion and magnified views of selected samples of the 0.35-CP-M series at different time points during PBS conditioning at 37°C. The individual layers that constitute the neat-PLA rod can be clearly distinguished in Figure 3.24a.

Figure 3.24b shows that the non-degraded 0.35-CP-M forged composite rod sample experienced extensive fibre pull out. The fibres presented a clean surface and without any matrix debris attached. No differences in the appearance of the fibres were observed at day 3 (Figure 3.24d). The fibres still exhibited a clean surface without any signs of interaction with the conditioning medium. By day 7 (Figure 3.24e), most of the fibres had developed into a core-shell structure. Multiple shells could be observed from day 15 (Figure 3.24f). These shells remained seemingly unaffected by the interaction with the conditioning medium up to day 30 as seen in Figure 3.24h, however, the diameter of the fibre cores was observed to have decreased with conditioning time as illustrated by Figures 3.24e and 3.24f, until their full dissolution throughout most of the forged composite rod cross section by day 30.

3.3.5.3 Effect of Conditioning Time on Reinforcing Fibre Composition in PGF-PLA Composite Rods Fabricated via Forging

The results from the compositional EDX analysis conducted on the core-shell structures observed in the cross section of $0.35v_f$ composite forged rods prior and after immersion in PBS are summarised in Table 3.9. The time points at which samples were recovered from the conditioning media are indicated by the characters after the dash in Table 3.9 (e.g. D7 stands for day 7).

The chemical composition of the fibre cores was observed to remain constant (within experimental error) at the composition of the non-degraded glass fibres (labelled as Fibre-D0) throughout the entire degradation study until their total dissolution and therefore only the latter is listed in Table 3.9. The theoretical composition of the P45Fe2 glass fibres is also shown for comparison purposes.

Table 3.9: Summary of reinforcing P45Fe2 glass fibres EDX analysis (±SD) at different conditioning time points.

Sample Code	Na/P	Mg/P	K/P	Ca/P	Fe/P	O/P
P45Fe2	0.289	0.267	-	0.178	0.044	3.156
Fibre-D0	0.284±0.002	0.279±0.002	-	0.1749+0.0002	0.041±0.001	3.157±0.002
Shell-D7	0.219±0.015	0.288±0.006	0.006±0.004	0.244±0.006	0.078±0.001	3.261±0.008
Shell-D15	0.150±0.004	0.301±0.002	0.018±0.002	0.323±0.012	0.080±0.015	3.328±0.026
Shell-D23	0.137±0.011	0.302±0.001	0.020±0.004	0.331±0.006	0.105±0.004	3.369±0.004
Shell-D30	0.140±0.011	0.316±0.006	0.022±0.002	0.338±0.001	0.106±0.001	3.393±0.007

From examination of Table 3.9 it can be observed that the relative content of Na in the shells first observed at day 7 decreased with respect to the fibre

cores and the non-degraded glass fibres. Furthermore, the Na content in the shells progressively diminished to less than 50% of the sodium originally present in the glass fibres by day 30. On the contrary, the relative contents of Mg, Ca, and Fe in the shells progressively increased with conditioning time, reaching concentrations 13%, 80% and 140% higher than the respective elements in the fibre cores.

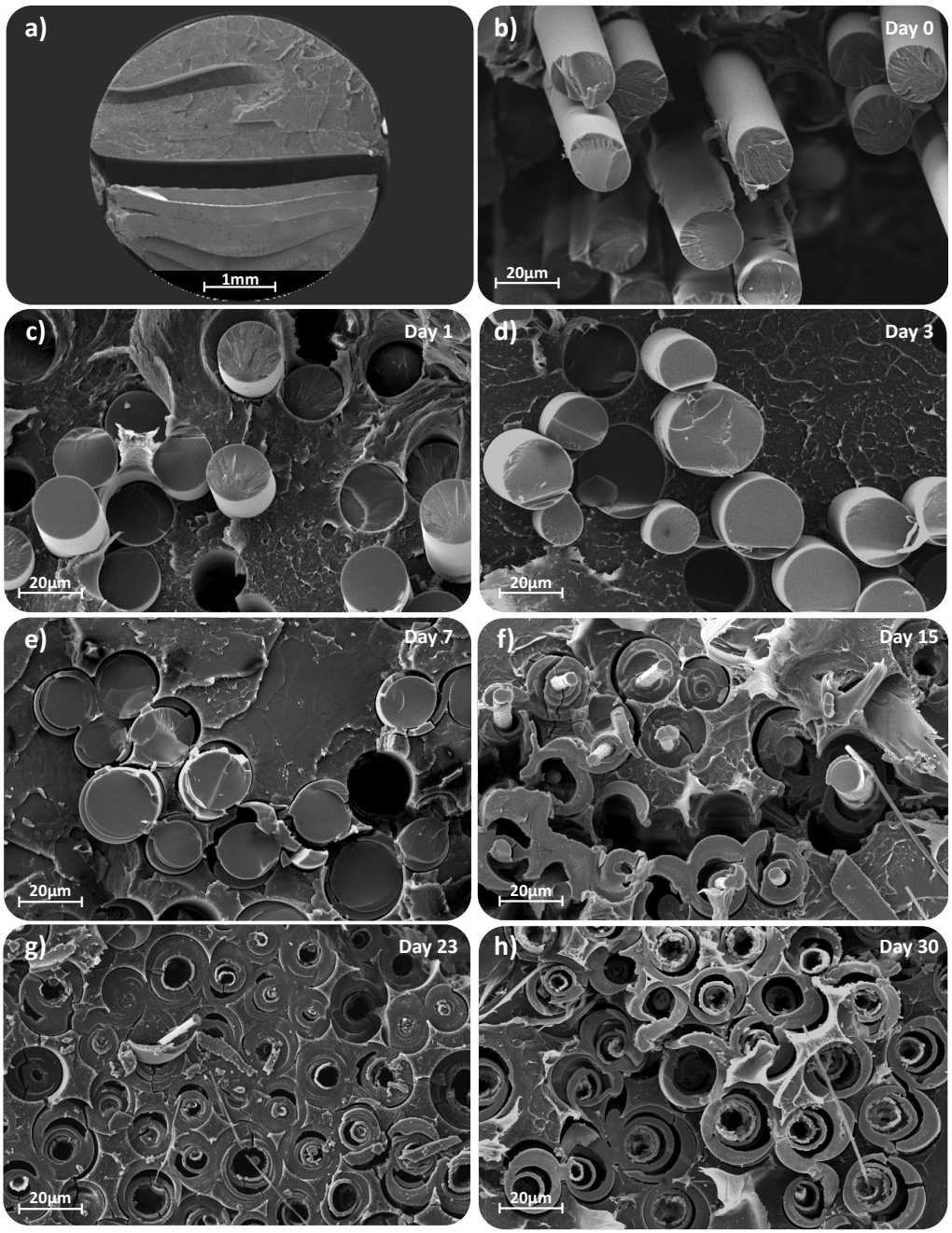


Figure 3.24: SEM images of the fracture surfaces of a representative neat-PLA rod prior immersion and a 0.35-CP-M forged composite rods at different PBS conditioning time points in PBS at 37°C. (a) Macroscopic view of a fractured non-degraded neat-PLA rod. Magnified fracture surfaces of conditioned samples at (b) day 0, (c) day 1, (d) day 3, (e) day 7, (f) day 15, (g) day 23 and (h) day 30, respectively.

In addition, a trace amount of potassium was detected in the shells whose relative concentration increased with conditioning time. Finally, the oxygen to phosphorous ratio also increased from 3.16 to 3.39 with conditioning time.

3.3.5.4 Effect of Conditioning Time on the Mass of PGF-PLA Composite Rods Fabricated via Forging

Figure 3.25 shows the mass changes experienced by the forged composite rod samples as a result of conditioning at 37°C in PBS. The PLA reached its moisture saturation content of ca. 0.8% by day 1, staying relatively constant for the remainder of the degradation study. The amount of water absorbed by the composite samples increased with both fibre content and conditioning time, reaching a maximum water uptake of 27% at day 30. The 0.45-CP-M forged composite sample exhibited the highest water uptake at each time point. No significant differences arising from the consolidation pressure were observed between the water uptake profiles for the $0.25v_f$ and $15v_f$ forged composite rod series.

For all fibre volume fractions, the rate of water absorption (indicated by the slope of the curve) was greater between day 3 and day 15, after which the moisture content appeared to equilibrate in the $0.15v_f$ and $0.25v_f$ cases, whereas for the $0.35v_f$ and $0.45v_f$ forged composite specimens, water uptake continued.

Figure 3.25b illustrates the mass loss profiles of the forged composites and neat-PLA control samples calculated after vacuum drying as described in §2.16. The mass of the neat-PLA forged rods did not vary throughout the degradation study. Conversely, the dry mass of the forged composite rods did vary throughout the degradation study. The changes in dry mass increased with fibre volume fraction and conditioning time. The 0.45-CP-M forged composite rods presented the highest mass losses at each time point reaching a maximum dry mass loss of 30% at day 30. Similarly to the water uptake experiments, the consolidation method did not seem to retard dissolution of the glass fibres as demonstrated by the similar dry mass loss values at each degradation time point associated with both CP and SP samples in the $0.15v_f$ and $0.25v_f$ series, respectively. In these samples, the highest rates of mass loss were observed within the period spanning from day 7 to day 15 (which presented a good correlation with the fibre morphology changes as stated previously) after which the mass loss rate decreased considerably, which

coincided with the start of the water uptake equilibrium. For the 0.35-CP-M and 0.45-CP-M, the highest mass loss rates were observed between day 3 and day 15. Following this stage, the slope of the respective curves appeared to decrease slightly.

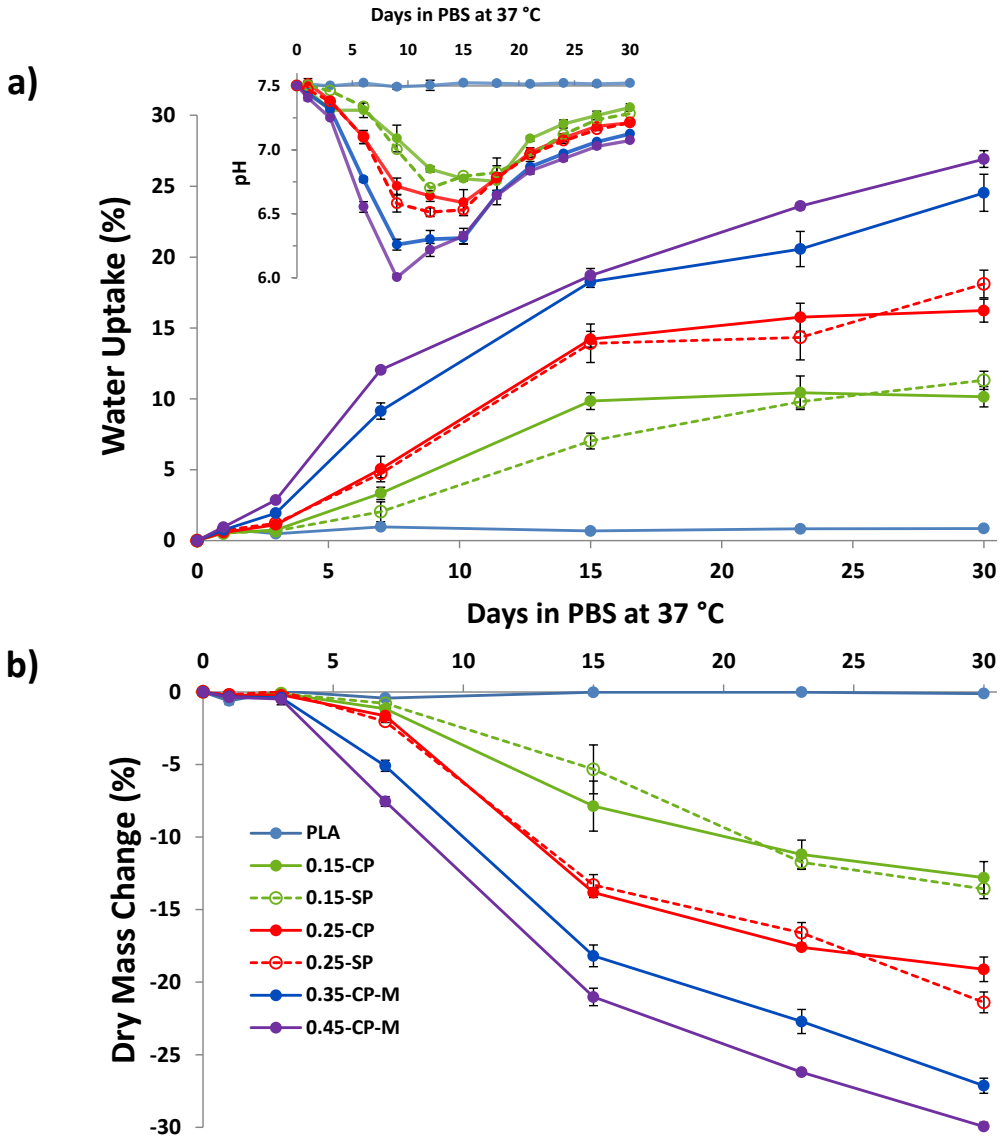


Figure 3.25: (a) Water uptake (±SD) and (b) dry mass change profiles (±SD) for PGF-PLA plane strain forged composite rods and neat PLA control rods conditioned in PBS at 37°C. The inset of (a) shows the variation of pH (±SD) for the studied samples. The profiles of the forged composite rods obtained from plates consolidated under cyclic pressure (CP) are denoted by solid lines, whereas the profiles of the composite rods obtained from plates consolidated under static pressure (SP) are denoted by dashed lines.

3.3.5.5 Effect of Conditioning Time on the Conditioning Media pH of PGF-PLA Composite Rods Fabricated via Forging

Similar trends were observed in the pH readings as illustrated by the inset in Figure 3.25a. Within experimental error, the pH of the medium collected from

vials containing forged neat-PLA rods, did not vary throughout the study. On the other hand, a decrease of the initial pH of the PBS solution in direct proportion to the fibre volume fraction was observed in the forged composite rod samples. The negative tendency for the pH readings in the composites samples continued up to day 15, after which the pH started to increase towards neutral.

3.3.6 Thermal Analysis of PGF-PLA Composite Rods Fabricated via Forging

The thermal properties obtained from the first heating cycle, namely: i) glass transition temperature T_g (the subscripts 1 and 2 were used to differentiate between the respective heating cycles), ii) onset of cold crystallisation T_{X0}, iii) cold crystallisation peak temperature T_{x1}, iv) melting temperature T_m and crystallinity content X_c, of selected compression moulded composite plates and the respective non-degraded plane strain forged rods are shown in Table 3.10. Thermal properties of the compression moulded plates were denoted by 'P' at the end of the sample code, whereas the corresponding forged composite rods where denoted by 'R', respectively. The glass transition temperature of the second heating cycle T_{g2} was also included to rule out the effect of aging on T_{g1}.

Table 3.10: Thermal properties (±SD) of compression moulded composite plates 'P' and non-degraded plane strain composite forged rods 'R'.

Sample Code	T_{g1} (°C)	T_{g2} (°C)	T_{X0} (°C)	T_{X1} (°C)	T_m (°C)	X (%)
PLA-P	56.2±0.1	58±0.1	91±2.4	114±1.6	171±0.3	3.0±0.3
PLA-R	60±0.2	57±0.5	90±0.5	102±0.4	171±0.8	8.1±1.7
0.15-CP-P	63±2.3	58±0.1	92±0.7	109±0.2	171±0.3	3.9±2.6
0.15-CP-R	60±0.3	57±0.1	83±0.5	97±0.3	171±0.2	20.2±2.5
0.15-SP-P	60±1.0	58±0.4	91±1.3	104±0.4	171±0.4	5.7±0.9
0.15-SP-R	60±0.1	56±0.4	84±1.9	96±2.0	171±0.3	23.8±8.3
0.25-CP-P	60±1.0	59±0.3	97±1.1	109±0.8	171±0.6	5.4±0.7
0.25-CP-R	62±0.1	57±0.1	87±0.5	99±0.8	171±0.4	11.7±1.0
0.25-SP-P	60±1.2	58±2.6	89±2.6	102±0.8	170±0.5	7.0±1.9
0.25-SP-R	61±1.1	57±0.2	84±0.2	96±0.6	170±0.1	23.2±3.0
0.35-CP-M-P	56±0.1	58±0.4	90±0.5	106±0.2	170±0.1	4.4±0.1
0.35-CP-M-R	63±0.7	57±0.3	83±0.3	95±1.0	170±0.4	26.2±1.2
0.45-CP-M-P	58±2.3	59±0.2	88±0.7	104±1.0	170±0.2	4.9±0.5
0.45-CP-M-R	61±2.1	58±0.3	83±0.3	95±0.7	170±0.3	28.0±3.3

The cold crystallisation peak temperature of the PLA in the composite plates shifted towards lower values in proportion to the fibre volume fraction upon fibre addition. It was noted that for samples with the same fibre content (i.e. $0.15v_f$ and $0.25v_f$), the T_{x1} was considerably lower for the samples with consolidated under static pressure. In the case of the forged rods, the highest T_{x1} value (ca. 102°C) was associated with the control PLA rod and presented similar values for all the composites regardless of the fibre content and consolidation method. In a similar way, the onset of cold crystallisation T_{x0} was lower for the forged rods when compared to the composite plates and it seemed to decrease in proportion with the fibre volume fraction. No clear trend was observed for the T_g.

As a result of the samples being heated to the 90-100°C prior to forging, the crystallinity of the forged composite rods increased considerably in comparison to the initial composite plates. The crystallinity content was greater for the forged composite rods than for the forged neat PLA sample and, with the exception of the 0.25-CP samples, it appeared to increase in proportion to fibre volume fraction, reaching a maximum initial crystalline content of 28% as seen for the 0.45-CP-M series.

3.3.6.1 Effect of Conditioning Time on the Crystallinity of PGF-PLA Composite Rods Fabricated via Forging

Figure 3.26a illustrates the variation of the crystallinity against time for the forged composite rods and control forged neat-PLA samples conditioned in PBS at 37°C. For all the samples, the crystallinity progressively increased in with conditioning time. The increase in crystallinity was in average 64% greater for the forged composites rods sample relative to the control forged neat-PLA. The maximum crystallinity content at day 30 was observed for the 0.45-CP-M, reaching ca. 37.5%. In contrast, the corresponding crystallinity value for the control PLA was ca. 20%.

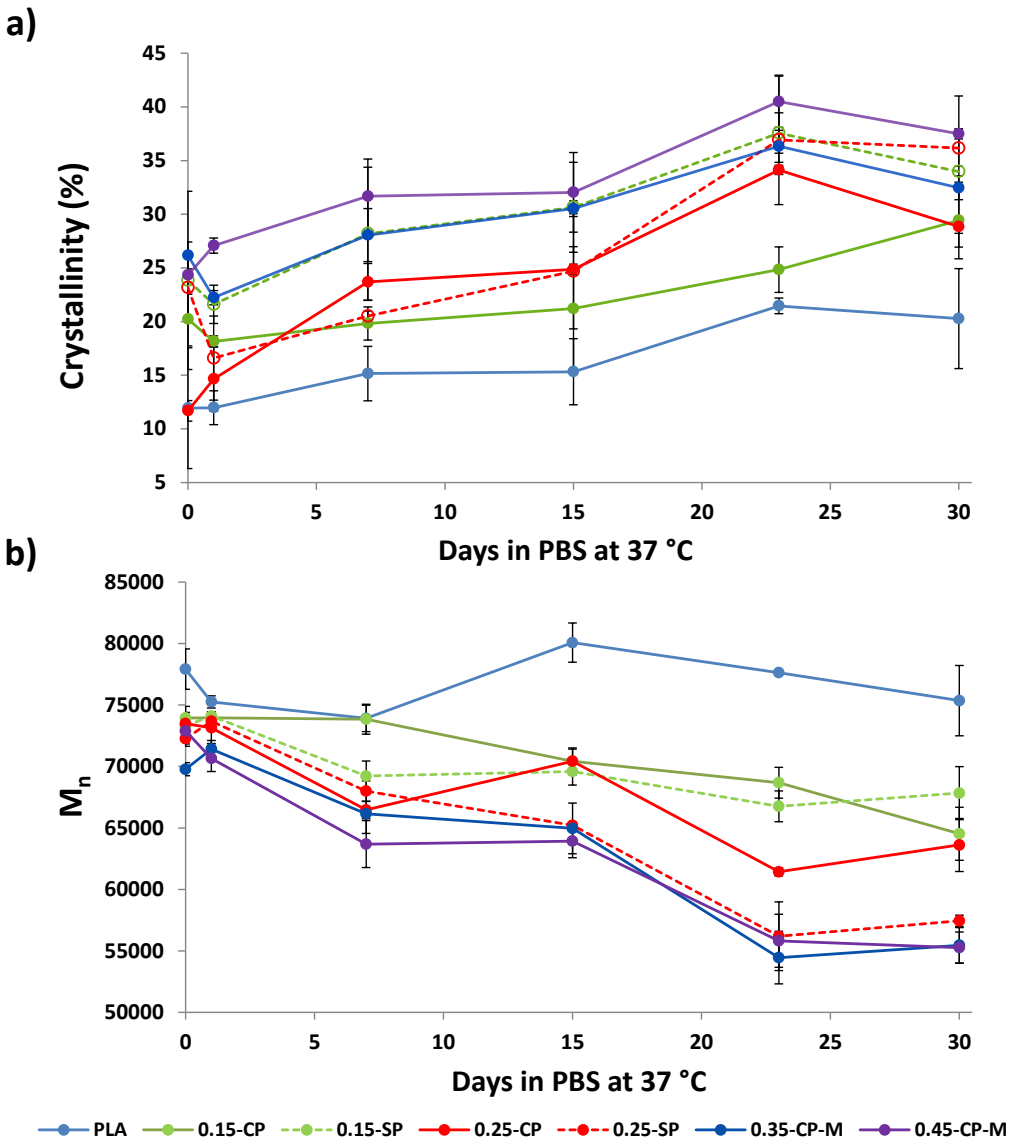


Figure 3.26: a) Evolution of the crystallinity content (±SD) for the PLA matrix in the PGF-PLA forged composite rods conditioned in PBS at 37°C and (b) variation of number average molecular weight, M_n, (±SD) of the PLA matrix in the composite rods with increasing conditioning time in PBS at 37°C. The profiles of the composite rods obtained from plates consolidated under cyclic pressure (CP) were denoted by solid lines, whereas the profiles of the composite rods obtained from plates consolidated under static pressure (SP) were denoted by dashed lines.

3.3.7 GPC Analysis of PGF-PLA Composite Rods Fabricated via Forging

Figure 3.26b shows the evolution of number average molecular weight against degradation time for the samples studied. With the exception of the neat-PLA sample, whose number average molecular weight appeared to remain constant within experimental error throughout the entire study, a gradual decrease in M_n was observed for all the samples conditioned in PBS at 37°C. For all the forged composite rods, the initial number average molecular weight

was lower in respect of to the neat-PLA control. The maximum decrease in M_n was observed for the 0.35-CP-M and the 0.45-CP-M, whose molecular weight reduced to ca. 81% and 77% of their day 0 values, respectively. This decrease in average number molecular correlated well with the water uptake and the decrease in pH of the conditioning medium collected from the composite samples.

3.4 Manufacture of Fully Bioresorbable Composite Rods via Compression Moulding of Polymer Sheathed Fibre Bundles

3.4.1 Production of Bare PLA-sheath via Crosshead Extrusion

Table 3.11 summarises the results of bare PLA-sheath production at 165°C using three different screw speeds separated by 10 rpm increments. The extrusion line was driven by a haul-off unit operated at increasing speeds. Extrudate was collected at increasing haul-off speed until melt fracture was observed.

Figure 3.27a shows the volumetric feeder output in $g \cdot min^{-1}$ as determined by a five minutes collection of PLA pellets at seven different speed sets. The feeder output was noticed to be directly proportional to the feeder speed set.

From Table 3.11, it can be observed that the pressure at the crosshead die entry at 165°C increased in proportion to both feeder input and screw speed. The pressure scaled from ca. 21 bar at 10 rpm with a feeder output of 5.7 $g \cdot min^{-1}$ up to 59 bar at 30 rpm and 10.4 $g \cdot min^{-1}$. Apart from the 10 rpm case, where polymer accumulation was observed at the extruder gas vent, the extrudate mass flow ($g \cdot min^{-1}$) was in good agreement with the feeder output ($g \cdot min^{-1}$). The extrudate mass flow was independent of the haul-off speed.

Table 3.11: Summary of bare PLA-sheath production at 165°C.

Screw Speed (RPM)	Feeder Output ($g \cdot min^{-1}$)	Die Pressure (bar)	Haul-Off Speed ($m \cdot min^{-1}$)	Extrudate Mass Flow ($g \cdot min^{-1}$)
10	5.7	20.5±0.7	5	3.90±0.21
			10	3.79±0.03
20	5.7	30±1.4	5	5.02±0.07
			10	5.80±0.67
	6.6	32.5±0.7	5	6.91±0.18
			10	6.92±0.03
			20	6.88±0.03
			30	6.82±0.04
	7.6	34.5±0.7	5	7.78±0.07
			10	7.76±0.06
			20	7.80±0.05
			30	7.90±0.09
30	5.7	41.5±2.1	5	4.77±0.11
			10	5.14±0.13
			15	5.30±0.09
			20	5.11±0.09
	6.6	44.5±0.7	5	6.68±0.04
			8	6.66±0.05
			9	6.73±0.04
			10	6.65±0.04
			15	6.45±0.10
			20	6.43±0.13
			30	6.91±0.07
	7.6	46.5±0.7	5	7.37±0.26
			10	7.47±0.05
			20	7.22±0.04
	10.4	59.0±1.4	5	10.40±0.21
			10	10.50±0.08
			20	10.32±0.07
			30	10.42±0.29

Apart from the pressure measured at the crosshead die entry, which was noticed to decrease in a linear fashion as the extrusion temperature was increased (cf. Figure 3.27b), similar extrudate mass flows were obtained at 170°C, 180°C and 190°C, and therefore, are not presented here.

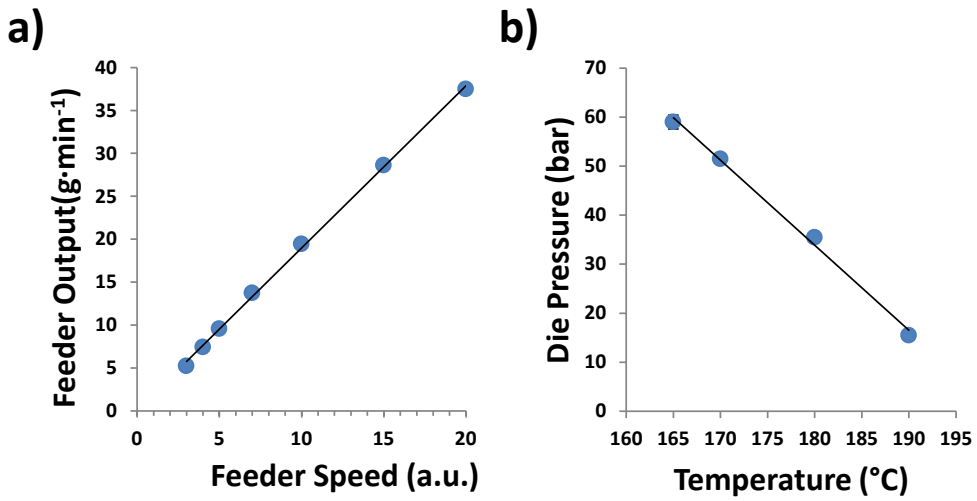


Figure 3.27: (a) Variation of feeder output (±SD) with feeder speed. (b) Influence of extrusion temperature on the pressure (±SD) measured at the crosshead die entry.

PLA-sheaths produced at 165°C using a screw speed of 30 rpm with a feeder output of ca. 6.6 grams and different haul-off speeds were chopped into 80 mm segments. The variation of 80 mm PLA-sheath segments mass with haul-off speed is shown in Figure 3.28. It can be observed that the 80 mm segment mass followed a trend best described by a 1/x behaviour.

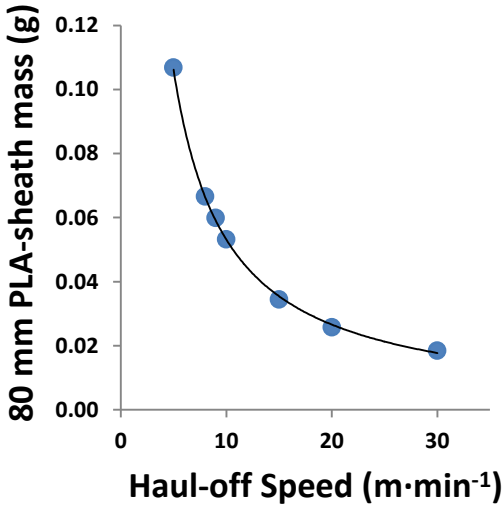


Figure 3.28: Variation of PLA-sheath mass per 80 mm produced with increasing haul-off speed. The PLA-sheath was extruded at 165°C using a screw speed of 30 rpm and a feeder output of 6.6 g.

The best-fitting line equation was used to determine the haul-off speed at which continuous fibre bundles of different linear densities, m_B, should be pulled through the crosshead die to achieve a specific PLA-sheath linear density, m_s, as required by the intended fibre volume fraction of the PLA-sheathed fibre bundles. The parameters used in the production of the different PLA-sheathed fibre bundles used in this study were summarised in Table 2.2 in §2.13.2.

3.4.2 SEM Cross Sectional Imaging of PGF-PLA Composite Rods Fabricated via PLA-sheathed Fibre Bundle Compression Moulding

Figure 3.29 shows the backscattered electron images of the transverse polished cross section of representative bioresorbable composite rods with 0.15, 0.25, 0.35 and 0.45 fibre volume fractions manufactured via compression moulding of PLA-sheathed fibre bundles (also referred to as compression moulded composite rods elsewhere in this document). No differences other that the rougher appearance of the annealed fibres were noted, and therefore no distinction has been made in terms of fibre type.

It can be clearly observed that the fibres are segregated in regions corresponding to the constituent PLA-sheathed fibre bundles. Magnified images of selected regions were enclosed by dashed lines and displayed at the right of the respective composite rods. It can be observed that the PLA matrix (deposited as an outer coating during fibre bundle sheathing) managed to fully percolate through the compact fibre network in all the cases despite increasingly the larger bundle used for the 0.35 and the 0.45 fibre volume fraction composite rods as stated in Table 2.2. Irregularly shaped voids could be observed in the polymer-rich zones located between the fibre bundles of the $0.35v_f$ and $0.45v_f$ compression moulded composite rods shown in Figure 3.29c and Figure 3.29d, respectively.

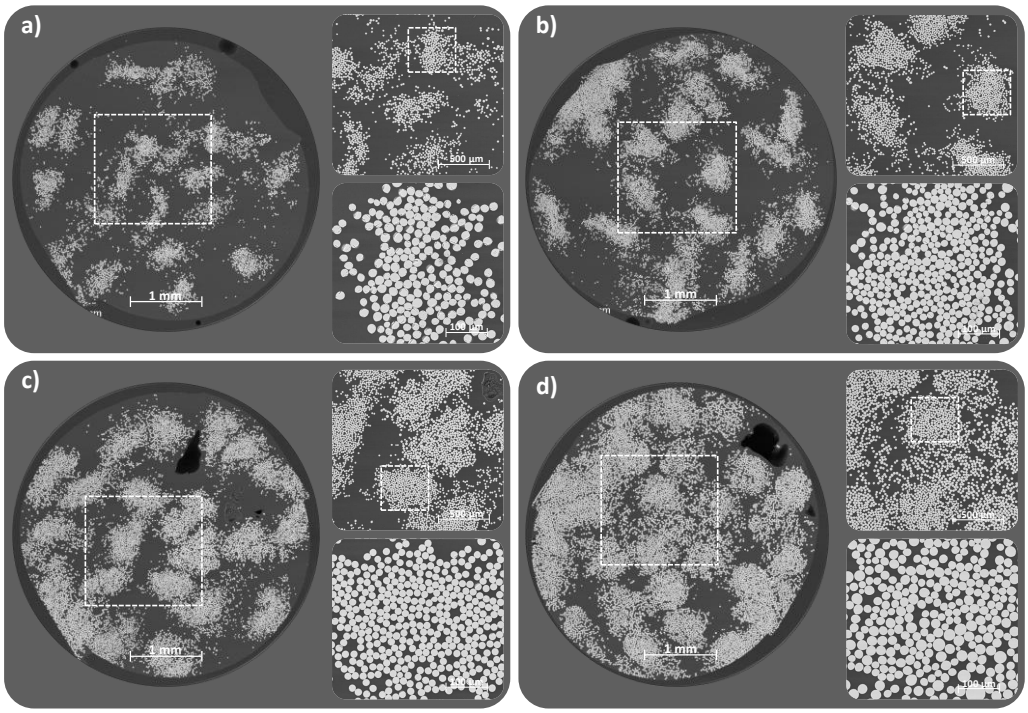


Figure 3.29: Backscattered electron images of the transverse cross section of representative PGF-PLA composite rods with (a) 0.15, (b) 0.25, (c) 0.35 and (d) 0.45 fibre volume fractions fabricated through the consolidation of PLA-sheathed glass fibre bundles. Magnifications of selected regions enclosed by white dashed lines are also shown at the right of the respective rods.

3.4.3 Void Content Analysis of PGF-PLA Composite Rods Fabricated via PLA-sheathed Fibre Bundle Compression Moulding

The results of the composite void content analysis conducted as detailed in §2.15 in fibre reinforced composite rods fabricated via compression moulding of PLA-sheathed fibre bundles are outlined in Table 3.12. It can be seen that the theoretical maximum content of voids created from uneven contraction decreases with fibre volume fraction. However, no clear tendencies could be observed in the experimentally determined void contents. The void contents seemed to be independent of the fibre volume fraction and the fibre type. In average, the highest void content was calculated for the 0.15 fibre volume fraction samples. As shown in Table 3.12 within experimental error, the experimental volume fraction approximated reasonably the intended fibre volume fraction.

Table 3.12: Summary of experimental volume fraction and void content analysis (±SD) for fibre reinforced composite rods fabricated via compression moulding of PLA-sheathed glass fibre bundles.

v_f Nominal	Fibre Type	v_f Experimental	ϕ_v (%)	ϕ_t (%)
0.15	A	0.150±0.003	5.04±2.16	8.45
	NA	0.170±0.010	5.70±1.25	
0.25	A	0.245±0.005	1.04±1.27	6.80
	NA	0.234±0.014	3.63±0.35	
0.35	A	0.333±0.006	4.59±0.70	5.42
	NA	0.351±0.014	5.19±1.16	
0.45	A	0.414±0.024	1.96±0.43	4.25
	NA	0.430±0.003	2.89±1.24	

3.4.4 Flexural Properties of PGF-PLA Composite Rods Fabricated via PLA-sheathed Fibre Bundle Compression Moulding

Figure 6 shows the variation of flexural properties with fibre volume fraction of the PGF-PLA composite rods manufactured through compression moulding of PLA-sheathed bundles of annealed and as-drawn fibres.

From Figure 6b it can be seen that the mean modulus values of the composites reinforced with annealed fibres were higher than those attained with as-drawn fibre reinforcement. However only in the 0.15 and 0.25 fibre volume fraction cases the difference was statistically significant ($p < 0.05$). For both fibre types, the composite rod modulus was directly proportional to the fibre volume fraction, and in all cases the composite moduli fell within or even surpassed the human cortical bone modulus range, reaching values in excess of 30 GPa for the 0.45 fibre volume fractions.

In similitude to the flexural modulus, the flexural strength of the PGF-PLA compression moulded composite rods comprising either annealed or as-drawn fibres was directly proportional to the fibre volume fraction. Aside from the 0.45 fibre volume fraction samples, whose strength values were superior, the flexural strengths of the annealed fibre reinforced composites were within the range of human cortical bone. In contrast, for all but the 0.15 as-drawn fibre volume fraction specimens, the strengths of the composites containing as-drawn fibres exceeded the range of human cortical bone properties.

Excepting the 0.15 fibre volume fraction, the flexural strengths of compression moulded composite rods reinforced with as-drawn fibres were in average 36% greater with respect to the composite rods containing annealed fibres, reaching ca. 371 MPa for the $0.45v_f$ compression moulded composite rods reinforced with as-drawn fibres, in comparison to 278 MPa for the samples with the corresponding annealed fibre volume fraction.

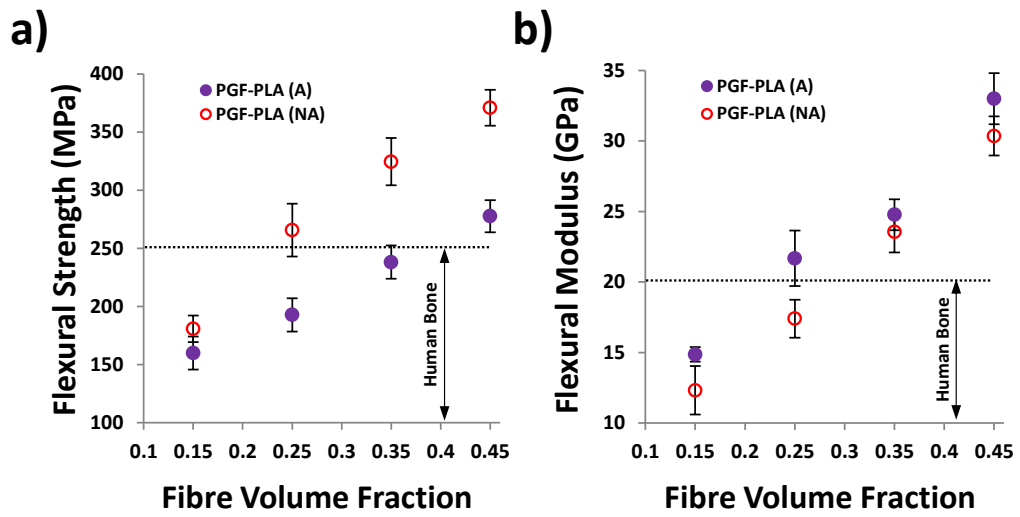


Figure 3.30: Influence of fibre volume fraction on the (a) flexural strength (±SD) and (b) flexural modulus (±SD) of PGF-PLA composite rods manufactured through compression moulding of PLA-sheathed bundles of either annealed or as-drawn glass fibres. The ranges of human cortical bone flexural properties were denoted by the black dotted lines.

3.4.5 *In Vitro* Degradation of PGF-PLA Composite Rod Fabricated via PLA-sheathed Fibre Bundle Compression Moulding

3.4.5.1 Effect of Conditioning Time on the Mechanical Properties of PGF-PLA Composite Rods Fabricated via PLA-sheathed Fibre Bundle Compression Moulding

Figure 3.31 shows the flexural mechanical properties degradation profiles for bioresorbable PGF-PLA composite rods manufactured via compression moulding of PLA-sheathed annealed and as-drawn fibre bundles during conditioning in PBS at 37°C. From figure 3.31a it can be observed that immersion in PBS impaired the mechanical performance of all the compression moulded composite rods with respect to the initial flexural properties, regardless of the fibre type. After 1 day of immersion, except for the $0.15v_f$ samples (which presented a ca. 30% decrease in flexural strength), the PGF-PLA composite rods comprising bundles of as-drawn fibres lost approximately 50% of their initial flexural strength.

After a short stabilisation period between day 1 and day 3, the flexural strength of the as-drawn fibre reinforced PLA compression moulded composite rods continued to decrease, reaching values inferior to the lower limit of cortical bone strength by day 15. For the second half of the study, the strength further decreased to values in the order of 10% of the initial flexural strength prior conditioning for the 0.25, 0.35 and 0.45 fibre volume fraction samples. In the case of the $0.15v_f$ samples, the day 30 strength value represented approximately 20% of the day 0 flexural strength.

The flexural strength of the PGF-PLA compression moulded composite rods reinforced with annealed fibre bundles also presented an immediate decrease after 1 day of immersion. The extent of the reduction in strength was lower in comparison to the as-drawn fibre reinforced composite rods, with a maximum reduction of 40% for the $0.45v_f$ samples. The flexural strength of the 0.15, 0.25 and 0.35 fibre volume fraction samples was reduced by 35%, 18% and 32% of the day 0 strength value. The flexural strength of the annealed fibre reinforced composite rods further decreased with conditioning time, although with a slower rate when compared to the as-drawn fibre reinforced composite rods, such that their flexural strengths neighboured the lower limit of the cortical bone for the 0.25, 0.35 and 0.45 fibre volume fractions up to day 30. The flexural strength of the $0.15v_f$ specimens reinforced with annealed fibres, decreased to values lower than the cortical bone lower flexural strength limit by day 15 and stabilised in this region for the remainder of the in vitro degradation study.

Excepting the $0.15v_f$ specimens, the variation of flexural modulus for as-drawn fibre reinforced compression moulded composite rods corresponded well to the flexural strength trend as shown by Figure 3.31b. The modulus for the 0.25, 0.35 and 0.45 fibre volume fraction samples immediately decreased to 83%, 72% and 65% of the initial modulus value, respectively, after one day of immersion and stabilised at this point for up to day 3. Subsequently, the modulus progressively decreased to values in the order of 20% of the initial modulus values, which were well below the cortical bone lower modulus limit.

The $0.15v_f$ samples presented only a slight reduction to 97% of the day 0 modulus value after one day of immersion. Further decreases in modulus for the $0.15v_f$ samples occurred at a slower rate in comparison to other as-drawn fibre reinforced composites, finally stabilising at ca. 3.5 GPa.

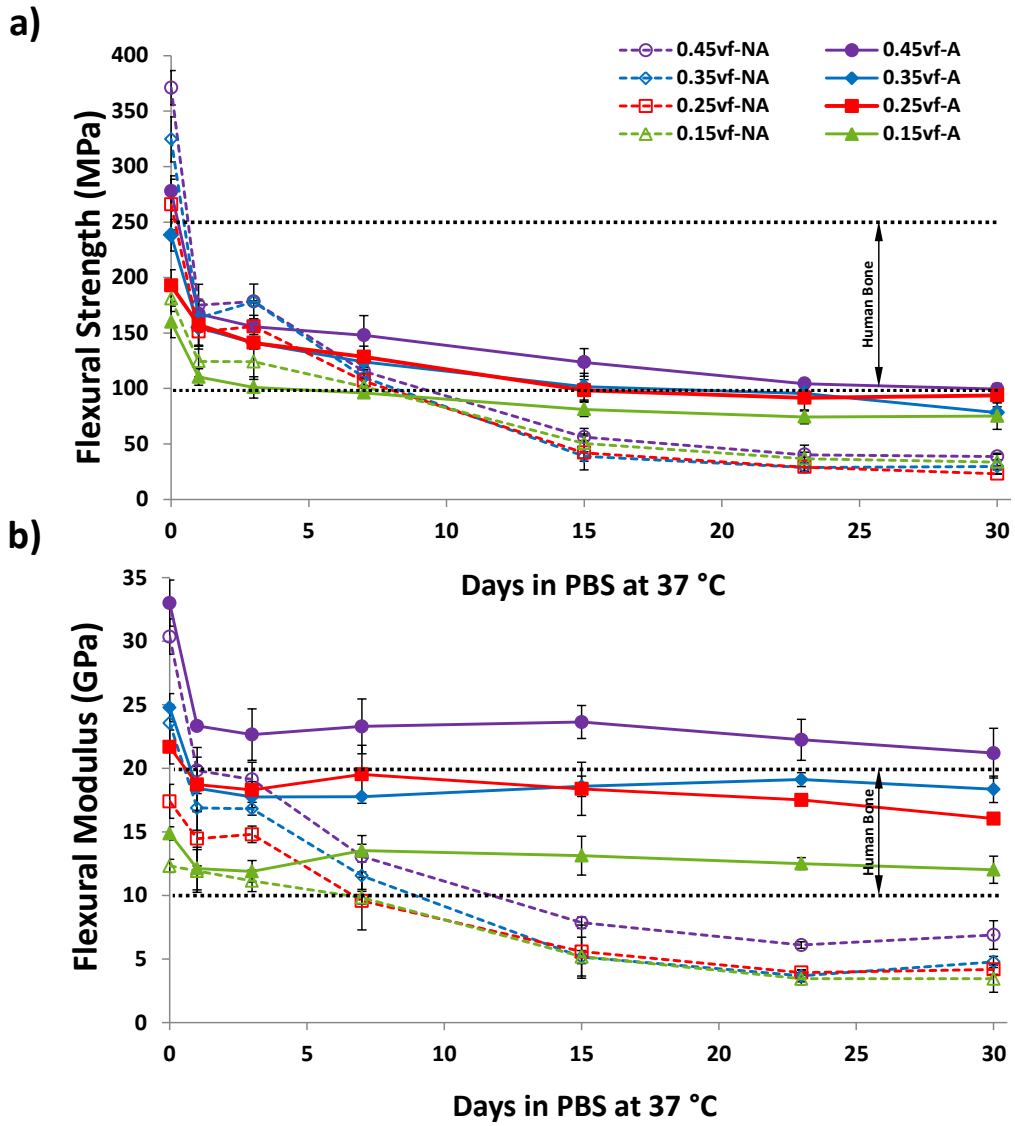


Figure 3.31: Variation of flexural properties of PGF-PLA compression moulded composite rods during conditioning in PBS at 37°C: (a) Flexural strength (±SD) and (b) flexural modulus (±SD). The flexural strength and modulus variation profiles of the composite rods manufactured from PLA-sheathed as-drawn fibre bundles were represented by open markers and dashed lines. The ranges of human cortical bone flexural properties were denoted by black dotted lines.

As demonstrated by Figure 3.31b, a reduction in flexural modulus was also observed for annealed fibre reinforced compression moulded composite rods during conditioning in PBS at 37°C. The modulus of the 0.15, 0.25, 0.35, and 0.45 fibre volume fraction samples decreased to 71%, 74%, 86%, and 81% of the day 0 values after one day of immersion. However, in clear contrast to the behaviour of the compression moulded composite rods containing as-drawn fibres, no further reductions in the modulus of the annealed fibre reinforced composite rods were observed. The modulus values for all the PGF-PLA compression moulded composite rods containing annealed fibres remained

within (or even exceeded) the human cortical bone modulus range up to day 30.

3.4.5.2 Effect of Conditioning Time on the Mass of PGF-PLA Composite Rods Fabricated via PLA-sheathed Fibre Bundle Compression Moulding

Figure 3.32 shows the mass changes experienced by the PGF-PLA composite rods as a result of conditioning at 37° C in PBS. From Figure 3.32a, it can be observed that the amount of water absorbed by the composite samples containing fibres in the as-drawn condition increased with both fibre content and conditioning time. Within experimental error, the water absorption profiles of the 0.35 and 0.45 fibre volume fraction samples were equal and corresponded to the highest amount of water absorbed at each time point, reaching values in excess of 25% at day 30. For all the composite rods reinforced with as-drawn fibres, the rate of water absorption (indicated by the slope of the curve) was greater between day 3 and day 15. The water absorption rate appeared to decrease for the subsequent time points.

Compared to the as-drawn fibre reinforced compression moulded composite rods, the specimens containing annealed fibres, absorbed a minuscule amount of water as demonstrated by respective curves in Figure 8a. In these samples, the amount of water absorbed tended to slightly increase with conditioning time, reaching values of approximately 1.25%, 1.97%, 1.60% and 1.30% for the 0.45, 0.35, 0.25 and 0.15 annealed fibre volume fractions at day 30, respectively.

Figure 3.32b illustrates the mass loss profiles of the bioresorbable compression moulded composite rods reinforced with either as-drawn or annealed fibres, calculated after vacuum drying as described in §2.16. The dry mass of the compression moulded composites reinforced with as-drawn fibres decreased throughout the degradation study. The reduction in dry mass increased with fibre volume fraction and conditioning time. Similarly to the wet mass absorption, the 0.45 and 0.35 fibre volume fractions presented the highest mass losses at each time point, reaching values in the order of 27% at day 30. The highest rates of mass loss for the as-drawn fibre reinforced compression moulded composites were observed within the period spanning from day 7 to day 15. Subsequently, the rate of mass loss decreased,

coinciding with the diminution of the amount of water absorbed by these composite samples.

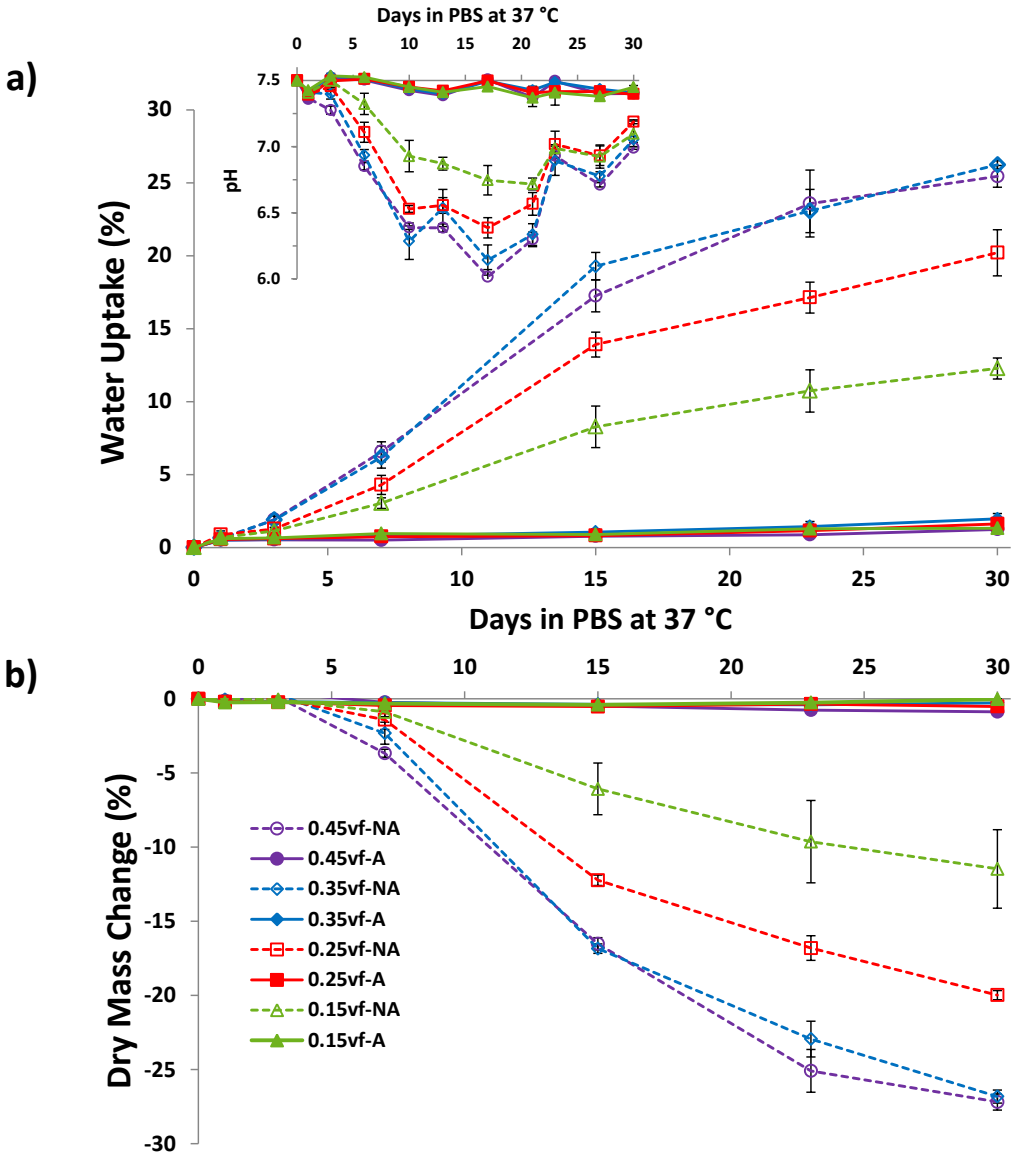


Figure 3.32: (a) Water uptake, m_G, (±SD) and (b) dry mass change, m_L, profiles (±SD) for bioresorbable composite rods manufactured through compression moulding of PLA-sheathed bundles of either annealed of as-drawn fibres conditioned in PBS at 37° C. The inset of (a) shows the pH variation (±SD) of the collected conditioning media for the studied composite rods. The profiles of the bioresorbable composite rods containing as-drawn fibres were denoted by open markers and dashed lines, whereas the profiles of the bioresorbable composite rods containing annealed fibres were denoted by solid markers and solid lines.

Unlike the compression moulded composite rods reinforced with as-drawn fibres, the samples containing annealed fibres did not presented considerable reductions in dry mass, in good agreement the water uptake behaviour. The % mass loss for the 0.45, 0.35, 0.25 and 0.15 fibre volume fractions at day 30 were 0.87%, 0.27%, 0.51% and 0.02%, respectively.

3.4.5.3 Effect of Conditioning Time on the Conditioning Media pH of PGF-PLA Composite Rods Fabricated via PLA-sheathed Fibre Bundle Compression Moulding

Similar trends were observed in the pH variation of the compression moulded composite rod conditioning media as illustrated by the inset in Figure 3.32a. Within experimental error, the pH of the media collected from vials containing annealed fibre reinforced compression moulded composite samples, did not vary throughout the study with respect to the initial pH of the PBS solution. On the other hand, a decrease of the initial pH of the PBS solution in direct proportion to the fibre volume fraction was observed in the composite rod samples containing as-drawn fibres. The negative tendency for the pH readings in the as-drawn fibre reinforced composites samples continued up to day 17. At this point, the lowest pH values of the entire degradation study were registered for the respective as-drawn fibre volume fraction sample series. Subsequently, the pH started to increase towards neutral, in good agreement with the decrease in the rate of water uptake and dry mass loss.

3.4.5.4 Effect of Conditioning Time on Reinforcing Fibre Structure in PGF-PLA Composite Rods Fabricated via PLA-sheathed Fibre Bundle Compression Moulding

Figure 3.33 shows representative SEM images of the fracture surface of $0.35v_f$ composite rod samples manufactured through compression moulding of PLA-sheathed bundles of either annealed or as-drawn fibres, respectively, at selected time points during conditioning in PBS at 37°C. The insets of Figure 3.33 show the backscattered electron images of the $0.35v_f$ corresponding rods at the respective time points to further emphasise the changes in the fibre morphology observed in the fracture surface images throughout the compression moulded composite degradation study. Fibres appear as white solid circles, whereas the matrix is represented by the black background.

Figures 3.33a and 3.33b show the images of the fracture surface of $0.35v_f$ compression moulded composite rods containing annealed and as-drawn fibres before immersion in PBS. Pulled-out fibres with a clean surface and without any matrix debris attached were observed on the fracture surface of both types of composite rods.

No differences in the fibre morphology between the annealed and the as-drawn fibre reinforced compression moulded composite rods, other than the seemingly rougher appearance of the annealed fibres cross sections) were

observed until day 3 (data not shown). A thin shell was observed to have developed around some of the as-drawn fibres. By day 7 most of the as-drawn fibres had developed into a well-defined core-shell structure (more evident in the backscattered electron inset) with a thick shell, as illustrated by Figure 3.33f. No such morphological changes could be observed in the annealed fibre reinforced compression moulded composites. Multiple shells surrounding a progressively shrinking core were noticed by day 15 (Figure 3.33h) only in the as-drawn fibre reinforced compression moulded composites. These shells remained seemingly unaffected by the interaction with the conditioning medium up to day 30 as seen in Figure 3.33h.The dimensions of the fibre cores in the as-drawn fibre reinforced compression moulded composites was observed to decrease with conditioning time, until their dissolution throughout most of the composite cross section by day 30.

No noticeable changes in the diameter could be observed for the annealed fibres in the composites. Up to day 30, no gaps between the fibre and the matrix could be noted. However, at day 30, some pits could be observed in the annealed fibre periphery

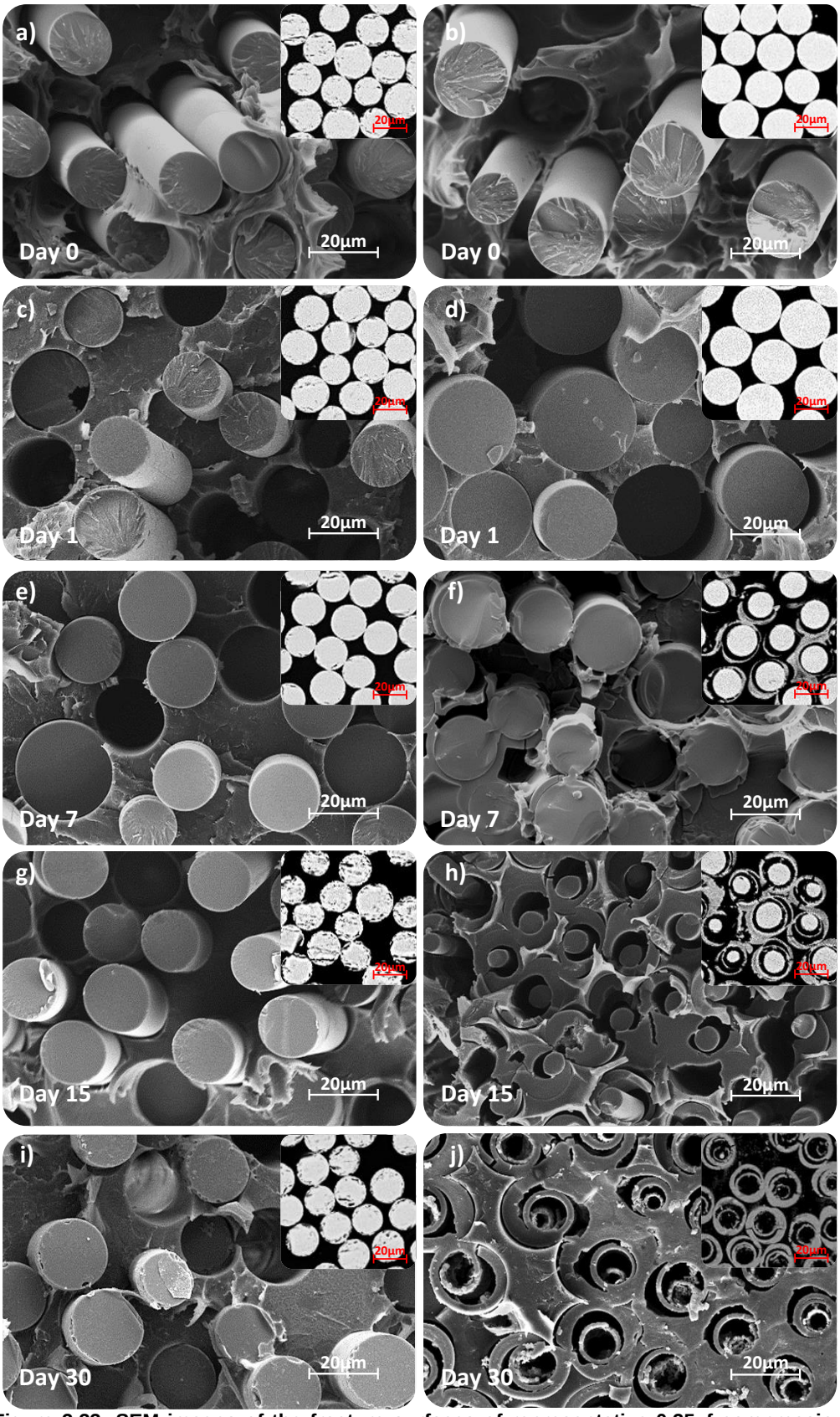


Figure 3.33: SEM images of the fracture surfaces of representative 0.35vf compression moulded composite rods reinforced with (right) annealed and (left) as-drawn phosphate glass fibres at (a) & (b) day 0, (c) & (d) day 1, (e) & (f) day 7, (g) & (h) day 15, (i) & (j) day 30, respectively, during conditioning in PBS at 37°C. The insets show the backscattered electron images of the corresponding polished cross sections at the respective conditioning time points.

3.4.5.5 Effect of Conditioning Time on Reinforcing Fibre Composition in PGF-PLA Composite Rods Fabricated via PLA-sheathed Fibre Bundle Compression Moulding

The results from the compositional EDX analysis conducted on the reinforcing fibres in $0.35v_f$ compression moulded composite rods during conditioning in PBS at 37°C are displayed in Table 3.13. The data corresponding to the annealed fibre is shown in the rows labelled as Fibre-A. The data corresponding to the non-degraded as-drawn fibres and the as-drawn fibre cores were displayed in the rows labelled as Fibre-NA. The chemical compositions of the shells around the as-drawn fibre cores (cf. Figure 3.33) were displayed in the rows labelled as Shell-NA and highlighted in red for the benefit of the reader. The theoretical P45Fe2 composition of the glass fibres is also shown in Table 3.13.

Excepting the Na/P ratio, in which a slight decrease was observed with conditioning time to finally reach 90% and 89% of the non-degraded annealed and as-drawn glass fibre compositions, respectively, the relative amounts of the glass modifying cations in the as-drawn fibre cores and annealed fibres was observed to remain constant up to day 30 (within experimental error) at the composition of the respective non-degraded glass fibres. From examination of Table 2 it can be observed that the relative content of Na in the shells (first observed at day 3) progressively decreased with respect to the fibre cores and the non-degraded glass fibres with conditioning time. By day 30, the Na content in the shells had diminished to around 40% of the sodium originally present in the non-degraded glass fibres.

In contrast, the relative concentrations of the other glass constituents, namely, Mg, Ca, and Fe progressively increased with conditioning time in the shells, reaching concentrations 18%, 99% and 121% in excess of the respective elements with respect to the non-degraded as-drawn fibres. In addition, a trace amount of potassium was detected only in the shells, whose relative concentration increased with conditioning time. Finally, the oxygen to phosphorous ratio also increased from 3.17 to 3.39 with conditioning time as shown in Table 3.13.

Table 3.13: Summary of EDX analysis conducted on the reinforcing P45Fe2 glass fibres in 0.35vf compression moulded composite rods at different conditioning time points. The time point at which the rods were recovered from solution is indicated by the number at the end of the sample code.

Sample Code	Na/P	Mg/P	K/P	Ca/P	Fe/P	O/P
P45Fe2	**0.289**	**0.267**	**-**	**0.178**	**0.044**	**3.156**
Fibre-A-D0	0.297±0.002	0.283±0.001	-	0.175±0.002	0.041±0.001	3.167±0.001
Fibre-NA-D0	0.286±0.003	0.277±0.002	-	0.176±0.001	0.041±0.001	3.157±0.003
Fibre-A-D1	0.292±0.004	0.280±0.003	-	0.174±0.001	0.041±0.001	3.163±0.003
Fibre-NA-D1	0.284±0.003	0.274±0.002	-	0.177±0.001	0.040±0.001	3.154±0.003
Fibre-A-D3	0.295±0.002	0.280±0.004	-	0.177±0.001	0.040±0.001	3.165±0.003
Fibre-NA-D3	0.274±0.002	0.272±0.001	-	0.177±0.001	0.040±0.001	3.147±0.003
Shell-NA-D3	**0.241±0.02**	**0.279±0.010**	-	**0.174±0.001**	**0.038±0.006**	**3.130±0.014**
Fibre-A-D7	0.279±0.002	0.280±0.004	-	0.174±0.001	0.040±0.001	3.153±0.005
Fibre-NA-D7	0.277±0.002	0.278±0.002	-	0.175±0.001	0.041±0.001	3.152±0.003
Shell-NA-D7	**0.215±0.002**	**0.280±0.003**	**0.004±0.001**	**0.170±0.005**	**0.029±0.003**	**3.104±0.008**
Fibre-A-D15	0.277±0.004	0.282±0.003	-	0.173±0.002	0.040±0.001	3.153±0.006
Fibre-NA-D15	0.267±0.002	0.277±0.004	-	0.174±0.001	0.041±0.001	3.146±0.002
Shell-NA-D15	**0.159±0.011**	**0.282±0.01**	**0.014±0.005**	**0.302±0.014**	**0.083±0.010**	**3.295±0.013**
Fibre-A-D23	0.280±0.002	0.276±0.002	-	0.176±0.001	0.041±0.002	3.154±0.001
Fibre-NA-D23	0.250±0.015	0.270±0.003	-	0.177±0.001	0.042±0.002	3.135±0.006
Shell-NA-D23	**0.127±0.007**	**0.303±0.010**	**0.020±0.002**	**0.328±0.012**	**0.089±0.0120**	**3.339±0.023**
Fibre-A-D30	0.267±0.001	0.279±0.001	-	0.174±0.001	0.041±0.001	3.148±0.001
Fibre-NA-D30	0.254±0.001	0.269±0.001	-	0.177±0.001	0.041±0.001	3.135±0.003
Shell-NA-D30	**0.120±0.010**	**0.328±0.0120**	**0.023±0.002**	**0.350±0.0120**	**0.091±0.010**	**3.391±0.024**

3.4.6 Thermal Analysis of PGF-PLA Composite Rods Fabricated via Compression Moulding of PLA-sheathed Fibre Bundles

The thermal properties of non-degraded PGF-PLA composite rods fabricated via compression moulding of PLA-sheathed fibre bundles recorded in two different heating cycles as described in §2.18 were summarised in Table 3.14. The same features previously described in §3.2.3 could be observed in the respective DSC traces, namely: i) a glass transition phenomenon T_g, ii) a cold crystallisation peak (of which the maximum temperature T_{X1} and onset of crystallisation X_0 are reported in Table 3), iii) a polymorphic transition peak (denoted by T_{X2}) and iv) an endothermic peak (characterised by T_m) associated with the melting of crystalline phases.

No distinctive features, other than a single glass transition phenomenon were noticed during the cooling segments of the programmed thermal cycle and therefore are not presented here.

Table 3.14: Thermal properties (±SD) of non-degraded glass fibre reinforced composite rods fabricated via PLA-sheathed glass fibre bundle compression moulding.

Cycle	Sample Code	T_g (°C)	T_{X0} (°C)	T_{X1} (°C)	T_{X2} (°C)	T_m (°C)	X_c (%)
1	**0.45-NA**	61.5±0.3	87.0±0.5	94.7±0.3	154.9±0.1	168.44±0.04	16.7±1.1
	0.35-NA	61.3±0.4	90.5±0.6	96.3±0.8	155.1±0.3	169.9±0.3	12.7±1.7
	0.25-NA	60.8±0.2	90.7±0.2	96.4±0.4	155.6±0.5	170.7±0.4	12.8±2.2
	0.15-NA	62.8±2.0	91.2±1.0	96.9±0.9	155.3±0.4	170.6±0.4	12.1±4.3
	0.45-A	59.22±0.04	90.2±0.7	97.6±0.6	155.8±0.2	170.0±0.1	12.9±0.9
	0.35-A	58.81±0.01	91.1±1.4	97.3±1.1	156.0±0.3	170.2±0.2	11.1±2.7
	0.25-A	59.8±0.2	90.2±1.3	96.0±1.0	155.1±0.7	169.3±0.8	11.4±1.0
	0.15-A	58.56±0.01	90.8±0.5	96.2±0.7	155.4±0.5	170.1±0.5	11.3±0.7
2	**0.45-NA**	56.63±0.04	89.4±0.1	95.8±0.4	154.3±0.2	168.2±0.1	5.3±0.9
	0.35-NA	56.9±2	91.0±0.2	96.9±0.3	154.7±0.1	169.0±0.1	5.0±0.3
	0.25-NA	57.1±0.3	91.8±0.4	97.6±0.4	155.1±0.1	169.3±0.3	5.1±0.5
	0.15-NA	56.9±0.4	91.5±0.3	96.9±0.3	154.6±0.4	168.7±0.2	4.8±0.4
	0.45-A	57.4±0.9	90.7±1.0	97.6±1.1	155.6±0.5	169.7±0.1	5.2±0.6
	0.35-A	57.8±0.3	91.8±0.9	98.2±0.7	155.6±0.2	169.5±0.2	4.4±0.1
	0.25-A	57.2±0.3	91.8±0.1	97.2±0.2	154.7±0.4	168.8±0.5	5.4±0.3
	0.15-A	57.4±0.1	91.6±0.9	96.9±1.1	154.8±0.8	169.1±0.6	4.8±0.1

Excepting the glass transition temperature, T_g, which tended to be higher for the as-drawn fibre reinforced composites, no significant differences stemming from fibre type were observed at the other relevant thermal events during the first heating cycle. Both annealed and as-drawn fibre reinforced composite rods contained similar values of crystallinity (formed during sample manufacture). The $0.45v_f$ samples presented the highest crystallinity content, with ca. 17% and ca. 13% for the as-drawn and annealed fibre reinforced composites, respectively.

Having eliminated variation in thermal history as a result of the 5 min isothermal hold at 190°C, no significant differences could be noted in the temperatures of the characteristic thermal events recorded during the second heating. Composites reinforced with as-drawn and annealed fibres developed around 5% of crystallinity upon cooling.

Figure 3.34 illustrates the thermograms corresponding to the second heating cycle of the compression moulded composite rods reinforced with as-drawn and annealed fibres, respectively.

In contrast to the compression moulded plates, no shoulders were evident in the cold crystallisation peak regardless of the type of reinforcing fibre. The cold crystallisation peak featured similar shapes for all the fibre volume fractions in both type of reinforcing fibres. The area of the cold crystallisation and melting peaks (corresponding to crystallisation and melting enthalpies) tended to decrease with increasing fibre volume fraction for both types of fibres, however the decrease was more pronounced for increasing annealed fibre volume fraction in comparison to as-drawn fibres.

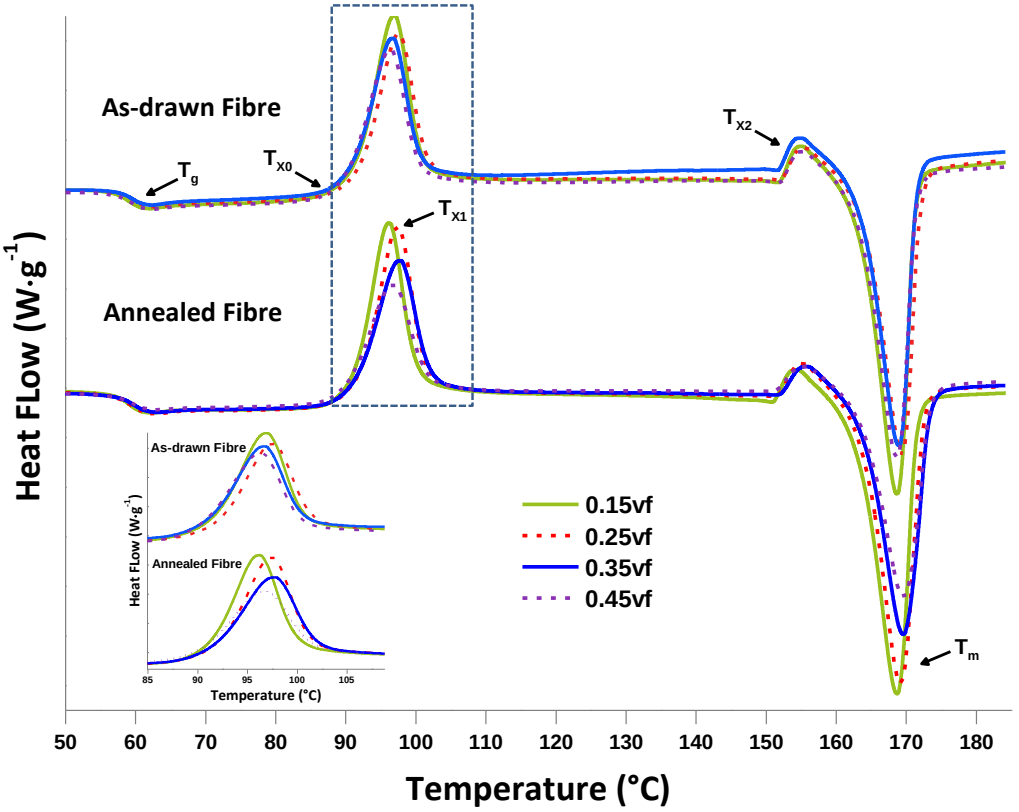


Figure 3.34: Representative DSC traces of as-drawn and annealed fibre reinforced compression moulded composite rods recorded during the second heating cycle once differences in thermal history have been eliminated. The inset shows a magnified view of the region enclosed by the blue dashed line.

The cold crystallisation and melting enthalpies for the $0.45v_f$ as-drawn fibre reinforced compression moulded composite rods contracted to 93% and 95% of the corresponding values for the $0.15v_f$ as-drawn fibre reinforced compression moulded composite rods, respectively. On the other hand the cold crystallisation and melting enthalpies for the $0.45v_f$ annealed fibre reinforced compression moulded composite rods contracted to 78% and 81%

of the corresponding values for the $0.15v_f$ annealed fibre reinforced compression moulded composite rods, respectively.

3.4.6.1 Effect of Conditioning Time on the Crystallinity of PGF-PLA Composite Rods Fabricated via Compression Moulding of PLA-sheathed Fibre Bundles

Figure 3.35a illustrates the variation of the crystallinity during PBS conditioning at 37°C for the composite rods fabricated via compression moulding of PLA-sheathed fibre bundles.

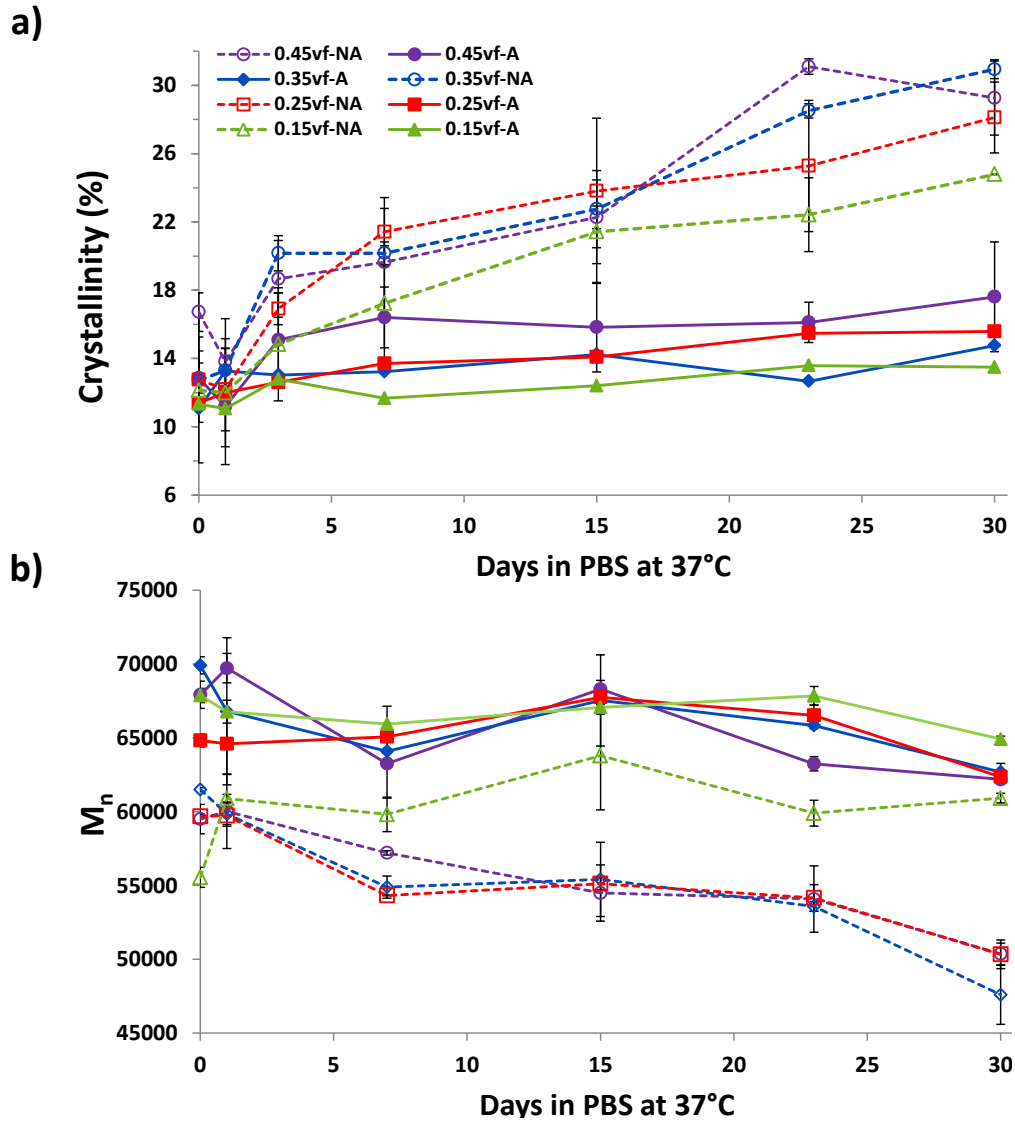


Figure 3.35: (a) Evolution of the crystallinity content (±SD) for of the PLA matrix in the PGF-PLA compression moulded composite rods conditioned in PBS at 37°C and (b) variation of number average molecular weight, M_n, of the PLA matrix with conditioning time in PBS at 37°C for the bioresorbable compression moulded composite rods reinforced with either annealed or as-drawn glass fibres. The profiles of the bioresorbable composite rods containing as-drawn glass fibres were denoted by open markers and dashed lines, whereas the profiles of the bioresorbable composite rods containing annealed glass fibres were denoted by solid markers and solid lines.

The crystallinity in the compression moulded composite rods reinforced with as-drawn fibres progressively increased with conditioning time. The crystallinity seemed to increase with the relative content of as-drawn fibres, however, no significant differences ($p>0.05$) were observed between the 0.45, 0.35 and 0.25 fibre volume fraction samples which in average presented a crystallinity content of ca. 29%.

On the contrary, the crystallinity content of the annealed fibre reinforced compression moulded composite rods, regardless of the fibre volume fraction, seemed to remain constant throughout the entire degradation study. The maximum crystallinity content at day 30 for annealed fibre reinforced compression moulded composites was observed in the 0.45 fibre volume fraction samples, with an approximated 18% of crystallinity (significantly lower than the crystallinity content of the corresponding as-drawn fibre reinforced compression moulded composite rod).

3.4.7 GPC Analysis of PGF-PLA Composite Rods Fabricated via Compression Moulding of PLA-sheathed Fibre Bundles

Figure 3.35b shows the evolution of number average molecular weight against degradation time for the bioresorbable PGF-PLA compression moulded composite samples studied. It can be observed that within experimental error, the number average molecular weight of the PLA matrix in the composite rods reinforced with annealed fibres remain seemingly constant up to day 30 for all the fibre volume fractions studied. Conversely, excepting the $0.15v_f$ specimens, a gradual decrease of $\boldsymbol{M_n}$ was observed for all the compression moulded composite rods containing as-drawn fibres to around 84%, 77% and 85% of the initial number average molecular weight prior immersion in PBS for the 0.25, 0.35 and 0.45 fibre volume fraction samples, respectively. Furthermore, the initial number average molecular weight of the as-drawn fibre reinforced compression moulded composite rods was in average 10% lower than the initial number average molecular weight of the samples with corresponding fibre volume fractions in the annealed fibre series. The number average molecular weight of the $0.15v_f$ samples reinforced with as-drawn fibres, remained roughly constant within experimental error up to day 30 of the composite degradation study.

4 Discussion

4.1 Characterisation and *In Vitro* Degradation Studies of Bioresorbable Bulk Glass and Fibres of the $45P_2O_5{\cdot}16CaO{\cdot}13Na_2O{\cdot}24MgO{\cdot}2Fe_2O_3$ mol% composition

The unique ability of phosphate based glasses to completely dissolve in aqueous media has greatly attracted the attention of researchers, particularly in the biomedical field as a result of the potential applications in soft and hard tissue repair [127]. Such glasses can be synthesised to incorporate ions which naturally occur within the human body in order to elicit specific cell responses following their dissolution, expediting the body healing mechanisms [134]. Furthermore, unlike silicate based bioglasses, they can be easily processed into useful morphologies like fibres and microspheres, making them the foremost candidate for the reinforcement of fully bioresorbable composites [248, 249].

4.1.1 Melt-Drawn production and Characterisation of P45Fe2 Phosphate Glass Fibres

The P45Fe2 composition was synthesized based on the results of previous investigations involving meta- and polyphosphate compositions [129, 136, 250]. Despite the manufacturing advantage conferred by their superior spinnability [251], the high concentration of highly hydrolysable P-O-P bonds in metaphosphate glasses, makes them more prone to premature degradation in comparison to polyphosphate compositions [252]. Therefore, the inevitable exposure to environmental conditions may lead to the rapid creation of surface flaws as a result of water condensation at the fibre surface, greatly reducing fibre strength.

It has been demonstrated that iron oxide additions to phosphate glasses increases the strength of the network due to the enhanced crosslinked structure [250, 253]. In spite of the beneficial effects on mechanical properties and resistance to water-mediated degradation, the addition of Fe_2O_3 was limited to 2 mol% since the strong interaction of the iron cation with phosphate structures impairs fibre drawing ability of phosphate glasses by hindering the alignment of polymer-like chains with the fibre axis [254].

Fibres of P45Fe2 glass could be readily obtained through molten glass jet attenuation by the continuous tension sustained by a rotating drum. As demonstrated by Table 3.1, the nozzle yield could be accurately calibrated at roughly 1 g·min^{-1} by controlling both the bushing head (height of glass above the nozzle) and the drawing temperature (associated with the glass viscosity, cf. Figure 3.2).

The structure of glasses is characterised by the point at which the structural relaxation time, τ, greatly exceeds the experimental time scale on account of the sudden increase in viscosity and the corresponding decrease in molecular mobility ($\tau \approx 100\ s - 1000\ s$) [255, 256].

As a result of the rapid increase of relaxation time, the enthalpy curve (or specific volume among other physical properties) departs from the supercooled liquid line at a temperature which depends on the cooling rate. Such temperature is referred to as fictive temperature, T_f, and corresponds to the intersection of the extrapolated supercooled liquid enthalpy line with the one associated with glass behaviour [257]. Accordingly, the glass structure can be described in terms of the liquid-like structure frozen at the respective fictive temperature; the higher the cooling rate, the higher the fictive temperature and the more open the liquid-like structure.

The higher cooling rates associated with fibre drawing in comparison to bulk glass casting (in the order of a 10-100 fold difference [140]) results in a disparity of the densities between both morphologies. This is in line with the lower density obtained for the as-drawn fibres (2.643±0.005 g·cm^{-3}) with respect to the bulk glass (2.762±0.001 g·cm^{-3}) in this study.

No crystallisation of the glass mass in the cone was observed during fibre drawing when freshly prepared glass was used. The amorphous nature of the fibres and the bulk glass was verified via X-ray powder diffraction. As shown in Figure 3.4, only amorphous halos were present in the respective diffractograms of bulk glass and as-drawn glass fibres. Discrete crystallisation peaks were also absent in the annealed glass fibre curve after isothermal heat treatment at 460°C. Additionally, no significant differences from the theoretical P45Fe2 composition were noted in the EDX results of the bulk glass or in the glass fibres in both the annealed and as-drawn conditions.

Differences in thermal history between the bulk glass and both fibre types were evident in the curves obtained through calorimetric studies. The presence of a small cold crystallisation peak, denoted by $\mathbf{T_{x1}}$, at 571°C, and the corresponding shoulders in the respective melting peaks (cf. Figure 3.5) in both of the fibre thermograms, was attributed to the enhanced heterogeneous nucleation ability of the pulverised fibres in comparison to the bulk glass (whose thermal behaviour was determined from a glass chunk) resulting from the larger surface area of the fibre powder. The increased surface area also resulted in the shift of the main cold crystallisation peak, denoted by $\mathbf{T_{x2}}$ in Figure 3.5, towards lower temperatures for both types of fibres.

A small endotherm, identified as an enthalpy relaxation peak was observed at the glass transition region in the single case of the annealed fibre thermogram. Being in a non-equilibrium state characterised by an excess of thermodynamic properties (namely, enthalpy, entropy, volume and so forth), the as-quenched glass will tend to slowly relax towards a lower energetic and more compact metastable state if held at a temperature close to the glass transition temperature as occurred during annealing [257, 258]. Upon heating through the glass transition region during calorimetric solicitation, additional energy should be supplied to compensate for the reduced molecular mobility associated with the relaxed state. The small endothermic peak at T_g, is the calorimetric consequence of the relaxation of the glass network occurred during fibre annealing.

The conformational changes experienced during annealing resulted in the shift of the main cold crystallisation in the annealed fibre curve, towards lower temperatures, with respect to the as-drawn fibre sample as shown in Figure 3.5.

The 50% reduction in the annealed fibres tensile strength with respect to the as-drawn condition (presented in Table 3.3) could not be explained by the creation of crystalline defects during thermal treatment as demonstrated by the X-ray powder diffraction scans, in which no discrete crystalline diffractions peaks could be observed. Similar decreases in the strength of the phosphate glass fibres with similar compositions have been previously reported in [146, 158].

The application of uniaxial stresses during metaphosphate glass fibre production is known to produce an elongated network, of otherwise entangled and twisted chains, due to the shear flow-mediated alignment of its structural units and also to orient and stretch defects created during fibre drawing or glass synthesis (such as striae, microbubbles and inhomogeneous domains) [149, 150]. As the temperature approximates the glass transition temperature region during melt cooling, stress relaxation is hindered by the exponential increase in viscous resistance, locking the glass structural units and defects in their oriented positions. The orientation of both phosphate chain molecules and defects parallel to the fibre axis in phosphate glass fibres has been suggested to contribute to the strength differences between glass fibres and bulk samples [147, 149, 150].

The possible loss of defect orientation and the structural anisotropy relaxation through local structural rearrangements during heat treatment could have accounted, at least partly, to the decrease in tensile strength and strain to break for the annealed fibres [147]. Furthermore, tensile stresses and cracks have been observed to develop at the surface of phosphate glasses after annealing in atmospheres containing water vapour [259]. Water molecules cleave the P-O-P bonds in the phosphate chains at the surface, generating chain terminating hydroxyl groups [260]. As a result of lower connectivity of the glass network and the higher hydroxyl concentration, the surface contracts at a greater extent with respect to the bulk during cooling, producing a permanent tensile stress which decreases the glass resistance to the propagation of a sub-critical crack during the application of an external load [259]. The formation of such a tensile layer at the fibre surface could have been a contributing factor towards the considerable reduction in strength of the annealed fibres observed in this study.

The mean tensile modulus of the annealed fibres was greater than the corresponding value of the as-drawn fibres. However, such increase was accounted statistically non-significant in a 95% confidence interval. Unlike strength, which is deemed a non-physical value due to its dependence on both internal and external factors, the elastic modulus is directly related to the inter-atomic forces and the structure energy [147, 261]. A change in modulus of the glass fibres was expected in virtue of the enthalpy relaxation experienced as a

result of heat treatment (cf. Figure 3.5), as has been reported in previous studies dealing with both silicate and phosphate glass fibres [146, 158, 262]. In spite of this, the extent of structure relaxation experienced after one hour treatment at 460°C for the P45Fe2 glass fibres composition may have not been enough to prompt a clear change in the elastic modulus. Alternatively, a slight increase in modulus could be masked by experimental artifacts, especially during the glass fibre diameter evaluation.

4.1.2 Dissolution Studies of P45Fe2 Bulk Glass and Glass Fibres

Aqueous dissolution of P45Fe2 bulk glass was observed to occur in two stages. The linear behaviour observed during the major part of the analysis is characteristic of a reaction-controlled degradation process in which a core of unreacted glass progressively contracts with increasing conditioning time [13, 125, 133].

The decreasing mass loss tendency spanning the first five days of the bulk glass degradation study was better described by $t^{1/2}$ kinetics. Such behaviour is consistent with a process controlled by the diffusion of water molecules into the bulk glass and the corresponding development of a hydrated surface layer [13, 125].

Transition from the diffusion controlled to the reaction controlled dissolution process occurs once the hydrated layer has reached its full thickness. The transition time has been found to be influenced by leaching solution chemistry and glass composition [13, 133]. These observations are in line with the lengthier transition period observed for the P45Fe2 bulk glass (~5 days) in comparison to those previously reported for calcium metaphosphate compositions (in the range of minutes to hours) [13, 126] as a result of Fe_2O_3 incorporation, which effectively retards the dissolution of phosphate glasses through the formation of strong crosslinks between phosphate chains [263].

Following hydration, entire phosphate chains can then detach from the bulk glass and float into solution [13, 125]. A steady dissolution rate will be reached when the hydration front advances with identical velocity to the glass-media interface, accounting for the linear dissolution behaviour of the bulk glass observed after day 5.

The degradation rate determined through linear regression on the linear portion of the bulk glass dissolution curve (4×10^{-8} $g\cdot cm^{-2}\cdot h^{-1}$) was in good agreement with values reported in previous investigations with similar compositions where the values ranged in the 1×10^{-7} $g\cdot cm^{-2}\cdot h^{-1}$ 1×10^{-9} $g\cdot cm^{-2}\cdot h^{-1}$ [132, 250]. The non-zero intercept of the extrapolated linear stage of the bulk glass %mass loss can be attributed to the decelerating dissolution behaviour associated with the development of the glass hydrated layer during the first 5 days of the study.

Since it has been shown that biocompatibility of phosphate-based glasses containing non-toxic elements is strongly related to the degradation rate [127, 252], the similarity of the degradation figures obtained in this study give a good estimate of the potential biocompatibility of the P45Fe2 composition, yet to be confirmed by follow-up cytocompatibility studies.

Multiple studies have observed a shift in the solution pH towards acidic values as a result of phosphate glass dissolution [13, 125, 126, 132, 137]. Such decrease in the pH evidence the release of acidic species into the solution as a result of the phosphate glass corrosion. No significant pH variations of the bulk glass conditioning media were noticed throughout the degradation analysis, in spite of glass dissolution, as demonstrated by Figure 3.6. This is may be related to order of magnitude the lower degradation rate of P45Fe2 bulk glass with respect to those previously reported (in the order of 1×10^{-6} $g\cdot cm^{-2}\cdot h^{-1}$) [13, 125, 137], coupled with the buffer capacity of PBS which is capable to compensate for small concentrations of both acid and basic species.

Glass fibres of the P45Fe2 composition presented markedly higher mass losses with respect to bulk glass, regardless of the conditioning media or fibre type. Annealed and as-drawn glass fibres conditioned in PBS presented mass losses approximately 52 and 122 times greater than the corresponding value for bulk glass at day 30 (~0.65%), respectively. Phosphate glass dissolution was greatly accelerated in the studied glass fibres on account of the extensive differences in exposed hydrophilic surface area.

As demonstrated by the linear mass loss and the fibre diameter reduction profiles in Figure 3.9, annealed fibres dissolved in PBS via uniform surface erosion. Phosphate glass dissolution takes place via hydration and

detachment of entire phosphate chains from the outer glass surface. Water molecules penetrate into the glass network and disrupt the interchain M-O-P bonds (M=Na, Ca, Fe, Mg) via ion exchange with protons, resulting in the development of a hydrated layer that advances into the fibre core [13, 133], in such way that the glass fibre shrunk uniformly and in direct proportion to conditioning time.

On the other hand, the as-drawn fibres degraded faster and also in a nonlinear fashion (cf. Figure 3.9) possibly suggesting a diffusion controlled reaction [133]. Quick dissolution of as-drawn glass fibres led to the saturation of the leaching PBS solution and the subsequent precipitation of stable phases on the fibre surface. Precipitates were first detected in the form of flakes which later developed into continuous shells as conditioning time elapsed as shown in Figure 3.7. The observed decrease in as-drawn glass fibre dissolution rate after day 15 could be attributed to i) the formation of a precipitate layer which could have hindered the interdiffusion of reactive species and glass dissolution by-products and/or ii) to the decrease in the thermodynamic driving force of glass dissolution caused by compositional changes of the leaching solution [264].

The enhanced glass durability of annealed fibres in PBS at 37°C with respect to as-drawn fibres (cf. Figure 3.7) was attributed to the reorganisation of the glass into the (metastable) equilibrium entangled chain configuration during heat treatment at 460°C via thermally activated relaxation processes, namely: i) relaxation of the energetically unstable frozen-in anisotropic strains produced by the applied axial stress during fibre drawing and, to some extent, ii) enthalpy relaxation (as evidenced by the presence of a small endothermic peak in the glass transition region in the annealed fibre thermogram in Figure 3.5) of the isotropic open liquid-like structure frozen at the fictive temperature during quenching [147, 152, 153]. The lower degradation rate with respect to as-drawn fibres in conjunction with the periodic refreshment of the conditioning medium prevented the saturation of the solution and the concomitant formation of precipitates on the annealed fibre surface throughout *in vitro* degradation in PBS at 37°C. Increases in the chemical durability of fibres immersed in aqueous media after heat treatment at temperatures close to the glass transition temperature have also been reported in [146, 158, 159].

The close correspondence of both PBS and deionised dissolution behaviour of annealed fibres indicated that solution saturation with respect to solvated PO_4^- species does not influence the degradation rate of glasses consisting of long chains of phosphate tetrahedra, since the P-anions released from the glass are polymer-like chains rather than monomeric orthophosphate units. This is in good agreement with previous investigations where glass dissolution was found to progress in spite of solution saturation with apatite [13].

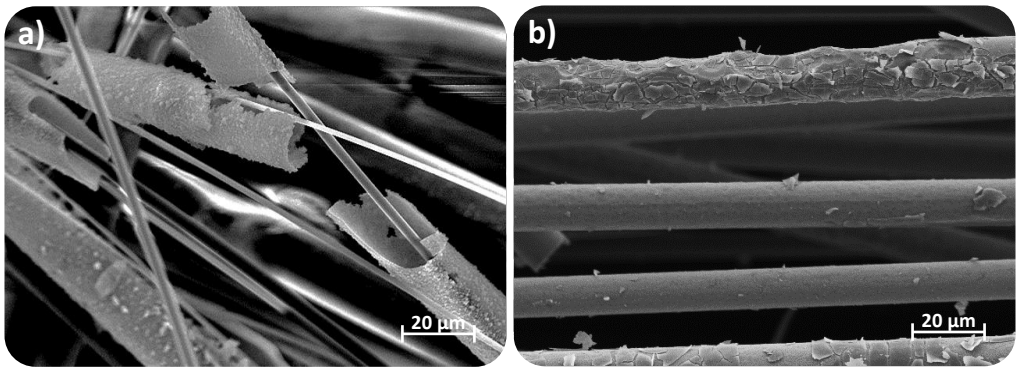


Figure 4.1: Comparison of as-drawn glass fibres conditioned in (a) PBS and (b) deionised water during 15 days at 37°C.

Similar to PBS conditioning, the as-drawn fibres immersed in deionised water dissolved at a greater extent in comparison to annealed ones as shown in Figure 3.9. The mass loss profile of as-drawn fibres in deionised water corresponded well to PBS conditioning up to day 15. From this point onwards, as-drawn fibres dissolution behaviour in deionised water and PBS significantly diverged. The greater mass losses observed for deionised water conditioning for time points in excess of day 15, may be attributed to the arresting effect of the increased ionic strength of PBS in comparison to deionised water [264]. Contrary to PBS, no continuous tube-like structures were formed as a result of glass dissolution in deionised water, but presented corrosion pits randomly distributed throughout the fibre body, as exemplified in Figure 4.1b.

The formation of precipitate residues during PBS conditioning could have also accounted for the differences of mass loss observed after day 15. As conditioning time elapses and phosphate glass fibres dissolve, the fraction of precipitate increased which could have masked the real mass losses experienced at the latest time points. This observation is further supported by the estimation of as-drawn mass loss via the reduction in fibre diameter, from which similar results for deionised water and PBS (in excess of 90%) were obtained at day 30.

The late materialisation of flake-shaped debris (at day 15 in deionised water in comparison to day 1 for PBS conditioning, as shown in Figure 3.7 and Figure 3.8) and the complete absence of well-defined tube-like structures in deionised water conditioning, suggests that although solution saturation with orthophosphates do not supress glass dissolution, it is a prerequisite to the formation of precipitates on the fibre surface.

Unlike deionised water, which is virtually depleted of all ionic species, PBS has an initial P concentration (in the form of orthophosphates) of 11.9 mM, which corresponds to 14.76 mg of phosphorous in a 40 ml aliquot of as-prepared PBS. Such amount is equivalent to 12% of the P initially present in the 400 mg samples of P45Fe2 glass fibre investigated, which, given the mass loss profiles described by as-drawn fibres in both PBS and deionised water up to day 15, should have been released after roughly 3 days of sustained dissolution. It should be kept in mind that the phosphate chains released into solution are not immediately hydrolysed (making possible the use of solution techniques to characterise phosphate glass structure), which in addition to the periodic media refreshment (see §2.8), prevented the solution from reaching the cut-off concentration of orthophosphate anions for the nucleation and subsequent growth of tube-like precipitates.

These conclusions are in line with the morphology changes observed previously during *in vitro* degradation of iron-metaphosphate glass fibres [158, 160]. Although the formation mechanism was different from the one proposed here and discussed in §4.3.4, the aforementioned tube-like structures where observed following static dissolution (the conditioning media was not changed throughout the entire study) in deionised water at 37°C of phosphate glass fibres.

The corrosion pits observed in some of the as-drawn fibres conditioned in deionised water (cf. Figure 4.1b) could have been created as a result of accelerated local dissolution due to the presence of defects in the glass fibres (surface flaws, striae and anisometric inhomogeneous domains) which could have formed during glass synthesis or created in the course of fibre drawing. These pits may have been also formed in as-drawn fibres conditioned in PBS, but their presence could have concealed by the outer precipitate shell.

Hydrolytic cleavage of P-O-P bonds in hydrated phosphate chains (preferentially via end-group clipping) results in the formation of ortho- and polyphosphate anions that can be deprotonated at the thermodynamic conditions of the solution, decreasing the pH of the medium, which in turn accelerates phosphate glass dissolution and promotes further release of acidification of the conditioning medium [13, 265, 266]. These observations are in good agreement with the decrease in the pH of the conditioning media during the first days of the *in vitro* fibre degradation study from 7.45 to 6.99 and the higher mass losses experienced by the as-drawn fibres in comparison to annealed ones as presented in Figure 3.9. The reduction in the reacting area as the glass fibres core progressively contracts resulted in a decrease in the concentration of acidic entities and the gradual rise towards the pH of the as-prepared PBS solution.

4.2 Manufacture of Fully Bioresorbable Fibre Reinforced PGF-PLA Composite Plates via Cyclic Pressure-assisted Compression Moulding

Melt processing is a widely used technique at the industrial level for the manufacture of thermoplastic products and its fibre reinforced variants [173]. One of the main issues that precludes fibre reinforced thermoplastic products from structural applications, is the difficulty in achieving thorough melt impregnation using conventional equipment without inducing considerable fibre attrition or significantly degrading the matrix consequent to long term exposures to high temperatures. Therefore, alternate approaches to alleviate the viscosity hindrance other than those relying on high temperature and/or high stresses, such as the pressure cycling method presented here, are likely to enhance the composite performance and pave the way for product adoption.

4.2.1 Rheological Characterisation of 3251D Poly(lactic acid)

Linear viscoelastic properties of 3251D PLA in the 170°C-200°C range are shown in Figure 3.11. For all test temperatures but 170°C, PLA remained within the Newtonian plateau throughout the range of solicited frequencies, as suggested by the shear rate independency of the complex viscosity. Typical liquid-like behaviour of 3251D PLA at all test temperatures, excepting 170°C,

was indicated by i) the position of the G'' curve above the storage modulus and ii) the scaling factors proportional to $\sim\omega$ and $\sim\omega^2$ for the loss and storage moduli over the whole frequency range as demonstrated by Figure 3.11a [267, 268]. The increase of the storage modulus in proportion to the oscillation frequency squared was associated with the reduction of the measurement time-scale ($\sim\omega^{-1}$). As the frequency is progressively increased, the measurement time-scale becomes comparable to the materials relaxation time-scale (commonly assumed as the reciprocal of the crossover frequency), so the material's capacity to dissipate stresses becomes less effective in favour of a more elastic response [269].

The shift of the complex viscosity, storage and loss moduli towards lower values with increasing temperature was a consequence of the increase mobility of the polymer chains. The observed deviation at 170°C from the progressive shift of the curves obeyed in the 175°C-200°C temperature range for the storage and loss moduli, which almost superpose each other, is an indication of a transition from liquid-like to solid-like behaviour. This is in good agreement with the DSC results for virgin 3251D PLA presented in Table 3.4. At 170°C a fraction of PLA chains remains in the compact crystalline form, which has a solid-like behaviour.

Zero-shear viscosity values at each of the test temperatures were estimated using the Carreau-Yasuda equation. As expected, zero shear viscosity values decreased as the solicitation temperature increased due to the increased mobility of the polymer chains. Based on these results, and due to the prone degradation of PLA at temperatures in excess of the melting point [270], 180°C was selected for the manufacture of fibre reinforced composite plates, as it was considered to be the lowest temperature with an appropriate safety margin in case of temperature variation during compression moulding.

4.2.2 Effect of Processing Variables in Cyclic Pressure-assisted Compression Moulding of Fibre Reinforced Composite Plates

Figure 3.16 demonstrates that the magnitude of consolidation pressure is the most relevant parameter for the manufacture of fibre reinforced composite plates via of cyclic pressure-assisted compression moulding. The ca. 30% higher flexural strength of the fibre reinforced composite plate consolidated at

40 bar cyclic pressure with respect to the plate consolidated at 30 bar cyclic pressure was attributed to the enhanced wetting of the fibres as a result of the higher pressure applied. As shown by Figure 3.16a, pressures in excess of 40 bar resulted in a progressive decrease of the flexural strength as a consequence of the higher compaction of the fibre network, which could not be completely relaxed in the course of the unloading part of the pressure cycle, impairing fibre impregnation.

Pressure is partly transferred to both polymer melt and reinforcement during consolidation [165, 271]. Since, the load-share of the fibre network increases with compaction, pressure increases will force the fibres into a more densely packed array, effectively reducing the space through which molten polymer can seep through and fully wet individual filaments. Decreases in the strength of fibre reinforced thermoplastic composites with increasing pressurisation of the polymer melt have been reported in [272, 273].

In spite of the reduction in viscosity at the increasingly higher processing temperatures (30% and 50% reduction with respect to the zero shear viscosity at 180°C, cf. Figure 3.12), which in theory should lead to better mechanical properties as a result of easier polymer percolation, no significant differences ($p>0.05$) were noted in the flexural strengths of the fibre reinforced composite plates fabricated at different temperatures as demonstrated in Figure 3.17a. The independence of the flexural strength with respect to processing temperature further demonstrates the efficiency of cyclic pressure implementation in the manufacture of composite products with thermally unstable polymer matrices.

The reduction in the 200°C-composite plate thickness with respect to the reference plate fabricated at 180°C (see Table 3.8) was attributed to the loss of polymer during composite consolidation. Polymer leakage from the mould was facilitated by the reduced viscosity at 200°C as demonstrated in Figure 3.12. Moreover uniformly dispersed small bubbles (vacuum voids) were noted in the matrix in the single case of the 200°C-composite plates. Such defects were suggested to form as a result of non-uniform contraction in response to matrix depletion during the cooling stage of composite manufacture. Vacuum voids formation will be further discussed in §4.4.

These observations were in good agreement with the results of void content analysis. The higher void content in the 30 bar- and the 200°C-composite plates were associated with the higher content of microvoids product of insufficient consolidation pressure in the former and the formation of vacuum voids as a result of non-uniform polymer contraction in the latter, respectively.

No significant differences ($p>0.05$ in all cases) in flexural modulus with respect to the 180°C-reference composite plate were prompted by increases in consolidation pressure or processing temperature. Such behaviour is in line with the results highlighted elsewhere, in which, unlike the flexural strength, the modulus was observed to be negligible affected by the impregnation quality of the composite.

The results presented here highlight the potential of the PGF-PLA system and the significant advantages of the implementation of cyclic pressure in compression moulding for the manufacture of structural composite products with optimum mechanical properties and limited thermal degradation.

Although this work was mainly concerned with poly(lactic acid)-phosphate glass fibre composites, the effects of cyclic pressure here demonstrated are not restricted to this particular system and may find application in the manufacture of alternative thermoplastic products.

4.2.3 Characterisation of Compression Moulded Composite Plates

The absence of air bubbles in the interply regions (see Figure 3.15) and the overall low void contents calculated for the fibre reinforced composite plates fabricated through both pressure profiles indicated that the initial pressure cycling managed to successfully eliminate pockets of air trapped between the laminae and vapour possibly generated from moisture adsorbed during mould loading.

Typically, for each 1% increase in void content, the mechanical properties (tensile, flexural and compressive) of fibre reinforced composites show a reduction of approximately 7% [273-276]. Considering the similar, and rather low void contents (listed in Table 3.6) calculated for the SP and CP series of composite plates, the substantial difference observed in flexural strengths

(going from ca. 30% for the 0.15, 0.25 and 0.35 volume fractions up to ca. 50% in the 0.45v_f sample) cannot be solely based on the detrimental effects of macroscopic voids, if present.

As determined via Equation 3.2, the effective fibre strength in the CP composite plates series (ca. 950 MPa) was 36% higher than that associated with the SP composites plate series (700 MPa). Such a difference was suggested to arise at least partly from the superior degree of impregnation achieved by cycling the applied pressure, and the associated reduction in the interstitial areas of trapped air between individual filaments (referred to as microvoids) [273, 277]. This statement is better illustrated in the case of the 0.45v_f composites. The poor fibre wetting achieved via application of static pressure resulted in the large voided areas observed in the cross section of the 0.45-SP composite plate specimen (Figure 3.15g). Conversely, no such defects can be observed in the cross section of the 0.45-CP composite plate consolidated under cyclic pressure (Figure 3.15h).

As schematically shown in Figure 4.2, the application of static pressure compacts the fibre network, hindering the percolation of the polymer through the micron-sized inter-filament gaps [272, 273, 278]. Due to viscoelastic response of the polymer melt, the stresses induced by the application of pressure gradually relax, and so does the fibre network, allowing a partial recovery of the fibre network permeability and penetration of the polymer melt. Viscous relaxation inevitably causes a gradual reduction in pressure-driven melt penetration, limiting the fibre wet-out efficiency of the static pressure consolidation profile.
However, through cyclic pressure implementation, recovery of the fibre mat permeability may occur during the unloading part of the pressure cycle (see upper part of Figure 4.2). Upon loading resumption, the pressurised fluid percolates more readily through the interstices in the relaxed fibre network. This process was repeated in successive cycles, leading to discrete polymer percolation steps which rendered an overall superior fibre wet-out in the cycled pressure composite plate series in comparison to the static pressure counterpart.

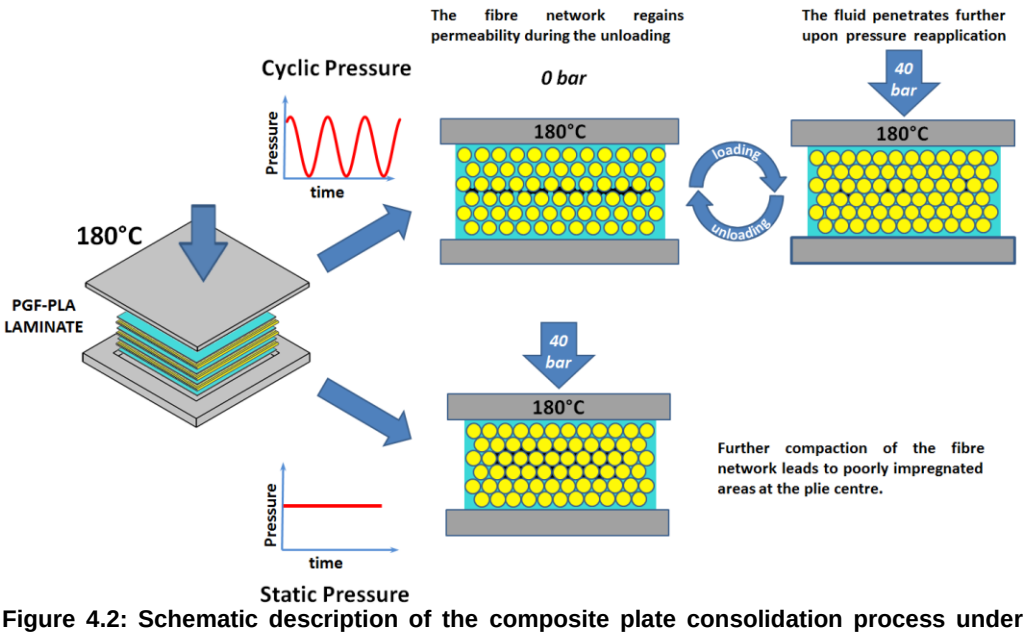


Figure 4.2: Schematic description of the composite plate consolidation process under cyclic and static pressure.

Another advantage of cyclic pressure is its ability to compensate for adverse capillary effects. As the flow front advances, air volume within the individual lamina is progressively reduced, leading to the development of an internal back pressure in the remaining microvoids which counters the externally applied load [273]. At this stage, further penetration of the polymer melt would then be controlled mainly by capillary forces as a result of the reduction in the applied pressure.

In systems where differences of surface energies exist (as is the case of the hydrophilic bioactive glass surfaces and the hydrophobic poly(α-hydroxyacid) melts [191, 279]), the capillary pressure tends to oppose further resin penetration [280]. Consequently, in composite systems consolidated via static pressure, a considerable amount of entrapped air could remain at the centre of the fibre bed in the form of elongated bubbles preferentially located in the region adjacent to the fibres to minimise their surface tension. The longer the diffusion path of the penetrating fluid, the more severe the concentration of residual air will be.

In contrast to static pressure consolidation where relaxation of the applied pressure is slow, the entrapped gas volume is able to quickly change in response to the pulsating motion and reduce the opposing capillary pressure through cyclic pressure implementation. Since the restraints imposed by the surrounding medium relax in the course of the unloading part of the cycle, elongated air bubbles can reduce their surface energy by coalescing and

adopting a spherical shape. When the load is resumed, the highly stable spherical bubbles resist being deformed and are forced to abandon the interstices between neighbouring fibres.

Additionally, due to the pseudoplastic behaviour of PLA [281, 282], the application of cyclic pressure may induce a redistribution of shear stresses in the melt, leading to a local alignment of the polymer chains and the concomitant reduction of the apparent melt viscosity, ultimately allowing easier percolation through the fibre network interstices. Recent publications on augmented injection moulding process have suggested that an altered rheological state can be induced in non-Newtonian fluids through the application of oscillatory forces [283-286]. However, since the early study of Barnes et al. [287] it was known that the induction of pulsed sinusoidal pressure gradients with non-zero means resulted in superior flowability of a non-Newtonian fluid causing a reduction in melt viscosity due to the shear-thinning.

The enhanced impregnation quality and concomitant composite densification through combination of the aforementioned mechanisms accounted for the higher flexural strengths of the CP-composites series. Furthermore, the physical effects of cyclic pressure in this study resulted in the highest hitherto reported mechanical properties for PGF-PLA composites [17, 195, 232, 288]. The mechanical properties of the cyclic pressure-composite plates were even found to be 26% and 45% greater to those cases where the fibre surface had been treated with 3-aminopropyltriethoxy silane and sorbitol ended PLA oligomers, respectively, to improve the fibre-matrix adhesion [230].

The similarity in modulus for both composite plate series indicated that, contrary to the flexural strength, the flexural modulus was less sensitive to the presence of interfacial defects in agreement with previous studies [275, 289]. This was expected since composite's elastic response result from volume-averaged stress and strain fields [290]. On the other hand, matrix dominated properties like flexural strength are influenced by defect location throughout the cross section as a result of the non-uniform stress distribution during bending [289]. Nonetheless, divergence from the theoretical behaviour described by the rule of mixtures (Figure 3.13b) in the 0.35 and 0.45 fibre volume fraction cases, suggested that the dominating factor for the

observance of maximum stiffness values could be ascribed to the distribution of the reinforcement throughout composite plate's cross section.

To better evaluate the impregnation efficiency of both methods, the laminated composite plates were assembled from progressively thicker fibre mats. As a result, fibres were increasingly segregated as the nominal volume fraction increased. Therefore, the presence of polymer rich zones and fibre clustering gave rise to modulus values lower than those theoretically achievable since modulus estimation via rule of mixtures assumes a uniform distribution of the reinforcement throughout the entire composite cross section [228]. Similar effects of laminating composition on composite modulus have been reported for compression moulded PLA-PGF composites plates [195].

It has been shown that the improvement gained by the incorporation of reinforcements can be one order of magnitude greater for semi-crystalline matrices in comparison to amorphous products [291]. Such a difference has been attributed to the occurrence of a transcrystalline layer around the reinforcement resulting from the high heterogeneous nucleation ability of the fibre surface [292-294]. A transcrystalline interphase is thought to perform as a strong mechanical interlock which improves stress transfer between fibre and matrix. The effect is thought to particularly relevant in composites with poor matrix-fibre interfacial adhesion as is the case PLA-PGF composites [293].

Previous investigations in polymer processing have demonstrated that one of the effects of the in-mould manipulation of the polymer melt is the change in the crystallisation kinetics and the resultant crystal morphology of the thermoplastic product [295, 296].

As illustrated by Table 3.5, crystallinity developed upon cooling during manufacture of both composite plate series, the extent of which was greater for the SP samples. Decreases in the molecular weight have been shown to significantly affect the crystallisation of PLA as a result of the increased mobility of shorter polymer chains, however these increases in diffusion were found negligible in samples with molecular weights in the range of 10^5 $g \cdot mol^{-1}$ or higher [297, 298]. Therefore, the crystal content increase in proportion to the fibre volume fraction for both composite series can be attributed to the nucleation and growth of crystals favoured by the fibre surface [299]. In spite

of the low crystallinity content (maximum ca. 5.5%), its occurrence could be significant to the mechanical properties of the fibre reinforced composite if located at the fibre-matrix interface.

The shift of the crystallisation peak and the progressive evolution of a shoulder in the low temperature side for the CP composite plate series evidenced the heterogeneous nucleation ability of phosphate glass fibres, which reduced the thermal energy barrier for nucleation and crystal growth upon heating. Such a shoulder, absent in the neat-PLA plate sample, has been attributed to a crystallisation kinetics decay once the growth of surface nucleated spherulites is restricted to directions perpendicular to the fibre surface by steric hindrance, giving rise to a transcrystalline layer [300, 301]. The transcrystalline envelope continues to grow until further development is hindered by the impingement with bulk spherulites, after which the crystallisation rate rapidly declines.

No such shoulder was observed on the crystallisation peaks of the composites in the whole SP composite plate series. All the peaks equally shifted towards lower temperatures and exhibited a shape analogous to the neat-PLA plate. The close resemblance of the crystallisation peaks in the SP composite plates to neat-PLA, which progressively shrank due to less availability of polymer matrix in proportion to the fibre content, and the peak displacement were indicative of the absence of transcrystallinity in these samples, in favour of bulk spherulites. This result agreed with previous findings where unsized glass fibre was denoted as a poor transcrystallinity former under quiescent conditions in various composite systems [302, 303].

The difference in matrix crystallisation behaviour upon heating and its persistence after remelting in this study suggested a local chain alignment consequent to the application of cyclic pressure. This configuration might be stabilised in the molten state by the physical arrest imposed on the polymer chains as a result of the intimate contact with the glass fibres, or alternatively by polar interactions of the carboxylic moieties in PLA with the hydroxyl groups on the fibre surface.

Pre-alignment of polymer chains near the fibre surface may account for the preferential occurrence of transcrystallinity in the cyclic pressure composite plate series. At this stage, it is unclear if the relatively low crystallinity and the

development of transcrystallinity in the PLA-PGF composite system leads to a beneficial effect on the interfacial shear strength in the CP composite plate series. Further studies on transcrystallinity in the PLA-PGF system and its effect on interfacial shear strength should be conducted to address this issue.

Despite the limitation of the processing temperatures to 180°C and the thorough evacuation of moisture before processing, the chromatography results suggested that PLA was increasingly degraded throughout the composite plate manufacturing sequence as shown in Table 3.7.

Thermal degradation was more noticeable in the composite plates, especially in the 0.35 and 0.45 volume fractions, where the post-processing molecular weight decreased to *ca.* 85% and 80% of the number average molecular weight of virgin PLA respectively. The similarity between the neat-PLA plate strength processed at 180°C (75±3 MPa) and the effective matrix strength in the composites (ca. 77 MPa), suggested that the mechanical properties of the matrix were not significantly altered due to molecular weight decrease associated with the matrix-fibre interactions at the processing temperature. This result is in good agreement with previous studies where no significant difference in strength and modulus were observed for PLA tensile specimens with molecular weight reductions in the order of 10^4 g·mol^{-1} [304, 305].

Due to the hygroscopic nature of the PLA and the high surface energy of phosphate glass fibres [306], both constituents tend to collect low energy compounds present in the local environment including water vapour and organic contaminants during mould loading. The higher the volume fraction of the composite, the more moisture was likely to be present in the laminate before consolidation. Upon heating, the polymer melt reacts with the adsorbed water, leading to reduced molecular weight [70, 106].

Similar observations with respect to molecular weight decrease of PLA have been reported in the melt processing of particulate Bioglass® reinforced-PLA products [191, 207]. A significant drop to ca. 30% of the original poly(lactic acid) molecular weight was reported in spite of the small filler content used (ca. 2% in volume) [207]. The reduction was also attributed to the severe hydrolytic reaction between PLA and the hydrated glass particles occurring at the processing temperatures. This effect, in addition to the poor glass/polymer

interface and the porosity stemming from bubble generation during extrusion, led to composite mechanical properties lower than those of neat PLA [207].

4.3 Effect of Forging on Mechanical Properties and *In Vitro* Degradation of Fully Bioresorbable Fibre Reinforced PGF-PLA Composite Rods

More than often, open fracture reduction is required to restore the bone anatomy, which entails the surgical implementation of a fixation device, generally in the form of metallic plates, rods, pins and screws. Nevertheless, as a consequence of the altered mechanical environment, the bone remodelling equilibrium will be displaced towards bone resorption, which ultimately results in bone mass loss in the shielded region. As such, the development of materials with bone matching properties which could provide immediate fracture stabilisation and progressively transfer load to the healing bone tissue are highly sought after.

The differences in mechanical properties of the composite plates used in the current study (cf. Figure 3.19 and Figure 3.20) for the subsequent fabrication of forged composite rods were attributed to the degree of impregnation and low void contents achieved via implementation of cyclic pressure in comparison to static pressure consolidation as stated in §4.2.

4.3.1 Effect of Uniaxial Compression Forging on Fibre Reinforced Composite Rods

The 35% and 17% increase in flexural strength and modulus, respectively, in the uniaxial compression forged neat-PLA rods with respect to the neat-PLA plate, as shown in Figure 3.19a, was ascribed to the alignment of poly(lactic acid) chains along the rod axis, resulting from extensional flow within the die channel induced during uniaxial compression forging. Similar effects have been reported in previous publications where the high collimation of polymeric chains consequent to solid state drawing resulted in a considerable increase in mechanical properties for thermoplastic materials including poly(lactic acid) [191, 307].

On the other hand, the deleterious effect of uniaxial compression forging on the mechanical properties of the composite rod samples in relation to those of the initial fibre reinforced composite plates was attributed to fibre breakage

during processing as illustrated by Figure 3.21d. Due to the low strain to failure of the reinforcing phosphate glass fibres (ca. 1.5% [308]) at the forging temperature, the glass fibres could not stretch sufficiently to accommodate the extensional deformation introduced during uniaxial compression. As seen in 3.21d, the fibre breakage descried a sinusoidal pattern that spanned the entire ***y-z section*** of the composite rod, providing a preferential path for crack growth upon sample loading.

The higher the fibre content, the greater the number of compromised zones with fractured fibres that could nucleate or propagate a crack, accounting for the greater reduction in strength for the $0.25v_f$ and $0.35v_f$ uniaxial compression forged composite samples in relation to the $0.15v_f$ specimens. The presence of these forging induced defects prevented the uniaxial compression forged rods from being loaded up to the point where fibre fracture is observed during testing (composite failure was always observed to occur in an angled plane created by the sinusoidal fibre breakage pattern), and therefore no differences in strength were observed between the uniaxial compression forged composite rods obtained from composite plates consolidated under different pressure schemes.

Continuous unidirectional fibre and random discontinuous fibre bioresorbable composite rods have been produced from phosphate glass fibres and poly(lactic acid) under similar processing conditions in previous investigations via forging of preconsolidated composite blanks [15, 18, 231]. In these studies, composite blanks with fibre volume fractions in excess of 0.3 were heated to 90-100°C and subsequently reshaped into cylindrical rods through uniaxial compression forging with an estimated 20% extensional ratio (calculated from the reported rectangular blank and cylindrical rod dimensions and considering the composite as an incompressible solid).

Contrary to the results here presented, enhanced mechanical properties for the uniaxial compression forged composite rods in relation to those of the composite plates found were ascribed to the alignment of the polymer chains [15]. However, no mechanical tests were conducted on the “parent” composite plates from which the bars were obtained to support such a claim and to rule out the possibility of simply a batch-to-batch variation in the mechanical properties of the composite plates. In addition, no remarks were made on the

changes experienced by the continuous fibre reinforced composite rods consequent to an extension of 20%; the phosphate glass fibres remained arguably unaffected despite the use of an extensional ratio that doubled the one in the current study [15, 18, 231].

Deformation of continuous fibre reinforced thermoplastic composites can be achieved without fibre breakage through multiple flow processes of which interply slippage is the most commonly observed. At temperatures close to the melting point of the polymer matrix, the individual plies of the composite structure become spontaneously deconsolidated (prompted by release of elastic energy stored in the composite as residual stresses after compaction [309]) and can easily slide relative to each other as a result of the lubricating action of the interply resin-rich layers, consequent to the application of normal pressure [310, 311]. Nevertheless at 90-100°C, the PLA matrix is still able to transfer stresses into the fibre-rich layers by interfacial shearing which ultimately results in tensile failure of the fibres.

4.3.2 Effect of Plane Strain Forging on Fibre Reinforced Composite Rods

In contrast to uniaxial compression forging, extensional flow in the z-direction was prevented due to confinement of the sample within the die channel during plane strain forging. As a result, the mechanical properties of the initial flat laminates were preserved seemingly unaffected in the plane strain forged composite rods for the neat-PLA, 0.15 and 0.25 volume fractions samples. Conversely, for the $0.35v_f$ and $0.45v_f$ composites series, the mechanical properties were deleteriously affected by plane strain forging, regardless of the impregnation quality in the fibre reinforced composite plate, as demonstrated in Figure 320a.

No such reduction was observed in the 0.35-CP-M composites following plane-strain forging, and in the case of 0.45-CP-M forged composite rod samples, the decrease in mechanical properties was considerably lower in comparison to that experienced by both the 0.45-CP and 0.45-SP plain strain forged composite rods obtained from composite plate fabricated using thick glass fibre mats. As a result of the processing conditions, the matrix was still capable of transferring compressive stresses to the fibres. These stresses can be relaxed through plastic deformation of the individual plies in the ***x-y*** plane. However, due to shortage of lubricating resin-rich zones in the highly

segregated and compact fibre-rich zones in composites with 0.35 and 0.45 volume fractions fabricated from thick glass fibre mats, such relaxation process is hindered, leading to the creation of delamination cracks as an alternative stress relieving mechanism as illustrated by Figure 3.21b. The growth of these pre-existing cracks during mechanical testing resulted in the significant reduction of flexural properties for the thick-mat $0.35v_f$ and $0.45v_f$ plane strain forged composite rod samples as illustrated by Figure 3.20a.

4.3.3 Effect of Glass Fibre Mat Thickness in Plane Strain Forged Fibre Reinforced Composite Rods

The nucleation of intra-ply cracks was reduced through the inclusion of a greater number of polymer layers which effectively reduced the intra-ply friction associated with fibre-fibre contacts and assisted the compressive stress relaxation through deformation of the laminate plies for $0.15v_f$, $0.25v_f$, 0.35-CP-M, 0.45-CP-M sample sets during plain strain forging. The beneficial role of inter-ply polymer layers in the post-processing of thermoplastic laminates has previously been observed in [310, 311]. In these studies, the resin located in the interply spaces was observed to behave as a viscous fluid confined between two plates sliding relative to each other, as described by Couette laminar flow.

Intra-ply cracking during the plane strain forging process could also have been assisted by the longitudinal compressive stresses generated in response to the constraint imposed by the tool's walls at the respective end of the inner channel. Longitudinal compression creates transverse tensile stresses which tend to primarily disrupt the interfacial fibre-matrix bond. It has been suggested that the magnitude of such transverse tensile stress components is proportional to the inter-fibre distance [312]. Therefore, the thicker the polymer-rich zones, the greater the magnitude of the transverse tensile stresses in the fibres bordering these regions. This seemed to be in good agreement with the greater reductions in flexural strength for the forged composite rods obtained from thick-mat composites, in which the thickness of the polymer-rich zones was greater than those in the composites fabricated using thinner glass mats.

The decrease in mechanical properties observed in the 0.45-CP-M forged composite rods in comparison to the composite plates regardless of the use of

thin glass fibre mats could be taken as an indication of the cut-off fibre volume fraction (~0.35) that can be safely processed in plane strain forging conditions at 90-100°C without the creation of intra-ply cracks.

Optimum impregnation and reinforcement dispersion are two variables that play a dominant role in the mechanical performance of thermoplastic composites [313]. Easier percolation of the polymer melt and enhanced through-thickness distribution of the fibre reinforcement can be readily attained through the stacking of thinner glass fibre mats as it was the case of the 0.35-CP-M and the 0.45-CP-M fibre reinforced composite plates. In spite of this and contrary to the expectation, the flexural strength of the 0.35-CP-M and the 0.45-CP-M compression moulded composite plates were lower than those of the plates with matching volume fraction constructed with thick glass fibre mats and also consolidated under cyclic pressure.

Such a reduction in flexural strength was suggested to arise from the greater number of interfacial defects at the meeting point between opposite polymer melt flows (weld-lines) for the 0.35-CP-M and the 0.45-CP-M laminates, in which the number of glass fibre mats were 67% and 150% greater than the number of mats used in the 0.35-CP and 0.45-CP thick-mat composite plates, respectively. The presence of such defects can be clearly observed in the fracture surface of neat-PLA rods in Figure 3.24a. The detrimental effect of these weld-lines in thermoplastic products has been thoroughly reported in the literature [314, 315]. The presence of weld-lines in injection moulded products was also reported to reduce the mechanical properties of tensile test specimens. The effect was more pronounced in the case of brittle thermoplastics (like PLA) where the tensile strength was observed to decrease by a factor of two [316].

Unlike the flexural strength, the modulus of the compression moulded composite plates fabricated with thin glass fibre mats was not negatively affected by the presence of weld-lines. In fact, the 0.45-CP-M compression moulded composite plate presented a significant modulus increase in excess of 10% with respect to both $0.45v_f$ composite plates fabricated from thick glass fibre mats and consolidated via static and cyclic pressure, respectively. This is in line with the conclusions drawn from composite consolidation under different pressure profiles in §4.2, where it was determined that contrary to the strength, flexural modulus was less sensitive to the presence of interfacial

defects. The increase in modulus for the 0.45-CP-M compression moulded composite plate could be associated with the enhanced distribution of the reinforcement throughout the plate cross section (cf. Figure 3.18 and Figure 3.22) achieved by stacking a larger number of thin glass fibre mats.

The smooth surface of the glass fibres at day 0 in the fracture surface of the plane strain forged composite rod illustrated in Figure 3.24b was indicative of the poor adhesion between the composite constituents, as a result from the incompatibility between the hydrophilic phosphate glass fibres and the hydrophobic poly(lactic acid) matrix, and the lack of coupling agents or fibre surface treatments. This in turn, facilitated the interfacial capillary transport (wicking) of water molecules and the subsequent dissolution of the phosphate glass fibres [317, 318].

4.3.4 In Vitro Degradation Study of Bioresorbable Fibre Reinforced Composite Rods Manufactured via Plane Strain Forging of Preconsolidated Composite Blanks

Figure 3.23 demonstrates that after one day of immersion in PBS, both the flexural strength and modulus of all the specimens, including the forged neat-PLA rod samples, were significantly impaired by the interaction with the conditioning medium regardless of the pressure profile used during composite plate consolidation. In contrast to previously observed behaviour of PLA products fabricated by direct melting of polymer pellets, in which the flexural strength was observed to not significantly vary throughout a 30 day period, the 43% decrease in flexural strength of the laminated neat-PLA forged rods after immersion in PBS was attributed to the presence of the aforementioned weld-line defects [231, 232]. It is reasonable to think that in laminated neat-PLA products, water molecules could diffuse more quickly through the weld-lines than in the bulk polymer and plasticise the imperfect union between the multiple layers, impairing the mechanical properties. Weld-lines could also occur in pellet-derived specimens, however, the far greater number of these interfacial defects in the latter, poses a much more tortuous diffusion path in comparison to inter-laminar weld-lines.

At day 1, only slight variations respecting the dry mass loss, water uptake and pH were registered for all the forged composite rods. No changes in the fibre morphology as a result of the interaction with the conditioning medium were

observed at this time point on the composite fracture surface as shown in Figure 3.24c. The steep decrease in mechanical properties demonstrated in Figure 3.23 and the minor changes in the said variables at day 1, especially in terms of water uptake and fibre structure, indicated that the small quantity of water absorbed was preferentially allocated along the interface between the unsized fibres and the PLA.

As a consequence of the lubricating action of the absorbed water and the lack of coupling agents and/or fibre surface treatments to enhance the fibre-matrix interfacial adhesion, the matrix could no longer efficiently transfer stresses to the glass fibres by interfacial shearing. At this point, the fibre-matrix interaction was probably governed by the frictional resistance to sliding between the fibres and the matrix (slippage), accounting for the mechanical properties of the fibre reinforced forged composites, still superior to those of neat-PLA forged rods at this stage [319].

The increased loss of strength for the 0.45-CP-M forged rods in comparison to the other forged composite rods was ascribed to the presence of intra-ply cracks induced by plane strain forging. The presence of process-induced defects, namely voids, cracks and microcracks, has been reported to accelerate the rate of fluid penetration in composite samples immersed in aqueous media [193, 320].

Forged composites rods with 0.15 and 0.25 fibre volume fractions obtained from composite plates consolidated under cyclic pressure remained stronger than the forged composite rods fabricated from plates consolidated under static pressure after one day of immersion in PBS at 37°C. This could be related to the superior fibre wetting achieved by implementation of cyclic pressure which constricted somewhat the more efficient diffusion paths of the water molecules at the interface [308].

The brief period of stabilisation in mechanical properties observed up to day 3, suggested that the reinforcement-matrix interfaces were fully saturated by day 1. Additional water absorbed was accommodated in the polymer matrix free volume. Water absorption was greater for the forged composite rods in comparison to neat-PLA forged rods (which stabilised at around 1%) as a result of the internal paths provided by the continuous hydrophilic fibres which

spanned the entire length of the composite samples, reducing the diffusion distance for the water molecules, which otherwise would have to diffuse through the bulk polymer.

The rate of water diffusion along the fibre/matrix interface has been reported to be 100-400 times faster than through the bulk polymer matrix free volume [321]. No significant differences in the water uptake behaviour arising from the impregnation quality of the composites with $0.15v_f$ and $0.25v_f$ were noticed. The proportional increase in water uptake with the fibre volume fraction was associated with the increased number of fibre-matrix interfaces susceptible to water absorption as a result of the lack of coupling agents.

Changes in reinforcing fibre morphology were first noted at day 7 as demonstrated by Figure 3.24e. The development of a core-shell structure was ascribed to the formation of insoluble glass degradation by-products as a consequence of the hydrolysis of the phosphate glass fibres surface, in similitude to the bare fibre in vitro degradation studies (see §4.1). Figure 4.3 schematically represents the suggested sequence of structural changes observed for the phosphate glass fibres in the forged composite rods as a result of exposure to PBS solution. The yellow circles represent the phosphate glass fibres and the PLA matrix is depicted by the blue background. Backscattered electron images of the polished cross sections of representative 0.35-CP-M forged composite rods at the specified conditioning time were also included to further emphasise the structural changes suggested throughout the composite rods degradation studies.

Initially, as shown in Figure 4.3a, an intimate contact exists between the fibres and the matrix as a result of the higher thermal contraction of the PLA matrix in relation to the glass fibres during the cooling stage of composite plate compression moulding. During day 1 of immersion in PBS, the fibre-matrix interface is disrupted due to the preferential absorption of water at the interface and a hydrated glass layer starts to develop as a result of the penetration of water molecules into the bulk glass. Interfacial water is represented by the blue dashed line around the phosphate glass fibres in Figure 4.3b, and the hydrated layer is represented by the solid blue line.

Further conditioning time leads to water uptake by the PLA matrix and to its consequent swelling. Water that has been accommodated in the polymer matrix free volume is denoted by the small circles with blue dotted lines surrounding the water molecule's chemical formula. At this point, the hydrated layer of glass on the fibre surface has developed to its full thickness and constantly advances inwards as the outer layer of the glass fibre is dissolved. Hydrolysis of hydrated phosphate chains takes place and as a result, the interfacial solution becomes saturated with phosphate glass degradation by-products, which in turns leads to the precipitation of insoluble phases. As stated in §4.1, the presence of orthophosphate anions In PBS may have encouraged the formation of precipitate shells around the glass fibres.

During the early stages of glass dissolution, precipitates are formed at a higher rate than the fibre reduces diameter. As a result of the constrained growth of the precipitate layer in between the fibre core and the polymer case around the fibre, the precipitates are forced into a compact shell (represented by the solid red lines around the yellow glass fibre cores in Figure 4.3c). Radial pressures arising from the polymer swelling could have contributed to precipitate compaction. The suggested compaction forces are depicted by black arrows. Formation of a precipitate layer around the glass fibre core can also be seen in the respective backscattered electron images in Figure 4.3.

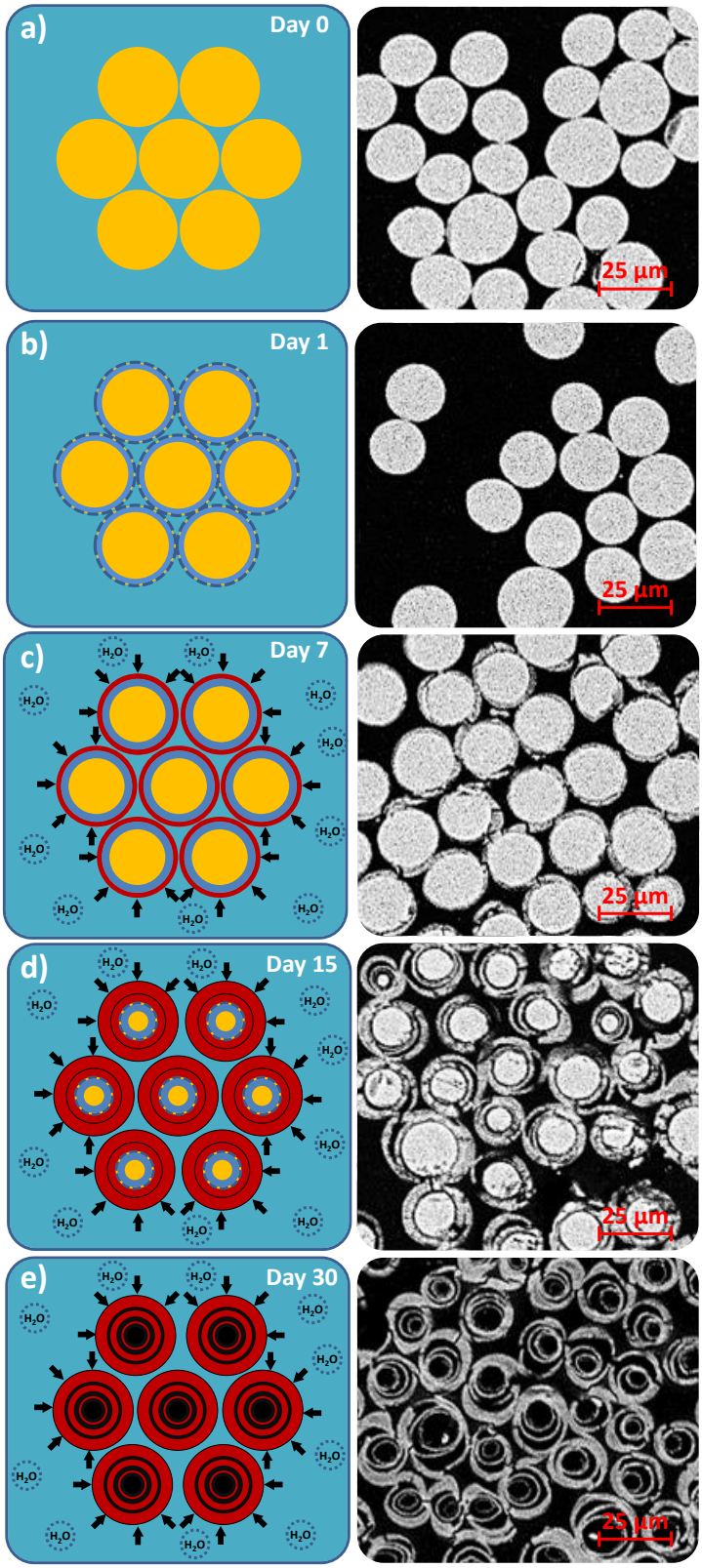


Figure 4.3: (Left) Schematic of the structural changes observed in the reinforcing phosphate glass fibres throughout the forged composite rods degradation study. The glass hydrated layer is represented by the solid blue lines and the precipitate formations are illustrated by the red solid lines enclosing the yellow fibre cores. The PLA matrix is represented by the blue background. Water molecules absorbed by the PLA matrix are depicted by the dotted lines enclosing the water's chemical formula. Water adsorbed at the interface has been represented by dashed blue lines. (Right) Backscattered electron images of the polished cross sections of representative composite rods degraded in PBS at the specified conditioning time point.

As the phosphate glass fibre dissolution continues, the volume of fibre core contracts further and the newly formed insoluble phases thicken the precipitate shell. The growth of the shell continues until it becomes unstable, possibly due to i) residual compressive stresses introduced during its formation in the presence of a curved substrate within a confined space, or ii) the reduction in fibre diameter at a higher rate than the shell growth, ultimately spalling from the glass fibre core [322, 323]. The spallation of the initial precipitate layer leads to the sequential formation of multiple shells around the shrinking core and facilitates diffusion of additional water (depicted by the blue dashed line) to the glass-media interface as schematically represented in Figure 4.3d.

Dissolution of the glass fibre continues until its total dissolution as illustrated in Figure 4.3e. At this point only the insoluble precipitate shells remain. It was also noted that in the cases where no direct contact existed between the multiple precipitate layers, thin inner shells developed with a morphology consisting of interconnected globules as shown in Figures 3.24g and 3.24h (analogous to that observed in PBS conditioned as-drawn fibres (cf. Figure 4.1a)), instead of the compact morphology always observed in the outermost shell and in some inner shells where no gaps prevented the compaction of secondary layers via the constricting action of the polymer matrix (cf. Figure 3.24g).

The formation of calcium phosphate precipitate layers on the sample surface have been previously observed and reported for *in vitro* degradation studies featuring biodegradable glasses containing phosphorous oxide, including silica-based bioactive glasses [324, 325] and notably phosphate glasses with O/P ratios in the ranges here reported [13, 320, 326, 327].

Tube-like structures, arguably resulting from the hypothetical exfoliation of a stable hydrated layer on the glass fibre surface during in vitro degradation, have also been reported in [115, 160, 328]. These structures were proposed to originate from the heterogeneous through-thickness distribution of drawing stresses and cooling rates during glass fibre manufacture, which led to the formation of an outer layer with chemical properties significantly different to those of the glass fibre core. Following immersion in aqueous media, preferential hydrolysis of the core was suggested to occur in favour of the

surface hydrated layer whose morphology remained unchanged even after 18 months of immersion in deionised water. The chemical durability of the said hydrated layer was attributed to the high collimation of phosphate chains at the fibre surface due to the fast cooling experienced during fibre drawing.

Structural differences due to frozen-in deformations and orientations have been observed to occur in melt-drawn phosphate glass fibres §4.1 [149]. The applied drawing stress produces an anisotropic open network of polymeric phosphate chains, suggested to be preferentially oriented in the fibre drawing direction. Glass network rearrangements towards the metastable liquid-like equilibrium structure are prevented by the fast cooling experienced during manufacturing. The higher the cooling rate, the lower the density (larger interstitial/free volume) of the structure frozen into the glassy state and the higher the residual strains and stresses caused by the differences in specific volume between the bulk and the outer layers of glass [329].

Potential differences in the structure of phosphate glass fibres could be possibly introduced as a result of thermal gradients throughout the fibre cross section. However, such differences, if present, are expected to be minor due to the small fibre dimensions (in the tens of micron range) which prevent large thermal gradients to be established between the core and the outer skin layer. In fact, the small dimensions of glass fibres (in the range of tens of microns) is the basis of the impracticality of glass fibre strengthening via thermal tempering (which requires the glass products to have thicknesses greater than 2 mm to achieve the necessary thermal gradients via air cooling) [154, 330, 331].

In any case, the faster cooling of the surface in relation to the bulk would produce residual compressive stresses in the surface which should be balanced by tensile stresses in the bulk [332]. Tensile stresses have been demonstrated to exponentially accelerate water diffusion into the glass network; the opposite occurring with compressive stresses [333, 334]. The rate of water diffusion in glasses is primarily controlled by steric hindrances imposed by the size of the interstices within the glass network [335]. Since hydration is the dominant reaction in the dissolution of phosphate glasses, glass networks with larger interstices along with the presence of residual tensile stresses should in fact favour the dissolution of outer glass layers

instead of the bulk (which should be under compressive state), contrary to the internal hydrolysis degradation mechanism for iron phosphate glass fibres suggested in [160].

Moreover, as conclusively demonstrated in this study and in previous investigations, [159, 160], the relaxation of precisely the anisotropic features frozen-in during fibre drawing through thermal treatment considerably decrease the overall degradation rate of phosphate glass fibres. Such conclusion is again at odds with the occurrence of a durable glass surface layer whose chemical stability was suggested to stem from phosphate chains locked in highly oriented positions.

The interconnected formations observed around the glass fibre cores which spanned multiple orifices in the PLA matrix (especially evident in bottom left side of Figure 3.24f) supports the suggested formation and consolidation of calcium phosphate precipitates into compact structures since, unlike in silicate-based glasses, repolymerisation of phosphates does not occur under the temperature-pressure conditions here investigated [266]. The dimensional stability of the outer and inner shells throughout the entire degradation study conflicts yet again with the hypothesis of the stability of detached hydrated layers of glass since earlier studies have shown that the aqueous degradation of phosphate glasses occurs via dissolution of phosphate chains precisely from the hydrated layer [13, 264, 336]

It has been thoroughly demonstrated that the degradation of phosphate glasses with structures based on long polymeric phosphate anions (namely, meta- and polyphosphate compositions) occurs via congruent dissolution provided that the Fe/P ratio is relatively low (around 0.12) [13, 133, 264, 336]. Congruent dissolution of phosphate glasses implies that there is no divergence of the hydrated layer stoichiometry with respect to the bulk glass. The variation in the relative concentrations of all the modifier cations in the shells with respect to the fibre core and the non-degraded glass presented in Table 3.9 further supports the formation of precipitates from glass dissolution by-products.

The detection of potassium (exogenous to the P45Fe2 glass composition) in the precipitates can be traced back to the phosphate buffered solution used as

conditioning media. Comparable stoichiometric changes (i.e. a decrease in the Na content and an increase in Ca and Fe contents with respect to the non-degraded glass composition) in the layers formed during in vitro degradation in deionised water have also been reported in [160]. These stoichiometric changes in the suggested hydrated layers were associated with the diffusion of metallic cations into the glass to charge balance the preferential leaching of Na ions, neglecting the congruent dissolution of phosphate glasses with low Fe/P rations (the two phosphate glass compositions studied in [160] featured Fe/P ratios of 0.1 and 0.06, which are inferior to the lowest value for which congruent dissolution was still observed in iron phosphate glasses with a comparable content of phosphorous oxide [133]) as demonstrated by compositional analysis of the hydrated layer which has been found identical to the pristine glass [13, 133, 336].

The reduction in fibre diameter first observed at day 7 as shown in Figure 3.24 suggested that the transfer of stresses from the matrix to the reinforcement via frictional slip becomes less effective due to the reduced fibre-matrix contact.

This coincided with the changes observed at day 7 in Figures 3.23 and 3.25, namely: i) the renewed decrease in flexural properties observed for all forged composite rod samples (most noticeable in the 0.35-CP-M and 0.45-CP-M forged composite rods which presented decreases in both flexural strength and modulus of around 40% with respect to day 3 values), ii) the significant reduction in mass in the dried composites (ranging from 0.8% for the 0.15-CP forged composite rods to a maximum of 7.6% for the 0.45-CP-M forged composite rods), and iii) the considerable increase in water uptake for all the forged composite samples (ranging from 2% for the 0.15-SP samples to a maximum of 12% for the 0.45-CP-M forged composite rods) in relation to the neat-PLA control which presented values of ca. 0% and 1% for dry mass changes and water uptake, respectively.

At this stage, the flexural strength of the rods forged from composite plates consolidated under cyclic pressure remained superior (22% and 16% for the $0.25v_f$ and $0.15v_f$ forged composite rods respectively), although only modestly with respect to those obtained from static pressure-consolidated plates.

The reinforcing effect of the phosphate glass fibres was completely lost for all the forged composite rods regardless of the consolidation scheme by day 15 as demonstrated by the inflexion of all the composites strength profiles which plateaued close to the PLA values at this time point. In addition, as the glass fibres dissolve, more space is available within the orifices in the PLA matrix to accommodate additional water, which resulted in an increased water uptake proportional to the glass fibre volume fraction as seen in Figure 3.25a.

The decrease in the pH of the PBS solution, also noted during in vitro bare glass fibre dissolution, was attributed to the creation and release of acidic phosphate anions consequent to the breakage of P-O-P bonds through hydrolysis of phosphate chains. Hydrolysis of P-O-P bonds is catalysed in acid environments, which further increased the rate of dissolution of the glass reinforcement in the forged composite rods [266, 327]. It was expected that the higher the phosphate glass content in the forged composite rods, the greater the number of hydrated phosphate chains leached into solution which in turn increased the concentration of acidic species created as a result of phosphate chain hydrolysis. This was in good agreement with the observed pH decrease in direct proportion to the fibre volume fraction illustrated by the inset in Figure 3.25a. Similar changes in the pH of the conditioning media have also been previously reported in glass powder dissolution studies with composition having O/P ratios similar to the one discussed here [266, 327].

As shown by Figure 3.24f (where mostly fibre cores of ca. 5 μm can be observed), the majority of the phosphate glass fibres were dissolved by day 15 which coincided with the increase in pH. This fact suggested that the increased concentration of acidic species in solution up to day 15 can be attributed to dissolution by-products of the hydrolysis of condensed phosphates rather than to the dissociation of carboxylic acid end groups originated from the PLA matrix of the forged composite samples. After day 15, the concentration of acidic phosphate anions created via dissolution of the unreacted glass volume started to decrease as a result of the conditioning media refreshment, leading to a gradual increase in the pH of the conditioning medium towards neutral.

The thermal properties of the PLA matrix were affected as a result of the incorporation of phosphate glass fibres. As shown in Table 3.10, the cold

crystallisation peak in the thermograms of the composite laminates was shifted towards lower temperatures upon fibre inclusion in comparison to the neat-PLA control plate. This shift was attributed to the heterogeneous nucleation of PLA crystalline phases promoted by the glass fibre surface. The preferential nucleation of crystallites at the fibre surface resulted in an increased crystallinity content in the forged composite rods with respect to the neat PLA control plate.

As previously stated in §4.2, the implementation of cyclic pressure during composite consolidation resulted in altered crystallisation kinetics of the PLA matrix [308]. The differences in the shift of the cold crystallisation peak in addition to the evolution of a shoulder in this region for the cyclic pressure samples were attributed to the presence of a transcrystalline layer which could in part be responsible for the enhanced properties of laminates consolidated under cyclic pressure [308]. Changes in the value of T_g between the first and second heating cycle of the laminates were attributed to physical ageing of the amorphous regions in the PLA matrix [337, 338].

During the forging process, the samples were heated to 90-100°C to soften the thermoplastic, allowing the relaxation of compressive stresses via viscous flow of the polymer matrix. As demonstrated in Table 3.10, the processing temperature range exceeded the onset of PLA crystallisation in all fibre reinforced composite plates. As a result, the crystallinity content in the composite forged rods increased significantly ($p<0.05$) in comparison to the composite plates, with the 0.45-CP-M forged composite rods having the highest initial crystallinity content.

Following immersion in PBS at 37°C, the crystallinity of all the rods studied increased gradually in proportion to the immersion time as demonstrated by Figure 3.26a. With the exception of the forged composite rods obtained from the composite plates consolidated under static pressure, the crystallinity content seemed to gradually increase in proportion to the glass fibre volume fraction. The increase in crystallinity was be attributed to the preferential hydrolysis of the ester bonds in the amorphous regions of the PLA matrix and/or to the rearrangement of PLA chain fragments concentrated in the hydrolysed amorphous regions into crystallites as a result of PLA plasticisation due to absorbed water [339, 340]. As shown in Figure 3.25a, the forged

composite rods absorbed a greater amount of water in comparison to the neat-PLA control forged rod due to the presence of continuous hydrophilic glass fibres, which could have led to a faster degradation of the amorphous regions in the composites. Increases in the crystallinity of the PLA matrix have been reported in aqueous degradation studies of neat and reinforced PLA [189, 340]. Hydrophilic fillers were suggested to expedite the degradation rate of PLA as a result of the higher volume of polymer matrix in direct contact with water preferentially absorbed at the filler-matrix interface [340, 341].

Other factors to consider in the study of the hydrolytic degradation of reinforced PLA are the acid/base properties of the degradation by-products in the case of soluble reinforcements. Provided the incorporation of an adequate amount of alkaline fillers, carboxylic end groups can be buffered via a neutralisation reaction with basic moieties, which considerably reduces the hydrolysis rate of polyesters by preventing the autocatalytic effect of carboxylic acids [192, 342]. The formation of acidic by-products through dissolution of the glass reinforcements as with the case of phosphate anions generated from hydrolysed polymeric phosphate chains, can accelerate ester bonds cleavage in poly(lactic acid) chains by lowering the pH [343].

The enhanced hydrolytic degradation of the PLA matrix in the forged composite rod samples via hydrolytic cleavage of ester bonds compared to the neat-PLA control (cf. Figure 3.24b) can be explained in terms of i) the increased amount of water absorbed by the composites due to the inclusion of hydrophilic phosphate glass fibres and to ii) the catalytic effect of acid environments promoted by the formation of acidic phosphate anions from phosphate glass dissolution. The higher the phosphate glass fibre content, the higher the water intake and the greater the reduction in pH as demonstrated by Figure 3.32a. These observations are in good agreement with the reductions in number average molecular weight, which were greater for the forged composite rods with higher content of phosphate glass fibres as shown in Figure 3.34b.

4.4 Manufacture of Fully Bioresorbable Composite Rods via Compression Moulding of Polymer Sheathed Fibre Bundles

Fracture fixation orthopaedic market remains heavily dominated by metallic implants that are intrinsically incompatible with osseous tissue due to the extensive differences in mechanical properties and the constituent materials. Ideally, a prosthetic device should provide sound structural support without entirely restricting localised movements of the bone fragments relative to each other, and gradually transfer load to the recovering tissue [344, 345]. Fully bioresorbable fibre reinforced thermoplastic composites could eliminate the shortcomings associated with metallic implants and accelerate fracture healing by the controlled release of therapeutic ions, eventually replacing them as the gold standard for fracture fixation. To achieve this, commercially advantageous manufacturing methods should be designed for the effective and efficient processing of highly viscous thermoplastic melts and fragile fibre reinforcement.

4.4.1 Production of bare PLA-sheath via Tubing-type Crosshead Extrusion

The production of bare PLA-sheath was investigated at four different processing temperatures and three different screw speeds. In consideration of PLA instability at temperatures higher than the melting point, 165°C was selected for fibre bundle sheathing (cf. Table 2.2) at the highest possible screw speed to minimise residence of the polymer melt inside the extruder. Screw speeds in excess of 30 rpm at 165°C resulted in the escalation of pressure at the die entry up to the safety limit. In spite of the extrusion temperature being lower than PLA melting point (~170°C), a continuous flow of PLA could be obtained at 165°C due to the energetic contribution of the extruder viscous shearing.

By virtue of the screw pumping action, increases in the rotational speed resulted in the increment of mass flow and the concomitant increase in the pressure gradient at the die entry as shown in Table 3.11. In all cases but for 10 rpm (in which case the volumetric feeder was set at the minimum practical speed, accounting for the differences between the extrudate mass flow and the feeder output shown in Table 3.11), the extruder feeding was

progressively increased up to the flooding point at which polymer started to accumulate at the gas venting.

The decrease in the pressure registered at the die entry with increases in the extrusion temperature as shown in Figure 3.27b were attributed to the decrease in viscosity of molten PLA as a result of the higher mobility of polymeric chains. Higher extrusion temperatures allowed for higher screw speeds and greater feeder outputs to be implemented without exceeding the safety pressure limits of the equipment.

Due to the independence of the extrudate mass flow with respect to the haul-off speed (demonstrated in Table 3.11), the extrusion line could be calibrated to produce PLA-sheath of the required linear density (cf. Table 2.2) by fixing both the screw speed and feeder output and simply adjusting the haul-off speed as demonstrated Figure 3.28.

4.4.2 Characterisation of Bioresorbable Fibre Reinforced Composite Rods Manufactured via Compression Moulding of PLA-sheathed Fibre Bundles

The backscattered electron images of the composite rods polished cross sections in Figure 3.29, show that fibre bundles (at least up to ~600 fibres) can be fully impregnated by via radial percolation of molten PLA initially deposited as an outer coating, in spite of the low processing temperature and short time under pressure (~180°C and 5 min, respectively). These observations, demonstrate the effectiveness of the PLA-sheathed fibre bundle hybrid preform, which can be continuously produced at high speeds (in the order of several hundreds of meters per minute), without the need of intermediate steps involving polymer reshaping as in powder impregnation and commingling (where the polymer has to either ground into powder form or spun into fibres), which increase the cost of the overall processing cycle [184].

Furthermore, the combination of the glass reinforcement and the thermoplastic polymer matrix within a hybrid preform via fibre bundle sheathing, completely avoids the application of stresses and handling operations required during commingling, powder impregnation and especially pultrusion, which damage the fibres, reducing the reinforcement effectiveness. This is particularly relevant in the processing of fragile reinforcements like annealed phosphate

glass fibres, which experience embrittlement following heat treatment as demonstrated by the reduction in strain to failure (cf. Table 3.3). In fact, annealed fibres had to be manipulated with extreme caution during processing, to prevent bundle fragmentation.

The irregularly shaped black regions observed in the unreinforced polymer-rich regions among the fibre bundles in Figure 3.29 were identified as “vacuum” voids created as a result of restrained volume contraction throughout the cooling stage of composite manufacture [346, 347].

Since the density of PLA at 180°C is lower with respect to the room temperature value (1.12 $g \cdot cm^{-3}$ cf. 1.25 $g \cdot cm^{-3}$, respectively, as calculated by Equation 2.12) a certain amount of polymer, which is inversely proportional to the volume fraction, will be squeezed out of the cavity upon pressure application provided the mould is not hermetically sealed.

During the cooling stage, contraction of the polymer in-between the fibre bundles is restrained by both the i) outer layers (that solidify first by virtue of their direct contact with the mould walls) and the ii) fibre reinforced regions. In the event of matrix deprivation (caused by polymer seeping through the mould parting lines during compaction), restrained shrinkage will prompt the formation of voids.

The nature of the observed defects was confirmed by gently heating large bubbles located close to the surface in bare polymer rods produced by consolidating bare PLA-sheath using a heat gun set at 100°C. After heating, the softened skin layer was observed to collapse inwards in response to the atmospheric pressure. Conversely, if the voids were caused by air entrapment, the surface skin would have been raised as a result of the volumetric thermal expansion of the gas inside the bubble. These observations are in good agreement with the proposed origin of the small bubbles and the lower thickness observed in the fibre reinforced composite plates fabricated at 200°C. As mentioned in §4.2, the lower viscosity of 3251D PLA at 200°C facilitated polymer leakage upon compaction, leading to matrix deprivation and the formation of voids in these specimens.

Due to the reduction in the effective fibre-matrix interfacial area, microvoids located at the interstices between fibres (resulting from the incapacity of the polymer to percolate through the compact fibre array) negatively impact the mechanical properties of fibre reinforced composites at a much greater extent in comparison to defects confined in the polymer-rich zones [308, 348]. A higher void content than the theoretical maximum (calculated as described in §2.15) would have indicated the presence of a considerable number of dry zones within the fibre bundles in addition to the vacuum void concentrated in the polymer-rich regions. As shown in Table 3.13, the void content was below the estimated maximum value, ϕ_t, for all the fibre volume fractions studied, and no evidence of voidage within the fibre bundle could be detected in the composite cross sections as demonstrated by the images detailing the dashed-line enclosed areas in Figure 3.29.

Polymer escape during composite consolidation and the consequent formation of vacuum voids can be prevented by improved mould design. However, the simple tool used in this pilot study (cf. Figure 2.16) was deemed appropriate for conceptual validation. Refinement of processing variables and mould design will be conducted in future investigations.

The flexural strength increments in direct proportion to fibre volume fraction, as shown in Figure 3.30, in spite of the increasingly larger fibre bundle diameter (cf. Table 2.2) further evidenced the reinforcement efficiency that can be attained via compression moulding of PLA-sheathed fibre bundles. Apart from the $0.15v_f$ samples (in which there was a 13% difference in flexural strength between the as-drawn and annealed fibre reinforced composites), as-drawn fibre reinforced compression moulded rods were in average 35% stronger with respect to compression moulded rods containing annealed fibres. The significantly higher flexural strength of the composite rods reinforced with as-drawn fibre bundles in comparison to annealed fibre reinforced composite rods was a direct consequence of the reduction in strength caused heat treatment of the glass fibres as already discussed in §4.1.

As mentioned in §4.3, the mechanical performance of forged rods depend on the initial mechanical properties of the laminates from which composite blanks are obtained (for subsequent forged), and the presence of forging induced

defects. In the cases where the mechanical properties of forged rods were not impaired during forging (i.e. the mechanical properties of the rods were equivalent to those of the composite plates), namely, the $0.15v_f$ and $0.25v_f$ plane strain forged composite rods, the mechanical properties of the as-drawn fibre reinforced compression moulded rods fell between those of the rods obtained from composite plates consolidated under cyclic pressure and static pressure.

The flexural strength of the $0.35v_f$ and $0.45v_f$ compression moulded rods reinforced with as-drawn fibres were higher than the composite rods forged from thick mat composite plates consolidated under static and cyclic pressure profiles (43%-74% higher for the $0.35v_f$ samples and 95-300% higher for the $0.45v_f$ specimens, respectively), due to the presence of forging induced defects in the latter as demonstrated in §4.3.

The flexural strength of the $0.35v_f$ as-drawn fibre reinforced compression moulded composite rods was similar to the strength of the 0.35-CP-M composite plates and the respective plane strain forged rods since the creation of additional forging-induced defects was prevented by stacking a greater number of glass fibre mats and PLA films as concluded in §4.3. Conversely, the strength of the $0.45v_f$ compression moulded rods reinforced with as-drawn fibres was 23% higher than the flexural strength of the 0.45-CP-M plane strain forged rods but comparable to the strength of the 0.45-CP-M plates (the mean strength value of the 0.45-CP-M composite plates was 8% greater than the corresponded compression moulded rod, however such difference was found non statistically significant in a 95% confidence interval), as a result of the generation of intra-ply cracks during plane strain deformation of composite blanks with fibre volume fractions in excess of 0.35. No valid comparisons between annealed fibre reinforced compression moulded rods and forged composite rods or compression moulded plates could be made, on account of the reduction in fibre strength following heat treatment.

Despite the significantly higher void contents in compression moulded rods in comparison to the composite plates (cf. Table 3.6 and 3.12), the higher mechanical properties of the former with respect to the laminates consolidated under static pressure, further evidences the efficiency of the PLA-sheathed fibre bundles as a hybrid preform over conventional laminate stacking. It

should be noted that the PLA-sheathed fibre bundles were consolidated under a static pressure profile held for a shorter time (5 min) in comparison to the composite plates (10 min). Optimisation of the compression moulded composite rods could be achieved by implementation of cyclic pressure during the consolidation of PLA-sheathed fibre bundles. Adjustments in the pressure profile and mould design should be conducted in a follow-up study.

The modest increase in elastic moduli obtained for the annealed fibre reinforced compression moulded composite rods, despite the lower fibre content in the annealed fibre reinforced composites (with the exception of the 0.25 fibre volume fraction specimens) as demonstrated in Table 3.12, could be an indication of the increase in phosphate glass fibres elastic modulus consequent to structural relaxation of the glass network during heat treatment. Increases in the elastic modulus of annealed phosphate glass fibres have been reported in [146, 158, 262], and in fact the mean elastic modulus of the annealed fibres was found to be higher than that of as-drawn fibres, however such increment was deemed not significant after statistical analysis as discussed in §4.1.

The flexural moduli of the composites rods manufactured through the consolidation of annealed and as-drawn PLA-sheathed fibre bundles are the highest hitherto reported for bioresorbable composites, even to those cases where phosphate glass fibres with superior mechanical properties in comparison to those in this study were used to reinforce PLA [15, 18, 195, 232, 308].

The modulus of the as-drawn fibre reinforced composite rods with $0.45v_f$ and $0.35v_f$ manufactured via compression moulding of PLA-sheathed fibre bundles were 15% and 13% higher with respect to the modulus of the 0.45-CP-M and 0.35-CP-M plane strain forged composite rods (which were the best performing in terms of modulus as shown in Figure 3.20b), respectively. This comparison can be extended to the respective composite plates from which composite blanks were obtained (and subsequently forged) since, as stated in §3.3.4, no significant differences in modulus were observed between the rods and the composite plates fabricated by staking a greater number of thin glass mats following plane strain forging.

The difference in modulus was even higher for the $0.45v_f$ and $0.35v_f$ composite rods fabricated via compression moulding of PLA-sheathed annealed fibre bundles with respect to the best performing laminated composite plates with matching fibre volume fraction (in the order of 25% and 19%, respectively), however such a difference could be related to the potential increase in elastic modulus of the fibres after thermal treatment.

The elastic response of reinforced plastics is determined mainly by volume-averaged strain and stress fields [290]. Therefore, it would be reasonable to expect a variation in flexural modulus as a result of the change in the reinforcement distribution throughout the composite cross section as suggested in [195, 308]. The unique fibre reinforcement distribution achieved via compression moulding of PLA-sheathed fibre bundles (cf. Figure 3.29 and Figure 3.22) could have contributed to the larger modulus of this type of rods in comparison to the conventional composites manufactured via laminate stacking, even to those in which enhanced reinforcement distribution was obtained by stacking a larger number if thin glass fibre mats.

Figure 4.4 illustrates the flow diagrams of the two composite rod manufacturing processes here studied. It is evident that the manufacture of fibre reinforced composite rods via compression moulding of PLA-sheathed fibre bundles involves less stages in comparison to forging of preconsolidated composite blanks. PLA-sheathed fibre bundle preforms can be continuously produced at high speeds (in the order of several hundreds of meters per minute) limited only by the extruder throughput since no stresses are applied to the fibres during the sheathing operation. The preform can then be chopped into segments of the required length by a downstream cutting unit and subsequently loaded into moulds with complex shaped cavities for composite consolidation, making the compression moulding of PLA-sheathed fibre bundles a semi-continuous operation suited for large production rates. Moreover, micron or nanosized particles can be compounded with the PLA and incorporated into the sheath to produce particle/fibre reinforced composites with enhanced functionality.

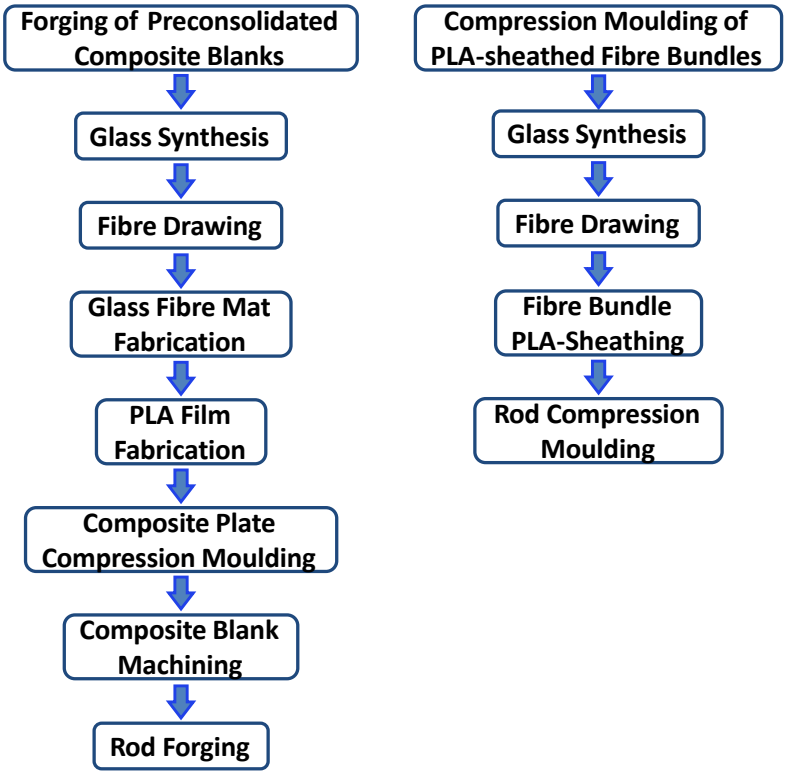


Figure 4.4: Flow diagrams for the manufacture of fibre reinforced composite rods via (right) forging of preconsolidated composite blanks and (left) compression moulding of PLA-sheathed glass fibre bundles.

Conversely, composite rod manufacture via forging of preconsolidated composite blanks is a labour intensive batch process comprising a large number of discrete operations (therefore, highly susceptible to the introduction of variation), only capable of producing fairly simple shapes. Furthermore, the characteristics of forged composites are limited by i) fibre volume fraction, ii) reinforcement distribution through the cross section and iii) dimensions of the composite blank, which have to be similar to those of the final product, as demonstrated in §4.3. None of these constraints are applicable to compression moulding of PLA-sheathed fibre bundles.

4.4.3 In Vitro Degradation Study of Bioresorbable Fibre Reinforced Composite Rods Manufactured via Compression Moulding of PLA-sheathed Fibre Bundles

Figure 3.31 illustrates the degradation of mechanical properties as a consequence of immersion in PBS at 37°C for compression moulded composite rods. After a single day, both the flexural strength and modulus of all the specimens, regardless of the type of reinforcing fibre, were considerably impaired by the interaction with the conditioning medium. In similitude to the changes observed upon PBS conditioning of composite

forged rods described in §4.3, the minor variations in water uptake (less than 1%), dry mass and pH of the conditioning media (cf. Figure 3.32) in conjunction with the absence of morphological alterations for either as-drawn or annealed fibres as a result of the interaction with the aqueous solution at day 1 (cf. Figure 3.33) were indicative of the deleterious effect of even a small amount of absorbed water on the mechanical performance of PGF-PLA composites, regardless of the manufacturing method.

Due to the hygroscopic nature of phosphate glass fibres, regardless of the heat treatment, and the lack of a strong adhesion between the PLA matrix and the reinforcing fibres (no sizing or other type of fibre surface modification was conducted on the fibre bundles before PLA-sheathing), water readily diffused by capillary action through the fibre-matrix interface and impaired the transfer of stresses from the matrix to the glass fibres, resulting in the steep decrease in mechanical properties (in the order of 50% reduction for as-drawn fibre reinforced compression moulded rods).

The percentage reduction in mechanical properties for the compression moulded composite rods after 1 day of immersion in PBS was similar to that experienced by composite forged rods (cf. Figure 3.23 and Figure 3.31), indicating the need of surface modification to fully exploit the manufacturing advantages of leaner production methods based on polymer melt impregnation. Significant reductions in the mechanical performance of composites reinforced with either chemically stable (silicate glass) partially soluble (bioactive glass) and fully degradable (phosphate glasses) resulting from the disruptive effect of water at the fibre-matrix interface have been previously reported in [193, 231, 349, 350].

The stabilisation of composite mechanical properties for both types of fibres observed between day 1 and day 3 suggested that complete water-mediated disruption of the fibre-matrix interface was consummated during the first day of immersion, in good agreement with behaviour observed in the composite forged rods degradation study. Once stress transfer through interfacial shearing is no longer possible, the matrix and the fibre can still interact via frictional resistance to sliding [351, 352].

Following day 3, further conditioning time led to the continued reduction in flexural strength for both compression moulded composite rod series. Annealed fibre reinforced composites experienced a smoother decrease in flexural strength in comparison to the composites containing as-drawn fibres. Such a reduction was attributed to the faster degradation rate of as-drawn fibres with respect to annealed ones as demonstrated in Figure 3.9. The significant decrease in fibre diameter consequent to glass dissolution via surface erosion, evident in the dissolution studies of as-drawn glass fibres in PBS by day 3 (cf. Figure 3.9), but only noted in the images of the as-drawn fibre reinforced composite rods fracture surface by day 7 (cf. Figure 3.33), implicate a reduction in fibre matrix contact so that the fibre-matrix interaction via frictional slippage becomes less effective as conditioning time elapses, accounting for the continued decrease in mechanical properties observed in the as-drawn fibre reinforced compression moulded composite rods, in line with the behaviour also described by the composite forged rods.

In contrast to bare annealed glass fibres degraded in PBS (cf. Figure 3.9), no decrease in the reinforcing fibre diameter was noticed in the fracture surface of the annealed fibre composite series during the entire *in vitro* degradation study (cf. Figure 3.33). As a result of the quick dissolution of as-drawn fibres, additional diffusion pathways in the form of micro-channels were formed in the compression moulded composite rods, increasing the water absorption capacity of the composite structure and allowing a quick exchange of reactive species and corrosion by-products.

Conversely, due to the low reactivity of annealed glass fibres, water at the fibre-matrix interface preferentially diffused into the polymer. In response, the polymer around the fibres swelled to accommodate the penetrating water and exerted a radial pressure that arrested further ingress of water, ultimately decelerating glass fibre dissolution with respect to bare annealed fibres which were in direct contact with the conditioning medium (cf. Figure 3.9).

The water uptake and the dry mass changes presented in Figure 3.32 are in excellent agreement with the phosphate glass fibre degradation mechanism here proposed. The proliferation of micro-channels as a result of the continued dissolution of as-drawn fibres led to increasing water uptake and higher mass losses in the composite structure. The higher the fibre volume fraction, the

larger the number of channels created, accounting for i) the increasing amount of absorbed water and ii) the higher dry mass losses in proportion to the fibre content as shown in Figure 3.32. The close correspondence of the water uptake and dry mass loss curves for the as-drawn fibre reinforced compression moulded composite rods with 0.35 and 0.45 fibre volume fractions was attributed to the higher content of voids in the former (as demonstrated in Table 3.12). The higher void content accelerated water uptake and created conditions that favoured glass dissolution. It has been demonstrated that the presence of voids dramatically increases the equilibrium water absorption and expedites the diffusion of water in fibre reinforced composites [350, 353].

The radial pressure exerted by the swollen polymer matrix against the slowly dissolving annealed glass fibres restricted the penetration of additional water through the fibre-matrix interface. On account of the constriction of the interfacial diffusion pathway, water intake (and thus glass dissolution) was considerably reduced since the diffusion of water along the fibre-matrix interface is 100-400 times faster than through the bulk matrix [321].

Variations in the pH of the composite conditioning media correlated well with the trends observed during bare fibre in vitro degradation studies (cf. Figure 3.9 and Figure 3.25). The absence of significant variations in the pH of the media collected from vials containing annealed fibre reinforced compression moulded composites with respect to the as-prepared PBS solution were attributed to the limited dissolution experienced by the annealed fibres encased within the PLA matrix.

The pH of the as-drawn fibre reinforced composite conditioning media quickly shifted towards acidic values whose magnitude were in proportion to the fibre volume fraction of the composite rods. The higher the fibre volume fraction, the more protons were generated as the ultimate result of P-O-P bond hydrolytic cleavage. Furthermore, P-O-P hydrolysis is catalysed in acid environments, which further increased the rate of dissolution of the glass reinforcement, and thus, the production of acidic species [266, 327].

The minimum pH reading for the 0.15 fibre volume fraction compression moulded composite samples, whose fibre content was virtually identical to the

mass of fibres used in the bare fibre degradation studies (~400 mg, cf. Table 2.2) was more acidic than the value registered in the as-drawn bare fibre in vitro degradation studies (6.72 and 6.95, respectively). Additional protons liable for the lower pH readings of the conditioning media collected from the $0.15v_f$ compression moulded composite rods should have been generated from the dissociation of carboxyl moieties product of PLA ester bond hydrolysis.

Water uptake, dry mass loss and pH variation profiles of forged composite rods and compression moulded composite rods reinforced with as-drawn fibres were remarkably similar and practically superposed at time points in excess of day 7 for all fibre volume fractions (cf. Figure 3.25 and Figure 3.32). In spite of the higher void content in the $0.45v_f$ and $0.35v_f$ compression moulded composite rods (which in theory should have accelerated water diffusion), the corresponding forged composite rods absorbed more water (6.6% and 6.2% in comparison to 12% and 9.2%, respectively) and consequently lost a comparably higher amount of mass at day 7. The higher content of water in the forged composite rods with 0.45 and 0.35 fibre volume fractions during the first quarter of the degradation study could be attributed to the combined effect of weld-lines and delamination cracks created during plane strain forging which, unlike isolated vacuum voids, spanned the whole length of the forged composite rods.

In contrast, the water uptake, mass loss and pH variation profiles of compression moulded rods reinforced with annealed fibres were practically indistinguishable from those of neat-PLA forged rods, supporting the proposed restriction of further water ingress by the constraining action of the swollen polymer matrix around the slowly dissolving annealed glass fibres.

The modulus degradation profiles for the as-drawn fibre reinforced compression moulded composites mirrored the observed reductions in flexural strength following the reduced fibre-matrix contact due to the quick dissolution of as-drawn fibres as demonstrated in Figure 3.31. No such reduction in diameter was observed for the annealed fibres within the composite as discussed earlier, which allowed the matrix and the fibre to interact via frictional resistance to sliding, in spite of the fibre-matrix disruption by water, throughout the entire composite degradation study. As long as no significant

reductions in fibre diameter occur, the fibres are capable of resisting matrix deformation (provided isostrain conditions are maintained in the conditioned composites) with the same efficiency, accounting for the plateauing of the modulus for the remainder of the study after an initial reduction.

The morphological changes experienced by as-drawn fibres embedded in compression moulded composite rods were equivalent to those observed in forged composite rods (cf. Figure 3.24 and Figure 3.33) and consequently were ascribed to preferential nucleation and growth of precipitates at the fibre surface following the saturation of the solution by glass corrosion by products as stated in §4.3. Compaction forces created as a result of the swelling of the polymer case around the individual fibres resulted in the consolidation of precipitates into a compact thick outer shell. Detachment of the precipitate shell once further thickening became unstable resulted in the formation of a sequence of shells with progressively smaller dimensions which mirrored the shrinking fibre core.

On the other hand, the development of compaction forces acting against slowly degrading fibres, behaved as a water absorption deterrent, further decelerating the glass dissolution. This is in good agreement with the stability of the annealed fibres observed in the fracture surface of the respective compression moulded composite rods shown in Figure 3.33, where no morphological changes, other than the formation of small corrosion pits in the fibre periphery, were noted throughout the *in vitro* degradation study.

Qualitatively and quantitatively, the compositional changes experienced by the precipitate shells in the as-drawn fibre reinforced compression moulded rods were remarkably similar to those observed in the forged composite rods (cf. Table 9 and Table 3.13). The progressive changes in the precipitate shells stoichiometry throughout composite degradation studies were attributed to the evolution of the transient solid phase (possibly in the form of amorphous calcium phosphate, which has been found to form almost invariably during the initial stages of calcium phosphate precipitation in basic to neutral aqueous solutions [354, 355]) towards an apatite-like phase through heterogeneous exchange between the solid phase and the supernatant solution [355, 356].

The slight decrease in the single case of sodium relative content in both annealed and as-drawn fibre cores with conditioning time in compression moulded composite rods could be attributed to the increasing depth of alkali depletion in the glass fibres due to the hydrolytic cleavage of the low hydration energy-bonds between sodium and non-bridging oxygens, and to the high mobility of Na^+ ions within the hydrated layer [133]. However, since such decrease was not observed in the forged composite rods, this may be associated with experimental quantification error or to normal variations in the composition of glass during synthesis or fibre drawing.

Implementation of cyclic pressure during composite plate consolidation resulted in altered crystallisation kinetics of the PLA matrix as revealed by the evolution of a shoulder in the cold crystallisation peak, which was attributed to the presence of a transcrystalline layer around the reinforcing glass fibres [308]. In good agreement with the pressure profile used to consolidate the PLA-sheathed fibre reinforced bundles (the pressure was kept constant throughput the entire consolidation and cooling stages) no such shoulder could observed in the thermograms of compression moulded composite rods. In general the compression moulded composite rods presented a narrower cold crystallisation peak with respect to that of the compression moulded plates (cf. Figure 3.14 and 3.34). Such a difference could be related to the presence of shorter polymer chains in the former, which can rearrange themselves into crystallites at temperatures lower than those necessary to activate the motion of the longer PLA chains in the compression moulded plates. The average molecular weight (M_n) of the as-drawn and annealed fibre reinforced compression moulded composite rods were in fact 45% and 37% lower in comparison to the average molecular weight of the compression moulded composite plates (cf. Table 3.7 and Figure 3.35). The lower molecular weights of PLA in compression moulded composite rods in comparison to the compression moulded plates could be associated to the thermomechanical degradation of PLA experienced during extrusion [357, 358].

The cold crystallisation and the melting peak of the compression moulded composite rods reinforced with annealed fibres, contracted significantly in proportion to the increase in fibre volume fraction. A decrease in the cold crystallisation and melting peak areas was also observed for as-drawn fibre

reinforced compression moulded rods upon further glass fibre incorporation, however, such decrease was far smaller in comparison. The greater contraction of the cold crystallisation peak (and the corresponding shrinkage of the melting endotherm) in the annealed fibre reinforced compression moulded composite rods could be associated with the reduced efficiency of annealed fibres to encourage heterogeneous nucleation of spherulites upon heating, in comparison to the highly reactive as-drawn fibres, as a result of the decrease in surface energy experienced following heat treatment.

The initial crystallinity content of compression moulded composite rods reinforced with annealed or as-drawn fibres was lower with respect to the forged composite rods. In average the crystallinity content for compression moulded composite rods was 12%, whereas in general, the crystallinity in the forged composite rods exceeded 20%. The higher crystallinity content in forged composite rods was associated with the heating of the preconsolidated composite blanks to 90-100°C prior to the stamping operation.

Following immersion in PBS at 37°C, the crystallinity of all the compression moulded composite rods reinforced with as-drawn fibres increased gradually in proportion to the immersion time as demonstrated by Figure 3.35a, in good agreement with the behaviour observed during the forged composite rods degradation study. Correspondingly, the increase in crystallinity was attributed to i) preferential hydrolysis of the ester bonds in the amorphous regions of the PLA matrix and ii) to the rearrangement of PLA chains into crystallites as a result of the plasticising effect of absorbed water [339, 340]. The crystallinity content seemed to increase with fibre volume fraction on account of the greater amount of water absorbed by the increasing content of hydrophilic glass fibres in good agreement with the trends presented in Figure 3.32.

In correspondence to the water uptake trend shown in 3.32, the crystallinity in the annealed fibre reinforced compression moulded composite rods remained constant throughout the *in vitro* degradation study. Unlike the annealed fibre reinforced compression moulded composite rods, the crystallinity in neat-PLA forged rods did increase with conditioning time despite the relatively low values of water uptake (~0.9%), which were similar for both types of samples. In fact the initially translucid neat-PLA forged rods were observed to become more opaque with conditioning time, which has been associated with the

presence of crystallites aggregates with refractive indices different from that the amorphous matrix [92, 359]; no such qualitative change in the sample transmittance could be observed in the annealed fibre reinforced compression moulded composite rods. The crystallinity stability in compression moulded rods reinforced with annealed fibres could be attributed to the restriction of the polymer chain mobility in the presence of the slow dissolving annealed fibres. Reduced mobility of polymer chains due to the presence of fillers in reinforced plastics has been observed previously in [360, 361].

The lower initial number average molecular weights of PLA in the as-drawn fibre reinforced compression moulded composite rods (in the order of 10% lower with respect to compression moulded rods reinforced with annealed fibres) can be attributed to the highly energetic surface of phosphate glass fibres in the as-drawn condition, which readily adsorbs low energy compounds present in the local environment (including water vapour and organic contaminants) during mould loading, in comparison to the more stable annealed fibres [306]. Upon heating, the polymer melt reacts with the adsorbed water, leading to reduced molecular weights [70, 106]. Similar observations with respect to the decrease in molecular weight of PLA during melt processing of particulate Bioglass® and phosphate glass fibre reinforced PLA products were reported in [191, 308, 362]. Significant reductions in the polymer molecular weight were attributed to the high temperature hydrolytic reaction between PLA and the hydrated glass reinforcements during extrusion.

The changes in the PLA molecular weight in the composites during PBS conditioning at 37°C were in good agreement with water uptake, dry mass loss and conditioning media pH changes described earlier. The higher amount of water absorbed, coupled with the catalytic effect of the acidic environment created by the deprotonation of ortho- and polyphosphate anions (formed during phosphate glass hydrolysis) resulted in the continued decrease in number average molecular weight observed in as-drawn fibre reinforced composites with more than 0.15 fibre volume fraction (cf. Figure 3.35b), in excellent agreement with the chromatography results for forged composite rod degradation (cf. Figure 3.26). The relatively low as-drawn fibre content of the $0.15v_f$ prevented the significant decrease in molecular weight at the extent observed for higher fibre volume fractions.

Conversely, the minor amount of water absorbed and the negligible changes in the pH of the conditioning media were reflected in the stability of the number average molecular weight for all the annealed fibre reinforced compression moulded composites during the 30 day conditioning period in PBS at 37°C as shown in Figure 3.35b.

4.5 Mechanical Performance of PLA-reinforced Composites in Wet Conditions

For comparison purposes, the retention of mechanical properties of selected PLA-based bioresorbable implants during a 30 day period in aqueous media were summarised in Figure 4.5, along with the best performing composite rods in this study (namely, those with 0.45 fibre volume fraction) produced via forging of preconsolidated composite blanks and compression moulding of PLA-sheathed fibre bundles in the annealed and as-drawn condition, respectively.

From inspection of Figure 4.5, it can be observed that the 0.45-CP-M composite forged rods were initially weaker and presented a greater loss of mechanical properties during the first 15 days of PBS conditioning with respect to compression moulded composite rods reinforced with as-drawn fibres. This may be associated with the presence of weld-lines and intra-laminar cracks in the former as a result of plane strain forging as discussed in §4.3.2 and §4.3.3.

The strength values at day 30 of the compression moulded composite rods reinforced with 0.45 volume fraction of annealed fibres were comparable to those in [18] and are the highest for phosphate glass fibre reinforced poly(lactic acid) composites fabricated via melt impregnation techniques hitherto reported. As shown in Figure 3.31a, the mean flexural strength at day 30 of annealed fibre reinforced compression moulded composite rods bordered the lower limit of the human cortical bone, however they still fell short from optimum values (which for safety reasons should still exceed the human cortical bone) especially in comparison to the strengths achieved with bioresorbable silica-based glass fibres reinforced poly(lactic acid) (SGF-PLA) as shown in Figure 4.5a. The superior flexural strengths of silica-based bioresorbable glass fibre reinforced poly(lactic acid) composites throughout the in vitro degradation study (771±48 MPa at week 0 and 275±21 MPa at

week 4) originated from i) the use of far stronger glass fibres in comparison to P45Fe2 annealed fibres (1983±244 MPa in comparison to 444±117 MPa) and ii) the application of organofunctional silane sizing on the fibres to improve fibre-matrix adhesion [193, 363].

As demonstrated in Figure 4.5b, modulus retention of annealed fibre reinforced composites at day 30 greatly exceeded the values reported for similar devices. It should be noted that in contrast to the case of the SGF-PLA composites mentioned earlier, no sizing was applied to the phosphate glass fibres used in this study, and thus future work should focus on the sizing of phosphate glass fibres to strengthen the fibre-matrix interface for longer retention of mechanical properties.

An exciting possibility is the sizing of the fibre surface with mussel inspired polydopamine coatings, whose functionalisation capacity has been shown to span virtually all types of material surfaces, even those with superhydrophobic characteristics [364-366]. Enhanced mechanical properties particle and fibre reinforced PLA composites have been attributed to the optimisation of the filler-matrix interface by the formation of covalent and non-convalent bonds [367-370].

It is expected that polydopamine coating on annealed and as-drawn phosphate glass fibres will i) increase initial mechanical properties of fibre reinforced composites and ii) stabilise or significantly reduce the decrease of composite mechanical properties conditioned in aqueous media. A follow-up study will investigate on these premises.

Alternatively, higher composite strengths prior and during immersion in aqueous medium could be achieved by increasing annealed fibre strength, since, as it was observed during composite degradation studies, the matrix is still capable of transferring stresses to the fibres via frictional resistance to sliding after disruption of the fibre-matrix interaction by capillary water. As it has been demonstrated elsewhere in this document, annealing of phosphate glass fibres resulted in a significant decrease in fibre strength as a result of structural relaxation and the formation of a tensile surface layer.

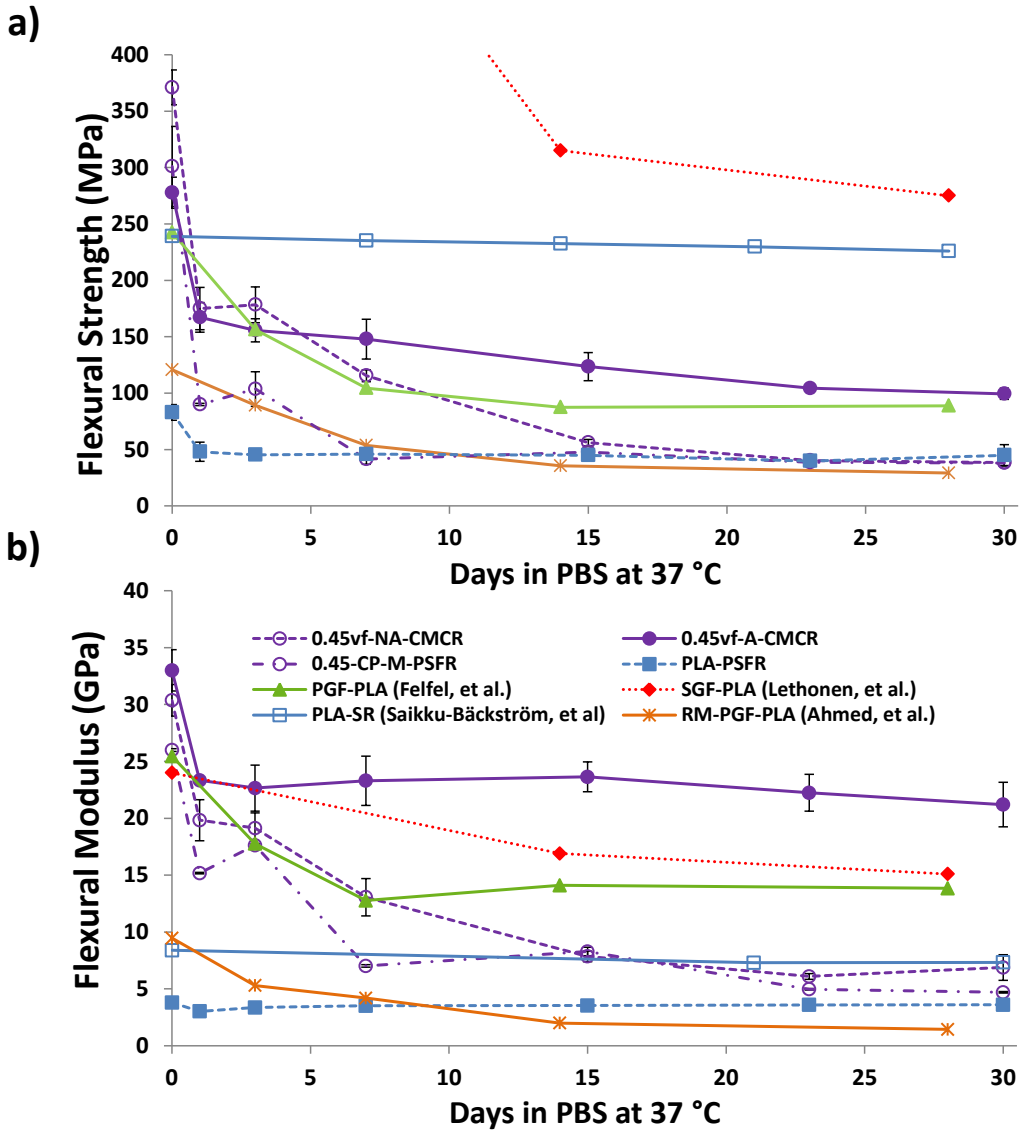


Figure 4.5: Comparison of the retention of a) flexural strength and b) flexural modulus of selected bioresorbable devices intended as orthopaedic implants, namely: i) 0.45vf compression moulded composite rod reinforced with as-drawn phosphate glass fibres (0.45vf-NA-CMCR), ii) 0.45v_f compression moulded composite rod reinforced with annealed phosphate glass fibres (0.45v_f-A-CMCR), iii) 0.45-CP-M plane strain forged composite rod (0.45-CP-MPSFR) iv) plane strain forged neat-PLA rod, v) phosphate glass fibre reinforced poly(lactic acid) (PGF-PLA) [18] vi) bioresorbable silica-based glass fibre reinforced poly(lactic acid) (SGF-PLA) [193], vii) self-reinforced poly(lactic acid) (SR-PLA) [371], and vii) random phosphate glass fibre reinforced poly(lactic acid) (RM-PGF-PLA) [215]. For clarity, only the best performing samples produced in this study were included.

It has been shown that the strength of glass fibres can be increased provided a sub-critical tensile stress is applied in the course of the heat treatment at a temperature below the glass transition temperature in the presence of water vapour. The strengthening effect was attributed to the formation of a residual compressive stress layer consequent to surface stress relaxation accelerated by water diffusion upon tensile load release [372, 373]. In such way, slowly degrading phosphate glass fibres (capable of frictionally interact with the

polymer matrix throughout a period suitable for bone fracture repair) with strengths comparable to or even exceeding the as-drawn condition values could be produced and subsequently embedded into PLA for enhanced composite strength retention in wet conditions.

5 Conclusions and Future Work

5.1 Conclusions

5.1.1 Characterisation and *In Vitro* Degradation Studies of Bioresorbable $45P_2O_5{\cdot}16CaO{\cdot}13Na_2O{\cdot}24MgO{\cdot}2Fe_2O_3$ mol% Bulk Glass and Glass fibres

Amorphous glass fibres of the P45Fe2 composition ($45P_2O_5{\cdot}16CaO{\cdot}13Na_2O{\cdot}24MgO{\cdot}2Fe_2O_3$) were continuously drawn and deposited at a rate of 1 $g{\cdot}min^{-1}$ at approximately 1000°C. Annealing of the fibres for 1 hr at 460°C resulted in the relaxation of the anisotropic structure of phosphate chains aligned parallel to the fibre axis and the enthalpy relaxation of the isotropic liquid-like structure quenched during fibre drawing as evidenced by the small endotherm in the glass transition region observed upon calorimetric solicitation of annealed fibres. The thermally assisted reorganisation of the anisotropic fibre structure towards an entangled chain equilibration configuration and the formation of a surface tensile layer through the interaction with environmental moisture during heat treatment were associated with the 50% decrease in tensile strength observed in annealed fibres with respect to as-drawn fibres.

The markedly higher degradation rate observed for both annealed and as-drawn phosphate glass fibres in comparison to the bulk glass was attributed to the larger surface area-volume ratio of the fibre morphology. The enhanced durability of annealed phosphate glass fibres with respect to as-drawn ones was associated with the relaxation of the highly unstable anisotropic structure in favour of a more compact arrangement of entangled chains after heat treatment.

Annealed phosphate glass fibres dissolved uniformly via surface erosion as revealed by the linear % mass loss profiles in both deionised water and PBS, without the formation of precipitation in the course of the 30 day-fibre degradation study. On the other hand, as-drawn fibres were observed to degrade in a decelerating fashion possibly due to the increase in ionic strength of the leaching solution. The presence of orthophosphate groups in PBS may have led to the precipitation of stable phases at the fibre surface that eventually developed into continuous tube-like structures. The slow hydrolysis

of phosphate chains prevented deionised water from reaching saturation with orthophosphates in between media refreshments, accounting for the absence of abundant precipitation during deionised water conditioning. Hydrolytic cleavage of P-O-P bonds in phosphate chains in solution leaded to the acidification of the conditioning media as a result of the deprotonation of polyphosphate anions.

5.1.2 Manufacture of Fully Bioresorbable Fibre Reinforced PGF-PLA Composite Plates via Cyclic Pressure-assisted Compression Moulding

Totally bioresorbable fibre reinforced composite plates were manufactured via compression moulding following two different consolidation approaches, namely, cyclic and static pressure. Composites with void contents lower than 1% could be manufactured through both processes at least up to 0.35 fibre volume fraction. Flexural strengths of composites plates manufactured through cyclic pressure were found to exceed the strengths of the samples manufactured via static pressure profile by at least 30%. The difference became more pronounced as the fibre volume fraction increased, reaching a maximum value of ca. 50% for the composite plates with 0.45 fibre volume fraction, whose flexural strength was 480 MPa, which is the highest value hitherto reported for PGF-PLA composites. This was explained by the ability of pressure cycling to potentially affect the permeability of the fibre network through relaxation and reapplication of pressure, leading to improved impregnation with respect to statically applied pressure. It was suggested that implementation of pressure cycles could also have an effect on the melt viscosity and the capillary pressure.

Composite modulus proved to be independent of the pressure profile. The deviation of the elastic moduli from the ideal behaviour for the composite plates with 0.35 and 0.45 fibre volume fractions was attributed to the increasing segregation of fibres throughout the composite cross section, resultant from the increasing thickness of the fibre mats used.

Differences in the DSC traces between the composite plates consolidated with cyclic and static pressure, respectively, suggested the preferential formation of transcrystallinity in all the composite plates of the CP series, probably, as a result of the local chain alignment induced by the pulsating motion. The

persistence of distinctive changes in crystallisation behaviour through multiple melting operations during calorimetric solicitation could be attributed to the physical arrest imposed on the polymer chains as a result of the intimate contact with the glass fibres, or alternatively, by polar interactions of the carboxylic moieties in the PLA chains with the hydroxyl groups on the fibre surface.

PLA progressively degraded as a result of the exposure to temperatures higher than the melting point throughout the composite plate manufacturing process. It was observed that the presence of phosphate glass fibres accelerated the thermal degradation of PLA. The extent of the degradation was found to be dependent on the fibre content. The molecular weight of the polymer matrix progressively decreased as the fibre volume fraction increased, reaching a minimum in the 0.45 fibre volume fraction composite plate of approximately 80% of the virgin PLA number average molecular weight as a result of the high temperature hydrolytic reaction of PLA with the moisture adsorbed on the phosphate glass fibre surface.

Consolidation pressure was observed to be the most important variable for the manufacture of composite plates via cyclic pressure assisted-compression moulding. Optimum flexural strength for $0.35v_f$ compression moulded plates was achieved with 40 bar cyclic pressure consolidation. Further increases in cyclic pressure magnitude resulted in the decrease of strength due to the excessive compaction of the fibre network which could not be efficiently relaxed in the course of the unloading part of the cycle, hampering polymer percolation. No significant increases in flexural strength of the composite plates were noted following PLA viscosity reduction by increasing processing temperature, demonstrating the efficiency of consolidation via cyclic pressure, making possible to avoid large decreases in molecular weight associated with the thermal instability of PLA at temperatures higher than the melting point.

In contrast to the flexural strength, the flexural modulus was independent of the impregnation quality of the compression moulded composite plates in the range of fibre volume fractions, pressures, and temperatures evaluated.

5.1.3 Effect of Forging on Mechanical Properties and In Vitro Degradation of Fully Bioresorbable Fibre Reinforced PGF-PLA Composite Rods

Uniaxial compression forging of bioresorbable composites reduced the flexural strength and elastic modulus of the composite rods regardless of their volume fraction or their impregnation quality by as much as 85% and 47% for the samples with $0.35v_f$ consolidated under cyclic pressure, respectively, in comparison to the compression moulded composite plates due to the fibres fracturing as a result of the extensional flow. The fibres fractured in a sinusoidal pattern which acted as a preferential path for crack propagation upon loading. Conversely, the extensional flow resulted in a flexural strength increase in the neat-PLA control rods with respect to compression moulded PLA laminates due to the alignment of polymer chains along the rod axis.

Fibre fracture was prevented through confinement of the deformation to the ***x-y*** plane during plane strain forging. The mechanical properties of the compression moulded composite plates were preserved in the forged composite rods with 0.15 and 0.25 fibre volume fractions and the neat-PLA control. The high segregation of fibres in the $0.35v_f$ and $0.45v_f$ compression moulded composite plates fabricated with thick mats led to the nucleation of intra-ply cracks during forging and the reduction of the forged composite rods mechanical properties with respect to the compression moulded composite plates regardless of their impregnation quality. Creation of intra-ply cracks during plain strain forging was reduced by the use of thinner glass fibre mats and a larger number of PLA films which decreased the intra-ply friction and allowed the fibre layers to easily accommodate to the die geometry. In spite of this, a 25% reduction in flexural strength was still observed in the 0.45-CP-M forged composite rods with respect to the compression moulded composite plates, suggesting that the maximum fibre volume fraction that can be safely forged under plain strain conditions is $0.45>v_f>0.35$. The lower strength of the compression moulded composite plates fabricated with thin glass fibre mats with respect to the thick mat compression moulded composite plates was attributed to the increased number of interfacial defects at the meeting point between polymer melt flows. The 10% increase in the flexural modulus of the 0.45-CP-M compression moulded composite plate with respect to the $0.45v_f$ compression moulded composite plates fabricated from thick mats was

attributed to the enhanced reinforcement distribution throughout the composite cross section achieved by stacking a larger number of thin glass fibre mats.

The properties of the forged composite rods were observed to decrease after immersion in PBS, regardless of the impregnation quality. The initial loss of strength and modulus was attributed to the lubrication of the fibre-matrix interface. Further decreases in mechanical properties were related to the fibre diameter reduction as a result of glass dissolution, which impaired the friction-mediated stress transfer. The faster loss of mechanical properties in the 0.45-CP-M forged composite rods was ascribed to the presence of intra-ply cracks, which expedited water uptake. Impregnation quality did not seem to significantly influence water uptake or dry mass loss of the forged composite rods obtained from cyclic pressure consolidated laminates with respect to the static pressure consolidated ones, possibly due to the high affinity of the phosphate glass fibres to water and the absence of a coupling agent to improve the fibre-matrix interfacial adhesion.

The pH decrease of the composite's conditioning media was indicative of the creation of acidic polyphosphates and orthophosphates through hydrolysis reactions. The conditioning medium became more acidic in proportion to fibre volume fraction in good agreement with the water uptake and dry mass loss tendencies.

The core-shell structures formed during the composite degradation study were associated with the formation of precipitates whose chemical composition differed from that of the original glass. Precipitates nucleated at the fibre surface were subsequently consolidated into a compact shell which progressively thickened, ultimately spalling from the fibre core due to residual compressive stresses introduced during its formation on a curved substrate or the reduction in fibre diameter at a higher rate than the shell growth. The sequential detachment of precipitate layers resulted in the formation of multiple inner shells around the shrinking glass fibre core.

The crystallinity of the composites samples was higher in comparison to the neat-PLA control due to the heterogeneous nucleation ability of the glass fibre surface, reaching a maximum of 28% for the forged composite rods with 0.45 fibre volume fraction. The crystallinity of the forged rods increased with

respect to the compression moulded composite plates as a result of heating to 90-100°C prior stamping. The increase in the crystallinity of all the rods during immersion in PBS at 37°C was attributed to the preferential hydrolysis of ester bonds in the PLA amorphous regions and the rearrangement of PLA chain fragments into crystallites. The greater crystallinity increase for the forged composite samples with respect to the neat-PLA control forged rods was attributed to the higher water uptake of the composites, reaching a maximum crystallinity content of 37% observed after 30 days of PBS conditioning for the 0.45-CP-M forged composite rods.

Enhanced PLA hydrolysis in the composites samples was associated with the higher amount of water absorbed by the composites due to the hydrophilic glass fibres and the catalytic effect of the acidic environment produced by phosphate glass dissolution. The number average molecular weight decreased in proportion to the fibre volume fraction as a result of the higher water uptake and the greater reduction in pH associated with the progressively higher content of phosphate glass fibres, reaching maximum M_n reductions of 81% and 77% for the $0.35v_f$ and $0.45v_f$ forged composite rods, respectively.

5.1.4 Manufacture of Fully Bioresorbable Composite Rods via Compression Moulding of Polymer Sheathed Fibre Bundles

PLA-PGF hybrid preforms with controlled masses could be continuously fabricated at high speeds by extruding a sheath of polymer at 165°C onto bundles of fibres using a purpose-built crosshead die. PLA-sheathing of fibre bundles is the most effective and efficient method for the production of thermoplastic hybrid preforms, as it combines polymer and fibres in a single operation. Since no stresses are applied on the fibres and no spreading is required, it was possible to process annealed phosphate glass fibres embrittled by heat treatment at 460°C.

Compression moulding of polymer-sheathed fibre bundles is a leaner manufacturing process which reduced the number of operation required to fabricate composite with circular cross sections in comparison to forging methods. Consolidation and shaping took place simultaneously on account of the packing efficiency of the hybrid preforms. In addition, the PLA-sheath

acted as a protective sleeve that prevented the fibres from contacting directly the mould walls.

The effectiveness of the PLA-sheathed fibre bundles was demonstrated by the full fibre impregnation via radial percolation of polymer as revealed by composite cross sectional studies. Comparatively stronger composites could be manufactured by embedding as-drawn fibres in a PLA matrix by compression moulding of PLA-sheath fibre bundles as a result of the decrease in fibre strength promoted by heat treatment. Maximum strength values for as-drawn and annealed fibre reinforced compression moulded rods were observed for the $0.45v_f$ samples reaching values of 370 MPa and 280 MPa, respectively, which surpassed the human cortical bone strength range.

The strength of the $0.45v_f$ compression moulded composite rods reinforced with as-drawn fibres was 23% higher in comparison with the respective forged composite rods as a result of the presence of intra-ply cracks in the latter, but 23% lower with respect to the composite plate fabricated from thick mats via cyclic pressure assisted-compression moulding on account of the static pressure profile used during consolidation of the PLA-sheathed fibre bundles. Further increases in composite strength can be expected by the implementation of cyclic pressure to compression moulding of PLA-sheathed fibre bundles.

The elastic modulus of composite rods fabricated via compression moulding of PLA-sheathed fibre bundles are the highest hitherto reported for bioresorbable composites. Values in the range of 33 GPa were achieved for annealed fibre reinforced composite rods. This was attributed to the unique distribution of reinforcing fibres throughout the composite cross section achieved by compression moulding of PLA-sheathed fibre bundles.

In vitro degradation of as-drawn fibre reinforced compression moulded composite rods was comparable to the behaviour observed for plane strain forged composite rods in PBS at 37°C. Compression moulded rods reinforced with as-drawn fibres presented an immediate reduction in mechanical properties upon immersion in aqueous media that continued gradually, stabilising at around 50 MPa by day 15. Unlike the 0.45-CP-M forged composite rods which featured a reduction in strength of approximately 70%

after one day of immersion and lost the reinforcing effect of fibres by day 7, the strength of $0.45v_f$ compression moulded rods reinforced with as-drawn fibres decreased by 40% after one day of immersion and retained mechanical properties within the range of human cortical bone for up to 15 days. The better retention of mechanical properties for $0.45v_f$ compression moulded composite rods with respect to forged composite rods with the same fibre volume fraction was attributed to the deleterious presence of intra-ply cracks in the latter, which expedited water absorption and glass fibre dissolution.

Initial loss of mechanical properties was associated with the disruption of the fibre-matrix interface by capillary water. Further decreases in mechanical properties were explained by reductions in the fibre diameter which impaired the transfer of stresses via frictional resistance.

A sudden decrease in mechanical properties was also observed in annealed fibre reinforced compression moulded composite rods. However, the rate at which the strength decreased after day one was much lower in comparison to as-drawn fibre reinforced compression moulded composite rods, remaining close to the lower limit of the cortical strength range for the remainder of the degradation study. For all the compression moulded composite rods reinforced with annealed fibres, the elastic modulus remained within the human cortical bone range throughout the 30 day study. Elastic modulus values at day 30 of conditioning in aqueous medium for the $0.45v_f$ composite samples reinforced with annealed fibres are the highest hitherto reported for bioresorbable composites. The better performance of annealed fibre reinforced compression moulded composite rods with respect to as-drawn fibre reinforced composites in wet conditions was attributed to the radial pressure exerted by the swollen polymer matrix against the slowly dissolving annealed fibres which restricted the penetration of additional water in good agreement with the water absorption trend.

Significant variations in the pH of the medium in the course of annealed fibre reinforced composites conditioning were prevented by the slow dissolution of annealed fibres. Conversely, the pH of the composite rods containing as-drawn fibres quickly shifted towards acidic values in proportion to the fibre volume fraction.

Precipitate shells were observed to form in the course of as-drawn fibre reinforced composite conditioning, on account of the quick saturation of the leaching solution with orthophosphate species. The chemical composition of such precipitates was observed to change with conditioning time as observed during PBS conditioning of forged composite rods. No precipitation or appreciable reduction in annealed fibre diameter was observed after examination of the composite fracture surface as a result of the slow dissolution of annealed fibres.

In comparison to as-drawn fibres, annealed fibres presented a reduced efficiency in the heterogeneous nucleation of spherulites as revealed by the significant contraction of the cold crystallisation with increasing in fibre volume fraction upon calorimetric solicitation, possibly due to the passivation of the glass fibre surface experienced following heat treatment.

In correspondence with the changes observed during forged composite rods conditioning, the crystallinity in the as-drawn fibre reinforced compression moulded composite rods increased with conditioning time as a result of the preferential hydrolysis of ester bonds in the amorphous regions of the PLA-matrix and the rearrangement of the PLA chains into crystallites due to the plasticising effect of water, reaching crystallinity contents in the order of 30% for most of the composite samples.

Restriction of water absorption through the action of the radial pressure exerted by the swollen PLA matrix against the slowly dissolving fibres prevented the increases in crystallinity content observed for as-drawn fibre reinforced compression moulded and forged rods. The presence of slowly dissolving annealed glass fibres could have also hampered the rearrangement of PLA chains necessary for the formation of new crystallites.

The 10% lower initial molecular weights of the PLA matrix in as-drawn fibre reinforced compression moulded composite rods with respect to annealed fibre reinforced composite rods was attributed to the highly energetic as-drawn fibre surface which readily adsorbs environmental moisture that subsequently reacts with the polymer melt at the processing temperature.

The higher amount of water absorbed, coupled with the catalytic effect of the acidic environment created by polyphosphate anions product of glass fibre hydrolysis resulted in the continued decrease in molecular weight for the as-drawn fibre reinforced compression moulded rods in the course of the 30 day degradation study, reaching a maximum reduction of 15% with respect to the initial molecular weight for the $0.45v_f$ composite samples.

Conversely, the minor amount of water absorbed and the negligible changes in the pH of the conditioning media were reflected in the stability of the number average molecular weight for all the annealed fibre reinforced compression moulded composites.

5.2 Future work

The following actions are suggested to further improve the performance of the bioresorbable composites manufactured through melt impregnation techniques and to gain further insight on the in vivo behaviour of these materials:

- Annealing of phosphate glass fibres while being subjected to a subcritical tensile stress may prevent the large reduction in strength associated with the formation of a residual tensile stress surface layer and the relaxation of the anisotropic fibre structure. Slowly dissolving annealed fibres with higher strengths should be able to increase the composite strength in wet conditions in accordance to the behaviour observed during the in vitro degradation studies.

- Implementation of cyclic pressure during the consolidation stage of compression moulding of PLA-sheathed fibre bundles to maximise the composite strength.

- Development of a clamping system to prevent polymer leakage through the mould parting lines during the manufacture of compression moulded composite rods.

- Functionalisation of phosphate glass fibres with polydopamine to improve the fibre-matrix interface and consequently, the retention of mechanical properties in wet conditions.

- Fabrication of composite rods with different structures (see Figure 5.1) only possible via compression moulding of PLA-sheathed fibre bundles, namely, i) discontinuous-aligned fibre reinforced composite rods, ii) continuous fibre reinforced composite rods with controlled lengths and iii) particle-continuous fibre reinforced composite rods and evaluation of the effect of the reinforcement architecture in the composite mechanical behaviour in wet conditions.

  Cations which may have a therapeutic effect (angeogenic, antibacterial, osteoinductive, osteoconductive, etc.) on the damaged tissue, but that may impair fibre drawing, can be incorporated in the bioresorbable composite as glass as a modifier in reinforcing glass particles. The glass particles can be compounded with PLA during the sheathing process.

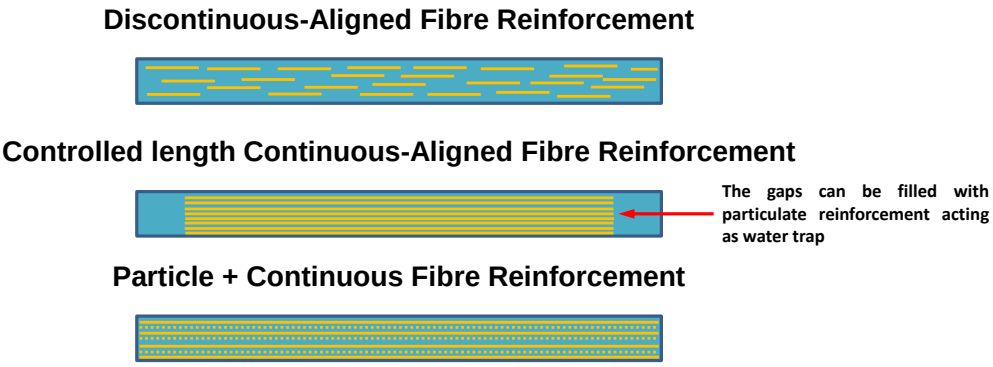


Figure 5.1: Bioresorbable composite rods with structures unique to compression moulding of PLA-sheathed fibre bundles. PLA-matrix is represented in blue and reinforcing phosphate glass fibres/particles are represented in yellow.

- Continuous manufacture of semi-finished (prepregs) or finished pultruded bioresorbable composite products via crosshead extrusion.

  To achieve this, a pultrusion attachment was designed. As shown in Figure 5.2, the pultrusion attachment assembly consists of i) an impregnation chamber, ii) 4 pairs of spreading pins whose alignment can be modified, iii) a forming die with a cavity shaped in the desired profile cross section and iv) a pressure-type tip attached to the spiral mandrel.

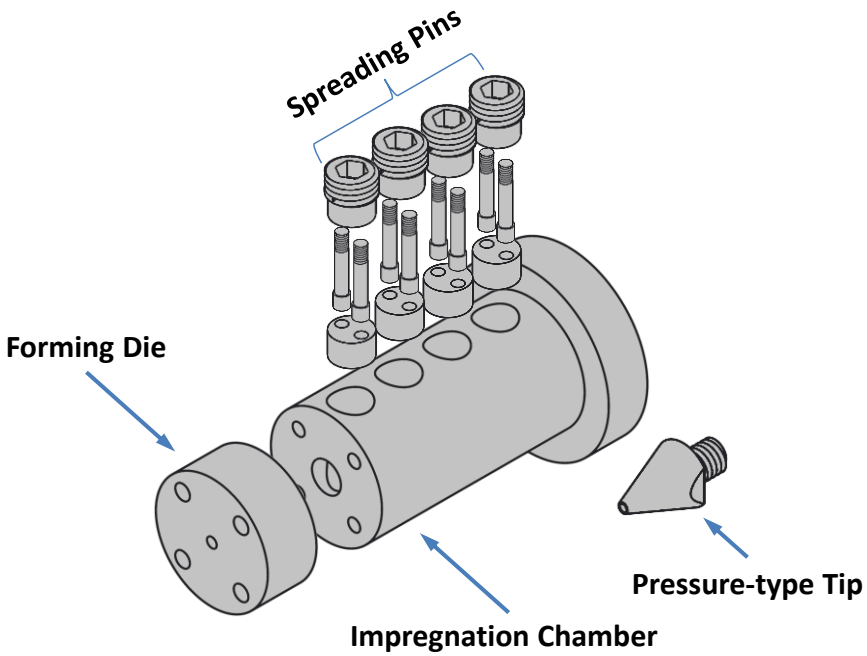


Figure 5.2: Exploded view of the pultrusion attachment assembly for the manufacture of semi-finished or finished bioresorbable pultruded composite products.

The cross section of the crosshead die in the pultrusion configuration is shown in Figure 5.3. The spreading pins are shown in the aligned position parallel to the pultrusion axis. The fibre bundle is flattened as a result of the contact with the spreading pins and subsequently impregnated with molten PLA, continuously pumped by the extruder. The impregnated bundles are then consolidated into the desired profile cross section in the forming die

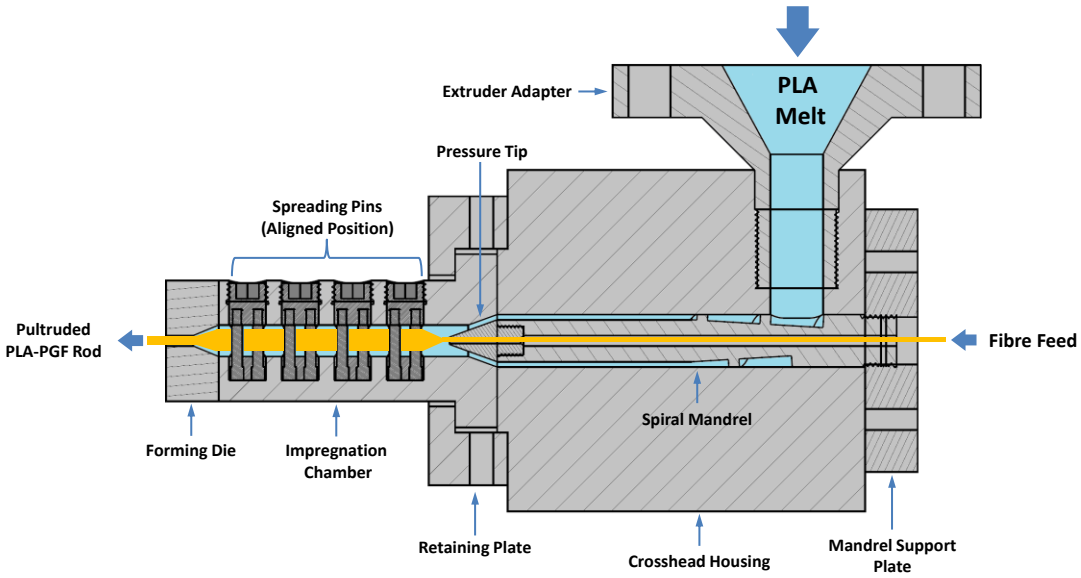


Figure 5.3: Cross section of the crosshead die in the pultrusion configuration. Fibres and molten PLA come into contact inside the impregnation chamber. The impregnated fibre bundles are then consolidated into the desired profile cross section inside the forming die.

The spreading pins can be rotated into two positions, as illustrated by the lateral and top cross sections of the pultrusion attachment shown in Figures 5.4 and 5.5, respectively. In Figure 5.4a and 5.5a the 4 pairs of spreading pins are positioned perpendicularly to the pultrusion axis. The fibre bundle is further compacted by the pressurised melt inside the impregnation chamber, so that a partially impregnated prepreg with a tick outer PLA coating is produced.

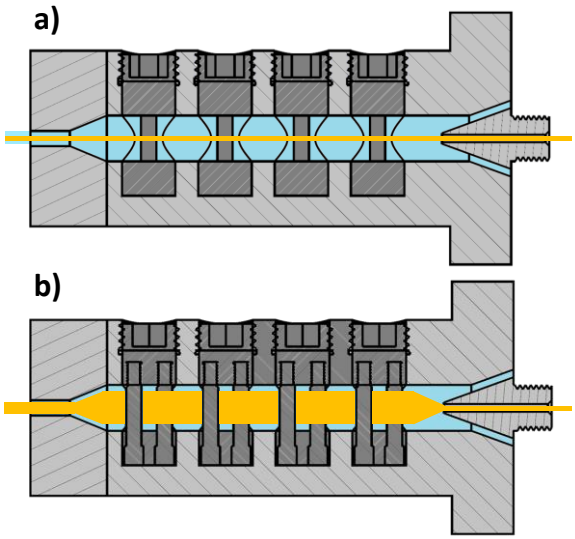


Figure 5.4: Lateral cross section of the pultrusion attachment showing the pins a) perpendicular and b) aligned parallel to the extrusion axis. PLA melt is represented in blue and the fibre bundle is shown in yellow.

Alternatively, as shown in Figure 5.4b and 5.5b, the fibre bundle can be flattened by rotating the spreading pins into a position aligned parallel to the extrusion axis, reducing polymer flow path so that full impregnation can be readily achieved. A pultruded composite profile of the desired cross section is obtained after passing through the forming die.

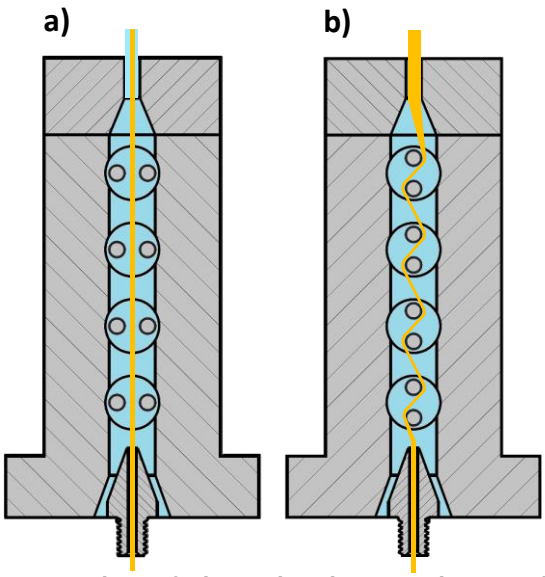


Figure 5.5: Top cross section of the pultrusion attachment showing the pins a) perpendicular and b) aligned parallel to the extrusion axis. PLA melt is represented in blue and the fibre bundle is shown in yellow.

- Conduction of cell viability and in vivo degradation studies to determine the effect of PLA-PGF composite degradation by-products on the surrounding tissue.

References

1. Salter, R.B., *Textbook of Disorders and Injuries of the Musculoskeletal System: An Introduction to Orthopaedics, Fractures, and Joint Injuries, Rheumatology, Metabolic Bone Disease, and Rehabilitation*. 1999: Williams & Wilkins.
2. Browner, B.D., *Skeletal Trauma: Basic Science, Management, and Reconstruction*. 2009: Saunders/Elsevier.
3. Hindley, C.J., et al., *Locked intramedullary nailing for recent lower limb fractures.* Injury, 1990. **21**(4): p. 239-44.
4. Wiss, D.A. and T. Gibson, *Intramedullary nailing of the femur and tibia: Indications and techniques.* Current Orthopaedics, 1994. **8**(4): p. 245-254.
5. Brumback, R.J., et al., *Intramedullary nailing of femoral shaft fractures. Part II: Fracture-healing with static interlocking fixation.* J Bone Joint Surg Am, 1988. **70**(10): p. 1453-62.
6. Navarro, M., et al., *Biomaterials in orthopaedics.* Journal of The Royal Society Interface, 2008. **5**(27): p. 1137-1158.
7. Narayan, R., *Biomedical Materials*. 2009: Springer.
8. Hench, L.L. and J.M. Polak, *Third-Generation Biomedical Materials.* Science, 2002. **295**(5557): p. 1014-1017.
9. Franz, S., et al., *Immune responses to implants - a review of the implications for the design of immunomodulatory biomaterials.* Biomaterials, 2011. **32**(28): p. 6692-709.
10. Suuronen, R. and C. Lindqvist, *Bioresorbable Materials for Bone Fixation: Review of Biological Concepts and Mechanical Aspects*, in *Craniomaxillofacial Reconstructive and Corrective Bone Surgery: Principles of Internal Fixation Using the AO/ASIF Technique*, A.M. Greenberg and J. Prein, Editors. 2002, Springer New York: New York, NY. p. 113-123.
11. Suzuki, S. and Y. Ikada, *Medical Applications*, in *Poly(Lactic Acid)*. 2010, John Wiley & Sons, Inc. p. 443-456.
12. Brauer, D.S., *Phosphate Glasses*, in *Bio-Glasses*. 2012, John Wiley & Sons, Ltd. p. 45-64.
13. Bunker, B.C., G.W. Arnold, and J.A. Wilder, *Phosphate glass dissolution in aqueous solutions.* Journal of Non-Crystalline Solids, 1984. **64**(3): p. 291-316.
14. Hoppe, A., V. Mourino, and A.R. Boccaccini, *Therapeutic inorganic ions in bioactive glasses to enhance bone formation and beyond.* Biomaterials Science, 2013. **1**(3): p. 254-256.
15. Felfel, R.M., et al., *Initial mechanical properties of phosphate-glass fibre-reinforced rods for use as resorbable intramedullary nails.* Journal of Materials Science, 2012. **47**(12): p. 4884-4894.
16. Han, N., et al., *Influence of screw holes and gamma sterilization on properties of phosphate glass fiber-reinforced composite bone plates.* J Biomater Appl, 2013. **27**(8): p. 990-1002.
17. Ahmed, I., et al., *Composites for bone repair: phosphate glass fibre reinforced PLA with varying fibre architecture.* J Mater Sci Mater Med, 2011. **22**(8): p. 1825-34.
18. Felfel, R.M., et al., *Cytocompatibility, degradation, mechanical property retention and ion release profiles for phosphate glass fibre reinforced composite rods.* Materials Science and Engineering: C, 2013. **33**(4): p. 1914-1924.
19. Bates, P.J., et al., *Pressure build-up during melt impregnation.* Composites Science and Technology, 2002. **62**(3): p. 379-384.

20. Mallick, P.K., *Fiber-Reinforced Composites: Materials, Manufacturing, and Design, Third Edition*. 2007: CRC Press.
21. Wang, P., N. Hamila, and P. Boisse, *Thermoforming simulation of multilayer composites with continuous fibres and thermoplastic matrix.* Composites Part B: Engineering, 2013. **52**: p. 127-136.
22. Jacobs, C.R., *Bone mechanics handbook (second edition): Stephen C. Cowin (Ed.); CRC Press, Boca Raton, FL, 2001, hardback ISBN 0-8493-9117-2.* Journal of Biomechanics, 2002. **35**(5): p. 723-724.
23. Olszta, M.J., et al., *Bone structure and formation: A new perspective.* Materials Science and Engineering: R: Reports, 2007. **58**(3–5): p. 77-116.
24. Burr, D.B. and O. Akkus, *Chapter 1 - Bone Morphology and Organization*, in *Basic and Applied Bone Biology*, D.B. Burr and M.R. Allen, Editors. 2014, Academic Press: San Diego. p. 3-25.
25. Vaughan, T.J., C.T. McCarthy, and L.M. McNamara, *A three-scale finite element investigation into the effects of tissue mineralisation and lamellar organisation in human cortical and trabecular bone.* Journal of the Mechanical Behavior of Biomedical Materials, 2012. **12**(0): p. 50-62.
26. Rho, J.-Y., L. Kuhn-Spearing, and P. Zioupos, *Mechanical properties and the hierarchical structure of bone.* Medical Engineering & Physics, 1998. **20**(2): p. 92-102.
27. Katsamenis, O.L., et al., *Load-bearing in cortical bone microstructure: Selective stiffening and heterogeneous strain distribution at the lamellar level.* Journal of the Mechanical Behavior of Biomedical Materials, 2013. **17**(0): p. 152-165.
28. Weiner, S. and H.D. Wagner, *THE MATERIAL BONE: Structure-Mechanical Function Relations.* Annual Review of Materials Science, 1998. **28**(1): p. 271-298.
29. Athanasiou, K.A., et al., *Fundamentals of biomechanics in tissue engineering of bone.* Tissue Eng, 2000. **6**(4): p. 361-81.
30. Keller, T.S., Z. Mao, and D.M. Spengler, *Young's modulus, bending strength, and tissue physical properties of human compact bone.* Journal of Orthopaedic Research, 1990. **8**(4): p. 592-603.
31. Prasad, K., et al., *Metallic Biomaterials: Current Challenges and Opportunities.* Materials, 2017. **10**(8): p. 884.
32. Augat, P. and S. Schorlemmer, *The role of cortical bone and its microstructure in bone strength.* Age and Ageing, 2006. **35**(suppl 2): p. ii27-ii31.
33. Fazzalari, N.L., et al., *A model for the change of cancellous bone volume and structure over time.* Mathematical Biosciences, 2012. **240**(2): p. 132-140.
34. Pivonka, P., et al., *Model structure and control of bone remodeling: A theoretical study.* Bone, 2008. **43**(2): p. 249-263.
35. Zebaze, R.M.D., et al., *Construction of the Femoral Neck During Growth Determines Its Strength in Old Age.* Journal of Bone and Mineral Research, 2007. **22**(7): p. 1055-1061.
36. Seeman, E., *Bone Modeling and Remodeling.* 2009. **19**(3): p. 219-233.
37. Doblaré, M., J.M. García, and M.J. Gómez, *Modelling bone tissue fracture and healing: a review.* Engineering Fracture Mechanics, 2004. **71**(13–14): p. 1809-1840.
38. Martin, T.J. and E. Seeman, *Bone remodelling: its local regulation and the emergence of bone fragility.* Best Practice & Research Clinical Endocrinology & Metabolism, 2008. **22**(5): p. 701-722.
39. Kular, J., et al., *An overview of the regulation of bone remodelling at the cellular level.* Clinical Biochemistry, 2012. **45**(12): p. 863-873.

40. Jahagirdar, R. and B.E. Scammell, *Principles of fracture healing and disorders of bone union.* Surgery (Oxford), 2009. **27**(2): p. 63-69.
41. Wraighte, P.J. and B.E. Scammell, *Principles of fracture healing.* Surgery (Oxford), 2006. **24**(6): p. 198-207.
42. Giannoudis, P., et al., *Fracture healing in osteoporotic fractures: Is it really different?: A basic science perspective.* Injury, 2007. **38**(1, Supplement): p. S90-S99.
43. Forster, M.C., B. Komarsamy, and J.N. Davison, *Distal femoral fractures: A review of fixation methods.* Injury, 2006. **37**(2): p. 97-108.
44. Harwood, P.J., J.B. Newman, and A.L.R. Michael, *(ii) An update on fracture healing and non-union.* Orthopaedics and Trauma, 2010. **24**(1): p. 9-23.
45. Dimitriou, R., E. Tsiridis, and P.V. Giannoudis, *Current concepts of molecular aspects of bone healing.* Injury, 2005. **36**(12): p. 1392-1404.
46. Marsell, R. and T.A. Einhorn, *The biology of fracture healing.* Injury, 2011. **42**(6): p. 551-555.
47. McKinley, T., *Principles of Fracture Healing.* Surgery (Oxford), 2003. **21**(9): p. 209-212.
48. Phillips, A.M., *Overview of the fracture healing cascade.* Injury, 2005. **36**(3): p. S5-S7.
49. Mackie, E.J., et al., *Endochondral ossification: How cartilage is converted into bone in the developing skeleton.* The International Journal of Biochemistry & Cell Biology, 2008. **40**(1): p. 46-62.
50. Son, D.-S., et al., *The finite element analysis for endochondral ossification process of a fractured tibia applied with a composite IM-rod based on a mechano-regulation theory using a deviatoric strain.* Composites Part B: Engineering, 2014. **56**(0): p. 189-196.
51. Bridgens, J.P. and D.L. Douglas, *Fractures of the Femoral Shaft.* Surgery (Oxford), 2003. **21**(9): p. 225-227.
52. Papakostidis, C., et al., *Femoral-shaft fractures and nonunions treated with intramedullary nails: The role of dynamisation.* Injury, 2011. **42**(11): p. 1353-1361.
53. Brumback, R.J., et al., *Intramedullary nailing of femoral shaft fractures. Part III: Long-term effects of static interlocking fixation.* J Bone Joint Surg Am, 1992. **74**(1): p. 106-12.
54. Perren, S.M., *Evolution of the internal fixation of long bone fractures. The scientific basis of biological internal fixation: choosing a new balance between stability and biology.* J Bone Joint Surg Br, 2002. **84**(8): p. 1093-110.
55. von Recum, J., et al., *Characteristics of two different locking compression plates in the volar fixation of complex articular distal radius fractures.* Bone and Joint Research, 2012. **1**(6): p. 111-117.
56. Delaunay, C., et al., *Survival analysis of an asymmetric primary total knee replacement: A European multicenter prospective study.* Orthopaedics & Traumatology: Surgery & Research, 2010. **96**(7): p. 769-776.
57. Anderson, J.M., A. Rodriguez, and D.T. Chang, *Foreign body reaction to biomaterials.* Semin Immunol, 2008. **20**(2): p. 86-100.
58. Krishna, B.V., S. Bose, and A. Bandyopadhyay, *Low stiffness porous Ti structures for load-bearing implants.* Acta Biomaterialia, 2007. **3**(6): p. 997-1006.
59. Joshi, M.G., et al., *Analysis of a femoral hip prosthesis designed to reduce stress shielding.* Journal of Biomechanics, 2000. **33**(12): p. 1655-1662.
60. Staiger, M.P., et al., *Magnesium and its alloys as orthopedic biomaterials: a review.* Biomaterials, 2006. **27**(9): p. 1728-34.

61. Gu, X.-N. and Y.-F. Zheng, *A review on magnesium alloys as biodegradable materials.* Frontiers of Materials Science in China, 2010. **4**(2): p. 111-115.
62. Witte, F., et al., *Degradable biomaterials based on magnesium corrosion.* Current Opinion in Solid State and Materials Science, 2008. **12**(5): p. 63-72.
63. Agarwal, S., et al., *Biodegradable magnesium alloys for orthopaedic applications: A review on corrosion, biocompatibility and surface modifications.* Materials Science and Engineering: C, 2016. **68**: p. 948-963.
64. Chen, Y., et al., *Recent advances on the development of magnesium alloys for biodegradable implants.* Acta Biomaterialia, 2014. **10**(11): p. 4561-4573.
65. Staiger, M.P., et al., *Magnesium and its alloys as orthopedic biomaterials: A review.* Biomaterials, 2006. **27**(9): p. 1728-1734.
66. Zheng, Y.F., X.N. Gu, and F. Witte, *Biodegradable metals.* Materials Science and Engineering: R: Reports, 2014. **77**: p. 1-34.
67. Griffith, L.G., *Polymeric biomaterials.* Acta Materialia, 2000. **48**(1): p. 263-277.
68. Teo, A.J.T., et al., *Polymeric Biomaterials for Medical Implants and Devices.* ACS Biomaterials Science & Engineering, 2016. **2**(4): p. 454-472.
69. Ramakrishna, S., et al., *Biomedical applications of polymer-composite materials: a review.* Composites Science and Technology, 2001. **61**(9): p. 1189-1224.
70. Lim, L.T., R. Auras, and M. Rubino, *Processing technologies for poly(lactic acid).* Progress in Polymer Science, 2008. **33**(8): p. 820-852.
71. Middleton, J.C. and A.J. Tipton, *Synthetic biodegradable polymers as orthopedic devices.* Biomaterials, 2000. **21**(23): p. 2335-46.
72. Jamshidian, M., et al., *Poly-Lactic Acid: Production, Applications, Nanocomposites, and Release Studies.* Comprehensive Reviews in Food Science and Food Safety, 2010. **9**(5): p. 552-571.
73. Middleton, J.C. and A.J. Tipton, *Synthetic biodegradable polymers as orthopedic devices.* Biomaterials, 2000. **21**(23): p. 2335-2346.
74. Sabir, M.I., X. Xu, and L. Li, *A review on biodegradable polymeric materials for bone tissue engineering applications.* Journal of Materials Science, 2009. **44**(21): p. 5713-5724.
75. Katti, K.S., *Biomaterials in total joint replacement.* Colloids and Surfaces B: Biointerfaces, 2004. **39**(3): p. 133-142.
76. Athanasiou, K.A., et al., *Orthopaedic applications for PLA-PGA biodegradable polymers.* Arthroscopy, 1998. **14**(7): p. 726-37.
77. Rokkanen, P.U., et al., *Bioabsorbable fixation in orthopaedic surgery and traumatology.* Biomaterials, 2000. **21**(24): p. 2607-13.
78. Ciccone, W.J., et al., *Bioabsorbable Implants in Orthopaedics: New Developments and Clinical Applications.* Journal of the American Academy of Orthopaedic Surgeons, 2001. **9**(5): p. 280-288.
79. Frokjaer, J. and B.N. Moller, *Biodegradable fixation of ankle fractures. Complications in a prospective study of 25 cases.* Acta Orthop Scand, 1992. **63**(4): p. 434-6.
80. Miketa, J.P. and M.M. Prigoff, *Foreign body reactions to absorbable implant fixation of osteotomies.* J Foot Ankle Surg, 1994. **33**(6): p. 623-7.
81. Kulkarni, R.K., et al., *Polylactic acid for surgical implants.* Arch Surg, 1966. **93**(5): p. 839-43.
82. Rasal, R.M., A.V. Janorkar, and D.E. Hirt, *Poly(lactic acid) modifications.* Progress in Polymer Science, 2010. **35**(3): p. 338-356.

83. Madhavan Nampoothiri, K., N.R. Nair, and R.P. John, *An overview of the recent developments in polylactide (PLA) research.* Bioresource Technology, 2010. **101**(22): p. 8493-8501.
84. Lasprilla, A.J.R., et al., *Poly-lactic acid synthesis for application in biomedical devices — A review.* Biotechnology Advances, 2012. **30**(1): p. 321-328.
85. Vaccaro, A.R., et al., *The use of bioabsorbable implants in the spine.* Spine J, 2003. **3**(3): p. 227-37.
86. Henton, D., et al., *Polylactic Acid Technology*, in *Natural Fibers, Biopolymers, and Biocomposites*. 2005, CRC Press.
87. Gupta, B., N. Revagade, and J. Hilborn, *Poly(lactic acid) fiber: An overview.* Progress in Polymer Science, 2007. **32**(4): p. 455-482.
88. MacDonald, R.T., S.P. McCarthy, and R.A. Gross, *Enzymatic Degradability of Poly(lactide): Effects of Chain Stereochemistry and Material Crystallinity.* Macromolecules, 1996. **29**(23): p. 7356-7361.
89. Fambri, L. and C. Migliaresi, *Crystallization and Thermal Properties*, in *Poly(Lactic Acid)*. 2010, John Wiley & Sons, Inc. p. 113-124.
90. Tsuji, H., *Hydrolytic Degradation*, in *Poly(Lactic Acid)*. 2010, John Wiley & Sons, Inc. p. 343-381.
91. Li, S., H. Garreau, and M. Vert, *Structure-property relattonslups in the case of the degradaUon of solid aliphatic poly (ot-hydroxy acids) in aqueous media. I'Poly (d/-lactic acid) or PLA50.* J. Mater. SCL Mater Med, 1990. **1**: p. 123-130.
92. Cam, D., S.-h. Hyon, and Y. Ikada, *Degradation of high molecular weight poly(l-lactide) in alkaline medium.* Biomaterials, 1995. **16**(11): p. 833-843.
93. Garlotta, D., *A Literature Review of Poly(Lactic Acid).* Journal of Polymers and the Environment, 2001. **9**(2): p. 63-84.
94. Södergård, A. and M. Stolt, *Properties of lactic acid based polymers and their correlation with composition.* Progress in Polymer Science, 2002. **27**(6): p. 1123-1163.
95. Tsuji, H., A. Mizuno, and Y. Ikada, *Properties and morphology of poly(L-lactide). III. Effects of initial crystallinity on long-term in vitro hydrolysis of high molecular weight poly(L-lactide) film in phosphate-buffered solution.* Journal of Applied Polymer Science, 2000. **77**(7): p. 1452-1464.
96. Tsuji, H. and Y. Ikada, *Blends of crystalline and amorphous poly(lactide). III. Hydrolysis of solution-cast blend films.* Journal of Applied Polymer Science, 1997. **63**(7): p. 855-863.
97. Tsuji, H. and Y. Ikada, *Stereocomplex formation between enantiomeric poly(lactic acid)s. XI. Mechanical properties and morphology of solution-cast films.* Polymer, 1999. **40**(24): p. 6699-6708.
98. Sharma, S.K., et al., *A Handbook of Applied Biopolymer Technology: Synthesis, Degradation and Applications*. 2011: Royal Society of Chemistry.
99. Tsuji, H. and Y. Ikada, *Properties and morphology of poly(L-lactide). II. Hydrolysis in alkaline solution.* Journal of Polymer Science Part A: Polymer Chemistry, 1998. **36**(1): p. 59-66.
100. Athanasiou, K.A., et al., *Orthopaedic applications for PLA-PGA biodegradable polymers.* Arthroscopy: The Journal of Arthroscopic & Related Surgery, 1998. **14**(7): p. 726-737.
101. An, Y.H., S.K. Woolf, and R.J. Friedman, *Pre-clinical in vivo evaluation of orthopaedic bioabsorbable devices.* Biomaterials, 2000. **21**(24): p. 2635-2652.
102. Al-Itry, R., K. Lamnawar, and A. Maazouz, *Improvement of thermal stability, rheological and mechanical properties of PLA, PBAT and their blends by reactive extrusion with functionalized epoxy.* Polymer Degradation and Stability, 2012. **97**(10): p. 1898-1914.

103. Kopinke, F.D., et al., *Thermal decomposition of biodegradable polyesters—II. Poly(lactic acid).* Polymer Degradation and Stability, 1996. **53**(3): p. 329-342.
104. Taubner, V. and R. Shishoo, *Influence of processing parameters on the degradation of poly(L-lactide) during extrusion.* Journal of Applied Polymer Science, 2001. **79**(12): p. 2128-2135.
105. David, E.H., et al., *Polylactic Acid Technology*, in *Natural Fibers, Biopolymers, and Biocomposites*. 2005, CRC Press.
106. Lim, L.-T., K. Cink, and T. Vanyo, *Processing of Poly(Lactic Acid)*, in *Poly(Lactic Acid)*. 2010, John Wiley & Sons, Inc. p. 189-215.
107. Vallet-Regí, M., *Evolution of bioceramics within the field of biomaterials.* Comptes Rendus Chimie, 2010. **13**(1): p. 174-185.
108. Chevalier, J. and L. Gremillard, *Ceramics for medical applications: A picture for the next 20 years.* Journal of the European Ceramic Society, 2009. **29**(7): p. 1245-1255.
109. Saikko, V.O., P.O. Paavolainen, and P. Slätis, *Wear of the polyethylene acetabular cup: Metallic and ceramic heads compared in a hip simulator.* Acta Orthopaedica Scandinavica, 1993. **64**(4): p. 391-402.
110. Kamitakahara, M., C. Ohtsuki, and T. Miyazaki, *Review Paper: Behavior of Ceramic Biomaterials Derived from Tricalcium Phosphate in Physiological Condition.* Journal of Biomaterials Applications, 2008. **23**(3): p. 197-212.
111. Affatato, S., A. Ruggiero, and M. Merola, *Advanced biomaterials in hip joint arthroplasty. A review on polymer and ceramics composites as alternative bearings.* Composites Part B: Engineering, 2015. **83**: p. 276-283.
112. Jones, J.R., *Review of bioactive glass: From Hench to hybrids.* Acta Biomaterialia, 2013. **9**(1): p. 4457-4486.
113. Kaur, G., et al., *A review of bioactive glasses: Their structure, properties, fabrication and apatite formation.* Journal of Biomedical Materials Research Part A, 2014. **102**(1): p. 254-274.
114. O'Donnell, M.D., *Melt-Derived Bioactive Glass*, in *Bio-Glasses*. 2012, John Wiley & Sons, Ltd. p. 13-27.
115. Abou Neel, E.A., et al., *Effect of iron on the surface, degradation and ion release properties of phosphate-based glass fibres.* Acta Biomaterialia, 2005. **1**(5): p. 553-563.
116. Khan, R.A., et al., *Preparation and Characterization of Phosphate Glass Fibers and Fabrication of Poly(caprolactone) Matrix Resorbable Composites.* Journal of Reinforced Plastics and Composites, 2010. **29**(12): p. 1838-1850.
117. Arstila, H., et al., *Factors affecting crystallization of bioactive glasses.* Journal of the European Ceramic Society, 2007. **27**(2): p. 1543-1546.
118. Groh, D., F. Döhler, and D.S. Brauer, *Bioactive glasses with improved processing. Part 1. Thermal properties, ion release and apatite formation.* Acta Biomaterialia, 2014. **10**(10): p. 4465-4473.
119. Döhler, F., et al., *Bioactive glasses with improved processing. Part 2. Viscosity and fibre drawing.* Journal of Non-Crystalline Solids, 2016. **432**: p. 130-136.
120. Brow, R.K., *Review: the structure of simple phosphate glasses.* Journal of Non-Crystalline Solids, 2000. **263–264**(0): p. 1-28.
121. Kaur, G., et al., *A review of bioactive glasses: Their structure, properties, fabrication, and apatite formation.* J Biomed Mater Res A, 2013.
122. Kingery, W.D., H.K. Bowen, and D.R. Uhlmann, *Introduction to ceramics*. 1976: Wiley.
123. Schubert, U., *Introduction to glass science and technology. Von J. E. Shelby. Royal Society of Chemistry, Cambridge, 1997. 244 S., Broschur, 18.95 £.— ISBN 0-85404-533-3.* Angewandte Chemie, 1997. **109**(22): p. 2637-2637.

124. Jones, J. and A. Clare, *Bio-Glasses : An Introduction*. 2012, Somerset, NJ, USA: John Wiley & Sons.
125. Gao, H., T. Tan, and D. Wang, *Dissolution mechanism and release kinetics of phosphate controlled release glasses in aqueous medium.* J Control Release, 2004. **96**(1): p. 29-36.
126. Gao, H., T. Tan, and D. Wang, *Effect of composition on the release kinetics of phosphate controlled release glasses in aqueous medium.* Journal of Controlled Release, 2004. **96**(1): p. 21-28.
127. Knowles, J.C., *Phosphate based glasses for biomedical applications.* Journal of Materials Chemistry, 2003. **13**(10): p. 2395-2401.
128. Vitale-Brovarone, C., et al., *Novel phosphate glasses with different amounts of TiO2 for biomedical applications: Dissolution tests and proof of concept of fibre drawing.* Materials Science and Engineering: C, 2011. **31**(2): p. 434-442.
129. Ahmed, I., et al., *Processing, characterisation and biocompatibility of iron-phosphate glass fibres for tissue engineering.* Biomaterials, 2004. **25**(16): p. 3223-32.
130. Abou Neel, E.A., W. Chrzanowski, and J.C. Knowles, *Effect of increasing titanium dioxide content on bulk and surface properties of phosphate-based glasses.* Acta Biomater, 2008. **4**(3): p. 523-34.
131. Noguera, O., et al., *Vibrational and structural properties of glass and crystalline phases of TeO2.* Journal of Non-Crystalline Solids, 2003. **330**(1–3): p. 50-60.
132. Abou Neel, E.A., et al., *Effect of iron on the surface, degradation and ion release properties of phosphate-based glass fibres.* Acta Biomater, 2005. **1**(5): p. 553-63.
133. Ma, L., R.K. Brow, and M.E. Schlesinger, *Dissolution behavior of Na2O–FeO–Fe2O3–P2O5 glasses.* Journal of Non-Crystalline Solids, 2017. **463**: p. 90-101.
134. Mouriño, V., J.P. Cattalini, and A.R. Boccaccini, *Metallic ions as therapeutic agents in tissue engineering scaffolds: an overview of their biological applications and strategies for new developments.* Journal of The Royal Society Interface, 2012. **9**(68): p. 401-419.
135. Gough, J.E., et al., *Synthesis, degradation, and in vitro cell responses of sodium phosphate glasses for craniofacial bone repair.* J Biomed Mater Res, 2002. **59**(3): p. 481-9.
136. Parsons, A.J., et al., *Synthesis and degradation of sodium iron phosphate glasses and their in vitro cell response.* J Biomed Mater Res A, 2004. **71**(2): p. 283-91.
137. Bitar, M., et al., *Soluble phosphate glasses: in vitro studies using human cells of hard and soft tissue origin.* Biomaterials, 2004. **25**(12): p. 2283-2292.
138. Gough, J.E., et al., *Long-term craniofacial osteoblast culture on a sodium phosphate and a calcium/sodium phosphate glass.* J Biomed Mater Res A, 2003. **66**(2): p. 233-40.
139. Muñoz, F., et al., *The effect of the hydrostatic pressure on the drawing process of phosphate glass fibres.* Glass Technology - European Journal of Glass Science and Technology Part A, 2006. **47**(4): p. 97-102.
140. Kostikov, V.I. and V.I. Kostikov, *Fibre Science and Technology*. 1995: Springer.
141. Sharmin, N., et al., *Structure, viscosity and fibre drawing properties of phosphate-based glasses: effect of boron and iron oxide addition.* Journal of Materials Science, 2016. **51**(16): p. 7523-7535.
142. Parsons, A.J., et al., *Viscosity profiles of phosphate glasses through combined quasi-static and bob-in-cup methods.* Journal of Non-Crystalline Solids, 2015. **408**: p. 76-86.

143. Kasuga, T., et al., *Apatite Formation on Calcium Phosphate Invert Glasses in Simulated Body Fluid.* Journal of the American Ceramic Society, 2001. **84**(2): p. 450-52.
144. Bingham, P.A., et al., *Effects of modifier additions on the thermal properties, chemical durability, oxidation state and structure of iron phosphate glasses.* Journal of Non-Crystalline Solids, 2009. **355**(28): p. 1526-1538.
145. Brow, R.K., et al., *The short-range structure of zinc polyphosphate glass.* Journal of Non-Crystalline Solids, 1995. **191**(1): p. 45-55.
146. Sharmin, N., et al., *Effect of boron oxide addition on fibre drawing, mechanical properties and dissolution behaviour of phosphate-based glass fibres with fixed 40, 45 and 50 mol% P(2)O(5).* Journal of Biomaterials Applications, 2014. **29**(5): p. 639-653.
147. Lund, M.D. and Y. Yue, *Impact of Drawing Stress on the Tensile Strength of Oxide Glass Fibers.* Journal of the American Ceramic Society, 2010. **93**(10): p. 3236-3243.
148. *Density and thermal expansion*, in *Introduction to Glass Science and Technology (2)*, J.E. Shelby, Editor. 2005, The Royal Society of Chemistry. p. 138-162.
149. Stockhorst, H. and R. Brückner, *Structure sensitive measurements on phosphate glass fibers.* Journal of Non-Crystalline Solids, 1986. **85**(1): p. 105-126.
150. Muñoz, F., et al., *A study on the anisotropy of phosphate glass fibres.* Glass Technology - European Journal of Glass Science and Technology Part A, 2008. **49**(1): p. 47-52.
151. Endo, J., S. Inaba, and S. Ito, *Mechanical Properties of Anisotropic Metaphosphate Glass.* Journal of the American Ceramic Society, 2015. **98**(9): p. 2767-2771.
152. Inaba, S., H. Hosono, and S. Ito, *Entropic shrinkage of an oxide glass.* Nat Mater, 2015. **14**(3): p. 312-317.
153. Yablon, A.D., *Optical and mechanical effects of frozen-in stresses and strains in optical fibers.* IEEE Journal of Selected Topics in Quantum Electronics, 2004. **10**(2): p. 300-311.
154. Lezzi, P.J. and M. Tomozawa, *An Overview of the Strengthening of Glass Fibers by Surface Stress Relaxation.* International Journal of Applied Glass Science, 2015. **6**(1): p. 34-44.
155. Ya, M., J. Deubener, and Y. Yue, *Enthalpy and Anisotropy Relaxation of Glass Fibers.* Journal of the American Ceramic Society, 2008. **91**(3): p. 745-752.
156. Ahmed, I., et al., *Phosphate glasses for tissue engineering: Part 2. Processing and characterisation of a ternary-based P2O5–CaO–Na2O glass fibre system.* Biomaterials, 2004. **25**(3): p. 501-507.
157. Ahmed, I., et al., *Phosphate glasses for tissue engineering: Part 1. Processing and characterisation of a ternary-based P2O5–CaO–Na2O glass system.* Biomaterials, 2004. **25**(3): p. 491-499.
158. Cozien-Cazuc, S., et al., *Effects of aqueous aging on the mechanical properties of P40Na20Ca16Mg24 phosphate glass fibres.* Journal of Materials Science, 2008. **43**(14): p. 4834-4839.
159. Choueka, J., et al., *Effect of annealing temperature on the degradation of reinforcing fibers for absorbable implants.* Journal of Biomedical Materials Research, 1995. **29**(11): p. 1309-1315.
160. Abou Neel, E.A., et al., *A Facile Synthesis Route to Prepare Microtubes from Phosphate Glass Fibres.* Advanced Materials, 2007. **19**(19): p. 2856-2862.

161. Massera, J., et al., *Phosphate-based glass fiber vs. bulk glass: Change in fiber optical response to probe in vitro glass reactivity.* Materials Science and Engineering: C, 2014. **37**: p. 251-257.
162. Haque, P., et al., *Degradation properties and microstructural analysis of 40P2O5–24MgO–16CaO–16Na2O–4Fe2O3 phosphate glass fibres.* Journal of Non-Crystalline Solids, 2013. **375**: p. 99-109.
163. Zhou, M., et al., *Transcrystalline formation and properties of polypropylene on the surface of ramie fiber as induced by shear or dopamine modification.* Polymer, 2014. **55**(13): p. 3045-3053.
164. Nygard, P. and C.-G. Gustafson, *Continuous Glass Fiber–Polypropylene Composites Made by Melt Impregnation: Influence of Processing Method.* Journal of Thermoplastic Composite Materials, 2004. **17**(2): p. 167-184.
165. Mallick, P.K., *Fiber-Reinforced Composites: Materials, Manufacturing, and Design, Second Edition*. 1993: Taylor & Francis.
166. Callister, W.D. and D.G. Rethwisch, *Materials Science and Engineering: An Introduction, 9th Edition: Ninth Edition*. 2013: John Wiley and Sons, Incorporated.
167. Askeland, D.R., *Polymers*, in *The Science and Engineering of Materials*. 1996, Springer US: Boston, MA. p. 488-548.
168. Mezzenga, R., L. Boogh, and J.-A.E. Månson, *A review of dendritic hyperbranched polymer as modifiers in epoxy composites.* Composites Science and Technology, 2001. **61**(5): p. 787-795.
169. Ballo, A. and T. Närhi, *3 - Biocompatibility of fiber-reinforced composites for dental applications A2 - Shelton, Richard*, in *Biocompatibility of Dental Biomaterials*. 2017, Woodhead Publishing. p. 23-39.
170. Tuusa, S.M.-R., et al., *Residual monomers released from glass-fibre-reinforced composite photopolymerised in contact with bone and blood.* Journal of Materials Science: Materials in Medicine, 2005. **16**(1): p. 15-20.
171. Muzzy, J.D. and A.O. Kays, *Thermoplastic vs. thermosetting structural composites.* Polymer Composites, 1984. **5**(3): p. 169-172.
172. Stefanovska, M., Samakoski, B., Risteska, S., Maneski, G. , *Influence of Some Technological Parameters on the Content of Voids in Composite during On-Line Consolidation with Filament Winding Technology* International Journal of Chemical, Biomolecular, Metallurgical, Materials Science and Engineering, 2014. **8**(5): p. 347-351.
173. Vaidya, U.K. and K.K. Chawla, *Processing of fibre reinforced thermoplastic composites.* International Materials Reviews, 2008. **53**(4): p. 185-218.
174. Vaidya, U.K., et al., *The process and microstructure modeling of long-fiber thermoplastic composites.* JOM, 2008. **60**(4): p. 43.
175. Chin, W.-K. and S.-W. Yang, *Mechanical properties of short fiber reinforced thermoplastic composites —I. Elastic properties and predictions.* Journal of Polymer Research, 1995. **2**(1): p. 31-37.
176. Thomason, J.L., *The influence of fibre length and concentration on the properties of glass fibre reinforced polypropylene: 5. Injection moulded long and short fibre PP.* Composites Part A: Applied Science and Manufacturing, 2002. **33**(12): p. 1641-1652.
177. Wolf, H.J., *Screw plasticating of discontinuous fiber filled thermoplastic: Mechanisms and prevention of fiber attrition.* Polymer Composites, 1994. **15**(5): p. 375-383.
178. Phelps, J.H., et al., *A model for fiber length attrition in injection-molded long-fiber composites.* Composites Part A: Applied Science and Manufacturing, 2013. **51**: p. 11-21.

179. van Rijswijk, K. and H.E.N. Bersee, *Reactive processing of textile fiber-reinforced thermoplastic composites – An overview.* Composites Part A: Applied Science and Manufacturing, 2007. **38**(3): p. 666-681.
180. Carlsson, A. and B. Tomas Åström, *Experimental investigation of pultrusion of glass fibre reinforced polypropylene composites.* Composites Part A: Applied Science and Manufacturing, 1998. **29**(5): p. 585-593.
181. Bourban, P.E., et al., *Material phenomena controlling rapid processing of thermoplastic composites.* Composites Part A: Applied Science and Manufacturing, 2001. **32**(8): p. 1045-1057.
182. Seo, J.W. and W.I. Lee, *A Model of the Resin Impregnation in Thermoplastic Composites.* Journal of Composite Materials, 1991. **25**(9): p. 1127-1142.
183. Baran, I., R. Akkerman, and J.H. Hattel, *Modelling the pultrusion process of an industrial L-shaped composite profile.* Composite Structures, 2014. **118**: p. 37-48.
184. Miller, A.H., et al., *High speed pultrusion of thermoplastic matrix composites.* Composites Part A: Applied Science and Manufacturing, 1998. **29**(7): p. 773-782.
185. Novo, P.J., et al., *Pultrusion of fibre reinforced thermoplastic pre-impregnated materials.* Composites Part B: Engineering, 2016. **89**: p. 328-339.
186. Marissen, R., L. Th. van der Drift, and J. Sterk, *Technology for rapid impregnation of fibre bundles with a molten thermoplastic polymer.* Composites Science and Technology, 2000. **60**(10): p. 2029-2034.
187. Babeau, A., et al., *Modeling of heat transfer and unsaturated flow in woven fiber reinforcements during direct injection-pultrusion process of thermoplastic composites.* Composites Part A: Applied Science and Manufacturing, 2015. **77**: p. 310-318.
188. Muzzy, J.D., X. Wu, and J.S. Colton, *Thermoforming of high performance thermoplastic composites.* Polymer Composites, 1990. **11**(5): p. 280-285.
189. Wang, Z., et al., *A comparative study on the in vivo degradation of poly(L-lactide) based composite implants for bone fracture fixation.* Scientific Reports, 2016. **6**: p. 20770.
190. Felfel, R.M., et al., *Bioresorbable screws reinforced with phosphate glass fibre: Manufacturing and mechanical property characterisation.* Journal of the Mechanical Behavior of Biomedical Materials, 2013. **17**: p. 76-88.
191. Niemelä, T., et al., *Self-reinforced composites of bioabsorbable polymer and bioactive glass with different bioactive glass contents. Part I: Initial mechanical properties and bioactivity.* Acta Biomaterialia, 2005. **1**(2): p. 235-242.
192. Boccaccini, A.R. and V. Maquet, *Bioresorbable and bioactive polymer/Bioglass® composites with tailored pore structure for tissue engineering applications.* Composites Science and Technology, 2003. **63**(16): p. 2417-2429.
193. Lehtonen, T.J., J.U. Tuominen, and E. Hiekkanen, *Resorbable composites with bioresorbable glass fibers for load-bearing applications. In vitro degradation and degradation mechanism.* Acta Biomaterialia, 2013. **9**(1): p. 4868-4877.
194. Ahmed, I., et al., *Retention of mechanical properties and cytocompatibility of a phosphate-based glass fiber/polylactic acid composite.* Journal of Biomedical Materials Research Part B: Applied Biomaterials, 2009. **89B**(1): p. 18-27.
195. Han, N., et al., *Influence of screw holes and gamma sterilization on properties of phosphate glass fiber-reinforced composite bone plates.* Journal of Biomaterials Applications, 2011.

196. Niemelä, T., *Effect of β-tricalcium phosphate addition on the in vitro degradation of self-reinforced poly-l,d-lactide.* Polymer Degradation and Stability, 2005. **89**(3): p. 492-500.
197. Amass, W., A. Amass, and B. Tighe, *A review of biodegradable polymers: uses, current developments in the synthesis and characterization of biodegradable polyesters, blends of biodegradable polymers and recent advances in biodegradation studies.* Polymer International, 1998. **47**(2): p. 89-144.
198. Plackett, D., et al., *Biodegradable composites based on l-polylactide and jute fibres.* Composites Science and Technology, 2003. **63**(9): p. 1287-1296.
199. Thompson, I. and L.L. Hench, *6.39 - Medical Applications of Composites*, in *Comprehensive Composite Materials*, A. Kelly and C. Zweben, Editors. 2000, Pergamon: Oxford. p. 727-753.
200. Mano, J.F., et al., *Bioinert, biodegradable and injectable polymeric matrix composites for hard tissue replacement: state of the art and recent developments.* Composites Science and Technology, 2004. **64**(6): p. 789-817.
201. Gerhardt, L.-C. and A.R. Boccaccini, *Bioactive Glass and Glass-Ceramic Scaffolds for Bone Tissue Engineering.* Materials, 2010. **3**(7): p. 3867-3910.
202. Thompson, I.D. and L.L. Hench, *Mechanical properties of bioactive glasses, glass-ceramics and composites.* Proc Inst Mech Eng H, 1998. **212**(2): p. 127-36.
203. Metsger, D.S., M.R. Rieger, and D.W. Foreman, *Mechanical properties of sintered hydroxyapatite and tricalcium phosphate ceramic.* J Mater Sci Mater Med, 1999. **10**(1): p. 9-17.
204. Bonfield, W., *Hydroxyapatite-reinforced polyethylene as an analogous material for bone replacement.* Ann N Y Acad Sci, 1988. **523**: p. 173-7.
205. Wang, M., L.L. Hench, and W. Bonfield, *Bioglass/high density polyethylene composite for soft tissue applications: preparation and evaluation.* J Biomed Mater Res, 1998. **42**(4): p. 577-86.
206. Bonfield, W., *Composites for bone replacement.* Journal of Biomedical Engineering, 1988. **10**(6): p. 522-526.
207. Blaker, J.J., et al., *Premature degradation of poly(alpha-hydroxyesters) during thermal processing of Bioglass-containing composites.* Acta Biomater, 2010. **6**(3): p. 756-62.
208. Niemela, T., et al., *Self-reinforced composites of bioabsorbable polymer and bioactive glass with different bioactive glass contents. Part I: Initial mechanical properties and bioactivity.* Acta Biomater, 2005. **1**(2): p. 235-42.
209. Niiranen, H., et al., *In vitro and in vivo behavior of self-reinforced bioabsorbable polymer and self-reinforced bioabsorbable polymer/bioactive glass composites.* J Biomed Mater Res A, 2004. **69**(4): p. 699-708.
210. Niemela, T., H. Niiranen, and M. Kellomaki, *Self-reinforced composites of bioabsorbable polymer and bioactive glass with different bioactive glass contents. Part II: In vitro degradation.* Acta Biomater, 2008. **4**(1): p. 156-64.
211. Zhang, K., et al., *Processing and properties of porous poly(L-lactide)/bioactive glass composites.* Biomaterials, 2004. **25**(13): p. 2489-500.
212. Ignatius, A.A., P. Augat, and L.E. Claes, *Degradation behavior of composite pins made of tricalcium phosphate and poly(L,DL-lactide).* Journal of Biomaterials Science, Polymer Edition, 2001. **12**(2): p. 185-194.
213. Prokop, A., et al., *Degradation of poly-L/DL-lactide versus TCP composite pins: a three-year animal study.* J Biomed Mater Res B Appl Biomater, 2005. **75**(2): p. 304-10.

214. Colquhoun, R. and K.E. Tanner, *Mechanical behaviour of degradable phosphate glass fibres and composites—a review.* Biomedical Materials, 2016. **11**(1): p. 014105.
215. Ahmed, I., et al., *Composites for bone repair: phosphate glass fibre reinforced PLA with varying fibre architecture.* Journal of Materials Science: Materials in Medicine, 2011. **22**(8): p. 1825-1834.
216. Han, N., et al., *Influence of screw holes and gamma sterilization on properties of phosphate glass fiber-reinforced composite bone plates.* Journal of Biomaterials Applications, 2013. **27**(8): p. 990-1002.
217. Felfel, R.M., et al., *Accelerated in vitro degradation properties of polylactic acid/phosphate glass fibre composites.* Journal of Materials Science, 2015. **50**(11): p. 3942-3955.
218. Kesenci, K., et al., *Preparation and properties of poly(L-lactide)/hydroxyapatite composites.* J Biomater Sci Polym Ed, 2000. **11**(6): p. 617-32.
219. Hile, D.D., S.A. Doherty, and D.J. Trantolo, *Prediction of resorption rates for composite polylactide/hydroxylapatite internal fixation devices based on initial degradation profiles.* J Biomed Mater Res B Appl Biomater, 2004. **71**(1): p. 201-5.
220. Damadzadeh, B., et al., *Effect of ceramic filler content on the mechanical and thermal behaviour of poly-L-lactic acid and poly-L-lactic-co-glycolic acid composites for medical applications.* J Mater Sci Mater Med, 2010. **21**(9): p. 2523-31.
221. Mathieu, L.M., P.E. Bourban, and J.A.E. Månson, *Processing of homogeneous ceramic/polymer blends for bioresorbable composites.* Composites Science and Technology, 2006. **66**(11–12): p. 1606-1614.
222. Shikinami, Y. and M. Okuno, *Bioresorbable devices made of forged composites of hydroxyapatite (HA) particles and poly-L-lactide (PLLA): Part I. Basic characteristics.* Biomaterials, 1999. **20**(9): p. 859-877.
223. Shasteen, C. and Y.B. Choy, *Controlling degradation rate of poly(lactic acid) for its biomedical applications.* Biomedical Engineering Letters, 2011. **1**(3): p. 163.
224. Feldman, D., *Composite materials technology. Processes and properties, P. K. Mallick and S. Newman, Eds., Hanser publishers, Munich-Vienna-New York, 1990.* Journal of Polymer Science Part A: Polymer Chemistry, 1992. **30**(2): p. 343-343.
225. Bader, M.G., *Selection of composite materials and manufacturing routes for cost-effective performance.* Composites Part A: Applied Science and Manufacturing, 2002. **33**(7): p. 913-934.
226. Kazmi, S.M.R., K. Jayaraman, and R. Das, *Single-step manufacturing of curved polypropylene composites using a unique sheet consolidation method.* Journal of Materials Processing Technology, 2016. **237**: p. 96-112.
227. Parsons, A.J., et al., *Phosphate Glass Fibre Composites for Bone Repair.* Journal of Bionic Engineering, 2009. **6**(4): p. 318-323.
228. Jones, R.M., *Mechanics Of Composite Materials*. 1998: Taylor & Francis.
229. Ahmed, I., et al., *Weight loss, ion release and initial mechanical properties of a binary calcium phosphate glass fibre/PCL composite.* Acta Biomater, 2008. **4**(5): p. 1307-14.
230. Hasan, M.S., et al., *The influence of coupling agents on mechanical property retention and long-term cytocompatibility of phosphate glass fibre reinforced PLA composites.* Journal of the Mechanical Behavior of Biomedical Materials, 2013. **28**: p. 1-14.

231. Felfel, R.M., et al., *In vitro degradation, flexural, compressive and shear properties of fully bioresorbable composite rods.* Journal of the Mechanical Behavior of Biomedical Materials, 2011. **4**(7): p. 1462-1472.
232. Sharmin, N., et al., *Cytocompatibility, mechanical and dissolution properties of high strength boron and iron oxide phosphate glass fibre reinforced bioresorbable composites.* Journal of the Mechanical Behavior of Biomedical Materials, 2016. **59**: p. 41-56.
233. Shah Mohammadi, M., et al., *Effect of phosphate-based glass fibre surface properties on thermally produced poly(lactic acid) matrix composites.* Journal of Materials Science: Materials in Medicine, 2011. **22**(12): p. 2659-2672.
234. Salih, V., et al., *Development of soluble glasses for biomedical use Part II: The biological response of human osteoblast cell lines to phosphate-based soluble glasses.* Journal of Materials Science: Materials in Medicine, 2000. **11**(10): p. 615-620.
235. Rahaman, M.N., et al., *Bioactive glass in tissue engineering.* Acta biomaterialia, 2011. **7**(6): p. 2355-2373.
236. Lindfors, N.C., et al., *A prospective randomized 14-year follow-up study of bioactive glass and autogenous bone as bone graft substitutes in benign bone tumors.* Journal of Biomedical Materials Research Part B: Applied Biomaterials, 2010. **94B**(1): p. 157-164.
237. Huang, W., et al., *Mechanisms for converting bioactive silicate, borate, and borosilicate glasses to hydroxyapatite in dilute phosphate solution.* Physics and Chemistry of Glasses - European Journal of Glass Science andTechnology Part B, 2006. **47**(6): p. 647-658.
238. Fagerlund, S. and L. Hupa, *Chapter 1 Melt-derived Bioactive Silicate Glasses*, in *Bioactive Glasses: Fundamentals, Technology and Applications*. 2017, The Royal Society of Chemistry. p. 1-26.
239. Haanappel, S.P., et al., *Forming of thermoplastic composites*, in *Key Engineering Materials*. 2012. p. 237-242.
240. Tanaka, K., et al., *Formability evaluation of non-crimp carbon fabric by non-contact 3D deformation measurement system*, in *Key Engineering Materials*. 2012. p. 493-496.
241. Khazanov, V.E., Y.I. Kolesov, and N.N. Trofimov, *Glass fibres*, in *Fibre Science and Technology*, V.I. Kostikov, Editor. 1995, Springer Netherlands: Dordrecht. p. 15-230.
242. *Standard Test Methods for Void Content of Reinforced Plastics*. 2016, ASTM International.
243. *Standard Test Methods for Density and Specific Gravity (Relative Density) of Plastics by Displacement*. 2013, ASTM International.
244. *Standard Test Method for Ignition Loss of Cured Reinforced Resins*. 2011, ASTM International.
245. Mohanty, A.K., M. Misra, and L.T. Drzal, *Natural Fibers, Biopolymers, and Biocomposites*. 2005: CRC Press.
246. Rich, J., et al., *In vitro evaluation of poly(ε-caprolactone-co-DL-lactide)/bioactive glass composites.* Biomaterials, 2002. **23**(10): p. 2143-2150.
247. Fambri, L. and C. Migliaresi, *Crystallization and Thermal Properties*, in *Poly(Lactic Acid): Synthesis, Structures, Properties, Processing, and Applications*. 2010. p. 113-124.
248. Arstila, H., et al., *Influence of heat treatment on crystallization of bioactive glasses.* Journal of Non-Crystalline Solids, 2008. **354**(2): p. 722-728.

249. Ylänen, H., et al., *Effect of immersion in SBF on porous bioactive bodies made by sintering bioactive glass microspheres.* Journal of Non-Crystalline Solids, 2000. **275**(1): p. 107-115.
250. Hasan, M.S., *Phosphate Glass Fibre Reinforced Composite for Bone Repair Applications: Investigation of Interfacial Integrity Improvements via Chemical Treatments*, in *Faculty of Engineering*. 2012, University of Nottingham: United Kingdom.
251. Muñoz, F., et al., *A study on the anisotropy of phosphate glass fibres.* Glass Technology: European Journal of Glass Science and Technology Part A, 2008. **49**(1): p. 47-52.
252. Abou Neel, E.A., et al., *Bioactive functional materials: a perspective on phosphate-based glasses.* Journal of Materials Chemistry, 2009. **19**(6): p. 690-701.
253. Kurkjian, C.R., *Mechanical properties of phosphate glasses.* Journal of Non-Crystalline Solids, 2000. **263–264**(0): p. 207-212.
254. Cozien-Cazuc, S., *Characterisation of Resorbable Phosphate Glass Fibres*, in *Faculty of Engineering*. 2006, The University of Nottingham: United Kingdom.
255. Badrinarayanan, P., et al., *The glass transition temperature versus the fictive temperature.* Journal of Non-Crystalline Solids, 2007. **353**(26): p. 2603-2612.
256. Queiroz, C.A. and J. esták, *Aspects of the non-crystalline state.* Physics and Chemistry of Glasses - European Journal of Glass Science andTechnology Part B, 2010. **51**(3): p. 165-172.
257. Matthieu, M., *Relaxation and physical aging in network glasses: a review.* Reports on Progress in Physics, 2016. **79**(6): p. 066504.
258. Gabbott, P., *A Practical Introduction to Differential Scanning Calorimetry*, in *Principles and Applications of Thermal Analysis*. 2008, Blackwell Publishing Ltd. p. 1-50.
259. Hayden, J.S., et al., *Surface tensile layer generation during thermal annealing of phosphate glass.* Journal of Non-Crystalline Solids, 2000. **263**: p. 228-239.
260. Suratwala, T.I., et al., *Effects of OH content, water vapor pressure, and temperature on sub-critical crack growth in phosphate glass.* Journal of Non-Crystalline Solids, 2000. **263**: p. 213-227.
261. Kingery, W.D., *Introduction to ceramics*. 1960: Wiley.
262. Thomason, J., P. Jenkins, and L. Yang, *Glass Fibre Strength—A Review with Relation to Composite Recycling.* Fibers, 2016. **4**(2): p. 18.
263. Yu, X., et al., *Properties and structure of sodium-iron phosphate glasses.* Journal of Non-Crystalline Solids, 1997. **215**(1): p. 21-31.
264. Delahaye, F., et al., *Acid dissolution of sodium–calcium metaphosphate glasses.* Journal of Non-Crystalline Solids, 1998. **242**(1): p. 25-32.
265. Kura, G., *Liquid chromatographic study of the hydrolysis reactions of cyclic and linear polyphosphates in aqueous solution.* Journal of Chromatography A, 1988. **447**: p. 91-101.
266. Dohler, F., et al., *31P NMR characterisation of phosphate fragments during dissolution of calcium sodium phosphate glasses.* Journal of Materials Chemistry B, 2015. **3**(6): p. 1125-1134.
267. Luo, Z., et al., *Liquid crystalline phase behavior and fiber spinning of cellulose/ionic liquid/halloysite nanotubes dispersions.* Journal of Materials Chemistry A, 2014. **2**(20): p. 7327-7336.
268. Song, H., et al., *Liquid Crystalline Phase and Gel–Sol Transitions for Concentrated Microcrystalline Cellulose (MCC)/1-Ethyl-3-methylimidazolium Acetate (EMIMAc) Solutions.* Biomacromolecules, 2011. **12**(4): p. 1087-1096.

269. Menard, K.P., *Dynamic Mechanical Analysis: A Practical Introduction, Second Edition*. 2008: CRC Press.
270. Signori, F., M.-B. Coltelli, and S. Bronco, *Thermal degradation of poly(lactic acid) (PLA) and poly(butylene adipate-co-terephthalate) (PBAT) and their blends upon melt processing.* Polymer Degradation and Stability, 2009. **94**(1): p. 74-82.
271. Lekakou, C., M.A.K.B. Johari, and M.G. Bader, *Compressibility and flow permeability of two-dimensional woven reinforcements in the processing of composites.* Polymer Composites, 1996. **17**(5): p. 666-672.
272. Ahmadi Z., G.S.R., Amiri D., *Continuous melt impregnation process: Materials parameters.* Iranian Polymer Journal (English) 2000. **9**(2): p. 125-130.
273. Mayer, C., X. Wang, and M. Neitzel, *Macro- and micro-impregnation phenomena in continuous manufacturing of fabric reinforced thermoplastic composites.* Composites Part A: Applied Science and Manufacturing, 1998. **29**(7): p. 783-793.
274. Liu, L., et al., *Effects of cure cycles on void content and mechanical properties of composite laminates.* Composite Structures, 2006. **73**(3): p. 303-309.
275. Hagstrand, P.O., F. Bonjour, and J.A.E. Månson, *The influence of void content on the structural flexural performance of unidirectional glass fibre reinforced polypropylene composites.* Composites Part A: Applied Science and Manufacturing, 2005. **36**(5): p. 705-714.
276. Thomason, J.L., *The interface region in glass fibre-reinforced epoxy resin composites: 1. Sample preparation, void content and interfacial strength.* Composites, 1995. **26**(7): p. 467-475.
277. Ruiz, E., et al., *Optimization of injection flow rate to minimize micro/macro-voids formation in resin transfer molded composites.* Composites Science and Technology, 2006. **66**(3–4): p. 475-486.
278. Mallick, P.K., *Composites Engineering Handbook*. 1997: Taylor & Francis.
279. Blaker, J.J., et al., *Wetting of bioactive glass surfaces by poly(alpha-hydroxyacid) melts: interaction between Bioglass (R) and biodegradable polymers*. 2005, EUROPEAN POLYMER FEDERATION.
280. Kang, M.K., W.I. Lee, and H.T. Hahn, *Formation of microvoids during resin-transfer molding process.* Composites Science and Technology, 2000. **60**(12–13): p. 2427-2434.
281. Othman, N., et al., *Wall slip and melt fracture of poly(lactides).* Rheologica Acta, 2011. **51**(4): p. 357-369.
282. Dorgan, J., H. Lehermeier, and M. Mang, *Thermal and Rheological Properties of Commercial-Grade Poly(Lactic Acid)s.* Journal of Polymers and the Environment, 2000. **8**(1): p. 1-9.
283. Xiao-chun, Y., et al., *Influence of pressure oscillation on injection molding process.* Journal of Thermoplastic Composite Materials, 2014. **27**(10): p. 1417-1427.
284. Yan, Z., et al., *Effect of vibration on rheology of polymer melt.* Journal of Applied Polymer Science, 2002. **85**(8): p. 1587-1592.
285. Layser, G.S. and J.P. Coulter, *Localized effects of dynamic melt manipulation on flow induced orientation and mechanical performance of injection molded products.* Polymer Engineering & Science, 2007. **47**(11): p. 1912-1919.
286. Ibar, J.P., *Control of polymer properties by melt vibration technology: A review.* Polymer Engineering & Science, 1998. **38**(1): p. 1-20.
287. Barnes, H.A., Townsend, P., Walters, K. , *On pulsatile flow of non-Newtonian fluid.* Rheologica Acta, 1971. **10**: p. 517-527.

288. Felfel, R.M., et al., *Investigation of Crystallinity, Molecular Weight Change, and Mechanical Properties of PLA/PBG Bioresorbable Composites as Bone Fracture Fixation Plates.* Journal of Biomaterials Applications, 2012. **26**(7): p. 765-789.
289. Olivier, P., J.P. Cottu, and B. Ferret, *Effects of cure cycle pressure and voids on some mechanical properties of carbon/epoxy laminates.* Composites, 1995. **26**(7): p. 509-515.
290. Wetherhold, R.C., *Statistical distribution of strength of fiber-reinforced composite materials.* Polymer Composites, 1986. **7**(2): p. 116-123.
291. Thomason, J.L. and A.A. van Rooyen, *The Transcrystallised Interphase in Thermoplastic Composites*, in *Controlled Interphases in Composite Materials*, H. Ishida, Editor. 1990, Springer Netherlands. p. 423-430.
292. Le Moigne, N., et al., *Study of the interface in natural fibres reinforced poly(lactic acid) biocomposites modified by optimized organosilane treatments.* Industrial Crops and Products, 2014. **52**: p. 481-494.
293. Xu, H., et al., *Toward Stronger Transcrystalline Layers in Poly(l-lactic acid)/Natural Fiber Biocomposites with the Aid of an Accelerator of Chain Mobility.* The Journal of Physical Chemistry B, 2014. **118**(3): p. 812-823.
294. Han, S., et al., *Enhanced interfacial adhesion via interfacial crystallization between sisal fiber and isotactic polypropylene: direct evidence from single-fiber fragmentation testing.* Polymer International, 2014. **63**(4): p. 646-651.
295. Costantino, A., et al., *Microstructure of PP/clay Nanocomposites Produced by Shear Induced Injection Moulding.* Procedia Materials Science, 2012. **1**: p. 34-43.
296. Bilewicz, M., J.C. Viana, and L.A. Dobrza¨½ski, *Development of microstructure affected by in-mould manipulation in polymer composites and nanocomposites.* Journal of Achievements in Materials and Manufacturing Engineering, 2008.
297. Pan, P., et al., *Polymorphous Crystallization and Multiple Melting Behavior of Poly(l-lactide): Molecular Weight Dependence.* Macromolecules, 2007. **40**(19): p. 6898-6905.
298. Mano, J.F., et al., *Cold Crystallization of PLLA Studied by Simultaneous SAXS and WAXS.* Macromolecular Materials and Engineering, 2004. **289**(10): p. 910-915.
299. G. Kalay, C.O., P. S. Allan and M. J. Bevis, *The Management of Microstructure in Semi-Crystalline Polymers.* Chemical Engineering Research and Design, 1995. **73a**: p. 798-809.
300. Billon, N. and J. Haudin, *Influence of transcrystallinity on DSC analysis of polymers.* Journal of Thermal Analysis and Calorimetry, 1994. **42**(4): p. 679-696.
301. Pompe, G. and E. Mäder, *Experimental detection of a transcrystalline interphase in glass-fibre/polypropylene composites.* Composites Science and Technology, 2000. **60**(11): p. 2159-2167.
302. Chen, Y., et al., *Preparation of polypropylene/glass fiber composite with high performance through interfacial crystallization.* Journal of Vinyl and Additive Technology, 2015: p. n/a-n/a.
303. Quan, H., et al., *On transcrystallinity in semi-crystalline polymer composites.* Composites Science and Technology, 2005. **65**(7–8): p. 999-1021.
304. Carrasco, F., et al., *Processing of poly(lactic acid): Characterization of chemical structure, thermal stability and mechanical properties.* Polymer Degradation and Stability, 2010. **95**(2): p. 116-125.

305. Ikada, Y. and H. Tsuji, *Biodegradable polyesters for medical and ecological applications.* Macromolecular Rapid Communications, 2000. **21**(3): p. 117-132.
306. Bismarck, A., et al., *Surface characterization of glass fibers made from silicate waste: Zeta-potential and contact angle measurements.* Journal of Materials Science, 2004. **39**(2): p. 401-412.
307. Kellomäki, M. and P. Törmälä, *Self Reinforced Polylactides, Optimization of Degradation and Mechanical Properties*, in *Biodegradble Polymers*. 2003. p. 211-235.
308. Barrera Betanzos, F., et al., *Cyclic pressure on compression-moulded bioresorbable phosphate glass fibre reinforced composites.* Materials & Design, 2016. **100**: p. 141-150.
309. Ye, L., et al., *De-consolidation and re-consolidation in CF/PPS thermoplastic matrix composites.* Composites Part A: Applied Science and Manufacturing, 2005. **36**(7): p. 915-922.
310. Chen, Q., et al., *Intra/inter-ply shear behaviors of continuous fiber reinforced thermoplastic composites in thermoforming processes.* Composite Structures, 2011. **93**(7): p. 1692-1703.
311. Hou, M., K. Friedrich, and R. Scherer, *Optimization of stamp forming of thermoplastic composite bends.* Composite Structures, 1994. **27**(1–2): p. 157-167.
312. Guild, F.J., P.J. Davy, and P.J. Hogg, *A model for unidirectional composites in longitudinal tension and compression.* Composites Science and Technology, 1989. **36**(1): p. 7-26.
313. Mallick, P.K., *Fiber-reinforced composites: materials, manufacturing, and design*. 2008: CRC Press.
314. Wu, C.-H. and W.-J. Liang, *Effects of geometry and injection-molding parameters on weld-line strength.* Polymer Engineering & Science, 2005. **45**(7): p. 1021-1030.
315. Kim, J.K., et al., *Morphology and mechanical properties of injection molded articles with weld-lines.* Polymer Engineering & Science, 1997. **37**(1): p. 228-241.
316. Vaxman, A., et al., *Weld-line characteristics in short fiber reinforced thermoplastics.* Polymer Composites, 1991. **12**(3): p. 161-168.
317. Grammatikos, S.A., et al., *Moisture uptake characteristics of a pultruded fibre reinforced polymer flat sheet subjected to hot/wet aging.* Polymer Degradation and Stability, 2015. **121**: p. 407-419.
318. Lassila, L.V.J., T. Nohrström, and P.K. Vallittu, *The influence of short-term water storage on the flexural properties of unidirectional glass fiber-reinforced composites.* Biomaterials, 2002. **23**(10): p. 2221-2229.
319. Mishnaevsky Jr, L. and P. Brøndsted, *Micromechanical modeling of damage and fracture of unidirectional fiber reinforced composites: A review.* Computational Materials Science, 2009. **44**(4): p. 1351-1359.
320. Navarro, M., et al., *In vitro degradation behavior of a novel bioresorbable composite material based on PLA and a soluble CaP glass.* Acta Biomaterialia, 2005. **1**(4): p. 411-419.
321. Ishida, H. and J.L. Koenig, *The reinforcement mechanism of fiber-glass reinforced plastics under wet conditions: A review.* Polymer Engineering & Science, 1978. **18**(2): p. 128-145.
322. Hohlfeld, E. and B. Davidovitch, *Sheet on a deformable sphere: Wrinkle patterns suppress curvature-induced delamination.* Physical Review E, 2015. **91**(1): p. 012407.

323. Hutchinson, J.W., *Delamination of compressed films on curved substrates.* Journal of the Mechanics and Physics of Solids, 2001. **49**(9): p. 1847-1864.
324. Pirhonen, E., et al., *Manufacturing, mechanical characterization, and in vitro performance of bioactive glass 13–93 fibers.* Journal of Biomedical Materials Research Part B: Applied Biomaterials, 2006. **77B**(2): p. 227-233.
325. Radin, S., et al., *In vitro transformation of bioactive glass granules into Ca-P shells.* Journal of Biomedical Materials Research, 2000. **49**(2): p. 264-272.
326. Cle´ment, J., et al., *Analysis of the structural changes of a phosphate glass during its dissolution in simulated body fluid.* Journal of Materials Science: Materials in Medicine, 1999. **10**(12): p. 729-732.
327. Ma, L.N., *Dissolution Behavior of Phosphate Glasses*, in *Materials Science and Engineering*. 2014, Missouri University of Science and Technology: US.
328. Cozien-Cazuc, S., et al., *Real-time dissolution of P40Na20Ca16Mg24 phosphate glass fibers.* Journal of Non-Crystalline Solids, 2009. **355**(50–51): p. 2514-2521.
329. Shelby, J.E., *Introduction to Glass Science and Technology*. 2005: Royal Society of Chemistry.
330. Fan, B.-W., et al., *Effect of glass thickness on temperature gradient and stress distribution during glass tempering.* Journal of Non-Crystalline Solids, 2016. **437**: p. 72-79.
331. Gy, R., *Ion exchange for glass strengthening.* Materials Science and Engineering: B, 2008. **149**(2): p. 159-165.
332. Narayanaswamy, O.S. and R. Gardon, *Calculation of Residual Stresses in Glass.* Journal of the American Ceramic Society, 1969. **52**(10): p. 554-558.
333. Matteo, C., *Stress-corrosion mechanisms in silicate glasses.* Journal of Physics D: Applied Physics, 2009. **42**(21): p. 214006.
334. Agarwal, A., M. Tomozawa, and W.A. Lanford, *Effect of stress on water diffusion in silica glass at various temperatures.* Journal of Non-Crystalline Solids, 1994. **167**(1): p. 139-148.
335. Bunker, B.C., *Molecular mechanisms for corrosion of silica and silicate glasses.* Journal of Non-Crystalline Solids, 1994. **179**: p. 300-308.
336. Gao, H., T. Tan, and D. Wang, *Dissolution mechanism and release kinetics of phosphate controlled release glasses in aqueous medium.* Journal of Controlled Release, 2004. **96**(1): p. 29-36.
337. White, J.R., *Polymer ageing: physics, chemistry or engineering? Time to reflect.* Comptes Rendus Chimie, 2006. **9**(11–12): p. 1396-1408.
338. Celli, A. and M. Scandola, *Thermal properties and physical ageing of poly (l-lactic acid).* Polymer, 1992. **33**(13): p. 2699-2703.
339. Hiljanen-Vainio, M., et al., *Modification of poly(L-lactides) by blending: mechanical and hydrolytic behavior.* Macromolecular Chemistry and Physics, 1996. **197**(4): p. 1503-1523.
340. Paul, M.A., et al., *Polylactide/montmorillonite nanocomposites: study of the hydrolytic degradation.* Polymer Degradation and Stability, 2005. **87**(3): p. 535-542.
341. Zhou, Q. and M. Xanthos, *Nanoclay and crystallinity effects on the hydrolytic degradation of polylactides.* Polymer Degradation and Stability, 2008. **93**(8): p. 1450-1459.
342. Li, S., *Hydrolytic degradation characteristics of aliphatic polyesters derived from lactic and glycolic acids.* Journal of Biomedical Materials Research, 1999. **48**(3): p. 342-353.
343. Göpferich, A., *Mechanisms of polymer degradation and erosion.* Biomaterials, 1996. **17**(2): p. 103-114.

344. Mehboob, H. and S.-H. Chang, *Evaluation of healing performance of biodegradable composite bone plates for a simulated fractured tibia model by finite element analysis.* Composite Structures, 2014. **111**: p. 193-204.
345. Mehboob, H. and S.-H. Chang, *Application of composites to orthopedic prostheses for effective bone healing: A review.* Composite Structures, 2014. **118**: p. 328-341.
346. Vaxman, A., et al., *Void formation in short-fiber thermoplastic composites.* Polymer Composites, 1989. **10**(6): p. 449-453.
347. Titomanlio, G., S. Piccarolo, and G. Marrucci, *Analysis of void formation in extruded bars.* Polymer Engineering & Science, 1985. **25**(2): p. 91-97.
348. Wisnom, M.R., T. Reynolds, and N. Gwilliam, *Reduction in interlaminar shear strength by discrete and distributed voids.* Composites Science and Technology, 1996. **56**(1): p. 93-101.
349. Roy, R., B.K. Sarkar, and N.R. Bose, *Effects of moisture on the mechanical properties of glass fibre reinforced vinylester resin composites.* Bulletin of Materials Science, 2001. **24**(1): p. 87-94.
350. Tsenoglou, C.J., S. Pavlidou, and C.D. Papaspyrides, *Evaluation of interfacial relaxation due to water absorption in fiber–polymer composites.* Composites Science and Technology, 2006. **66**(15): p. 2855-2864.
351. Hutchinson, J.W. and H.M. Jensen, *Models of fiber debonding and pullout in brittle composites with friction.* Mechanics of Materials, 1990. **9**(2): p. 139-163.
352. Mishnaevsky, L. and P. Brøndsted, *Micromechanical modeling of damage and fracture of unidirectional fiber reinforced composites: A review.* Computational Materials Science, 2009. **44**(4): p. 1351-1359.
353. Costa, M.L., M.C. Rezende, and S.F.M. de Almeida, *Effect of Void Content on the Moisture Absorption in Polymeric Composites.* Polymer-Plastics Technology and Engineering, 2006. **45**(6): p. 691-698.
354. Wang, L. and G.H. Nancollas, *Calcium Orthophosphates: Crystallization and Dissolution.* Chemical reviews, 2008. **108**(11): p. 4628-4669.
355. Despotović, R., N. Filipović-Vinceković, and H. Füredi-Milhofer, *Precipitation of calcium phosphates from electrolyte solutions.* Calcified Tissue Research, 1975. **18**(1): p. 13-26.
356. Brečević, L. and H. Füredi-Milhofer, *Precipitation of calcium phosphates from electrolyte solutions.* Calcified Tissue Research, 1972. **10**(1): p. 82-90.
357. Amorin, N.S.Q.S., et al., *Study of thermodegradation and thermostabilization of poly(lactide acid) using subsequent extrusion cycles.* Journal of Applied Polymer Science, 2014. **131**(6): p. n/a-n/a.
358. Fortunati, E., et al., *Development and thermal behaviour of ternary PLA matrix composites.* Polymer Degradation and Stability, 2010. **95**(11): p. 2200-2206.
359. Valapa, R.b., P. G, and V. Katiyar, *Hydrolytic degradation behaviour of sucrose palmitate reinforced poly(lactic acid) nanocomposites.* International Journal of Biological Macromolecules, 2016. **89**: p. 70-80.
360. Klein, N., et al., *Determining the role of interfacial transcrystallinity in composite materials by dynamic mechanical thermal analysis.* Composites, 1995. **26**(10): p. 707-712.
361. Romanzini, D., et al., *Influence of fiber content on the mechanical and dynamic mechanical properties of glass/ramie polymer composites.* Materials & Design, 2013. **47**: p. 9-15.

362. Blaker, J.J., et al., *Premature degradation of poly(α-hydroxyesters) during thermal processing of Bioglass®-containing composites.* Acta Biomaterialia, 2010. **6**(3): p. 756-762.
363. Lehtonen, T.J., J.U. Tuominen, and E. Hiekkanen, *Dissolution behavior of high strength bioresorbable glass fibers manufactured by continuous fiber drawing.* Journal of the Mechanical Behavior of Biomedical Materials, 2013. **20**: p. 376-386.
364. Ding, Y.H., M. Floren, and W. Tan, *Mussel-inspired polydopamine for bio-surface functionalization.* Biosurface and Biotribology, 2016. **2**(4): p. 121-136.
365. Lee, H., et al., *Mussel-Inspired Surface Chemistry for Multifunctional Coatings.* Science, 2007. **318**(5849): p. 426-430.
366. Nielsen, S.R., F. Besenbacher, and M. Chen, *Mussel inspired surface functionalization of electrospun nanofibers for bio-applications.* Physical Chemistry Chemical Physics, 2013. **15**(40): p. 17029-17037.
367. Larranaga, A., et al., *Coating of bioactive glass particles with mussel-inspired polydopamine as a strategy to improve the thermal stability of poly(l-lactide)/bioactive glass composites.* RSC Advances, 2015. **5**(80): p. 65618-65626.
368. Yi, M., et al., *Flexible fiber-reinforced composites with improved interfacial adhesion by mussel-inspired polydopamine and poly(methyl methacrylate) coating.* Materials Science and Engineering: C, 2016. **58**: p. 742-749.
369. Wen, X., et al., *Constructing Novel Fiber Reinforced Plastic (FRP) Composites through a Biomimetic Approach: Connecting Glass Fiber with Nanosized Boron Nitride by Polydopamine Coating.* Journal of Nanomaterials, 2013. **2013**: p. 7.
370. Bourmaud, A., et al., *Investigations of the use of a mussel-inspired compatibilizer to improve the matrix-fiber adhesion of a biocomposite.* Polymer Testing, 2009. **28**(6): p. 668-672.
371. SAIKKU-BÄCKSTRÖM, A., et al., *Material properties of absorbable self-reinforced fibrillated poly-96L/4 D-lactide (SR-PLA96) rods; a study in vitro and in vivo.* Journal of Materials Science: Materials in Medicine, 1999. **10**(1): p. 1-8.
372. Lezzi, P.J., et al., *Strength increase of silica glass fibers by surface stress relaxation: A new mechanical strengthening method.* Journal of Non-Crystalline Solids, 2013. **379**: p. 95-106.
373. Lezzi, P.J., J.H. Seaman, and M. Tomozawa, *Strengthening of E-glass fibers by surface stress relaxation.* Journal of Non-Crystalline Solids, 2014. **402**: p. 116-127.